ABSTRACT

Title of Document: NUMERICAL MODELING OF BALCONY SPILL PLUMES USING FIRE DYNAMICS SIMULATOR (FDS)

Johnson Lim, Master of Science 2010

Directed By: Associate Professor Arnaud Trouvé , Department of Fire Protection Engineering

Trends in modern architectural design have led to the proliferation of large atrium buildings. Fires in such buildings can result in significant loss of life and property damage as the propagation of smoke is unimpeded. The design of effective smoke management systems for atrium buildings requires reliable calculation methods to predict the quantity of smoke produced. Numerical modeling using FDS is performed in this research to examine the entrainment processes as the smoke flows from a compartment, through a balcony before discharging into an atrium. Different fire sizes and geometrical configurations are analyzed and empirical correlations are proposed for the mass flow rate of smoke at the spill edge and for the entrainment as the smoke rotates upwards around the spill edge. These correlations show good agreement with experimental data from previous work.

NUMERICAL MODELING OF BALCONY SPILL PLUMES USING FIRE DYNAMICS SIMULATOR (FDS)

By

Johnson Meng Kee Lim

Thesis submitted to the Faculty of the Graduate School of the
University of Maryland, College Park, in partial fulfillment
of the requirements for the degree of

Master of Science

2010

Advisory Committee:

Professor Arnaud Trouvé, Chair

Professor James A. Milke

Professor James G. Quintiere

Dedication

To my wife, Catherine and daughter,Clarice.

Acknowledgements

I would like to thank the Defence Science & Technological Agency for sponsoring my studies and giving me the opportunity to embark on this wonderful journey of education in fire science.

I would like to express my heartfelt gratitude to my advisors, Professor Arnaud Trouvé and Professor James Milke for their patience, advice and motivation throughout the entire course of my research. Without your support and guidance, none of this would not have been possible. Many thanks to Professor James Quintiere for his valuable time and support in the advisory committee, and for all the knowledge you have imparted me. I would also like to extend my appreciation to all faculties and staff of the Department of Fire Protection Engineering who has helped me throughout my stay in the University of Maryland. I would also like to thank my friends Ren Ning, Zheng Yinghui, Ding Haiwen, Wang Lei, Tom Dotson, Meghan Mckeever and Charles Chan for their encouragement and support.

Last but not least, I would like to thank my wonderful wife, Catherine, for all her sacrifices, encouragement and unwavering support.

Table of Contents

List of Tables

List of Figures

Nomenclature

Symbol	Description
A	Area (m^2)
b	Balcony breadth (m)
c	Heat of combustion (kJ/kg^1)
C	Entrainment Coefficient ($kgm/s.kW^{1/3}$)
C_m	Dimensionless entrainment coefficient
C_e	Entrainment Coefficient ($kg/s^1.m^{5/2}$)
c_p	Specific heat ($J/kg.K^{-1}$)
C_d	Coefficient of discharge
d	Depth of gas layer (m)
d_d	Depth of downstand (m)
D	Diameter (m)
g	Acceleration due to gravity (m/s^2)
h	Height above floor (m)
h_c	Convective heat transfer coefficient ($W/m^2.K$)
H	Ceiling height (m)
k	Thermal conductivity (W/m.K)
l	Characteristic length
l_T	Thickness of ceiling jet (m)
L	Characteristic linear height of the model
m	Mass
$\dot{m}$	Mass flow rate of gasses (kg/s)
$\dot{m}_{rot}$	Mass flow rate of air entrained into the rotation region (kg/s)
N	Height of neutral plane (m)
p	Fire perimeter (m)
Pr	Prandtl number
r	Radial distance (m)
Re	Reynolds number
$\dot{Q}_c$	Convective heat flow in the gas layer below the spill edge (kW)

$\dot{Q}$	Total heat generated by the fire (kW)
Q_H^*	Non-dimensional heat release rate
t_r	Response time of sprinkler or detector (s)
T	Absolute gas temperature (K)
T_r	Rated operating temperature of sprinkler or detector (°C)
T_{wall}	Surface temperature of wall (K)
$\bar{T}$	Mass weighted average absolute gas temperature (K)
u	Velocity (m/s)
u^+	Normalized streamwise velocity
W	Width or lateral extent (m)
δx	Grid cell size (m)
z	Vertical distance (m)
z_s	Height of rise of plume above the spill edge (m)
z_o	Height of virtual line source below the spill edge (m)
z^+	Normalized wall-normal distance

Greek symbol	Description
α	Entrainment constant for plume
α'	Entrainment constant for air mixing into the rotation region
γ	Regression coefficient
δ	Regression coefficient
ε	Regression coefficient
θ	Temperature above ambient (^{o}C)
$\bar{\theta}$	Mass weighted average temperature above ambient (^{o}C)
ρ	Density (kgm^{-3})
$\bar{\rho}$	Mass weighted average density (kg/m^3)
κ_m	Profile correction factor for mass flow rate of gases
τ	Time constant
τ_w	Wall shear stress (Pa)
μ	dynamic viscosity (kg/s.m)
λ	An empirical thermal plume constant

List of subscripts	Description
∞	An ambient property
air	A property of air
b	A property of balcony
e	An effective property
f	A property evaluated on full scale
m	A property evaluated on model scale
max	A maximum value
o	A property of fire compartment opening
p	Variable evaluated in the plume at an arbitrary height of rise
$room$	Variable evaluated within the fire compartment (room)
s	Variable evaluated in the gas layer flow below the spill edge
w	Variable evaluated in the horizontal layer flow at the fire compartment opening
$2D$	Two-dimensional spill plume

1. Introduction

1.1 Background

Modern architectural design trends have led to an increase in the integration of large, undivided spaces with many of the storeys. This feature is regularly found in shopping malls, airport terminals and hotels. The generic term “atrium” can be used to describe such large spaces within the building. The concept of an atrium can be found in Roman architecture, where it was used as an entrance hall in a house (1). The present day atrium is much larger and taller than the typical Roman house. At present, the tallest atrium at 182 m is located within the Burj Al Arab in Dubai, while the atrium with the largest volume of 820,000 m^3 is in the Luxor Hotel in Las Vegas, Nevada. The design intent of present day atria is to create visually and spatially an ideal external environment, indoors (1). Hence these atria are usually designed such that they are connected directly to the adjacent rooms or spaces over the height of the atria and the boundary with the adjacent spaces are usually glazed or completely open.

Atrium design contradicts the traditional compartmentation approach of fire protection to limit the spread of fire and smoke to areas of the building not directly affected by the fire. This lack of physical separation between spaces allows smoke to travel freely to areas remote from the fire source within short periods of time, hence putting more building occupants at risk at an early stage of the fire. Furthermore, atrium buildings can contain large amounts of combustibles and house a large number

of occupants. Hence, any fire occurring in these buildings would expose a large number of people to smoke, heat and toxic gases and the spread of fire and smoke would cause significant property damage.

Unprotected openings between adjacent rooms and the atrium, also known as communicating spaces, allows the unimpeded movement of smoke and affecting other areas of the building. Thus, the use of an effective smoke management system is essential to allow safe egress of occupants from the building by separating the occupants from the smoke or by providing a tenable condition for egress. An effective smoke management system also provides improved conditions for fire-fighting operations and rescue operations, and limits the spread and temperature of smoke by venting.

1.2 Smoke Hazards

Smoke is defined in NFPA 92B (2) as "The airborne solid and liquid particulates and gases evolved when a material undergoes pyrolysis or combustion, together with the quantity of air that is entrained or otherwise mixed into the mass." Smoke is generally recognized as the major cause of fatalities in fires and smoke has been known to cause death to building occupants who are remote from the fire (3), as in the case of the MGM Grand Fire where the majority of the 85 fatalities were at least 16 floors away from the fire which was located on the ground floor. People who are exposed to smoke for a sufficient period of time can be harmed as a result of exposure to toxic gases and high temperature. Smoke can also reduce visibility due to light obscuration, causing disorientation and increased evacuation time.

1.2.1 Smoke Toxicity

Smoke toxicity is as a result of exposure to asphyxiant gases, such as carbon monoxide (CO), carbon dioxide (CO_2) and hydrogen cyanide (HCN) and irritants, such as halogen acids, oxides of Nitrogen (NO_x), present in the combustion products. Generally, asphyxiant gases disturb the normal respiratory process after a sufficient dose has been inhaled. CO causes anemic hypoxia, which is the decrease in oxygen-carrying capacity of the blood to tissues (4). HCN prevents the cells of the body from utilizing oxygen properly (5). Excessive CO_2 stimulates breathing thus increasing the uptake of gases. It may also be an asphyxiant when the concentration level is greater than 5% (5). Asphyxiant gases may not have an immediate effect, but once incapacitation occurs, serious injuries or death is likely to occur within minutes. Irritant gases cause sensory and pulmonary irritations which reduces the efficiency of the building occupant to escape from the fire. Irritation of the eyes causes pain, reflex blinking and tearing, with severe irritation possibly leading to eye damage. Victims may shut their eyes, alleviating these effects temporarily, but impairing their egress, hence prolonging their exposure. Pulmonary irritation affects the lungs, causing coughing and bronchoconstriction, which leads to tissue inflammation and damage. In severe cases, it causes death within 6 to 48 hours (4).

1.2.2 Elevated Temperatures

Building occupants in a fire can be exposed to elevated temperatures by means of convected heat or radiant heat. When subjected to elevated temperatures, people may be incapacitated by hyperthermia (heat stroke), body surface burns and respiratory

tract burns. Tenability limits for radiant heat flux, temperature and exposure times are provided by Purser (5).

1.2.3 Light Obscuration

Light obscuration is not lethal by itself, but causes reduction in visibility, which results in the disorientation of building occupants and thus increases the evacuation time and exposure to smoke. Reduction in visibility also increases the susceptibility of building occupants tripping over obstacles and falling over railings. It also hamper fire-fighting and rescue operations. Limiting values of extinction coefficient ranging from 0.23 to 1.2 m^{-1} has been suggested (6). Design guidance by Spearpoint (7) suggests values of visibility of 5m for small rooms and 10 m for other rooms, equivalent to optical density of 0.2 m^{-1} and 0.1 m^{-1} respectively. Jin (8) suggests that tenability limits for egress purposes depends on the degree of familiarity with the building, with 3-5 m for those familiar with the building and up to 20 m for those who are not.

1.3 Atrium Smoke Management

1.3.1 Objectives

The five atrium smoke management objectives given by Milke (9) are:

1. Maintain a tenable environment in the means of egress in the atrium during the time required for evacuation.
2. Confine the smoke in the atrium to a limited region in that space.

3. Limit the migration of smoke into adjacent spaces from the atrium.
4. Provide conditions in the atrium to assist emergency response personnel in conducting search and rescue operations and locating and controlling the fire.
5. Contribute to the overall protection of life and reduction in property loss.

The smoke management system may be designed to meet one or a combination of the five objectives. To evaluate the design objectives, Milke suggests the use of one of the following hazard parameters which would have to be maintained within acceptable levels by an appropriate system. The hazard parameters are as follows:

- Smoke layer depth
- Visibility through smoke layer
- Carbon monoxide concentration
- Temperature rise in smoke layer

1.3.2 Atrium Smoke Management Methodologies

Various smoke management methodologies are available for atrium buildings (2), (3), (10). Some of these methodologies are briefly described below:

1.3.2.1 Smoke Filling

The approach of smoke filling is applicable when the time for evacuation is less than the atrium filling time (3). Generally, this approach is applicable for atria with a very large volume. The time for evacuation is the modeled evacuation time multiplied by

the evacuation efficiency plus the time delay in initiating an evacuation. The atrium filling time is the time for the smoke layer to descend to the critical level above the highest occupied floor. Empirical relationships to determine the smoke layer height above the fire with respect to time for steady fire and developing fire are given by NFPA92B (2).

1.3.2.2 Mechanical Exhaust

Mechanical smoke exhaust can be employed to remove smoke from a space such that the smoke layer is maintained at a predefined height in the space for an indefinite period of time or such that the rate of descent of the smoke layer is reduced for a period that allows the safe egress of building occupants (2). This methodology is also known as smoke and heat exhaust ventilation as described by Morgan et al. (10). Section 1.4 describes this methodology in more details.

1.3.2.3 Natural Venting

Natural smoke venting makes use of the buoyancy of hot smoke to drive smoke out of open vents at or near the top of the atrium. This form of smoke management generally has a high reliability due to the simplicity of design and operation. The major drawbacks of natural venting are the possibility of the smoke losing buoyancy due to sprinkler operation or positive wind pressure at the vent locations which could interfere with the venting of the hot smoke. Empirical equations for the steady conditions are given by Klote and Milke (3), while zone models can be used to analyze smoke flows for unsteady conditions.

1.3.2.4 Tenability Systems

Tenability systems are designed to maintain tenable conditions with building occupants exposed to smoke, as opposed to the previously discussed methodologies which have the objective of preventing occupants from being exposed to smoke during egress (3). Tenability systems are designed based on hazard analysis, which assesses the development of conditions generated by a fire considering the fire scenario, smoke transport, people movement and tenability.

1.3.2.5 Atrium depressurization

When the boundary between the atrium and adjacent spaces is not tightly sealed or there are small openings, smoke may travel from the atrium into the adjacent spaces. To prevent this from occurring, natural venting or mechanical exhaust can be provided for the atrium such that the neutral plane of the building is above the highest leakage path. While this methodology prevents the spread of smoke into the space adjacent to the atrium, it is not intended to provide smoke management for the atrium (10).

1.3.2.6 Hybrid design

A combination of the above methodologies can be applied for smoke management in atrium buildings. A common strategy is atrium depressurization with mechanical exhaust (10).

1.4 Smoke and Heat Exhaust Ventilation

When a fire occurs, the smoke from the fire rises as a plume and entrains air as it rises, reducing its temperature and velocity in the process. The smoke stops rising when it has reached a horizontal obstruction such as the ceiling, or when the temperature of the smoke is lower than the layer of air in the upper region of the space. For the former case, the smoke will be contained within the ceiling void, forming a smoke layer, which descends as more smoke is supplied from the plume. In the latter case, the smoke layer forms below the hot layer of air in the top of the atrium. For atrium buildings, the tall atrium allows large quantities of air to be entrained as the plume rises and hence increases the production of smoke. Thus, some form of smoke management is essential to allow safe egress of building occupants.

Smoke and heat exhaust ventilation systems (SHEVS) can be in the form of mechanical exhaust or natural venting. The mechanical exhaust form is the most common method of atrium smoke management in North America (3). Smoke is removed from the upper region of the atrium, to prevent or delay its descent and hence provides a clear layer beneath the buoyant hot smoke layer for the purpose of safe egress of building occupants. Physical barriers such as smoke curtains or channeling screens may be part of the integrated design to contain the smoke or direct the smoke to its intended path. Provision of inlet air to replace the removed hot gases is essential to ensure the effectiveness of SHEVS. The inlet air should be introduced in such a manner that it does not interact directly with the fire, the smoke plume or the smoke layer (6). In addition to providing favorable conditions for the egress of

building occupants during a fire, SHEVs can also provide improved conditions for fire-fighting and rescue operations and property protection by limiting the spread of smoke and temperature.

A critical design parameter of SHEVS is the height of the base of the buoyant smoke layer from the level of the fire, also known as the clear layer height. The clear layer height forms the basis of SHEVS design and is usually determined by the height above the highest occupied floor that is open to the atrium. Figure 1.1 shows a schematic of the clear layer height for a multi-storey atrium.

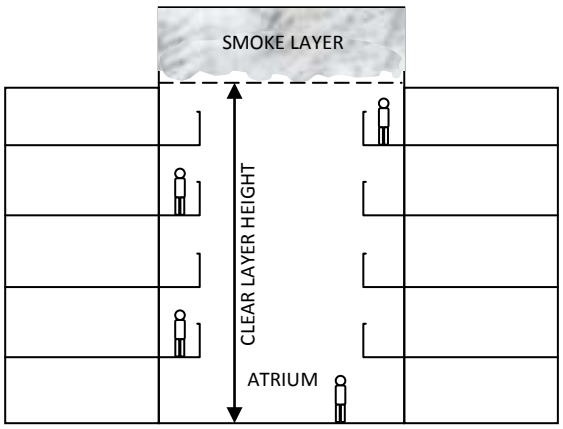

Figure 1.1: Schematic of clear layer height for multi-storey atrium

Factors that must be taken into consideration in the determination of the design clear layer height include (9): location of means of egress within the open space, separation of adjacent space from the open space and environmental and geometric factors. The clear height requirement according to NFPA 101 (11) states that the smoke layer interface should be kept above the highest unprotected opening to an adjoining space, or 1.83 m above the highest floor level of exit access open to the atrium, for a period equal to 1.5 times the calculated egress time or 20 minutes, whichever is the greater.

Current UK requirements are dependent on building type. For public buildings, a minimum clear height of 3.0 m above the highest egress route is required. For non-public buildings, the height is 2.5 m. For cases where the predicted smoke temperature is less than 50 °C above ambient temperature, the minimum clear height is increased by 0.5 m as the smoke layer interface may not be well defined.

1.5 Smoke Production

In the design of SHEVS, the amount of smoke to be removed has to be determined. For an atrium fire, the amount of smoke produced depends on the fire size and the amount of air entrained into the smoke plume. The fire size depends on the type and amount of fuel present, while the amount of entrainment depends on the configuration of plume.

1.5.1 Fire Size

Fire size is one of the factors affecting the production of smoke. For pre-flashover fires, fire size depends on the amount of fuel present. For a post-flashover fire, all the combustibles in the compartment are burning and the size of the fire is limited by the amount of air being supplied to the fire. The fire size is expressed in terms of growth rate, area, heat release rate per unit area or maximum heat release rate. Fire size for design purposes can be specified as a steady state fire with a constant heat release rate or a time-dependant fire, perhaps growing in accordance with a power law. Time-dependant fire growth rates given by NFPA72 (12) are as follows:

- Slow, $\dot{Q} = 0.00293t^2$
- Medium, $\dot{Q} = 0.01172t^2$
- Fast, $\dot{Q} = 0.0469t^2$

Traditionally, steady state design fires have been used for design of SHEVS due to a lack of robust data on fire growth rates for different building occupancies and fire scenarios. Morgan et al. (10) provides some data for steady state design fire sizes based on occupancy types. This approach uses the probable maximum fire size for the scenario hence simplifying the design process and also allows a conservative design to be developed. However, the use of a time-dependent fire has its merits as a more realistic solution.

1.5.2 Plume Configurations

Five plume configurations that may exist within an atrium are identified by Klote and Milke (3):

1. Axisymmetric plume
2. Wall Plume
3. Corner Plume
4. Spill Plume
5. Window Plume

1.5.2.1 Axisymmetric Plume

Axisymmetric plumes are formed when the fire is remote from walls, hence entraining air from all sides along the entire clear height of the plume. This plume configuration is expected from a fire located near the center of the atrium floor from which can rise freely to the atrium ceiling. Morton et al. (13) carried out analysis of axisymmetric plumes and the analysis was extended to turbulent plumes by Cetegen et al. (14) and Zukoski (15). Figure 1.2 shows a schematic drawing of an axisymmetric plume.

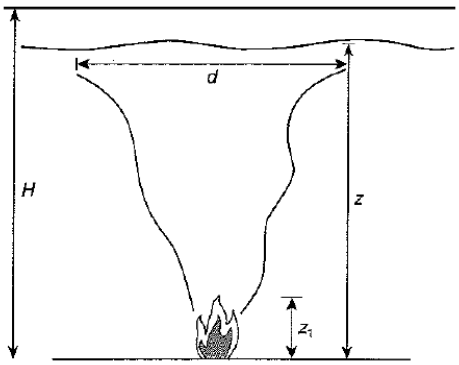

Figure 1.2: Schematic drawing of axisymmetric plume (2)

1.5.2.2 Wall and Corner Plumes

Fires near walls and corner entrain air only along the surface of the plume away from the wall or corner; hence the amount of smoke produced is reduced compared to axisymmetric plumes. Using the concept of reflection, a fire against a wall entrains air from half its perimeter and hence the smoke production rate is estimated as half of that from a fire that has twice its heat release rate (6). For corner plume, where the wall forms a 90 degree angle, it is estimated to be a quarter of the smoke production rate from a fire that is four times as large. Recent work by Poreh et al. (16) suggests

further research on wall and corner plume entrainment. Figure 1.3 shows schematic drawings of wall and corner plumes.

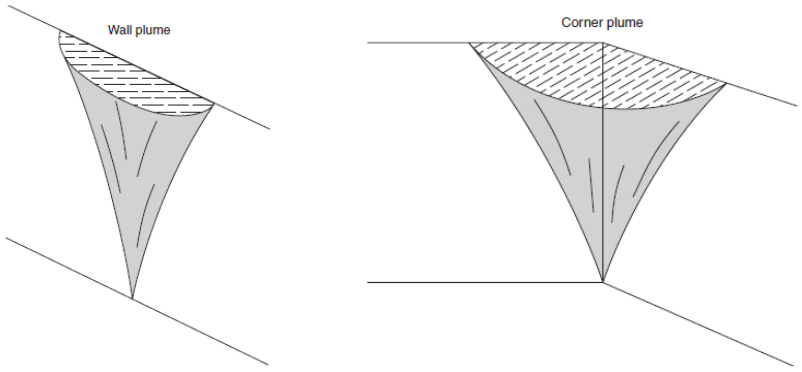

Figure 1.3: Schematic Drawing of Wall and Corner Plumes (6)

1.5.2.3 Balcony Spill Plume

A balcony spill plume occurs when smoke from a fire rises to an intermediate obstruction and travels horizontally under it towards the edge and then turns and rises vertically once past the edge. Characteristics of the balcony spill plume depends on the characteristics of the fire, width of the spill plume, height of the ceiling above the fire and the path of horizontal travel from the plume to the balcony edge. More details of balcony spill plumes are given in Section 1.6.

1.5.2.4 Window Plume

Window plumes arise when the plume from a post-flashover fire flows through an opening (window or doorway) into the atrium. In a post-flashover fire, all combustibles in the room are burning and the fire is in the ventilation controlled regime, where the heat release rate depends on the amount of air that is supplied to

the fire. Hence, window plumes usually have flames projecting out of the opening, where the interface of the volatized fuel and oxygen is located. Entrainment correlations for window plumes are given by Klote and Milke (3). Figure 1.4 shows a schematic of a window plume.

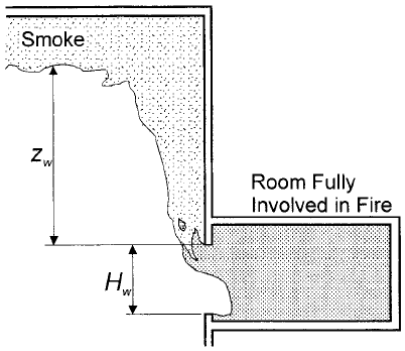

Figure 1.4: Schematic of a window plume (3)

1.6 Spill Plumes

When a fire occurs in a communicating space next to an atrium, the smoke from the fire rises vertically until it is impeded by an overhead obstruction such as the ceiling of the compartment. The smoke then spreads radially as a thin horizontal layer, known as a ceiling jet (17) until it reaches vertical obstructions which cause the ceiling jet to rotate downwards and back towards the fire or spill under the soffit of a doorway. If the compartment opening extends all the way to the ceiling, the smoke flows unhindered out of the compartment. In the presence of a balcony (horizontal projection) beyond the compartment opening, the smoke continues its horizontal path beneath the balcony and also spreads in the lateral direction, unless channeling screens are present. When the smoke reaches the edge of the balcony, it rotates upwards due to its buoyancy and rises as a plume into the atrium space as a thermal

spill plume. The edge of the balcony is commonly referred to as the "rotation" or "turning" region of the plume. As the plume is usually relatively long and narrow after the rotation, it is also known as a thermal line plume.

Thermal spill plumes are generally classified as balcony or adhered spill plume depending on the characteristics of the plume as it rises to the atrium space. Figure 1.5 shows a schematic drawing of a typical balcony spill plume.

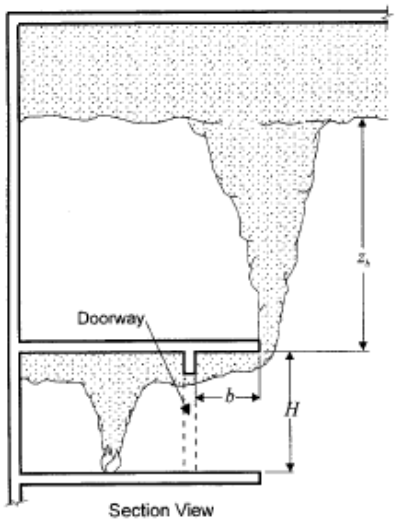

Figure 1.5: Schematic drawing of a balcony spill plume (3)

An adhered spill plume forms when there is no horizontal projection beyond the compartment opening and a wall is present above the spill edge, which is now at the compartment opening. The spill plume adheres to the wall as it rises in the atrium space. Hansell et al. (18) also suggested that adhered plumes can also be formed when the breadth of the horizontal projection is less than 2m and more likely with wider plumes. Intuitively, adhered spill plumes entrain less air into the plume as compared to a balcony spill plume since the entrainment process only takes place on

one side of the plume. Hence, adhered spill plumes are also known as single-sided plume. Figure 1.6 shows a schematic drawing of an adhered spill plume.

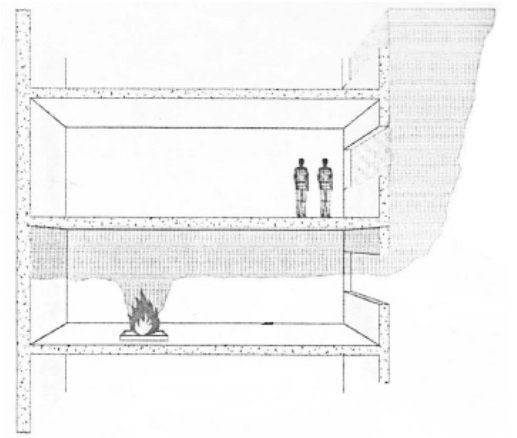

Figure 1.6: Schematic drawing of an adhered spill plume (10)

1.7 Entrainment process

The total mass flow rate of smoke in a spill plume is determined by the total amount of entrainment as the smoke flows from the compartment of fire origin to the point where it enters the smoke layer at the atrium space. Milke (6) compared the smoke production rate for axisymmetric plumes to balcony spill plumes, showing that for the same fire size, a balcony spill plume produces more smoke than an axisymmetric plume at lower heights as shown in Figure 1.7.

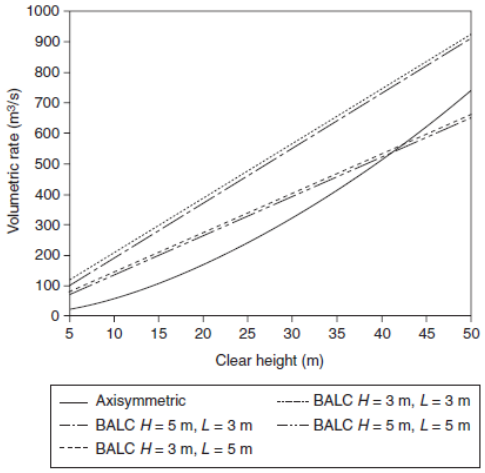

Figure 1.7: Comparison of smoke production rates for axisymmetric and balcony spill plume (6)

The entrainment processes for a balcony spill plume can be broadly divided into three regions, within the fire compartment, between the compartment opening and the spill edge and beyond the spill edge. The entrainment processes in each of these regions are defined below.

1.7.1 Entrainment in the Fire Compartment

Poreh et al. (19) identified the mass flow rate of gases at the compartment opening to be consisting of the mass flow rate of the fuel, mass flow rate of air entrained into the plume above the fire, mass flow rate of air entrained as the plume impinges into the smoke layer and entrainment of air into the horizontal flow layer in the fire compartment. These entrainment processes are shown in Figure 1.8.

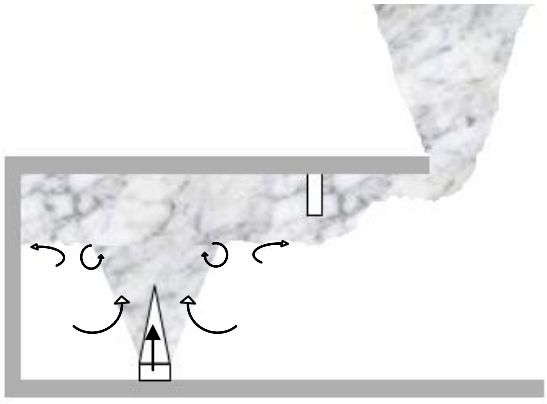

Figure 1.8: Entrainment processes in the fire compartment

The mass flow rate of the fuel, mass flow rate of air entrained due to plume impingement and entrainment of air into the horizontal flow layer are considered negligible compared to the entrainment into the rising plume. Hence, the mass flow rate of gases at the compartment opening is approximately equal to the smoke produced by the rising plume, which is dependent on the geometry of the compartment, location of the vents and location of the fire. Methods to determine the mass flow rate from the compartment opening is described in Section 2.1.

1.7.2 Entrainment between the fire compartment opening and the spill edge

The main entrainment process between the fire compartment opening and the spill edge occurs when the flow rises from beneath the downstand at the compartment opening to the balcony, as shown in Figure 1.9. In the absence of a downstand, it is generally recognized that there is no significant entrainment. Section 2.2 describes the methods to determine the under balcony entrainment. Channeling screens or other obstructions may be present beneath the balcony to prevent the lateral spread of smoke under the balcony. While the lateral spread of smoke does not cause

additional entrainment, a wider spill plume will entrain more air when it rises into the atrium space.

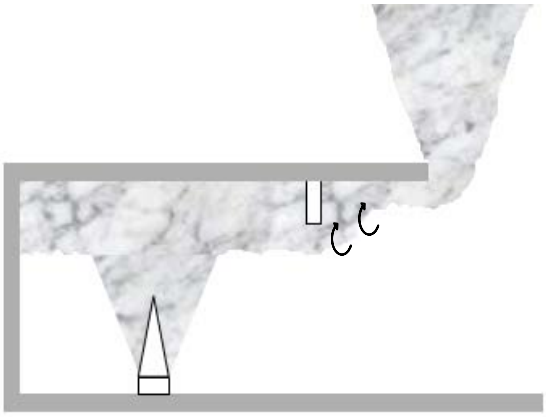

Figure 1.9: Entrainment process between the fire compartment opening and the spill edge

1.7.3 Entrainment beyond the spill edge

The two main entrainment processes beyond the spill edge occur when the smoke layer rotates around the spill edge and as the rotated plume rises into the atrium space. The entrainment rate during the plume rise into the atrium space depends on the type of spill plume produced. For a balcony spill plume, entrainment occurs on all surfaces of the plume as it rises. For an adhered plume, entrainment can only occur on the surface of the plume that is not in contact with the wall. Figure 1.10 shows these entrainment processes. Methods to calculate the entrainment are described in section 2.3.

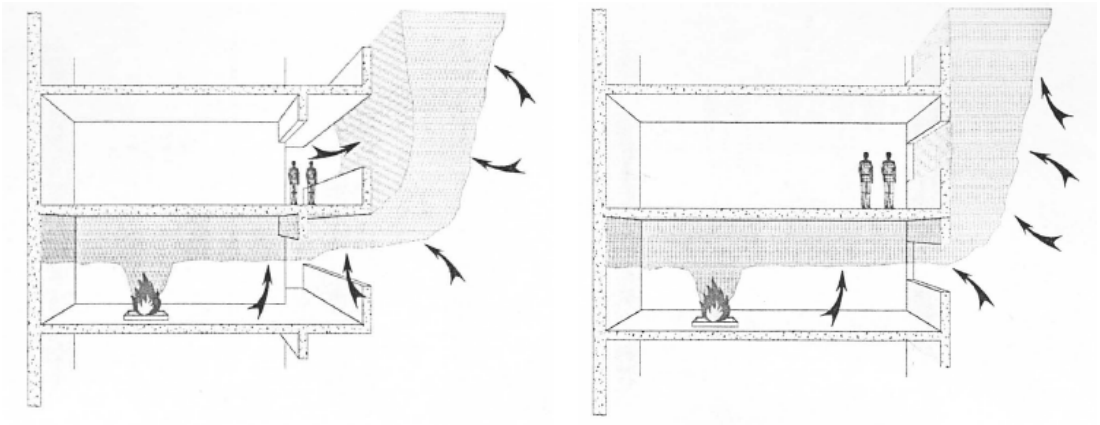

(a) balcony spill plume (b) adhered plume

Figure 1.10: Entrainment processes beyond the spill edge (10)

1.8 Research Objectives

There are several calculations methods to determine the smoke production rate of a thermal spill plume within an atrium building. Reasonably accurate and robust design formulae would allow engineers to design an efficient and cost effective SHEVS. However, there are limitations to these calculation methods and there are also areas of uncertainties and controversy of the accuracy and robustness of some of these design formulae. An area that warrants additional attention is the entrainment process as smoke flows out of the fire compartment, under the balcony before rotating and rising into the atrium as a thermal spill plume. The mass flow rate of smoke after rotation around the spill edge forms the source of spill plume. There are a few methods to calculate this mass flow rate, mainly with channeling screens under the balcony to limit the lateral spread of smoke. However, the current design guidance (10) suggests a rough estimation. Therefore, a comprehensive study is necessary to characterize the flow and entrainment processes.

The objectives of this research are described below:

1. Analyze the entrainment processes between the compartment opening and the spill edge for different compartment opening widths, downstand heights and balcony breadths.
2. Analyze the entrainment process as the flow rotates around the balcony edge.
3. Analyze the entrainment processes for different configurations of downstands and channeling screens

2. Literature Review

This chapter reviews some of the research in the characterization the entrainment of air into a balcony spill plume. The entrainment process can be broadly separated into three different regions, namely:

- Within the fire compartment
- Between the fire compartment opening and the spill edge
- Beyond the spill edge

This chapter will focus mainly on the first two regions and the rotation region at the spill edge.

2.1 Mass Flow Rate at the Fire Compartment Opening

This section gives a brief description of the various methods to calculate the mass flow rate of hot gases flowing out of a fire compartment under steady state conditions.

2.1.1 Steckler, Quintiere and Rinkinen

Flow through an opening is created by pressure difference across the opening. In the case of a compartment fire, one source of pressure difference is caused by the temperature difference between the room and its surroundings. Quintiere, et al. (20), applied Bernoulli's equation and hydrostatic principles with the assumption of

horizontal streamlines starting from rest to formulate an equation describing the mass flow rate of hot gases flowing out of the fire compartment as shown,

$$\dot{m}_w = W_0 \rho_\infty T_\infty C_d \int_N^{h_o} \left[\frac{2g}{T_{room}} \int_N^Z \left(\frac{1}{T_\infty} - \frac{1}{T_{room}} \right) dz \right]^{1/2} dz \qquad (2\text{-}1)$$

By considering steady state conditions and approximating the temperature to be independent of position, Steckler, et al. (21) reduced Equation (2-1) to

$$\dot{m}_w = \frac{2}{3} (2g)^{1/2} C_d \rho_\infty A_o {h_o}^{1/2} \left[\left(\frac{T_\infty}{T_{room}} \right) \left(1 - \frac{T_\infty}{T_{room}} \right) \right]^{1/2} \left(1 - \frac{\mathrm{N}}{h_o} \right)^{3/2} \qquad (2\text{-}2)$$

Steckler, et al. (21) also conducted full-scale experiments, using a methane diffusion burner, to determine the effects of heat release rate and location of fire on the flow rate through a doorway and window opening, for "small" compartment fires in the developing period of a fire. From the experimental data, Steckler, et al. observed that the mass flow rate is highest when the fire is in the center of the room, reduced when the fire is at the back wall and lowest when at the corner of two walls. This reduction is attributed to the decreasing effect of the door jet as well as reduced entrainment due to the proximity of the walls. The door jet effect is also observed Quintiere, et al. (20), where the plume entrainment increases when the plume is blown over by the door jet. By correlating the experimental data to Equation (2-2), the average flow coefficient, C_d was found to be 0.73 and the mass flow rates can be predicted to within 7% given the height of the neutral plane and temperatures of the room, at the opening and the ambient. The height of the neutral plane can be determined from the temperature distribution at the opening, hence the mass flow rates can be predicted from temperature measurements alone. The flow coefficient of 0.73 obtained in these

methane experiments is marginally higher than that of 0.68 suggested by Prahl and Emmons (23) for their water-kerosene analog experiments.

2.1.2 Thomas, Hinkley, Theobald and Simms

Thomas, et al. (24) developed an identical equation for wide fire compartment openings with a deep downstand, i.e. the width of the compartment opening greater than the height, as follows,

$$\dot{m}_w = \frac{2}{3} C_d \left(2g\theta_{max,w} T_\infty\right)^{1/2} \frac{W_0 \rho_\infty}{T_{max,w}} d_w^{3/2} \qquad (2\text{-}3)$$

Thomas applied Bernoulli's equation and assumed the gases in the fire compartment had zero initial velocity to obtain an expression for the velocity distribution of the outflow gases from the opening and hence the mass flow rate. Assuming a uniform vertical temperature profile, a flow coefficient of 0.6 was obtained by correlation with experimental data.

2.1.3 Morgan

Morgan (25) used the assumption of a virtual vena contracta outside the compartment opening, hence ignoring the upward acceleration of buoyant gases and that the gases were not accelerated from rest, but have an established velocity at the compartment opening. Instead of assuming a uniform vertical temperature profile in the flow layer, Morgan applied a correction factor, κ_m, to account for the variation in the temperature. The mass flow rate expression by Morgan is,

$$\dot{m}_w = \frac{2}{3} C_d{}^{3/2} \left(2g\theta_{max,w} T_\infty\right)^{1/2} \frac{W_0 \rho_\infty}{T_{max,w}} d_w{}^{3/2} K_m \qquad (2\text{-}4)$$

Morgan suggests that for a realistic layer flow, the value of κ_m should be halfway between that of a uniform profile and triangular profile for the same $\theta_{max,w}$. For design purposes, Morgan suggests a value of $\kappa_m = 1.3$ for Equation (2-4). For compartment openings with a flat ceiling, the suggested value of the flow coefficient is $C_d = 1$. For compartments with a downstand at the opening, the value of 0.6 is proposed, which reduces Equation (2-4) to an expression that is practically identical to Equation (2-3) developed by Thomas et al. For the case of a flat ceiling, Morgan's expression predicts a higher mass flow rate by 30 %, compared to Equation (2-3).

2.1.4 Hansell

Drawing on work by Zukoski (26) and Quintiere, et al. (22) to modify earlier studies by Thomas, et al. (24) and Hinkley (27), Hansell (28) showed that the entrainment into a vertical rising plume within a fire compartment can be described by,

$$\dot{m}_p = C_e p z_p{}^{3/2} \qquad (2\text{-}5)$$

C_e is an empirical entrainment coefficient which takes into account the various factors affecting entrainment in the fire compartment such as compartment geometry, effects of wall jets, proximity of the fire to walls and the tilt of the plume due to the incoming flow of air from the compartment opening. The following values of C_e are given for the various scenarios:

- $C_e = 0.19$ (kg/s/m$^{5/2}$), for large-area rooms where the ceiling is well above the fire, e.g. auditoria, stadia and atrium floors.
- $C_e = 0.21$ (kg/s/m$^{5/2}$), for large-area rooms where the ceiling is close to the fire, e.g. large open-plan offices.
- $C_e = 0.34$ (kg/s/m$^{5/2}$), for small rooms where the compartment opening is predominantly to one side of the fire, e.g. unit retail shops, cellular offices, hotel rooms and etc.

In the current BRE design guidance (10), it is suggested to use $C_e = 0.21$ wherever $z_p < 3\sqrt{A_f}$ for large area rooms. Demarcation of cellular rooms and open-plan layout, is determined by the ability of the plume to entrain air from all sides. A narrow room would restrict the flow of air to the back of the plume. The BRE design guide (10) suggests to use $C_e = 0.34$ when the maximum room dimension is less than or equal to five times the effective fire diameter, D_f, and the incoming air into the compartment is from one direction.

From Equation (2-5), Hansell (28) developed a simplified equation to describe the horizontal flow of gases from a compartment opening as follows,

$$\dot{m}_w = \frac{C_e p W_o {h_o}^{3/2}}{\left({W_o}^{2/3} + \frac{1}{C_d}\left(\frac{C_e p}{2}\right)^{2/3}\right)^{3/2}} \tag{2-6}$$

The number '2' in the denominator in Equation (2-6) is the result of combining various parameters and has dimensions. For compartment openings with a flat

ceiling, the suggest value of $C_d = 1$, while for compartment openings with a downstand, a values of $C_d = 0.65$ is suggested.

Equation (2-6) presents a very useful design tool as the only fire parameter required is the perimeter of the fire, p as compared to previous works which require the input of variables, such as smoke layer depth and temperature, which may not be known.

2.1.5 CIBSE

CIBSE (29) and BS 7974 (30) provide an expression to describe the mass flow rate of gases from a compartment opening given by,

$$\dot{m}_w = 0.09\dot{Q}_c^{1/3} W_o^{2/3} h_o \qquad (2\text{-}7)$$

Like Equation (2-6), Equation (2-7) provides a very useful expression for design purposes as the only fire parameter required is the convective heat release rate, Q_c.

2.2 Mass Flow Rate between the Fire Compartment and the Spill Edge

The presence of a downstand at the fire compartment opening with a projecting balcony that is higher than the compartment opening would cause additional entrainment as the hot gases flow from the compartment to the spill edge. Some of the research into this additional entrainment is described below.

2.2.1 Hansell

An iterative calculation method was developed by Hansell (18) to determine the entrainment of air as the hot gases from a compartment opening with a downstand to a projecting balcony that is higher than the height of the compartment opening. This method was included in a previous BRE design guide (31). The method was derived from a limited set of full scale experimental data with a maximum compartment opening width of 5m and height of 3m and channeling screens below the balcony.

A simplified procedure for the calculation included in previous BRE guidance (31) is as follows:

- Calculate the mass flow rate from Equation (2-6) with $C_d = 0.65$
- Calculate the buoyant depth layer from the following,

$$d_w = \frac{1}{C_d}\left[\frac{\dot{m}_w}{2W_o}\right]^{2/3} \tag{2-8}$$

- Calculate the discharge coefficient from the following,

$$C_d = 0.65\left[\frac{d_w + \mathrm{d}_d}{d_w}\right]^{1/3} \tag{2-9}$$

- Use the new value of C_d and repeat calculation of the mass flow rate until the difference between the current value of $\dot{m}_w$ and that from the previous calculation is less than 0.1 %.

Note: the number '2' in the denominator of Equation (5-8) is the result of combining various parameters and has dimension.

2.2.2 BRE

Due to the limited sets of experimental data used in the development, the method by Hansell (31) gives rise to predicted values of C_d that are unbelievably large when it is used for circumstances that are too different from the original geometries from which the correlations are based on. For cases where the design conditions are close to the experimental geometry, most of the calculated values of C_d for "intermediate-depth downstand" using Hansell's full method are approximately 0.8. Hence a simpler alternative is proposed in the current BRE guidance by Morgan et al. (10) as follows,

- Calculate an initial value of mass flow rate from Equation (2-6) using a trial value of C_d
- Calculate the flow layer depth, d_w from Equation (2-8)

It is suggested by BRE, without evidence, that if the depth of downstand is less than ¼ of the flow layer depth, i.e. $d_d < 0.25d_w$, the presence of the downstand can be ignored, hence $C_d = 1.0$. For cases where $d_d \gg d_w$, (BRE suggested without evidence to be $d_d > 2d_w$), the value of C_d is assumed to be 0.65. For all intermediate cases, the value of $C_d = 0.8$ is suggested.

Due to the nature of this approach, it is deemed as an unsatisfactory position which is expected to be superceded once a more comprehensive experimental study can lead to

a better validated correlation. As such, for purposes of engineering design, an entrainment rate of 100 % is suggested. Hence the mass flow rate at the spill edge is given by,

$$\dot{m}_s = 2\dot{m}_w \tag{2-10}$$

2.2.3 Harrison

Harrison (29) performed a series of 25 simulations of 1/10th scale models, using Fire Dynamics Simulator (Version 3) (33), to analyze the under balcony entrainment of balcony spill plumes. The geometry of the simulated fire compartment was similar to that of his physical model experiment. The fire compartment has a floor area of 1 m x 1 m and 0.5 m height. The width of the compartment opening was varied from 0.2 m to 1.0 m and the depth of downstand was varied from 0.1 m to 0.25 m. All of the simulations were carried out with the flows being channeled by screens from the compartment opening to the spill edge, such that the width of the flow at the spill edge is the same as the width of compartment opening. These channeling screens extend from the floor to the ceiling. The fire source is modeled as a block with a floor area of 0.17 m x 0.17 m and 0.05 m height, located along the longitudinal axis of the fire compartment, 0.05 m from the rear wall. The simulated heat release rate was mainly 10.3 kW, equivalent to a full-scale fire size of approximately 3,257 kW. An additional two simulations with heat release rates of 6 kW and 16 kW each, full-scale equivalent of 1,897 kW and 5060 kW, respectively were also carried out. For the majority of the simulations, the balcony breadth is fixed at 0.3 m. One simulation was carried out with the balcony breadth at 0.2 m and two with 0.5 m. The entire

computational domain was 1.8 m long, 1.0 m wide and 1.0 m high, which extends 0.5 m above and beyond the spill edge, to capture the initial flow beyond the spill edge. Five equally-spaced temperature and velocity measurements, 10 mm below the ceiling surface, were taken laterally across the width of the compartment opening and spill edge as a check for uniformity across the flow path. Temperature and velocity measurements were also taken at the center of the compartment opening and at the spill edge. These measurements were taken at equal intervals of 10 mm from the floor to the ceiling level. Assuming temperature and velocity uniformity across the compartment opening and spill edge, the mass flow rate at these respective locations were calculated using these temperature and velocity measurements.

From the FDS predictions, Harrison developed the following correlation to describe the under balcony entrainment,

$$\dot{m}_s = 0.89\left(\frac{h_o}{W_o}\right)^{-0.92}\left(\frac{h_b \dot{m}_w}{W_o}\right) \tag{2-11}$$

Due to its empirical nature, the correlation is subject to the following constraints,

$$1.16 < \left(\frac{h_o}{W_o}\right)^{-0.92}\left(\frac{h_b}{W_o}\right) < 2.23 \tag{2-12}$$

$$\left(\frac{h_b}{h_o}\right)\left(\frac{b}{h_b - h_o}\right) \geq 2.5 \tag{2-13}$$

As a validation, four experiments were carried out with a fire size of 10.3 kW and the prediction of the mass flow rate using the correlation below agreed well with the experimental results. In general, the entrainment rate is greatest for wide compartment openings with a deep downstand.

2.2.4 Ko

Ko (34) carried out a series of 52 simulations of full-scale balcony spill plumes, using FDS, to analyze the under balcony entrainment for flows that are both channeled and unchanneled. The heat release rate was varied from 1 MW to 5 MW located in the center of a fire compartment with a floor area of 13.6 m x 5.0 m and 5 m height with three different widths of the compartment opening ranging from 5 m to 10 m. The balcony breadth was 4.2 m, downstand depth was 1.6 m and channeling screens depth was 3 m. The simulated fire compartment has the same dimensions as the full-scale test facility at the National Research Council of Canada (NRCC). The mass flow rate at the spill edge is given by

$$\dot{m}_s = 1.2\left(\frac{h_b}{h_o}\right)^{0.5}\dot{m}_w \tag{2-14}$$

Ko et al. also examined flows without downstand and/or channeling screens below the balcony and provided a simple expression as follows,

$$\dot{m}_s = a\dot{m}_w \tag{2-15}$$

The suggested values of the entrainment coefficient, a is given in Table 2-1.

Table 2-1: Values of Entrainment Coefficient by Ko (34)

Case	Downstand	Channeling Screens	Entrainment Coefficient, a
1	No	Yes	1.15
2	Yes	Yes	1.6
3	No	No	1.4
4	Yes	No	2.0

Temperature and velocity predictions by FDS were compared to the experimental data from the full-scale tests conducted at NRCC. Generally, there was an under prediction of the maximum temperature and velocity of 10 – 20 % which was attributed to uncertainties in the experimental data and discrepancies in the domain boundaries and deemed as acceptable.

2.3 Mass Flow Rate beyond the Spill Edge

This section gives a brief description of the methods to predict the entrainment as the hot gases flow from the spill edge into the atrium void as a balcony spill plume. As the majority of spill plume formulae are based on the assumption that the plume is generated from a line plume with a virtual source of zero width located below the spill edge, a brief description of studies of entrainment into thermal line plumes is also included. The rest of this section focuses on the entrainment as the hot gases rotate around the spill edge.

2.3.1 Single Storey Malls

Earlier BRE design guidance by Morgan and Gardner (35) gives an expression (Equation 2-16) to evaluate the mass flow rate of hot gases for low height of rise of less than 2 m. This equation is based on work by Heselden (36).

$$\dot{m}_p = 0.38 p z_s^{3/2} \qquad (2\text{-}16)$$

2.3.2 Thermal line plumes

Lee and Emmons (37) performed experimental and theoretical studies of the behavior of line plumes. The plumes were characterized by measuring the horizontal temperature and velocity profiles with respect to height. The theory made the assumptions of self-similar Gaussian profiles for the horizontal temperature and velocity across the plumes and constant empirical entrainment coefficient, α, over the height of rise of the plume, where plume entrainment is proportional to the centerline velocity. With the assumption of Boussinesq approximation, the mass flow rate per unit width of the line plume is described as follows:

$$\frac{\dot{m}_p}{W} = C_m \left(\frac{\rho_\infty^2 g \dot{Q}_c}{c_{p,air} W T_\infty}\right)^{1/3} (z + z_0)$$

$$\dot{m}_p = C_m \left(\frac{\rho_\infty^2 g}{c_{p,air} T_\infty}\right)^{1/3} \dot{Q}_c{}^{1/3} W^{2/3} (z + z_0) \tag{2-17}$$

Where,

$$C_m = \sqrt{\pi}\alpha^{2/3}(1 + \lambda^2)^{1/6} \tag{2-18}$$

The values of the constants are empirically determined to be α = 0.16, λ = 0.9 which gives C_m = 0.58. Using typical values, $\left(\frac{\rho_\infty^2 g}{c_{p,air} T_\infty}\right)^{\frac{1}{3}}$ is approximately 0.36 and hence Equation (2-17) is commonly expressed as

$$\dot{m}_p = C \dot{Q}_c{}^{1/3} W^{2/3} (z + z_0) \tag{2-19}$$

Where,

$$C = C_m \left(\frac{\rho_\infty^2 g}{c_{p,air} T_\infty} \right)^{1/3} \quad (2\text{-}20)$$

Line plume studies by other researchers resulted in variations in the values of C_m and α. Poreh et al. (19) noted that the differences in the constants arise from the methods of determining the mass flow rate, whether from direct measurements or from calculations using temperature and velocity distributions. The values of C_m and α are shown in Table 2.2.

Table 2-2: Values of Coefficients C_m and α for Thermal Line Plumes

Researcher	C_m	α
Yuan and Cox (38)	0.51	0.126
Rouse et al. (39)	0.57	0.162
Zukoski (26) & Yokoi (40)	0.52	0.125
Kotsovinos (41)	0.66	0.20
Ramparian et al. (42)	0.48	0.117

2.3.3 Morgan and Marshall

Morgan et al. (43) conducted a series of 1/10th scale experiments simulating smoke flow from a compartment in the form of a balcony spill plume. The compartment was 0.5 m in depth and 0.5 m in height with a balcony breadth of 0.4 m. Two compartment opening widths of 0.7 m and 1.4 m were examined with channeling screens to prevent lateral spread of smoke from the compartment. The results from

the experiment were used to develop the BRE spill plume method which is included in the BRE design guides (10), (31).

The BRE spill plume method applies to cases where a horizontally flowing, thermally buoyant layer of hot gases approaches an opening in the compartment and rising at the spill edge as a balcony spill plume. The following assumptions are made,

- The horizontal flow of hot gases is beneath a flat ceiling or with a downstand at the compartment
- The flow is channeled by walls or screens
- The flow is fully developed and has parallel flow-lines which are perpendicular to the opening
- There is no immersed ceiling jet
- The velocity of the clear air below the smoke layer has a values smaller than that of the layer

The mass flow rate at the compartment opening is evaluated using Equation (2-4). While the entrainment in the rotation region is given by,

$$\dot{m}_{rot} = \frac{2}{3}\rho_{\infty} W_s \alpha' \left(\frac{2g\theta_{max,s}}{T_{\infty}}\right)^{1/2} {d_s}^{3/2} \qquad (2\text{-}16)$$

The value of the entrainment coefficient, α' was originally given by 0.9. It was later updated by Morgan and Hansell (44) to 1.1, which implies a large amount of entrainment. As explained in the current BRE guide (10), this large value is a result of treating all anomalous entrainment above the spill edge as if it occurred in the

rotation region. Later work by Miles, et al. (45) using CFD modeling and Yii (46) using salt water experiments show that the entrainment in the rotation region is small.

Combining Equation (2-4) and Equation (2-16) gives the mass flow rate of the vertical plume at the spill edge,

$$\dot{m}_{p,z_s=0} = \frac{2}{3}\rho_\infty W_s \alpha' \left(\frac{2g\theta_{max,s}}{T_\infty}\right)^{1/2} {d_s}^{3/2} + \frac{2}{3}{C_d}^{3/2}\left(2g\theta_{max,w}T_\infty\right)^{1/2}\frac{W_0\rho_\infty}{T_{max,w}}{d_w}^{3/2}\kappa_m \quad (2\text{-}17)$$

Using the theory of Lee and Emmons (37), Morgan et al. (43) calculated a virtual "Equivalent Gaussion Source" (EGS) in the horizontal plane and determined the source characterisitics of the vertical flow at the spill edge with entrainment coefficient, α = 0.16, similar to that determined by Lee and Emmons. This method, with the assumption of constant entrainment coefficient and self similar Gaussian temperature and velocity profiles, allows the calculation of mass flow rate of the plume without entrainment into the ends of the plume. Morgan and Marshall (47), using the assumption that the ends of the plume are rectangular-shaped instead of conical, gave an expression to determine the entrainment into the ends of the plume. The methods of calculation are included in the current BRE design guide (10).

2.3.4 Poreh, Morgan, Marshall and Harrison

Poreh et al. (19) developed Equation (2-17) describing the mass flow rate of a 2D spill plume using dimensional analysis with the assumption of a linear relationship between the mass flow rate and height, z_s with a correction for the virtual source, z_o.

$$\dot{m}_p = C\dot{Q}_c^{1/3}{W_s}^{2/3}(z_s + z_0) \quad (2\text{-}17)$$

Where

$$C = 0.3C_m P_\infty \tag{2-18}$$

By allowing the smoke layer in the reservoir to drop to the same level as the base of the smoke layer in the compartment, it was assumed that there was no additional entrainment into the flow beyond the spill edge, hence the mass flow rate in the plume, $\dot{m}_p = \dot{m}_s$. Using Equation (2-17), Poreh, et al. deduced that the mass flow rate at the spill edge is given by,

$$\dot{m}_s = C\dot{Q}_c^{1/3} W_s^{2/3}(-d_s + z_0) \tag{2-19}$$

Therefore, the location of the virtual origin is given by,

$$z_0 = d_s + \frac{\dot{m}_s}{C\dot{Q}_c^{1/3} W_s^{2/3}} \tag{2-20}$$

Experimental data from studies of 2D spill plumes by Marshall et al. (48) were used to determine the value of C. The correlation results in the value of C = 0.16 and C_m = 0.44. Hence, the mass flow rate of a 2D spill plume can be determined by

$$\dot{m}_p = 0.16\dot{Q}_c^{1/3} W_s^{2/3}\left(z_s + d_s + \frac{\dot{m}_s}{0.16\dot{Q}_c^{1/3} W_s^{2/3}}\right) \tag{2-21}$$

Re-arranging Equation (2-21) gives an expression of the amount of air entrained into the plume beyond the spill edge, which is given as guidance on balcony spill plumes in BS 7974 (30).

$$\dot{m}_p - \dot{m}_s = 0.16\dot{Q}_c^{1/3} W_s^{2/3}(z_s + d_s) \tag{2-22}$$

By setting z_s = 0 in Equation (2-22), the entrainment at the rotation region can be determined in terms of the mass flow rate at the spill edge and the layer depth, with the assumption of negligible entrainment from the bottom of the smoke layer in the reservoir.

$$\dot{m}_{rot} = 0.16 \dot{Q}_c^{\,1/3} W_s^{\,2/3} d_s \tag{2-23}$$

2.3.5 Thomas, Morgan and Marshall

Previous work by Poreh et al. (19) used the assumption of self-similarity in the temperature and velocity profiles across the plume and a constant entrainment coefficient. Thomas et al. (49) used dimensional analysis to develop a simplified spill plume formula, which does not require a term for the virtual source, nor does it make the assumption of self-similarity and constant entrainment coefficient. The dimensional analysis produced the general formula,

$$\frac{\dot{m}_p^{'}}{\dot{Q}_c^{'}} = \gamma \frac{z_s}{\dot{Q}_c^{'\,2/3}} + \delta \frac{\dot{m}_s^{'}}{\dot{Q}_c^{'}} + \varepsilon \tag{2-24}$$

Where

$$\dot{m}_p^{'} = \frac{\dot{m}_p}{W_s} \qquad \dot{m}_s^{'} = \frac{\dot{m}_s}{W_s} \qquad \dot{Q}_c^{'} = \frac{\dot{Q}_c}{W_s} \tag{2-25}$$

Using the experimental data from Marshall et al. (48), which was also used by Poreh et al. (19), the following correlation for 2D balcony spill plume was developed,

$$\frac{\dot{m}_{p,2D}^{'}}{\dot{Q}_c^{'}} = 0.16 \frac{z_s}{\dot{Q}_c^{'\,2/3}} + 1.2 \frac{\dot{m}_s^{'}}{\dot{Q}_c^{'}} + 0.0027 \tag{2-26}$$

Using data by Poreh et al. and method by Morgan (25), Thomas et al. derived an empirical relationship describing d_s.

$$\frac{d_z\left(\frac{\dot{Q}_c}{W_z}\right)}{\left(\frac{\dot{m}_s}{W_s}\right)} = 2.5\left(1 + \frac{\dot{Q}_c}{c_{p,air}\, T_\infty\, \dot{m}_s}\right) \tag{2-27}$$

Using Equation (2-27) and Equation (2-22), Thomas derived Equation (2-28) which is an alternative form of expression of the spill plume formula by Poreh et al. (19) but with the redundancy of requiring the calculation of both $\dot{m}_s$ and d_s removed.

$$\frac{\dot{m}'_{p,2D}}{\dot{Q}'_c} = 0.16\frac{z_s}{\dot{Q}'^{2/3}_c} + 1.4\frac{\dot{m}'_s}{\dot{Q}'_c} + 0.0014$$

$$\Rightarrow \dot{m}_{p,2D} = 0.16\dot{Q}_c^{1/3}W_s^{2/3}z_s + 1.4\dot{m}_s + 0.0014\dot{Q}_c \tag{2-28}$$

By setting z_s = 0 for Equation (2-26) and Equation (2-28), hence reducing to Equation (2-29) and (2-30) respectively, the mass flow rate of the plume after the rotation region can be determined using the following equations.

$$\dot{m}_{p,z_s=0} = 1.2\dot{m}_s + 0.0027\dot{Q}_c \tag{2-29}$$

$$\dot{m}_{p,z_s=0} = 1.4\dot{m}_s + 0.0014\dot{Q}_c \tag{2-30}$$

Thomas et al. then correlated four sets of experimental data for z_s = 0, using both Equation (2-29) and $\dot{m}_{p,2D} = 1.4\dot{m}_s$, with both showing good agreement to the experimental value. Hence, suggesting that the additional entrainment in the rotation region is 40% of the total mass flow rate at the spill edge. Thomas had concerns that the calculated mass flow rate, $\dot{m}_{p,2D}$ at z_s = 0, using Equation (2-21) were on average

11% higher than the measured values, indicating an overestimation and suggested further studies into it.

2.3.6 Ko

From the series of FDS simulations described in the section 2.24, Ko (34) derived the mass flow rate of the plume at the spill edge as follows:

$$\dot{m}_{p,z_s=0} = 3.0\left[\left(\dot{Q}_c^{1/5} W_{e,s}^{3}\right) \times \frac{1}{\left(\frac{h_b}{h_o}\right)^{1+K_c}} \times \frac{1}{\left(\frac{b}{h_o}\right)}\right]^{-0.57} \times \left(\frac{h_b}{W_{e,s} h_o}\right)^{-2} \times \dot{m}_{\mathrm{s}} \qquad (2\text{-}31)$$

Where $K_c = \frac{W_s}{W_o}$

The correlation is applicable to compartment geometries with and without downstand and/or channeling screens and was originally developed for buoyant jets with Richardson number ranging from 0.14 to 0.7. The correlation is not applicable to adhered plumes. The correlation shows good agreement when validated with experimental data from the NRCC test, Harrison (32) and Marshall et al. (48).

2.3.7 Harrison and Spearpoint

Harrison et al. (50) noted that the characterization of the entrainment in the rotation region carried out by Poreh et al. and Thomas et al. contains only 3 data points at z_s = 0, hence an additional 20 experiments were performed to determine the mass flow rate of the plume at z_s = 0. With data from previous studies by Marshall and Harrison (48) and Harrison and Spearpoint (51) included, Harrison developed the

following correlation to describe the mass flow rate per unit width of the spill plume at z_s = 0,

$$\dot{m}_{p,z=0} = 1.34\dot{m}_s \tag{2-32}$$

This is marginally lower than that suggested previously by Thomas et al. (49), which was deemed to be possibly overestimated due to inaccuracies, as described in the previous section.

2.4 Computer modeling of fire and smoke transport

The rapid advancement in computer technology in the past decade has led to the increase in use of computer modeling for fire and smoke transport (52). A comprehensive survey of computer models for fire and smoke carried out by Olenick et al. (52), identified 168 such computer modeling programs. This growth in computer modeling programs is also due to a move towards the use of performance-based building codes by North-European countries such as UK and Sweden, New Zealand, Australia, USA, Canada and Japan (7). Computer fire models can be broadly categorized into five different categories namely, zone models, field models, detector response models, fire endurance models and egress models.

Zone models are used for the prediction of the development of a fire inside a compartment or a series of compartments. Usually, the approach divides the compartment into two distinct zones, a hot upper smoke layer and a cool lower layer of air and solves the conservation equations of mass, momentum and energy for each

of these zones. Zone models are able to provide a reasonable approximation of compartment fires using minimal computer resources.

Field models divide the compartment into a large number of control volumes, also known as cells, and solve the conservation equations within each of these control volumes. Field models provide a more detailed solution and can also be used for more complex geometries which cannot be properly describe using two zones. However, field models require more input information and require more computational resources. Field models are essentially comprised of a computational fluid dynamics (CFD) code which provides the basic transport mechanisms for mass, momentum and energy and a fire model which contains detailed description of the combustion processes.

A brief description of computer modeling studies utilizing zone models and field models for balcony spill plumes is described in the next section. Detector response models, fire endurance models and egress models will not be discussed.

2.4.1 Modeling of Balcony Spill Plumes

Miles et al. (45) used the CFD package, JASMINE (53), to simulate $1/10^{th}$ physical scale model experiments by Marshall, et al. (48). Plumes were generated using temperature and velocity profiles at the spill edge, instead of modeling the fire and compartment. The model gave predictions that generally agreed well with the correlations by Poreh, et al. (19) and Thomas, et al. (49). From the analysis, Miles, et

al. concluded that there was only a small amount of entrainment in the rotation region.

Chow, et al. (54) developed CL-Atrium, a two-layer zone model, to analyze smoke filling in an atrium from a 2D balcony spill plume, with steady-state and unsteady t^2-fires. The smoke filling rate was compared using design formulae by Poreh et al. (19), Thomas et al. (49) and NFPA92B (55). A comparison was also made with the CFAST (56) zone model. The predictions from the model showed that the layer height and layer temperature in the atrium were similar using either Poreh et al. or Thomas et al. methods. The predictions using NFPA 92B formula were similar to that predicted by CFAST for both steady-state and unsteady t^2-fires and are greater than that predicted using Poreh et al. and Thomas et al. formulae.

Li et al. (57) used the CFD package, PHOENICS with FLAIR module (58), to analyze the smoke filling in an atrium from 2D and 3D balcony spill plumes. The predictions of mass flow rate of 2D spill plumes using PHOENICS is marginally lower than those by Poreh et al. (19) and Thomas et al. (49). The CFD prediction show better agreement to the BRE spill plume method (31) with the entrainment coefficient, α, set to 0.11 instead of 0.16. For 3D balcony spill plumes, predictions by PHOENICS are generally lower than methods by Thomas et al. (59), NFPA 92B (55) and BRE with entrainment coefficient set as 0.16.

McCartney (60) carried out CFD modeling of balcony spill plumes using FDS (version 4) for elevations of 50m. The simulated fire compartment had the same dimensions as that of the full-scale test facility in NRCC. From grid optimization

studies, McCartney recommend a grid cell size of 0.1 m in the 5m tall fire compartment and 0.5 m grid cell size in the atrium. Predicted centerline temperatures in the fire compartment are significantly lower than the experimental data and the variation is as much as 750 °C. The prediction of the smoke layer height in the compartment opening and atrium are in good agreement with the experimental data. McCartney attributed the large margin of error to radiation errors in the experimental data, which measured almost 1,200 °C in the fire compartment for a fire with heat release rate of 2 MW and compartment opening of 12 m width and 5 m height. For the studies of the balcony spill plume at high elevations of 50 m, 13 simulations were carried out heat release rates of 1 MW, 2 MW and 5 MW, and compartment opening widths of 5 m, 8 m and 10 m. Most of the flows were channeled by 2 m deep screens and had no downstand at the compartment opening. A small number of simulations were carried out with 1.5 m downstand at the compartment opening and others without channeling screens. A new correlation for mass flow rate of the balcony spill plume was suggested as follows:

$$\dot{m}_p = 0.52\dot{Q}_c^{1/3} W_s^{0.2} z_s + \dot{m}_{p,z_s=0} \qquad (2\text{-}33)$$

The use of the correlation is restricted to scenarios with channeling screens and no downstand at the compartment opening. It was suggest that the mass flow rate at the spill edge be estimated by existing guidance.

Ko et al. (34) and Harrison et al. (32), (50) carried out CFD modeling of balcony spill plumes using FDS. Sections 2.23, 2.24, 2.36 and 2.37 describe these studies in detail.

2.4.2 Modeling of Ceiling Jets

Balcony spill plumes are developed from hot gases flowing out of a compartment into the connecting atrium. The initial flow of the hot gases beneath the ceiling and balcony is in the form of a ceiling jet. A brief description of modeling of ceiling jets using fire dynamics simulator (FDS) is given in the following sections.

2.4.2.1 McGrattan, Hostikka, Floyd, McDermott and Prasad

McGrattan et al. (61) carried out validation of experiments using FDS as part of the FDS model validation process. Two of such validation involves the measurement of the temperature of the flow of hot gases beneath a relatively flat ceiling.

The first validation is for the series of 25 large scale experiments conducted by Factory Mutual Research Corporation (FMRC), under the direction of Sandia National Laboratories (SNL), for the U.S. Nuclear Regulatory Commission (NRC) (62). The fire compartment measures 18 m x 12 m x 6 m in height and the peak fire size was 516 kW. 3 of the 25 experiments are included in the validation study. The domain is defined as the entire fire compartment and it was divided into 5 meshes. A uniform fine grid of 5 cm is applied to the mesh near the fire source and a uniform course grid of 20 cm is applied to other meshes. The thermocouples closest to the ceiling (12 cm away from the ceiling, about 2% of ceiling height) and located along the longitudinal axis centerline furthest from the fire source are chosen as a surrogate for the ceiling jet temperature. FDS was able to give rather good prediction of the temperature, compared to the experimental data, after the initial growth period of the

fire. The discrepancies during the growth period is possibly attributed to the fact that the modeling of the fire growth in FDS is by means of linear "ramps" and did not accurately replicate the actual growth of the fire which follows approximately a power-law relationship.

The second validation is for the series of 15 large scale experiments, sponsored by NRC, conducted by NIST (63). The experiments have fire sizes ranging from 350 kW to 2.2 MW in a fire compartment of 21.7 m x 7.1 m x 3.8 m height. All 15 experiments were included in the validation study. The fire compartment was defined as the domain and mesh stretching using polynomial transformation was applied to the x and y co-ordinate directions, resulting in grid cell sizes that ranges from approximately 10.8 – 42.9 cm in the x co-ordinate direction, 9.8 – 37.8 cm in the y co-ordinate direction and 12 cm in the z co-ordinate direction. Similar to the FMRC experiments, the thermocouple closest to the ceiling (32 cm away from the ceiling, about 8.4% of the ceiling height) located along the longitudinal axis centerline furthest from the fire source is chosen as a surrogate for the ceiling jet temperature. For 8 of the experiments, the temperature in the compartment reaches a relatively steady state for duration of about 20 minutes. For these cases, FDS predictions were within 5 – 10 % of the experimental values.

2.4.2.2 Hurley and Munguia

Hurley et al. (64) compared predictions of fire plume and ceiling jet temperatures using FDS to experimental data from full scale tests conducted by Underwriters Laboratory (UL) (65). The experiments were conducted in a 36.6 m x 36.6 m facility

with a height-adjustable, smooth, flat, horizontal ceiling. The heat release rates from the heptane burner ranges from 350k W to 10.4 MW, while the ceiling height ranges from 3 m to 12.2 m. The domain of the FDS model does not cover the entire experimental facility as it was deemed that certain areas of the facility do not have influence nor were influenced by the fire. The domain consists of two meshes, a 10 m x 10 m space enclosing the fire and extending to the ceiling and another 10 m x 10 m space, located adjacent to the first mesh extending from the ceiling to half the distance of the ceiling height. The first mesh models the flow of the plume from the fire and the portion of the ceiling jet nearer to the plume axis, while the second mesh models the ceiling jet at greater radial distance from the plume axis. Temperature measurements were taken at the plume axis and at radial distances of 2.2 m, 6.5 m and 10.8 m, all at a distance of 10cm below the ceiling.

Grid convergence studies were performed using uniform grid cell sizes of 10 cm and 6.6 cm for scenarios with ceiling heights of 3 m and 6.1 m. The studies show that grid convergence was achieved for the ceiling jet region, but not for the plume region. Further studies to determine the grid convergence for the plume region were not carried out due to the large computational resource and time required. Validation studies carried out by McGrattan et al. (61) determined that FDS was able to predict the plume centerline temperature based on McCaffrey's correlation with very good accuracy for far field conditions, using a uniform grid cell size which is 0.1 times the characteristic diameter of the fire. With the limitation of non-convergence in the plume region, FDS prediction for gas temperatures were within a factor of 1.9 of the experimental data.

2.4.2.3 Ierardi and Barnett

Ierardi et al. (66) compared FDS predictions of temperature and velocity in the ceiling jet region with Alpert's ceiling jet correlation. Two scenarios similar to the experiments that form the basis of Alpert's ceiling jet correlations were modeled. The first scenario was a 1 m x 1 m ethanol fire with a heat release rate of 670 kW under an unconfined ceiling of 7 m height. The second scenario was a 0.6 m x 0.6 m heptane fire with a heat release rate of 1 MW under an unconfined ceiling of 7.2 m height. Uniform grid cell sizes of 20 cm to 60 cm were used for the models and temperature and velocity predictions were made for locations at radial distances from 0.6 m to 7.2 m, corresponding to the dimensionless r/H values of 0.083 to 1. From this study, FDS generally gave better predictions of the maximum ceiling jet gas temperature than velocity. For the first scenario, the grid cell size of 33.3 cm gave the best prediction compared to Alpert's correlation, while for the second scenario, the grid cell size of 60 cm gave the best prediction. There is more discrepancy in the prediction of maximum velocity as compared to maximum temperature. For both cases, the coarsest grid gave the better velocity prediction. However, a grid convergence analysis was not performed as the sole purpose of this study was to demonstrate the suitability of different error analysis techniques and not a validation study.

3. CFD modeling using Fire Dynamics Simulator

3.1 Fire Dynamics Simulator

FDS is a CFD fire simulation software developed by the Building and Fire Research Laboratory at the National Institute of Standards and Technology (NIST). The software is based on Fortran 90 and the first version was released in 2000. The current version, version 5, was released in 2007 (67). (Version 5.2 parallel is used for the simulations carried out in this research) FDS was developed to solve practical problems in fire protection engineering and provide a tool in the study of fundamental fire dynamics and combustion. It can be used to model phenomena such as, low speed transport of heat and combustion products from fire, radiative and convective heat transfer between the gas and solid surfaces, pyrolysis, flame spread and fire growth, sprinkler and detector activation, and sprinkler sprays and suppression by water. FDS is widely used in fire research and engineering communities due to its accessibility, simplicity and open source nature which allows modifications and improvement to be made fairly easily.

3.1.1 Hydrodynamic model

FDS uses an approximate form of the Navier-Stokes equation appropriate for low Mach number applications. The approximation filters out acoustic waves but allows for large variation in temperatures and densities. Computations can be treated as Direct Numerical Simulation (DNS) or Large Eddy Simulation (LES). For DNS, the

dissipative processes of viscosity, thermal conductivity and material diffusivity are computed directly. This usually requires very small grid cell sizes of the order of 1mm or less. In LES, the large-scale eddies are resolved while those smaller than the grid cell sizes, also known as sub-grid scale (SGS) eddies, are modeled. This is based on the assumption that the smaller eddies contribute a small amount of the total kinetic energy of the flow and can be approximated. The use of LES is intended to increase the temporal and spatial accuracy of predicted flow properties compared to Reynolds-averaged Navier-Stokes (RANS) turbulence models, where temporal averaging leads to an artificial smoothing of the predicted flow properties.

3.1.2 Combustion model

Two combustion models are available in FDS. The mixture fraction model is the default, and the other is the finite-rate reaction model. The finite-rate reaction model is used for DNS computations where the fine grid resolution allows the diffusion process of the gas species to be resolved. Mixture fraction is a conserved scalar quantity defined as the ratio of the mass of a species to the total mass present at a given point in the flow field. For most applications, a single-step, instantaneous reaction is a reasonable assumption, where the reaction of oxygen and fuel occurs rapidly and completely upon mixing. Hence, the gas mixture can be uniquely determined by solely the mixture fraction. There are situations, such as under-ventilated compartments, where the assumption of complete reaction is not valid. In such cases, a single-step with local extinction and two-parameter mixture fraction allows for the co-existence of unburned fuel and oxygen, where the mixture fractions

of burned fuel and unburned fuel are computed explicitly. Simple empirical rules are used to predict local extinction based on oxygen concentration and temperature of gases in the vicinity of the flame sheet. To account for the higher soot and carbon monoxide productions in under-ventilated fires, a two-step reaction is used where the first step is the oxidation of fuel to carbon monoxide and the second step is the oxidation of carbon monoxide to carbon dioxide. For this case, there are three mixture fraction parameters of unburned fuel; fuel that has completed the first reaction step and fuel that has completed the second reaction step.

3.1.3 Radiative transport model

Radiative heat transfer is modeled in FDS by solving the radiation transport equation for a non-scattering grey gas, with the option of a wide band radiation model. The radiation equation is solved using a similar technique as the finite volume method for convective transport. Using approximately 100 discrete angles, this finite volume method takes up approximately 20 % of the total CPU time of a calculation. FDS uses a default radiative fraction value of 0.35 which is applicable for most common fuels and commodities. For the simulations conducted as part of this thesis, the fuel used is enthanol which generates lower combustion products and thus has a lower radiative fraction of 0.25.

3.1.4 Tangential Velocity boundary condition

Theoretically, the velocity at a solid surface has a value of zero and increases rapidly through the narrow boundary layer region. For most practical applications, the grid

cell is too large to accurately resolve the boundary layer. To overcome this, a velocity boundary condition factor, known as the slip factor, is used to set the velocity at the wall to be a fraction of its value in the cell adjacent to the wall. This slip factor ranges from -1 to 1, representing a no-slip boundary condition and free slip boundary condition, respectively. For DNS computations, the slip factor is set to -1 to give no-slip boundary conditions. For general applications of fire simulations with grid cell sizes that are too course to resolve the boundary layer, it is recommended to use the default value of 0.5, representing a partial slip condition.

In FDS 5.4, Werner and Wengle (WW) wall model (68) is used to model wall flows. This is a significant improvement to the previous method of arbitrarily assigning a velocity value that is a fraction of the value of the first grid cell. A brief description of the WW wall model is described here. The nondimensional streamwise velocity and nondimensional wall-normal distance are given by:

$$u^+ \equiv u/u^* \tag{3-1}$$

$$z^+ \equiv z/l \tag{3-2}$$

where $u^* = \sqrt{\tau_w/\rho}$ is the near wall region friction velocity and $l = \mu/\rho u^*$. The law of the wall is given by,

$$u^+ \equiv z^+ \qquad \text{for } z^+ < 5 \tag{3-3}$$

$$u^+ \equiv 2.4 ln z^+ + 5.2 \qquad \text{for } z^+ > 30 \tag{3-4}$$

The buffer layer, where both viscous and inertial stresses are important, lies within the region where $5 < z^+ < 30$. Werner and Wengle propose a simplification to the law of the wall as follows:

$$u^+ \equiv z^+ \qquad \text{for } z^+ \leq 11.81 \qquad (3\text{-}5)$$

$$u^+ \equiv A(z^+)^B \qquad \text{for } z^+ > 11.81 \qquad (3\text{-}6)$$

where $A = 8.3$ and $B = 1/7$. A comparison of the WW model and the log law is shown in Figure 3.1.

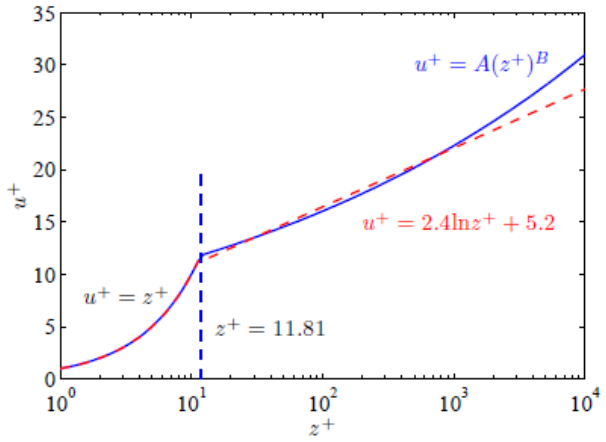

Figure 3.1: Comparison of log law and WW model

The WW model as implemented in FDS is given by

$$|\tau_w| = \frac{2\bar{\mu}|\tilde{u}|}{\Delta z} \qquad \text{for } z^+ \leq 11.81 \qquad (3\text{-}7)$$

$$|\tau_w| = \bar{\rho}\left[\alpha\left(\frac{\bar{\mu}}{\bar{\rho}\Delta z}\right)^{\beta} + \eta\left(\frac{\bar{\mu}}{\bar{\rho}\Delta z}\right)^{B}|\tilde{u}|\right]^{\gamma} \qquad \text{for } z^+ > 11.81 \qquad (3\text{-}8)$$

Where $\alpha = \frac{1-B}{2}A^{\frac{1+B}{1-B}}$

$$\beta = 1 + B$$

$$\eta = \frac{1+B}{A}$$

$$\gamma = \frac{2}{1+B}$$

The first off-wall velocity component is denoted by $\tilde{u}$, $\bar{\rho}$ and $\bar{\mu}$ are the average density and average molecular viscosity from the neighboring cell values, respectively. The effects of the change in the modeling of the near wall flows are discussed in Section 3.3.4.

3.2 Ceiling jet correlations

Ceiling jets are formed when the smoke from the rising fire plume impinge onto the ceiling and are deflected radially outwards as a shallow horizontal flowing layer (69). As the ceiling jet spreads along the ceiling, it entrains air from the room, causing the ceiling jet to grow thicker. The entrained air causes the velocity and temperature of the ceiling jet to reduce. Heat transfer to the ceiling also reduces the temperature of the layer of ceiling jet that is adjacent to the ceiling. Alpert's correlations for maximum excess temperature and velocity in the ceiling jet are as follows:

$$T - T_\infty = 5.38 \frac{\dot{Q}^{\frac{2}{3}}/H^{\frac{5}{3}}}{(r/H)^{\frac{2}{3}}} \tag{3-9}$$

Subject to $r/H \geq 0.18$

$$u = 0.195 \frac{(\dot{Q}/H)^{\frac{1}{3}}}{(r/H)^{\frac{5}{6}}} \tag{3-10}$$

Subject to $r/H \geq 0.15$

Heskestad (70) developed non-dimensional correlations for maximum ceiling jet excess temperature and velocity based on alcohol pool fire tests. Alpert analyzed these correlations and suggests that Heskestad's correlation for excess temperature and Alpert's theory for velocity be used for prediction of ceiling jet flows. These expressions are as follows:

$$\frac{T-T_\infty}{T_\infty} = Q_H^{*\frac{2}{3}}\left(0.225 + 0.27\frac{r}{H}\right)^{-\frac{4}{3}} \tag{3-11}$$

Subject to $0.2 \leq r/H \leq 4$

$$\frac{u}{\sqrt{gh}} = 1.06 Q_H^{*\frac{1}{3}}\left(\frac{r}{H}\right)^{-0.69} \tag{3-12}$$

Subject to $0.2 \leq r/H \leq 4$

The locations of these maxima are expected to range from about 1 – 2 % of the ceiling height for r/H from less than 1 – 2.

In more recent work, Alpert (17), reanalyzed his original data and developed a set of new correlations based on the convective heat release rate and also introduced the location of the virtual origin. The new correlations are as follows:

$$T - T_\infty = 7.14\frac{\dot{Q}_c^{\frac{2}{3}}}{(H-z_0)^{\frac{5}{3}}}\left(\frac{r}{H-z_0}\right)^{-0.647} \tag{3-13}$$

Subject to $\frac{r}{H-z_0} > 0.144$

$$u = 0.229 \frac{\dot{Q}_c^{\frac{1}{3}}}{(H-z_0)^{\frac{1}{3}}} \left(\frac{r}{H-z_0}\right)^{-1.017} \quad (3\text{-}14)$$

Subject to $\frac{r}{H-z_0} > 0.228$

Where the location of the virtual origin (70) is given by

$$z_0 = 0.083\dot{Q}^{2/5} - 1.02D_e \quad (3\text{-}15)$$

Thickness of the ceiling jet is defined as the distance below the ceiling where the excess gas temperature above the ambient value drops to 1/e or 0.368 of the maximum excess temperature. In general, the thickness of the ceiling jet is about 10-12 % of the ceiling height. Motevalli et al. (72) developed a correlation to determine this thickness, based on temperature measurements.

$$\frac{l_T}{H} = 0.112 \left[1 - \mathrm{e}^{-2.24\frac{\mathrm{r}}{\mathrm{H}}}\right] \quad (3\text{-}16)$$

Subject to $0.26 \leq \frac{r}{H} \leq 2.0$

3.3 CFD modeling of ceiling jet

The purpose of the preliminary studies is to determine the grid sensitivity of FDS in the prediction buoyant flows in close proximity to ceiling surfaces. Evaluation of FDS in the prediction of the temperature of such ceiling jets have been discussed in Section 2.4. FDS is able to predict the temperature to fairly accurately after the initial growth period of the fire. This gives confidence to the use of time-averaged steady-state temperature predictions by FDS. However, these validations do not evaluate if

FDS is able to accurately predict the temperature profile of the ceiling jet and the characteristics of the flow layer close to the ceiling. Therefore a more detailed analysis is required to give confidence to the use of FDS for such flow scenario and also to analyze the grid sensitivity of FDS in such predictions.

3.3.1 Preliminary CFD modeling of ceiling jet

A grid sensitivity study similar to that performed by Ierardi et al. (66), described in Section 2.4.2.3, was carried out to determine the grid cell size that would allow the predictions in FDS to converge. A 1 m x 1 m Ethanol fire with a heat release rate of 1000 kW was simulated under an unconfined ceiling of 5 m. Similar to Hurley et al. (64), 2 meshes were used to define the domain, as shown in Figure 3.2 with temperature contours.

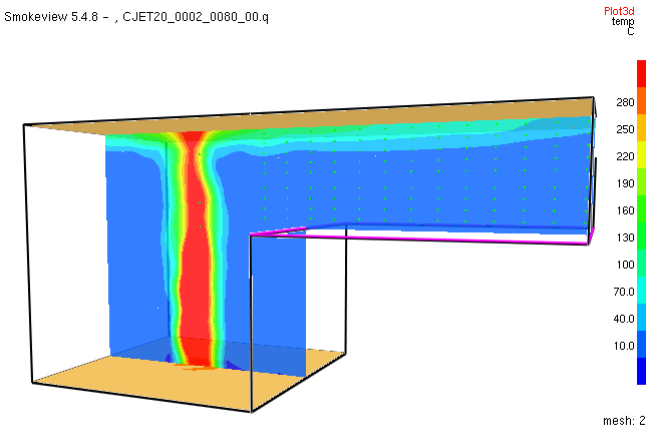

Figure 3.2: Computational domain for ceiling jet simulation

The first mesh, which models the fire source and the plume, covers an area of 5 m x 5 m with the fire at the center and extending to the ceiling. The second mesh of 5.25

m x 5 m, modeling the ceiling jet, is located adjacent to the first mesh, extending from the ceiling to 3m above the floor. Five simulations were carried out using grid cell sizes ranging from 2.5 cm to 25 cm. The simulation with the smallest grid cell size was used as a reference simulation for comparison with the other simulations. For the reference simulation, linear transformation was applied to cells within 1 m of the ceiling, reducing the grid cells in the z-direction (vertical) to 2.5c m. The dimensions in the x and y directions are 5 cm. Other grid cells are of uniform cubic dimensions of 5 cm. This transformation was necessary as the small grid cells meant that an impractically large number of cells are needed to fill the entire domain. Gas temperature and velocity measurements are recorded at regular intervals of 0.5 m, from radial distances of 1.5 m to 7 m. At each of these locations, the measurement devices are located at the center of each cell from the underside ceiling to a distance of 1m away. The maximum temperature and velocity at these locations are compared with the existing correlations by Alpert and Heskestad (17) as shown in Figure 3.3 and Figure 3.4.

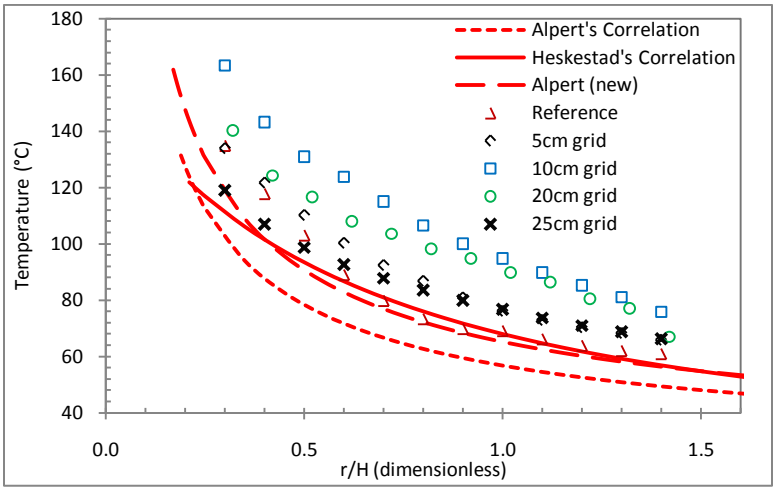

Figure 3.3: Comparison with ceiling jet correlations (temperature)

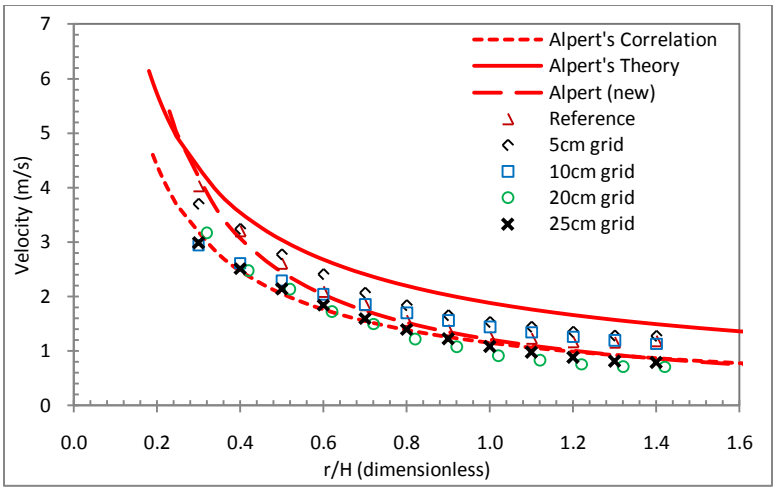

Figure 3.4: Comparison with ceiling jet correlations (velocity)

Alpert's previous ceiling jet correlation is shown in dotted line and his current correlation in dashed line. From the temperature plot, FDS predictions are generally higher than the correlations. The predictions from the reference simulation shows excellent agreement to Alpert's new correlation and Heskestad correlation for r/H values from 0.6 to 1.4. The simulations with 5 cm and 25 cm grid cell size gave predictions that are approximately within 15% of the correlations, with the latter showing better agreement throughout the whole range of r/H. Simulations with grid cell sizes of 10 cm and 20 cm gave predictions that are significantly higher.

The velocity predictions are lower than Alpert's theory but show better agreement to Alpert's new correlation. The reference simulation shows excellent agreement to Alpert's new correlation. The simulation with 5 cm grid cell size shows good agreement at smaller radial distances of r/H values of less than 1. In general, all the predictions are within 20 % of Alpert's new correlation. From these comparisons to the ceiling jet correlations, it seems that the simulation with 25 cm grid cell size gives

reasonably good temperature and velocity predictions. Due to this inconsistency of simulations with a larger grid cells giving better predictions than those with smaller grid cells sizes, the vertical temperature and velocity profiles were compared.

Figure 3.5 and Figure 3.6 show plots of the vertical temperature and velocity profiles of the five simulations at radial distance of r/H = 0.5. From the temperature plot, only the reference simulation shows a temperature drop at the grid cell adjacent to the ceiling. This is an indication of heat transfer from the gas to the ceiling. The simulation with 5cm grid cells shows a change in temperature gradient, hinting possible heat transfer, while the temperature gradient for the other simulations do not have significant changes. The simulation with 5 cm grid cells also shows the best agreement with the reference simulation. This is followed by the simulation with 25 cm grid cells. The simulation with 10 cm grid cells shows the highest temperature, about 30 % greater than that predicted by reference simulation. In general, at distances further from the ceiling, but still within the ceiling jet flow, all the simulations show a good match to the reference simulation.

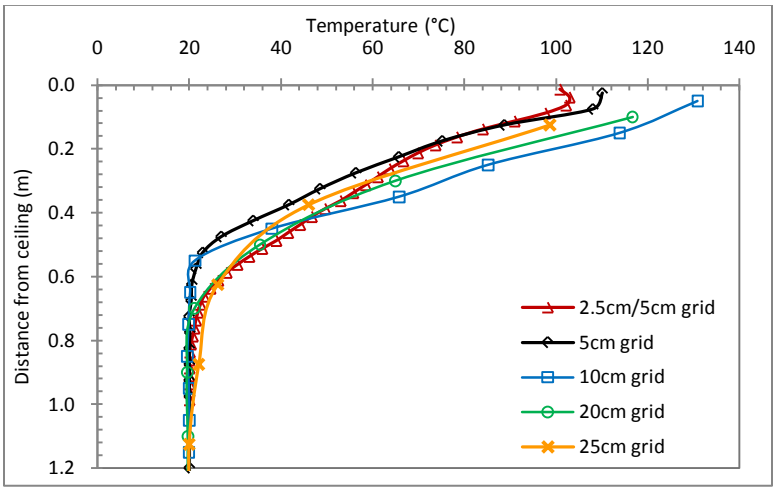

Figure 3.5 Temperature Profile at r/H=0.5

From the velocity plot, the profile of the 3 smallest grid cell sizes shows a decrease in velocity at the grid cell adjacent to the ceiling. The simulation with the 5 cm grid cell shows very good agreement with the reference simulation and predicted the same location of maximum velocity, 12.5 cm from the ceiling or 2.5 % of the ceiling height. The simulation with 10 cm grid cell predicted the location of the maximum velocity to be 15 cm from the ceiling and shows good agreement with the reference simulation at locations further from the ceiling. The two simulations with larger grid cells predicted maximum velocities that are lower in magnitude at the center of the grid cell adjacent to the ceiling, which happens to be 10 cm and 12.5 cm; hence the location is not far from the reference simulation. Appendix A shows all the temperature and velocity profiles for the various radial positions.

Alpert observed in his experiments that the position of the maxima is approximately 1 – 2 % of the ceiling height, which translates to a distance of 5 – 10 cm from the ceiling. Even with a grid cell size of 2.5 cm, the distance from the ceiling to the maximum is covered by 2 – 4 grid cells, which is far less than the generally accepted criteria of 8 – 10 grid cells within the characteristic length scale. Hence, an in-depth study is required to characterize the boundary layer flow, from the ceiling to the point where the maxima occur.

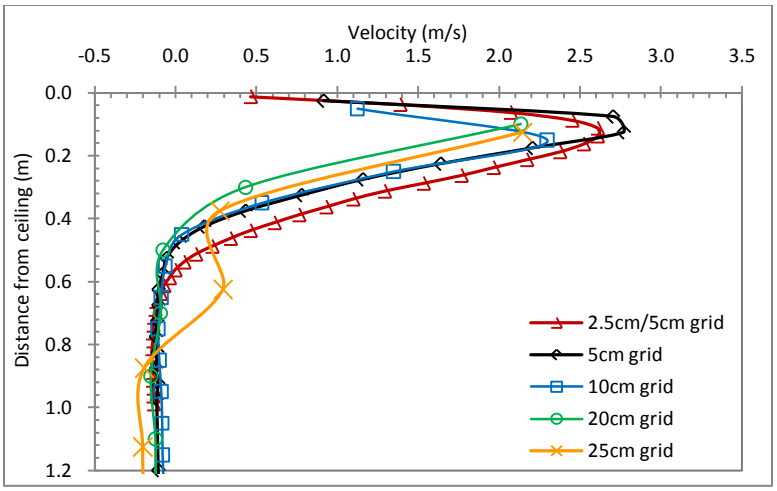

Figure 3.6: Velocity Profile at r/H=0.5

3.3.2 Characterization of the boundary layer

A study was carried out to fully characterize the retard layer by having at least 8 grid cells within the thickness of the retard layer. Due to the large number of grid cells required, it was necessary to run the simulation with multiple meshes.

The main concern of running simulations with multiple meshes is inaccuracies arising from the improper transfer of information from cells in one mesh to cells in a different mesh. This can be alleviated by ensuring that the temporal and spatial gradients are minimized when crossing the mesh boundaries. For ceiling jets formed by a circular or rectilinear fire source, the ceiling jets travel radially, which forms significant gradients in both the x-coordinate and y-coordinate directions, while the rising plume forms significant gradients in the z-coordinate directions. This results in a situation where the gradients in all directions are significant. To overcome this difficulty, an infinite line fire source is prescribed such that the significant gradients are in the x-coordinate and z-coordinate directions only as shown in Figure 3.7.

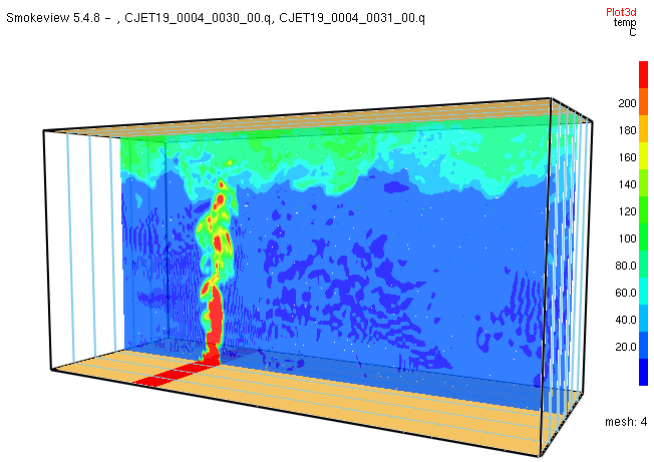

Figure 3.7: Computational domain for characterization of boundary layer

Six narrow meshes 16 m long and 1 m wide are placed adjacent to each other forming a domain that is 16 m long and 6 m wide and mirror symmetry is used at two ends of the domain to create an infinite line fire source. The fire source is a 1 m wide line source with a heat release rate of 1000 kW/m^2, located 4 m from one end of the domain, such that the ceiling jet can develop for a distance of 12 m under a 8 m tall unconfined ceiling. The ceiling is defined as having isothermal properties of 20 °C and non-slip boundary condition where the gas velocity at the ceiling is zero. The non-slip boundary condition is applicable in this case, since the small grid cells would allow the boundary layer to be sufficiently resolved.

Using Alpert's prediction of the maxima occurring within 1 – 2 % of the ceiling height as an estimate, the thickness of the boundary layer was assumed to be about 16 cm. This requires the grid cells to be about 1.6 cm, or about 31 million grid cells in a single mesh, which is technically and economically infeasible. Hence, mesh stretching using polynomial transformation in the z-coordinate direction was applied

such that there are 10 grid cells within the retard layer. The gird cell dimensions for the other two directions are 4 cm. Polynomial transformation has the advantage that the grid cell sizes are gradually changed to ensure a smooth transition. The drawbacks are that polynomial transformation is more difficult to define and the grid cell sizes vary throughout the entire range. To ensure that the flow in the other regions of the ceiling jet is properly characterized, grid size of less than 10cm is prescribed to ensure that the transition of grid cells is not too drastic. Furthermore, from Section 3.2, it is shown that predictions in this region with larger grid sizes show reasonable match to that of smaller grid sizes. To ensure proper characterization of the near field flows near the fire source, the grid cells in that region are specified to be no more than 10cm such that there are 10 grid cells across the width of the line fire source.

As a gird convergence study, simulations with larger grid sizes are also performed with a range of 2, 5 and 7 grid cells within the retard layer, all satisfying the criteria of 10cm within the ceiling jet region and 10 cm in the fire plume. The simulation with 10 grid cells in the retard layer is used as a reference simulation. Larger grid cell sizes ranging from 10 cm to 50 cm are also carried out. For these simulations, the criteria of 10 cm grid cells in the ceiling jet flow region are not met as it would result in large transformation of the grid cells, which is not recommended. However, the criterion of 10 cm grid cells in the fire plume is satisfied in order to ensure that the upstream flow of the ceiling jet is properly characterized. The no-slip boundary condition is applied to all simulations to maintain consistency, although for larger

grid cell sizes, a partial slip condition is more appropriate. Details of the simulations are shown in Table 3-1.

Table 3-1: Details of simulations for boundary layer flow

	Retard Layer		Ceiling Jet Region
Simulation	No. of cells	Average grid cell size (cm)	Average grid cell size (cm)
Reference	10	1.6	5
S2	7	2.3	5
S3	5	3.2	5
S4	2	6.5	6
S5	1	10	11
S6	1	15	15
S7	-	20*	20
S8	-	25*	24
S9	-	30*	29
S10	-	40*	39
S11	-	50*	48

*Size of the first grid cell at the ceiling

Figure 3.8 and Figure 3.9 show the temperature profile at radial distance of 4m or r/H = 0.5. From the temperature plot, predictions from simulations S2 to S9 are within 5 % of the reference. Prediction of the location of maximum temperature for the reference is at 9 cm from the ceiling. Simulations S2 to S5 predicted it to be within a range of 7-13 cm from the ceiling. Simulations with larger grid sizes predicted that the maximum temperature is at the ceiling. In general for all the simulations, at distances further from the ceiling, there is better agreement with the reference.

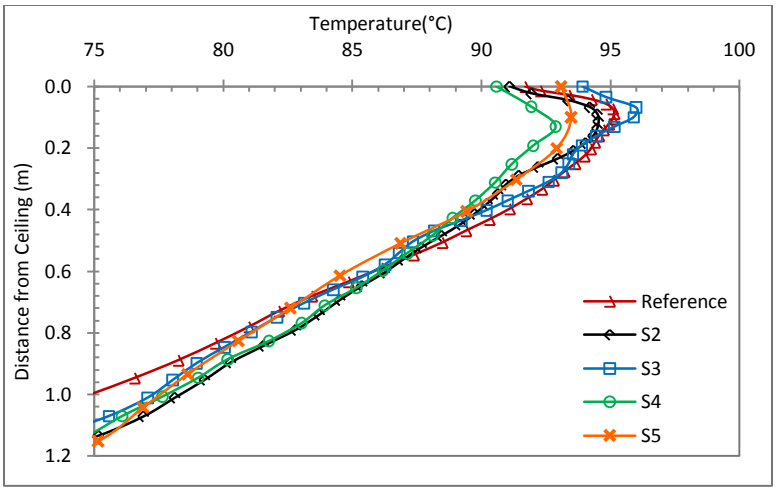

Figure 3.8: Temperature profile for simulations reference and S2 to S5 at r/H=0.5

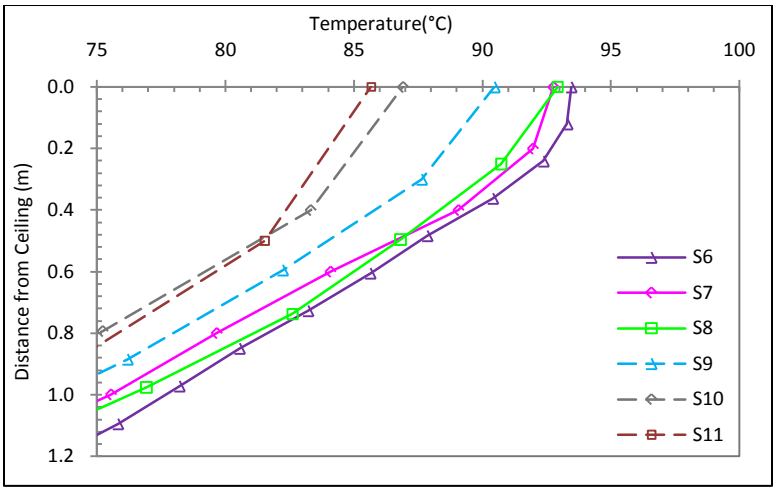

Figure 3.9 Temperature profile for simulations S6 to S11 at r/H = 0.5

From the velocity plots in Figure 3.10 and Figure 3.11, predictions from simulations S2 to S8 are within 10 % of the reference. Prediction of the location of maximum velocity for the reference is at 18 cm from the ceiling. Simulations S2 to S7 predicted the location of the maximum velocity at a distance of about 20 – 25cm below the ceiling. The remaining simulations predicted the maximum velocity at the location of the second grid cell from the ceiling surface, which results in the predicted location of

the maximum velocity to be further away from the ceiling. Similar to the temperature predictions, at distances further from the ceiling, there is better agreement with the reference.

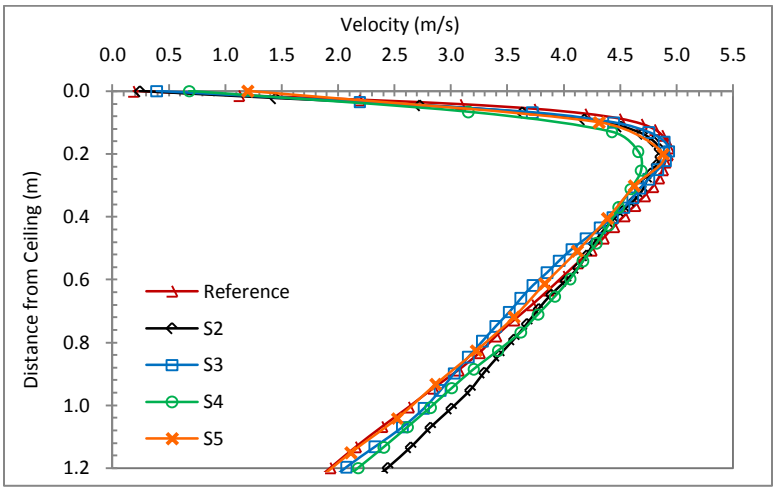

Figure 3.10: Velocity profile for simulations reference and S2 to S5 at r/H=0.5

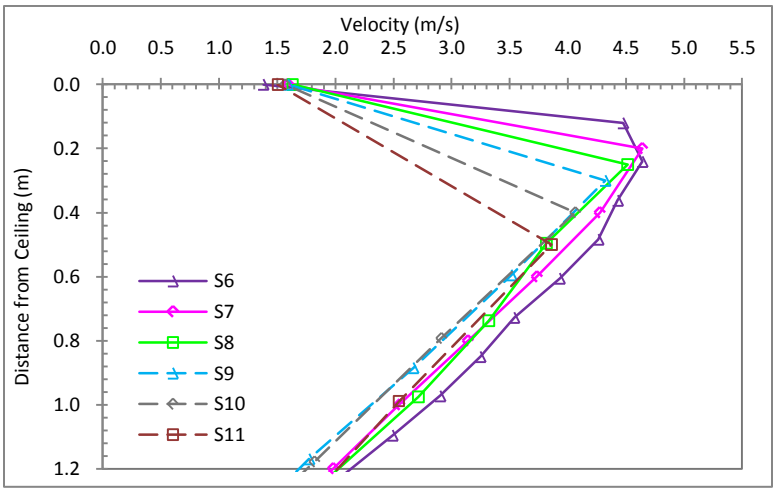

Figure 3.11: Velocity profile for simulations S6 to S11 at r/H = 0.5

The temperature and velocity plots for the radial positions of r/H = 0.75, 1.0, 1.25, 1.5 are also analyzed. Details of these plots are shown in Appendix B. From these temperature plots, the predictions from simulations S2 to S9 remained within 5 % of

the reference. The location of the maximum temperature shifts further away from the ceiling as the radial distance increases. At the furthest radial position, the prediction of the location of the maximum temperature from the reference simulation is a distance of 14 cm from the ceiling. At further radial positions, simulations S6 to S9 predicted that the location of maximum temperature is away from the ceiling. In general, the predictions from the simulations with larger grid sizes have better agreement with the reference at further distances from the ceiling. It is also observed that when the size of the grid cell is smaller than the distance between the location of the maximum temperature and the ceiling, the prediction of the magnitude of the maximum temperature improves, but the prediction of the location is largely determined by the grid cell size.

From the velocity plots, predictions from all the simulations fall within 10% of the reference as the radial distance increase. Similar to the temperature predictions, the location of the maximum velocity shifts further away from the ceiling as the radial distance increases. At the furthest radial position, the prediction of the location of the maximum velocity from the reference simulation is a distance of 25 cm from the ceiling. At distances further from the ceiling, the predictions from the simulations with larger grid cells show better agreement with the reference. At further radial positions, the prediction of the magnitude of the maximum velocity for simulations S2 to S9 is in very good agreement with the reference, while the location of the maximum velocity is very much determined by the grid cell size. From the various plots, we observe that a grid size of up to 25 cm, equivalent to 3.1% of ceiling height, is able to give good predictions of both temperature and velocity. At larger radial

distances, r/H > 0.5, grid cell size of up to 30 cm, equivalent to 3.8% of ceiling height, gives reasonably good predictions for both temperature and velocity compared to the reference simulation. If proper resolution of the retard layer, i.e. the flow layer between the ceiling and the location of the maximum, is required, much smaller grid sizes are required.

Due to the variation in the temperature and velocity predictions at and near the ceiling surface, it would be interesting to see how convective heat transfer to the surface of the ceiling varies due to the difference in grid sizes. Convective heat flux is calculated using the gas temperature and velocity values at the center of the cell adjacent to the solid surface using the following expression,

$$\dot{q}_c^{"} = h\left(T_g - T_{wall}\right) \tag{3-17}$$

The heat transfer coefficient is determined by the greater of the two values in the brackets of equations (3-9)

$$h_c = \left[C\left|T_g - T_{wall}\right|^{\frac{1}{3}},\ \frac{k}{L}0.037\ Re^{\frac{4}{5}}\ Pr^{\frac{1}{3}}\right] \tag{3-18}$$

where C is the coefficient of natural convection with a value of 1.52 for a horizontal surface and 1.31 for a vertical surface.

From Figure 3.12, for simulations up to S3, the convective heat fluxes are virtually equal. As the grid cell sizes increase, the predicted convective heat fluxes increase. This is mainly due to the significantly larger values of velocity predicted when using a larger grid size. From Figure 3.12, we can draw a conclusion that there should be at

least 5 grid cells within the retard layer, which has a thickness of approximately 0.02 h, to give a good prediction of the convective heat flux to the ceiling. This translates to approximately grid cell sizes of 0.004 h. However, using such a small grid size is impractical due to the long computational time and excessive computational resources required.

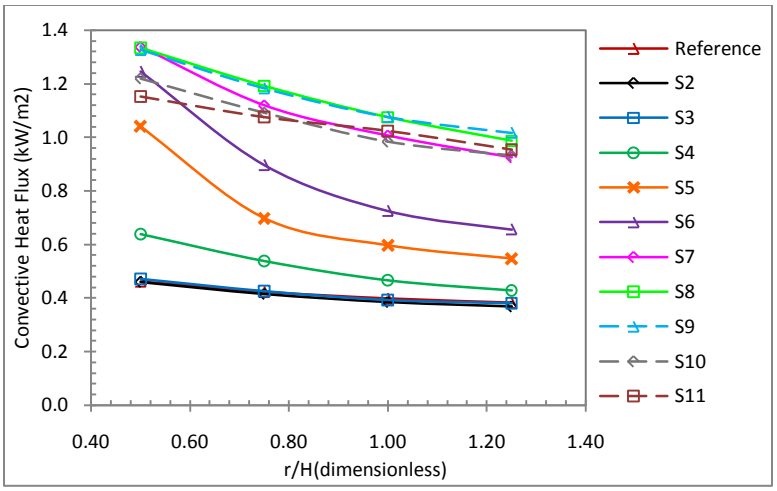

Figure 3.12: Plot of Convective heat flux with radial distance

In practical applications, FDS can be used to determine the response time of detectors or sprinklers. The response of detectors and sprinklers depends on the convective heat transfer to the detector element. Heskestad et al. (73) proposed the use of a time constant, τ to describe this heat transfer,

$$\tau = \frac{mc_p}{h_c A} \tag{3-19}$$

The characteristics of a given detector can be expressed using the response time index(73),

$$RTI = \tau u^{1/2} \tag{3-20}$$

The response time of a detector is given by

$$t_r = \frac{RTI}{u^{1/2}} ln\left(\frac{T-T_\infty}{T-T_r}\right) \quad (3\text{-}21)$$

From the temperature and velocity profiles, the response time can be calculated for typical detectors and sprinkler. Table 3-2 shows the calculated response time, for the different simulations, of a typical heat detector with RTI of 50 and rated operating temperature of 57°C located 10cm below the ceiling and a typical sprinkler with RTI of 80 and operating temperature of 68 °C located 20 cm below the ceiling, at radial distance of 4 m (r/H = 0.5).

Table 3-2: Variation in response time for typical heat detector

Simulation	Heat detector			Sprinkler		
	Response time t_r	Variation from S1		Response time t_r	Variation from S1	
		Absolute	Percentage		Absolute	Percentage
Reference	15.76	-	-	37.48	-	-
S2	16.46	0.69	4%	38.22	0.74	2%
S3	15.81	0.05	0%	37.93	0.45	1%
S4	17.96	2.20	14%	40.65	3.17	8%
S5	16.88	1.11	7%	38.43	0.95	3%
S6	17.28	1.52	10%	39.89	2.41	6%
S7	19.65	3.89	25%	40.76	3.28	9%
S8	20.82	5.06	32%	43.98	6.50	17%
S9	23.35	7.58	48%	50.16	12.68	34%
S10	27.11	11.35	72%	60.46	22.98	61%
S11	29.41	13.65	87%	67.32	29.83	80%

From Table 3-2, the calculated response time increases with an increase in grid cell size, with the exception of S3 and S5, which has a lower response time than S2 and S4, respectively. The increase in response time is explained by the lower temperature

and velocity predicted by the simulations with larger grid cells at those specific locations. In general, the simulations with larger grid cells predict lower temperature and velocity at locations in the ceiling jet region beyond the retard layer. Simulation S2 to S6 has calculated response times that deviate less than 15 % from that of the reference. Although the percentage deviation of the simulations with larger grid cells is high, the maximum deviation in the actual response time is less than 30s. Furthermore, a longer calculated response time leads to a more conservative design.

In conclusion, a very small grid cell of about 0.4 % of the ceiling height is required in order to have grid convergence for the prediction of the convective heat flux at the ceiling. Simulations with grid cell size of about 10cm, which corresponds to about 1.25 % of the ceiling height, give predictions of the location of maximum temperature and velocity that agrees well with that of the reference simulation. Simulations carried out with grid cell sizes of up to 25 cm, corresponding to about 3 % of the ceiling height, gives predictions of temperature and velocity within 10 % to that predicted by the reference simulation, for radial distance of half the ceiling height. At further radial distances, the grid cell size can be increased to 3 cm or about 4 % of the ceiling height with similar accuracy. This conclusion is drawn from this simulation with an infinite line fire source and should only be used as a rough guide in determination of the most effective grid cell size to use for other simulation. A grid convergence study is recommended prior to the start of actual simulation.

3.3.3 Simplified case of boundary layer flow

In the previous study of the ceiling jet, there is a need to ensure that the fire source is properly resolved so that the conditions at the ceiling jet are consistent for the different simulations. Due to the use of polynomial mesh stretching, it was not possible to ensure that the grid sizes in the plume are identical, though efforts are made to ensure that the fire source is properly resolved by having at least 10 grids across the fire source. Therefore, a simplified scenario of a vent supplying hot air just beneath the ceiling was used to simulate the flow of a ceiling jet.

A single mesh is used to define the 1.6 m long, 0.3 m tall and 0.1 m deep domain. The upper boundary of the domain is the isothermal ceiling and one of the vertical boundaries was defined as a wall with a vent to discharge hot air, such that the hot air jet can develop for a distance of 1.6m beneath the ceiling. Similar to the previous study, the ceiling was given a no-slip boundary condition. The size of the vent is 0.1 m deep and 0.1 m tall and discharges hot air at 100 °C with a velocity of 2 m/s. These properties are selected such that the ceiling jet resembles that from a $1/10^{th}$ scale model with 1m tall ceiling and a 10 kW fire. Hence, the maximum temperature and velocity are expected to be located within 1 – 2 cm from the ceiling.

A series of simulations, shown in Table 3-3 are carried out as a grid sensitivity study. In order to resolve the boundary layer which is expected to be located within 1 – 2 cm from the ceiling, 10 grid cells were specified within the first 1 cm from the ceiling for the reference simulation. Polynomial transformation for the z-coordinate direction is employed to ensure that the sizes of the grid cells are transformed gradually. The

other two dimensions of the grid cells are kept constant at 4 mm. For simulations with larger grid cells, transformation was not applied as the total number of grid cells in the domain was possible to allow running the simulation on a single processor.

Table 3-3: Details of simulations for simplified boundary layer flow

	First 10mm from ceiling	
Simulation	No. of cells	Average grid cell size (mm)
Reference	10	1
SA2	7	1.44
SA3	5	2
SA4	3	3.4
SA5	2	5
SA6	1	10
SA7	-	20
SA8	-	30
SA9	-	50

Figure 3.13 shows the temperature profile at a distance of 0.8 m from the vent. The reference simulation and simulations SA2 to SA4 predict the location of maximum temperature to be within the range of 7 – 9 mm from the ceiling. The predicted location of the maximum depends on the size of the grid cell. For simulations SA6 to SA9, the predicted maximum temperature is at the ceiling. With the exception of the first grid cell adjacent to the ceiling, predictions from SA2 to SA8 are generally within 15 % of the reference simulation. In general, the predictions from simulation with larger grid cell sizes improve as the distance from the ceiling increases. However, when the grid cell size is too large, e.g. simulation SA9, poor agreement with the reference simulation is observed. If the thickness of the flow layer is defined in a similar manner as that for a ceiling jet, then using the data from the reference

simulation, the thickness is about 36 mm. Hence, when the grid size is larger than the thickness of the flow layer, we should expect poor prediction of temperature.

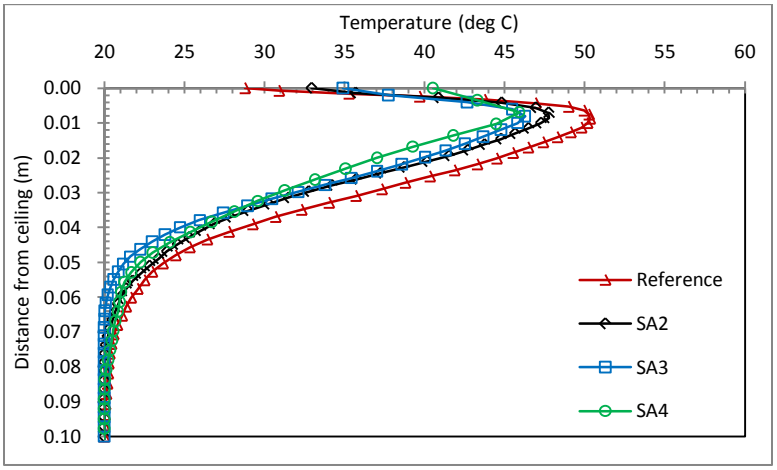

Figure 3.13: Temperature profile for simulations reference and SA2 to SA4 at 0.8 m

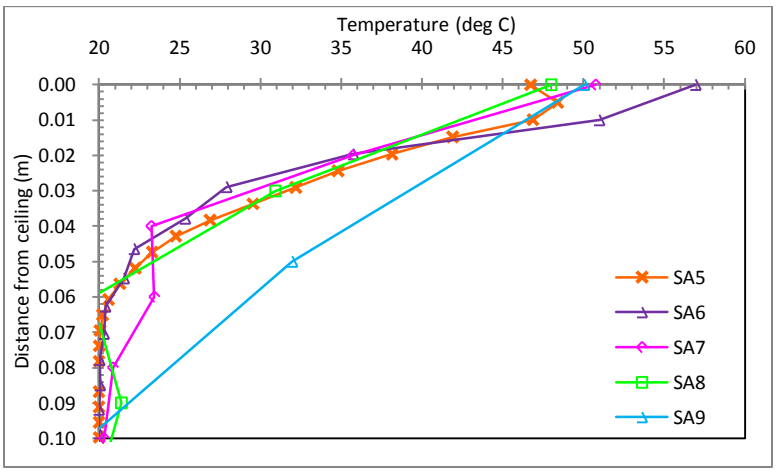

Figure 3.14: Temperature profile for simulations SA5 to SA9 at 0.8 m

From the plot of the velocity profile in Figure 3.15, the reference simulation and simulations SA2 to SA6 predict the location of maximum temperature to be within the range of 8 – 10 mm from the ceiling. For SA7, the maximum is located at the second grid cell from the ceiling while SA8 and SA9 predicted the maximum velocity

at the ceiling. Again the predicted location of the maximum largely depends on the size of the grid cell. The magnitude of the maximum velocity predicted by SA3 to SA6, which ranges from 0.79 – 0.85 m/s, is about 20 % lower than that of the reference. For coarser grid cells, the magnitude of the maximum velocity is less than half of the reference. In this case, both the magnitude and location of the maximum is very dependent on the grid cell size. For distances further from the ceiling, the agreement with the reference improves. Similar to that observed in the temperature plot, SA9 shows poor agreement with the reference.

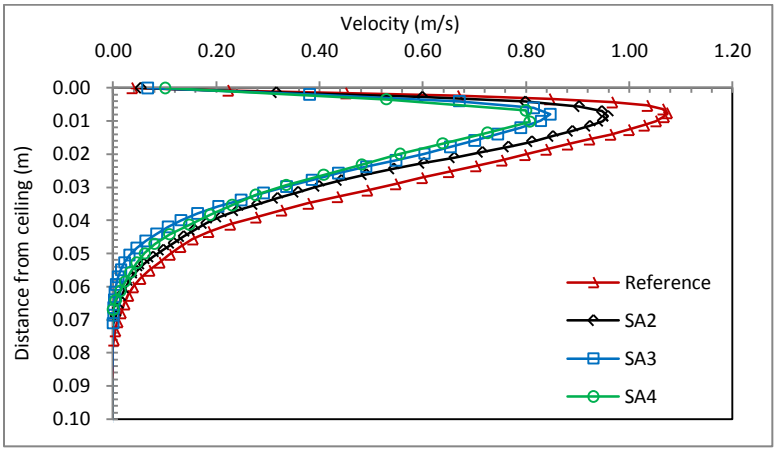

Figure 3.15: Velocity profile for simulations reference and SA2 to SA5 at 0.8 m

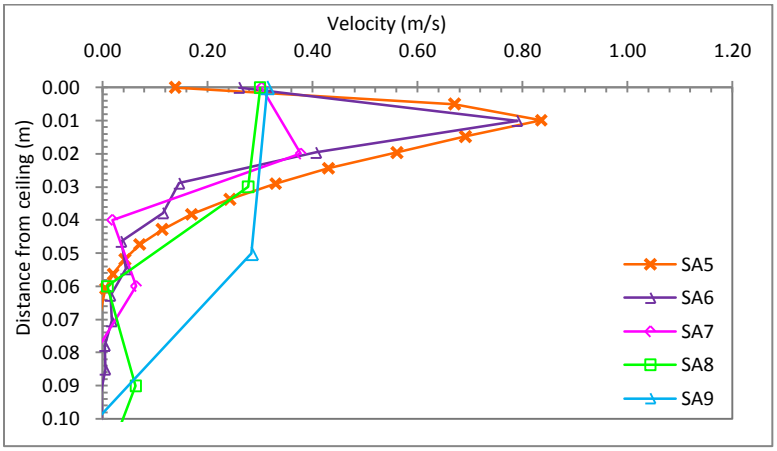

Figure 3.16: Velocity profile for simulations SA5 to SA9 at 0.8 m

Similar analyses were also performed for distances of 0.4 m, 1.2 m and 1.6 m. Details of the plots are shown in Appendix C. The flow layer thickness, temperature and velocity are reduced as the distance increases. Due to the reduced thickness of the flow layer at further distances, the prediction from simulations with larger grid cells show poorer agreement with the reference. This is in contrast with ceiling jet simulations which show better agreement at further radial distance due to the increasing thickness of the ceiling jet.

In this study, grid convergence was not observed. The predictions from simulations with larger grid sizes were also in poorer agreement as compared to the ceiling jet study. This can be attributed to the thinner flow layer with respect to the grid cell sizes. The thinner flow layer causes larger temperature and velocity gradients in the vertical orientation. We can also conclude that another important factor in the selection of grid cell size is the thickness of the flow layer. In order to achieve reasonable prediction of temperature or velocity, the grid cell has to be smaller than the thickness of the flow layer or the ceiling jet. To err on the safe side, it is suggested to have 2 – 3 grid cells within the thickness of the calculated flow layer. Since ceiling jets have thickness of about 10 – 12 % of the ceiling height (17), the previously recommended grid cell size of 4 % of the ceiling height would ensure that there are at least 2 – 3 grid cells within the ceiling jet.

3.3.4 Werner and Wenger Wall Model

The inclusion of the Werner and Wenger wall model in FDS version 5.4 improves the prediction of near wall velocity. As the simulations in this research have been carried

out using FDS version 5.2, an analysis is performed to compare the differences in the predictions. Figure 3.17 shows the predicted velocity profiles at r = 0.8 m, from FDS version 5.4 plotted with those from FDS version 5.2 with no slip boundary condition and default partial slip boundary condition. The predictions with no slip and default boundary conditions are about 5 % and 20 % lower than those from FDS version 5.4, respectively. The predicted location of the maxima is the same.

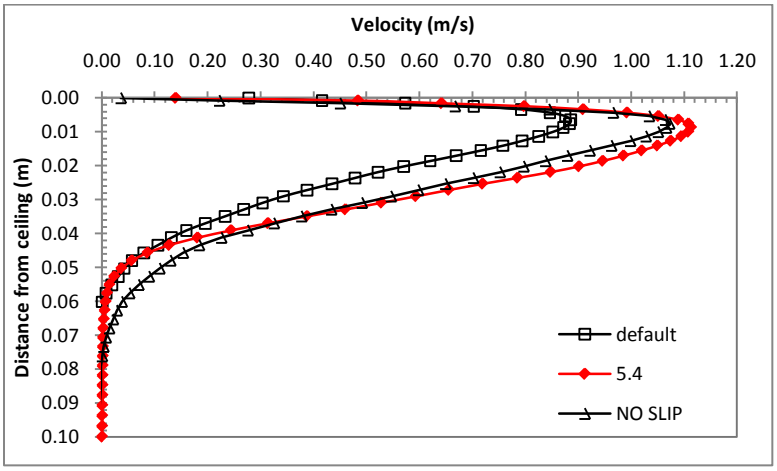

Figure 3.17: Velocity profiles for reference simulation with WW wall model

Figure 3.18 shows that the deviation in temperature profile is much greater than the velocity profile. The predictions from with no slip and default boundary conditions are about 29 % and 37 % lower than those from FDS version 5.4, respectively. The predicted location of the maxima is also different, 3 mm from the ceiling for FDS version 5.4 compared to 8 mm from the ceiling for that from version 5.2.

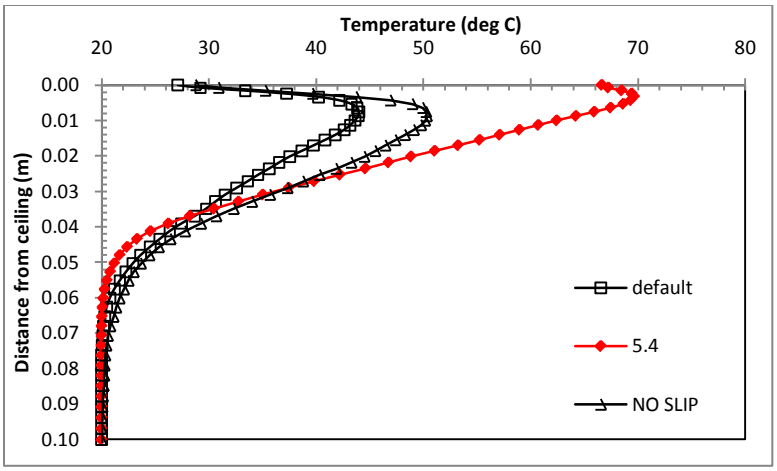

Figure 3.18: Temperature profiles for reference simulation with WW wall model

Using the values of temperature and velocity of the first grid cell away from the wall, the value of z^+ is calculated using Equation 3-2, which yields 3.57, 3.63 and 4.23 for FDS version 5.2 with no slip boundary condition, FDS version 5.4 and FDS version 5.2 with default boundary condition. Since these values are within the viscous sub-layer, it gives confidence that the boundary layer is well-resolved in all cases and the no slip boundary condition should be applicable.

The large deviation in the predicted temperatures at near wall locations raises the question of the applicability of the heat transfer model. In this case, the model for convective heat transfer to the wall is the same for both FDS versions. While the heat transfer model may be suitable for LES calculations in previous FDS versions, it may not be suitable for the current version with the WW wall model, especially for this case where the grid cell sizes are small.

4. CFD Modeling of Small-Scale Balcony Spill Plume

FDS was used to model the small-scale experiments carried out by Harrison (50). The purpose of modeling the small-scale experiments is to validate the FDS predictions with the experimental data, as well as performing a grid sensitivity analysis that could be adopted for modeling a typical compartment fire on a full scale. The optimum grid cell size for modeling ceiling jets was determined in Section 3 to be about 3.8% of the ceiling height. It is expected that the optimum grid cell size for modeling compartment fires to be about the same.

4.1 CFD modeling description

4.1.1 Geometry of fire compartment

The modeled fire compartment has a floor area of 1 m x 1 m and height of 0.5 m. The width of the compartment opening is 0.6 m and a balcony of 0.3 m breadth projects horizontally from the compartment opening. Channeling screens of 0.2 m depth are used to prevent the lateral spread of smoke under the balcony.

The walls of the fire compartment are described as fiber insulation boards with thickness of 25 mm. The balcony and channeling screens are described as fiber insulation boards of 10 mm thickness. The boards were given the following properties from Drysdale (75):

$$k = 0.041 W/m.K$$

$$\rho = 229kg/m^3$$

$$c_p = 2.09kJ/kg.K$$

A schematic diagram of the modeled fire compartment is shown in Figure 4.1.

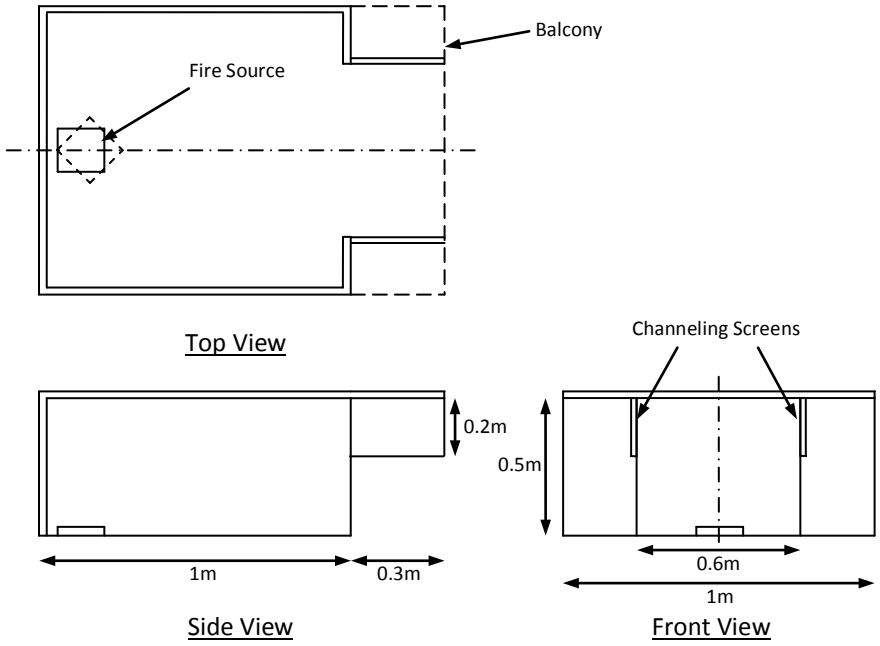

Figure 4.1 Schematic diagram of modeled fire compartment

4.1.2 Initial Computational domain

The initial computational domain is defined as 1.8 m in length, 1.2 m in depth and 0.6 m in height, extending 0.1 m beyond the three walls of the fire compartment and 0.5 m beyond the spill edge. This computational domain will be varied at a later stage to study the sensitivity of domain sizes on predictions. With a uniform grid cell size of 25 mm, the initial computational domain is divided into 82.944 uniform grid cells. With the exception of the lower boundary, all the exterior boundaries of the domain

were set as “OPEN”, which is defined as a passive opening to the outside at ambient conditions, where the ambient temperature is 20 °C.

4.1.3 Fire source

The fire source is defined as an obstruction with floor area of 0.14 m and 0.025 m in height, located 0.035 m from the rear wall. The heat release rate per unit area is specified as 527 kW/m^2, giving a total heat release rate of 10.3 kW. This equates to a full-scale heat release rate of 3257 kW. Since the experiment was performed by burning ethanol, the radiative fraction of 0.25 was used (76). It is noted that the fire tray in the experiment was positioned such that the corner of the tray was pointed towards the rear wall, as shown by the dashed lines in Figure 4.1. As compared to the modeled fire source in FDS, there is increased entrainment into the plume as the sides of the fire tray are further from the rear walls. Furthermore, there are only 1 – 2 grid cells between the wall and the modeled fire source in FDS, which could result in the entrainment effects being poorly resolved. Hence, an additional set of simulations, with the fire source located in the center of the fire compartment, was carried out to ensure that the entrainment from all four sides of the fire source is not constrained.

4.1.4 Instrumentations

In the small-scale experiments, gas temperatures and velocities are measured at the spill edge in the vertical and lateral orientation to determine the vertical profile and uniformity across the spill edge, respectively. Similar to the experiments, gas temperatures and velocities are measured at these locations. To determine the vertical

temperature and velocity profile, predictions are made at intervals of 10mm at the center of the spill edge for the first 0.2 m below the spill edge. The interval is increased to 20 mm between 0.2 m and 0.3 m below the spill edge and 50 mm for the remaining distance. For the lateral variation in temperatures and velocities, predictions are made at regular intervals of 50 mm at 10 mm below the spill edge. In addition to the temperature and velocity measurements, mass flow rates are predicted at the compartment opening and spill edge by specifying a vertical plane over the flow area at the respective locations. All predictions are logged at 0.5 s intervals. A simulation time of 900 s was specified to allow the conditions to achieve steady state.

4.1.5 Series of FDS simulations for grid sensitivity analysis

A series of simulations is carried out using various grid cell sizes to determine the optimum grid cell size for subsequent simulations to be carried out in the full-scale. The series of simulations includes grid cell sizes from 10 mm to 25 mm, equivalent to 2 % to 5 % for the ceiling height. Larger grid cell sizes were not examined as it was concluded that they do not give predictions that were satisfactory (50). The simulations are listed in Table 4-1.

Table 4-1: List of simulations for small-scale modeling

Simulation	Location of fire source	Grid Size		Total grid cells
		(mm)	(% of H)	
SC61	Experiment	25	5	82,944
SC61C	Center	25	5	82,944
SC62	Experiment	20	4	162,000
SC62C	Center	20	4	162,000
SC63	Experiment	15	3	384,000

Simulation	Location of fire source	Grid Size		Total grid cells
		(mm)	(% of H)	
SC63C	Center	15	3	384,000
SC64	Experiment	10	2	576,000
SC64C	Center	10	2	576,000

4.1.6 Error Analysis

The FDS predictions are time averaged over the sampling period once steady state conditions are achieved. The results are determined in terms of time-averaged mean values with associated standard errors. The standard error is determined by dividing the standard deviation of the sample by the square root of the sample population. The standard deviation is determined using the relevant function in Microsoft Excel.

4.2 Results of FDS simulations

The fire source was prescribed as a steady state source and the maximum heat release rate was achieved in less than 3 s. However, the flow properties may not achieve steady state until a much later time. In this study, the mass flow rate is the flow property of interest and the time variation of mass flow rate is plotted to determine the time required for steady state conditions.

4.2.1 Mass flow rate at spill edge

Figure 4.2 and Figure 4.3 show the variation of mass flow rate of hot gases at the spill edge for the simulations performed for the grid sensitivity analysis. A 50-point moving average was applied to the predicted mass flow rate to smooth the

fluctuations. Steady state is observed for all simulations after approximately 700 s, thus all relevant data are time-averaged from 700 – 900 s.

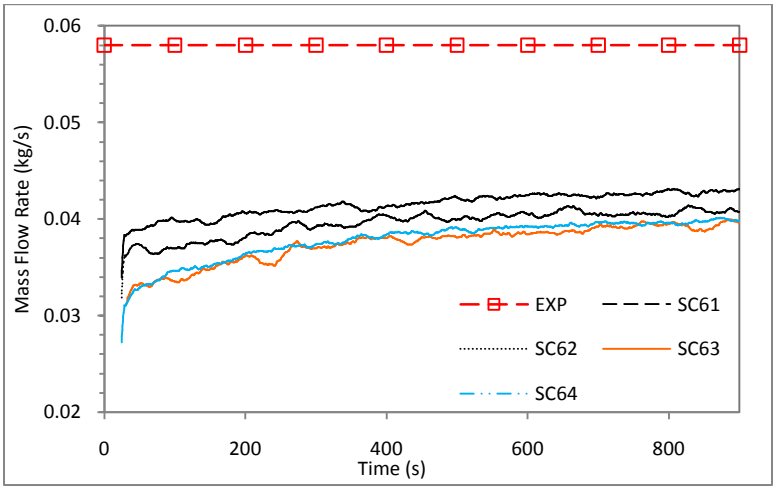

Figure 4.2: Mass flow rate at spill edge for fire source at rear of compartment

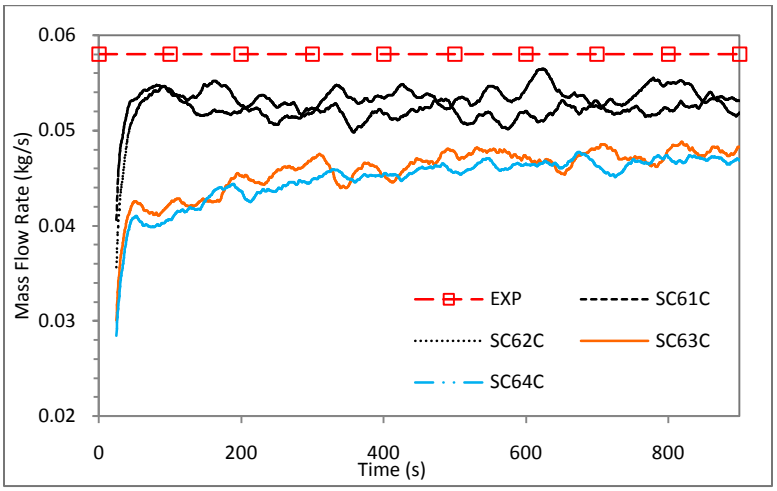

Figure 4.3: Mass flow rate at spill edge for fire source at center of compartment

From Figure 4.2, the predicted mass flow rates are significantly lower than the mass flow rate calculated from the experimental data. The predicted mass flow rate decreases as the grid cell size is reduced and those for simulations SC63 and SC64 are very similar.

The predicted mass flow rates in Figure 4.3 are significantly larger than those in Figure 4.2, but still 5 – 17 % lower than the experimental mass flow rate. A greater amount of fluctuation is observed as compared to Figure 4.2. Similar to that observed in Figure 4.2, predicted mass flow rates decreases as the grid cell sizes are reduced and the predicted mass flow rates for simulations SC63C and SC64C are very similar.

4.2.2 Velocity vectors at the fire source

To investigate the different mass flow rates for simulations with fire source at different locations, velocity vectors for the two scenarios are analyzed. From Figure 4.4, the distance between the rear wall and the fire source is equivalent to 1 grid cell. The velocity in that space between the rear wall and fire source is predominantly in the vertical direction. Therefore, it can be considered that there is no entrainment from the rear of the fire source. The door jet effect can be observed from the horizontal vectors on the front end of the fire source, but the plume axis remains fairly straight due to the proximity of the rear wall.

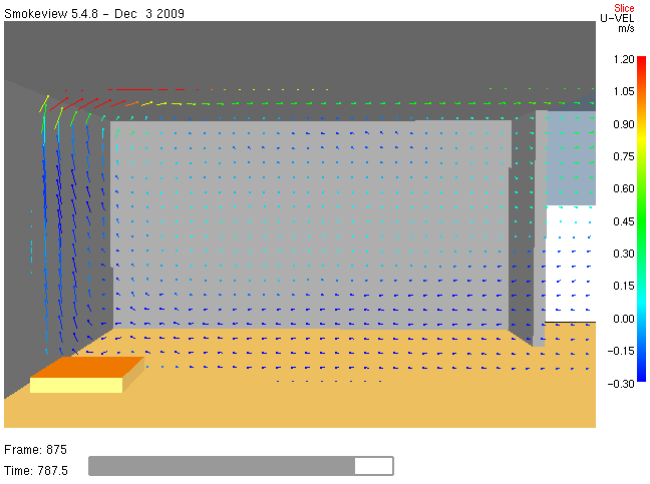

Figure 4.4: Velocity vectors for fire source at rear of compartment

Figure 4.5 shows that the door jet has a more significant effect as compared to the former scenario, causing the plume axis to tilt towards the rear of the compartment. Entrainment from both front and rear end of the plume can be observed from the horizontal vectors close to the vertical vectors of the plume. Therefore the combined effects of increased entrainment due to the door jet causing the tilt of the plume and entrainment from all sides of the plume results in a higher mass flow rate for simulations with fire source in the center of the compartment.

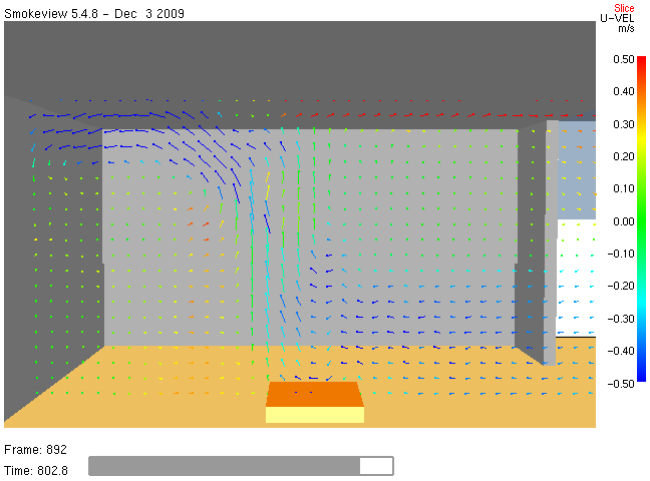

Figure 4.5: Velocity vectors for fire source at center of compartment

4.2.3 Excess temperature profile below spill edge

Figure 4.6 and Figure 4.7 show the predicted excess temperature profile at the center of the spill edge. In Figure 4.6, the predicted temperatures closer to the ceiling are significantly higher than the experimental data. At further distances, the predicted temperatures are lower and the predicted depth of the flow layer is smaller. The higher temperature and the smaller depth of the flow layer is due to the lower predicted mass flow rate for fire sources in the rear of the compartment.

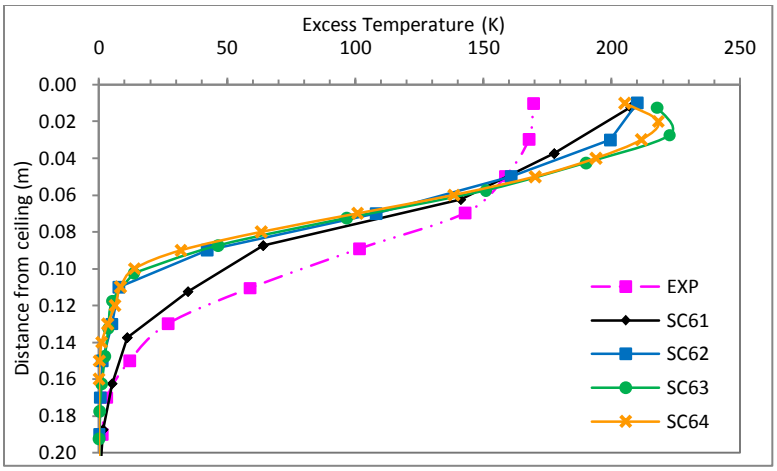

Figure 4.6: Excess temperature at spill edge for fire source at rear of compartment

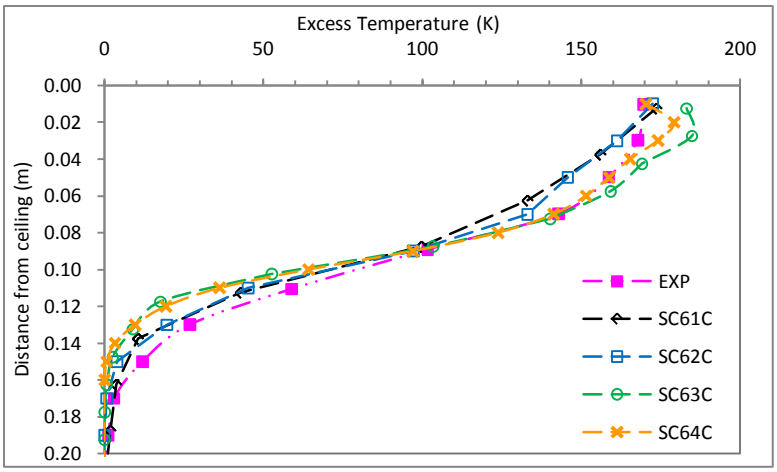

Figure 4.7: Excess temperature at spill edge for fire source at center of compartment

Figure 4.7 shows that the predicted temperature profiles for simulations with the fire source in the center of the compartment are in good agreement with the experimental data. Most of the predictions are within 10 % of the experimental data and the predicted depth of the flow layer is within 2 cm of the experimental data.

4.2.4 Velocity profile below spill edge

Figure 4.8 and Figure 4.9 show the predicted velocity profile at the center of the spill edge. In Figure 4.8, the predicted velocities are lower and the depths of the flow layer are smaller than the experimental data. Combined with the higher temperature observed in Figure 4.6, it is consistent with lower mass flow rates.

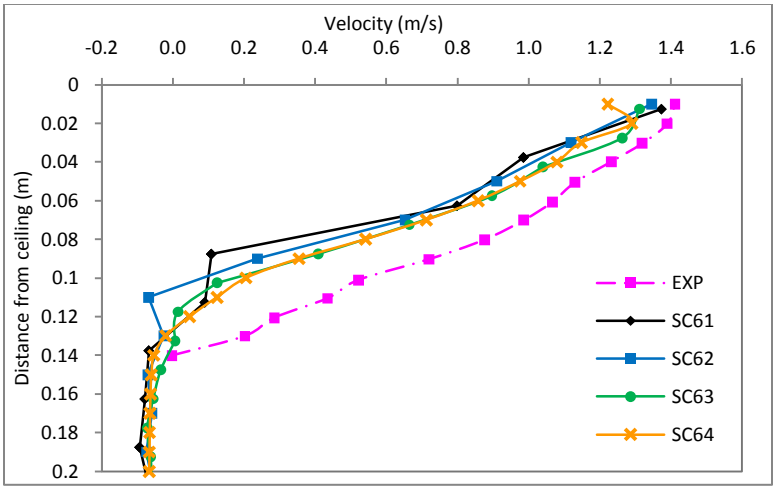

Figure 4.8: Velocity at spill edge for fire source at rear of compartment

Similar to the case of temperature profile, simulations with the fire source in the center of the compartment show good agreement with the experimental data. Most of the predictions are approximately 10 % lower, hence the lower mass flow rates observed in Figure 4.3. Although the position of the fire source is different from the experimental setup, the entrainment effects and mass flow rates are more accurately replicated.

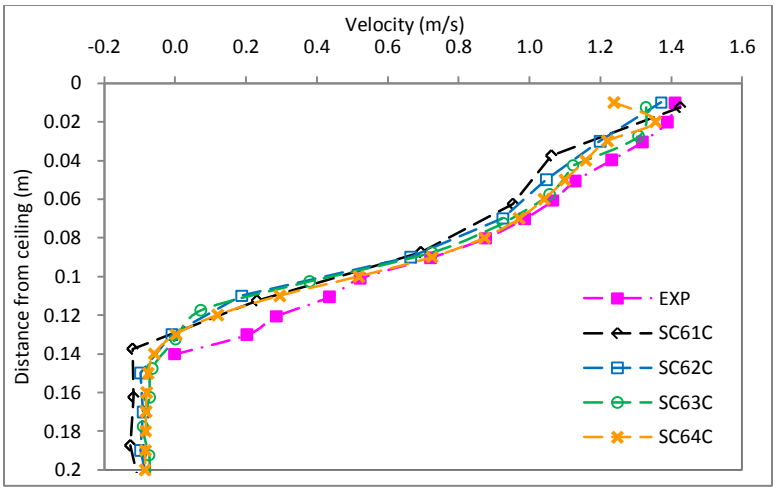

Figure 4.9: Velocity at spill edge for fire source at center of compartment

4.2.5 Lateral temperature and velocity profile across spill edge

Next, we analyze the lateral temperature and velocity profiles across the spill edge to determine the variation of flow properties across the spill edge. Mass flow rates from experiments are calculated based on the assumption of uniform temperature and velocity across the flow plane using Equation 4-1 below.

$$\dot{m}_s = W_s \int_0^{d_s} \rho u(z) dz \qquad (4\text{-}1)$$

Where the density of the hot gases is obtained from its temperature as follows:

$$\rho = \rho_\infty \frac{T_\infty}{T} \qquad (4\text{-}2)$$

The depth of the smoke layer is obtained visually or from the velocity profile.

Figure 4.10 shows the variation in temperature across the spill edge. While the temperature variation for the simulations with the fire source in the center of the

compartment remains fairly constant across the spill edge, those for simulations with the fire source at the rear of the compartment vary by approximately 7 %.

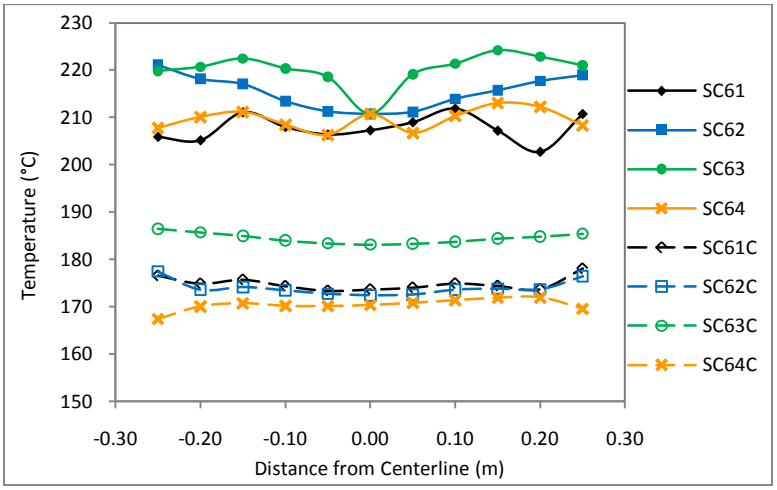

Figure 4.10: Temperature profile across spill edge

Figure 4.11 shows the temperature contours across the spill edge for simulation SC64 at 800 s, which is typical for flows during the steady state period. It can be seen that the temperature is not entirely uniform across the spill edge. Lower temperatures are observed at the interface with the wall surfaces and the contours have rounded corners (shown by the black arrows) leading to lower temperatures near the wall as compared to the flow away from the wall. The wavy contours at the bottom surface of the flow layer suggest that the flow depth varies across the spill edge. However, this phenomenon is transient and the use of time-averaged data filters out the variations.

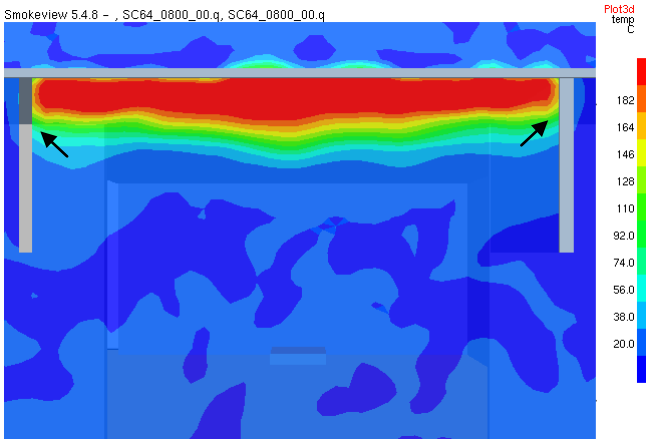

Figure 4.11: Temperature contours across spill edge for simulation SC64 at 800s

Figure 4.12 shows the variation in velocity across the spill edge. With the exception of simulations SC61 and SC61C, all simulations show an approximate 5 % reduction in velocity at the sides as compared to that in the middle. Thus, with a grid cell size of 25 mm, the effect of the wall on the velocity is not evident at a distance of 50 mm from the wall.

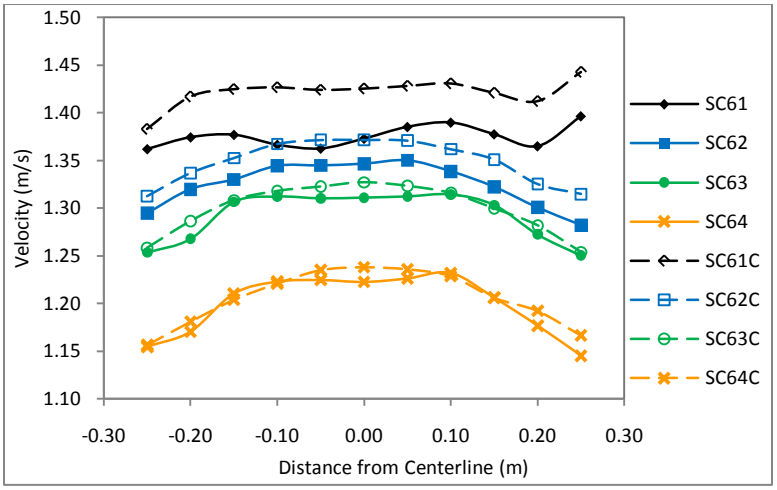

Figure 4.12: Velocity profile across the spill edge

Figure 4.13 shows the velocity contours for simulation SC64 at 800 s. The velocity contours are very similar to the temperature contours but the wall effects are more pronounced. The red band, showing areas where the velocity is in excess of 1 m/s, is much thicker in the center than at the sides. At 30 mm from the ceiling, the velocity at 45 mm away from the wall (shown by the black arrows) may be about 0.8 m/s or 80 % of the velocity in the center region.

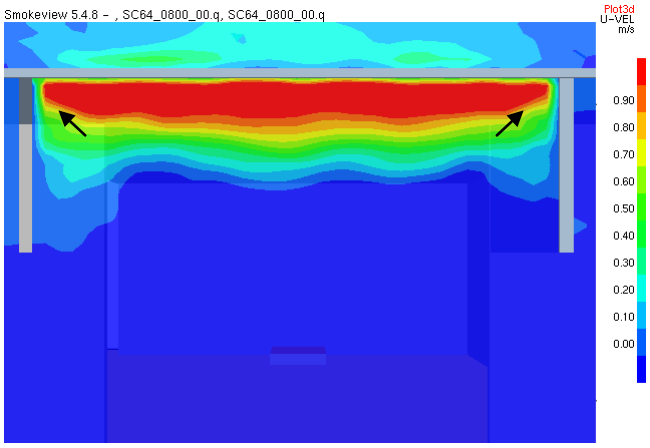

Figure 4.13: Velocity contours across spill edge for simulation SC64 at 800 s

Therefore, the assumption of uniformity of flow properties across the spill edge and calculation of the mass flow rate using Equation 4-1 would generally result in an overestimation. A comparison of mass flow rate calculated using Equation 4-1 and using the FDS function of "MASS FLOW +" is shown in Table 4-2.

Table 4-2: Comparison of Mass Flow Rates

Simulation	Mass Flow Rate, $\dot{m}_s$ (kg/s)		% difference	% difference from experiment after correction
	FDS	Equation 4-1		
SC61	0.040	0.039	-2.5	-32.8
SC61C	0.054	0.056	3.7	-3.4
SC62	0.039	0.039	0	-32.8

Simulation	Mass Flow Rate, $\dot{m}_s$ (kg/s)		% difference	% difference from experiment after correction
	FDS	Equation 4-1		
SC62C	0.052	0.055	5.8	-5.1
SC63	0.039	0.040	8.1	-31.0
SC63C	0.048	0.049	2.1	-15.5
SC64	0.040	0.041	10.8	-29.3
SC64C	0.049	0.051	4.1	-12.1

With the exception of simulations SC61 and SC62, the mass flow rate calculated using Equation 4-1 is higher than that calculated directly by FDS. For the majority of these cases, the calculated mass flow rate is at least 5 % higher. When "corrected" using Equation 4-1 as shown in the last column of table, the mass flow rates for simulations SC61C and SC62C are within 5.1 % of the experimental value of 0.058 kg/s.

4.2.6 Grid sensitivity Analysis

The mass flow rates at the compartment opening and spill edge for all the simulations, averaged over the time period of 700 – 900 s are presented in Table 4-3. The percentage difference between each simulation with simulation SC64 or SC64C are also computed to show the sensitivity of mass flow rates to the grid cell sizes.

Table 4-3: Mass flow rate at compartment opening and spill edge

Simulation	Approximate CPU Runtime (h)	Mass Flow Rate (kg/s)		Difference (%)	
		$\dot{m}_w$	$\dot{m}_s$	$\dot{m}_w$	$\dot{m}_s$
SC61	13	0.040 ± 0.0001	0.043 ± 0.0001	8.1	7.5
SC62	39	0.039 ± 0.0001	0.041 ± 0.0001	5.4	2.5
SC63	94	0.037 ± 0.0001	0.039 ± 0.0001	0	-2.5
SC64	200	0.037 ± 0.0001	0.040 ± 0.0001	-	-

Simulation	Approximate CPU Runtime (h)	Mass Flow Rate (kg/s)		Difference (%)	
		$\dot{m}_w$	$\dot{m}_s$	$\dot{m}_w$	$\dot{m}_s$
SC61C	13	0.049 ± 0.0001	0.054 ± 0.0001	4.3	10.2
SC62C	39	0.049 ± 0.0001	0.052 ± 0.0001	4.3	6.1
SC63C	94	0.045 ± 0.0001	0.048 ± 0.0001	-4.2	2.0
SC64C	200	0.047 ± 0.0001	0.049 ± 0.0001	-	-

Predictions from simulations SC63 and SC63C show very good agreement with SC64 and SC64C (less than 5 % deviation). Predictions from simulations SC62 and SC62C have a maximum deviation of about 6 % from SC64 and SC64C, respectively. Hence, the use of grid cell sizes of 10 mm, 15 mm and 20 mm do not yield significant difference in the mass flow rate of the hot gases at the compartment opening and spill edge. Comparing the CPU runtime, using 20 mm grid cell sizes (4 % of ceiling height) would be the prudent choice, which corroborates the recommendation in Section 3.3.2. Furthermore, it was shown in Section 4.2.5 that the mass flow rate for the simulation with 20 mm grid cell size is within 5.1 % of the experimental data when derived using Equation 4-1.

From the analysis, positioning the fire source in the center of the compartment yields a higher entrainment rate and presents a more conservative design approach. Therefore, the fire source in subsequent simulations is prescribed such that they are located in the center of the compartment.

4.3 Domain size sensitivity analysis

A series of simulations were carried out to determine the optimal domain size for modeling the balcony spill plume. The geometry of the fire compartment, fire source

and instrumentation is similar to that described in Section 4.1. An additional prediction for mass flow rate was made for the rotated flow by using the "MASS FLOW+" function over a horizontal plane that projects 0.2 m in the lateral direction on each side of the channeling screens and from the spill edge to the end of the computational domain in the longitudinal direction. Table 4-4 shows the list of simulations for this study.

Table 4-4: List of simulations for domain size sensitivity analysis

Simulation	Domain size			Distance beyond spill edge (m)	Total number of grid cells
	Length (m)	Depth (m)	Height (m)		
SC62B	2	1.6	0.8	0.7	320,000
SC62B1	2.2	1.6	0.8	0.9	352,000
SC62B2	2.5	1.6	0.8	1.2	400,000
SC62B3	2.2	1.6	1.0	0.9	440,000
SC62B4	2.5	1.6	1.0	1.2	500,000

Table 4-5 shows that the maximum deviation in the predicted mass flow rates for all areas is less than 3 %. Hence, the optimum domain size is the smallest domain size, which is simulation SC62B.

Table 4-5: Mass flow rates for domain size sensitivity analysis

Simulation	Mass Flow Rate (kg/s)		
	$\dot{m}_w$	$\dot{m}_s$	$\dot{m}_{p,z_s=0}$
SC62B	0.049 ± 0.0001	0.052 ± 0.0001	0.076 ± 0.0001
SC62B1	0.049 ± 0.0001	0.052 ± 0.0001	0.075 ± 0.0001
SC62B2	0.049 ± 0.0001	0.052 ± 0.0001	0.076 ± 0.0001
SC62B3	0.049 ± 0.0001	0.053 ± 0.0001	0.077 ± 0.0001
SC62B4	0.049 ± 0.0001	0.053 ± 0.0001	0.076 ± 0.0001

4.4 Full-scale simulations

The analysis carried out in the previous section gives confidence to the use of FDS in the simulation of small-scale balcony spill plume experiments. Due to a lack of suitable data for full-scale experiments, a useful comparison cannot be made. As such, the results from small-scale simulations are scaled up and compared with results from equivalent full-scale simulations.

Five simulations were performed using the equivalent full-scale dimensions of the fire compartment described in Section 4.1.1. The Froude number scaling laws as described by Klote and Milke (3) and Quintiere (76) are as follows:

$$\dot{Q}_c \propto L^{5/2} \Rightarrow \dot{Q}_{c,f} = \dot{Q}_{c,m} \left(\frac{L_f}{L_m}\right)^{5/2} \quad (4\text{-}3)$$

$$\dot{m} \propto L^{5/2} \Rightarrow \dot{m}_f = \dot{m}_m \left(\frac{L_f}{L_m}\right)^{5/2} \quad (4\text{-}4)$$

$$u \propto L^{5/2} \Rightarrow u_f = u_m \left(\frac{L_f}{L_m}\right)^{5/2} \quad (4\text{-}5)$$

The dimensions of the compartment for small-scale simulation are multiplied by a factor of 10 to yield the full-scale dimensions. The equivalent full-scale fire size is obtained by multiplying the small-scale fire size by a factor of $10^{5/2}$ which yields 3,257 kW. The size of the grid cells and computational domain are increased by a factor of 10, hence the total number of grid cells remains the same.

The predicted mass flow rates of these five simulations and comparison with the equivalent full-scale mass flow rate from small-scale simulations are shown in Table 4-6.

Table 4-6: Comparison of predicted mass flow rate from full-scale simulations with equivalent small-scale simulations

Simulation	Mass Flow Rate from full-scale simulations (kg/s)			Equivalent full-scale mass flow rate from small-scale simulations (kg/s)			% Difference		
	$\dot{m}_w$	$\dot{m}_s$	$\dot{m}_{p,z=0}$	$\dot{m}_w$	$\dot{m}_s$	$\dot{m}_{p,z=0}$	$\dot{m}_w$	$\dot{m}_s$	$\dot{m}_{p,z=0}$
FC61C	15.627	17.014	27.921	15.58	17.04	27.63	-0.31	0.16%	-1.05
FC62C	15.176	16.286	24.710	15.39	16.53	24.67	1.43	1.52%	-0.17
FC63C	13.510	14.396	20.246	14.18	15.06	20.91	4.93	4.62%	3.28
FC64C	13.497	14.304	18.033	14.77	15.60	19.46	9.42	9.05%	7.93

Table 4-6 shows that predictions from simulations FC61C and FC62C are in excellent agreement with the respective small-scale simulations of SC61C and SC62C. The predicted full-scale mass flow rates are within 2 % of the equivalent mass flow rate from small-scale simulations. As compared to the equivalent full-scale experimental mass flow rate of 18.34 kg/s, these predictions are 7 – 10 % lower. By applying the correction as described in Section 4.2.5, the deviations are expected to be reduced.

4.5 Conclusion

It is discovered in this study that prescribing a fire source close to a wall resulted in a reduction in the mass flow rate of gases from the compartment opening. This is caused by a reduced entrainment into the plume due to close proximity to the wall and insufficient grid cells between the wall and the fire source or plume to resolve the

flow field within that space. Hence, the predicted mass flow rates are at least 30% lower than the experiment and temperature and velocity profiles were not consistent with the experiment. By prescribing the fire in the middle of the compartment, the predicted mass flow rates are within 15 % of the experimental data.

From analysis of the velocity and temperature contours at the spill edge, it is concluded that the flow is not uniform across the spill edge. The experimental approach of using the temperature and velocity measurements at the center of the spill edge to calculate the mass flow rate generally result in an over prediction. However, this was acceptable as it produces a conservative estimate and the error is deemed to be small. By adopting the experimental approach of calculating the mass flow rate, the predictions from simulations with the fire source located in the middle of the compartment are within 3.4 to 15.5 % of the experimental data.

The grid sensitivity analysis carried out in this section shows that a uniform grid cell size of 20 mm, equivalent to 4 % of the ceiling height of the compartment, gives reasonably good predictions of mass flow rates at the spill edge. The domain size sensitivity analysis shows that an extension of 0.7 m in the longitudinal direction from the spill edge and 0.2 m in the lateral direction on each side of the channeling screens is sufficient to contain the entire flow field of the plume as it rotates around the spill edge.

Predictions from full-scale simulations are 7 – 10 % lower than the equivalent full-scale data for experiments. By using the calculation approach for experiments, the deviation is expected to be reduced.

5. CFD Modeling of Full-Scale Balcony Spill Plume

FDS was used to model full-scale balcony spill plume scenarios to analyze the entrainment processes of the hot gases as they flow from the fire compartment to the spill edge.

5.1 CFD modeling description

5.1.1 Geometry of fire compartment

The dimensions of the fire compartment are 10 m long by 14 m wide and 5 m tall. Three compartment opening widths of 2.4 m, 4.8 m and 10 m are studied with three configurations of flat ceiling, and downstand depth of 1 m and 2 m. Three balcony breadths of 3 m, 5 m and 8 m projecting horizontally from the compartment opening are also analyzed. Two configurations of channeling screens are modeled. In the first configuration, the channeling screens are placed such that the flow is fully channeled by the screens to prevent the spread of smoke under the balcony. This requires the separation between the channeling screens to be the same as the width of compartment opening. This configuration is termed “fully-channeled flows”. In another configuration, there are no channeling screens, such that the smoke from the compartment opening is able to spread laterally unhindered beneath the balcony. For these unchanneled flows, the width of the balcony is extended to 32 m to allow the lateral propagation of smoke. For the last configuration, the channeling screens are placed wide apart, equal to the width of the compartment. The smoke is only

partially constrained under the balcony as it is able to spread laterally to the extent of the screens. This configuration, termed "partially-channeled flows" is closer to practical application commonly observed in shopping malls where the beams under the balcony are spaced at intervals equal to the compartment width. The walls of the fire compartment are prescribed with the same properties as that in Section 4.1.1. A schematic drawing of the modeled fire compartment is shown in Figure 5.1.

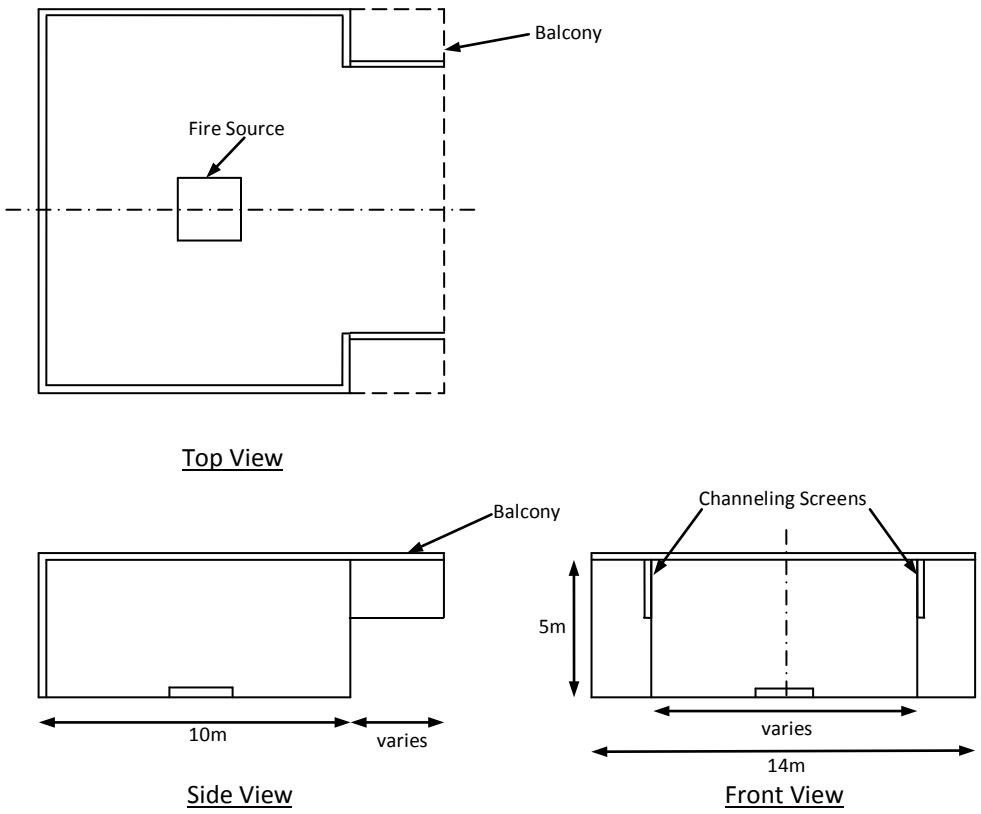

Figure 5.1: Schematic diagram of modeled fire compartment

5.1.2 Computational domain

The computational domain is defined as 20 m in length, 16 m in depth and 8 m in height for simulations with balcony breadth of 3 m. For larger balcony breadths, the domain length is increased by the same change as the balcony breadth. A uniform

grid cell size of 20 cm is adopted for all the simulations. With the exception of the lower boundary, all the exterior boundaries of the domain were set as "OPEN", which is defined as a passive opening to the outside at ambient conditions, where the ambient temperature is 20 °C.

5.1.3 Fire source

The heat release rates for the series of simulations are 1 MW, 2.5 MW and 5 MW. The fire source is modeled as an obstruction with a square footprint and 0.2 m height, with heat release rate per unit area of 625 kW/m^2. The floor area of the obstruction is varied to achieve the required heat release rates. Similar to the simulations in Section 4, the radiative fraction is prescribed as 0.25.

5.1.4 Instrumentations

Generally, the instrumentations for the full-scale simulations are similar to that of the small-scale simulations, with the exception that gas temperatures and velocities at the compartment opening are predicted as well. All the predictions are logged at intervals of 0.5 s. Predictions for the vertical temperature and velocity profiles are made at intervals of 0.2 m from 0.1 m below the compartment opening and spill edge to 0.5 m above the floor. For the lateral profiles, predictions are made at intervals of 0.5 m across the compartment opening and spill edge. Additional predictions are also made at widths of 2.4 m and 4.8 m coinciding with the compartment opening widths. Mass flow rates are predicted at the compartment opening and spill edge. To obtain the mass flow rate of the gas after the rotation region at the spill edge, a horizontal

plane is specified such that it projects from the spill edge to the domain boundary in the longitudinal direction and 2 m beyond each side of the channeling screen. A simulation time of 600 s was specified to allow the conditions to achieve steady state.

5.1.5 Series of FDS simulations

The series of 69 simulations for fully-channeled flows is listed in Table 5-1.

Table 5-1: List of simulations for fully-channeled flows

Simulation	Fire Size (kW)	Compartment Opening width (m)	Compartment Opening height (m)	Downstand depth (m)	Balcony breadth (m)
F1	5000	10	5	0	3
F2	5000	4.8	5	0	3
F3	5000	2.4	5	0	3
F4	5000	10	4	1	3
F5	5000	4.8	4	1	3
F6	5000	2.4	4	1	3
F7	5000	10	3	2	3
F8	5000	4.8	3	2	3
F9	5000	2.4	3	2	3
F10	5000	10	5	0	5
F11	5000	4.8	5	0	5
F12	5000	2.4	5	0	5
F13	5000	10	4	1	5
F14	5000	4.8	4	1	5
F15	5000	2.4	4	1	5
F16	5000	10	3	2	5
F17	5000	4.8	3	2	5
F18	5000	2.4	3	2	5
F19	5000	10	5	0	8
F20	5000	4.8	5	0	8
F21	5000	2.4	5	0	8
F22	5000	10	4	1	8
F23	5000	4.8	4	1	8
F24	5000	2.4	4	1	8
F25	5000	10	3	2	8
F26	5000	4.8	3	2	8
F27	5000	2.4	3	2	8
F1R	2500	10	5	0	3

Simulation	Fire Size (kW)	Compartment Opening width (m)	Compartment Opening height (m)	Downstand depth (m)	Balcony breadth (m)
F2R	2500	4.8	5	0	3
F3R	2500	2.4	5	0	3
F4R	2500	10	4	1	3
F5R	2500	4.8	4	1	3
F6R	2500	2.4	4	1	3
F7R	2500	10	3	2	3
F8R	2500	4.8	3	2	3
F9R	2500	2.4	3	2	3
F10R	2500	10	5	0	5
F11R	2500	4.8	5	0	5
F12R	2500	2.4	5	0	5
F13R	2500	10	4	1	5
F14R	2500	4.8	4	1	5
F15R	2500	2.4	4	1	5
F16R	2500	10	3	2	5
F17R	2500	4.8	3	2	5
F18R	2500	2.4	3	2	5
F19R	2500	10	5	0	8
F20R	2500	4.8	5	0	8
F21R	2500	2.4	5	0	8
F22R	2500	10	4	1	8
F23R	2500	4.8	4	1	8
F24R	2500	2.4	4	1	8
F25R	2500	10	3	2	8
F26R	2500	4.8	3	2	8
F27R	2500	2.4	3	2	8
F1RR	1000	10	5	0	3
F4RR	1000	10	4	1	3
F6RR	1000	2.4	4	1	3
F7RR	1000	10	3	2	3
F9RR	1000	2.4	3	2	3
F10RR	1000	10	5	0	5
F13RR	1000	10	4	1	5
F15RR	1000	2.4	4	1	5
F16RR	1000	10	3	2	5
F18RR	1000	2.4	3	2	5
F19RR	1000	10	5	0	8
F22RR	1000	10	4	1	8
F24RR	1000	2.4	4	1	8
F25RR	1000	10	3	2	8
F27RR	1000	2.4	3	2	8

A series of 9 simulations for partially-channeled flows is listed in Table 5-2.

Table 5-2: List of simulations for partially-channeled flows

Simulation	Fire Size (kW)	Compartment Opening width (m)	Compartment Opening height (m)	Downstand depth (m)	Balcony breadth (m)
F1F	5000	10	5	0	3
F2F	5000	4.8	5	0	3
F3F	5000	2.4	5	0	3
F4F	5000	10	4	1	3
F5F	5000	4.8	4	1	3
F6F	5000	2.4	4	1	3
F7F	5000	10	3	2	3
F8F	5000	4.8	3	2	3
F9F	5000	2.4	3	2	3

Three simulations are performed for unchanneled flows as listed in Table 5-3 below.

Table 5-3: List of simulations for unchanneled flows

Simulation	Fire Size (kW)	Compartment Opening width (m)	Compartment Opening height (m)	Downstand depth (m)	Balcony breadth (m)
F1F	5000	10	5	0	3
F2F	5000	4.8	5	0	3
F3F	5000	2.4	5	0	3

6. Results

Results of the series of FDS simulations described in Section 5.1.5 are presented in this section.

6.1 Onset of steady state conditions

The mass flow rates at the compartment opening, spill edge and of the rotated flow are used to determine the onset of steady state. Figure 6.1 shows the mass flow rates for a wide compartment opening (10 m) without downstand and balcony breadth of 3 m. The mass flow rates at the compartment opening and spill edge reached steady conditions after approximately 180 s. The mass flow rate of the rotated flow shows greater fluctuation. Reasonably steady conditions are achieved after 300 s. To ensure that steady state conditions are achieved for all other simulated scenarios, data of interest are time-averaged from 400 – 600 s.

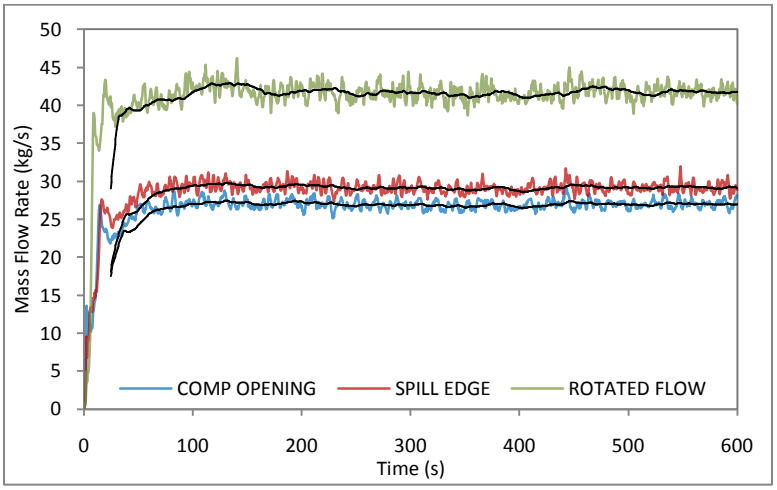

Figure 6.1: Mass flow rate for narrow compartment opening with 2 m downstand (Simulation F7)

6.2 Uniformity of flow across compartment opening and spill edge

The uniformity of the flow across the compartment opening and spill edge is analyzed in the same manner as in Section 4.2.5. Figure 6.2 shows that the temperature is reasonably uniform across the compartment opening and spill edge for simulations without downstand (simulations F10 and F12). For simulations with downstand of 2 m, the temperature across the compartment opening and spill edge is reasonably uniform for a narrow compartment opening. For wide compartment openings, there is a reduction of approximately 10 % at the sides of the compartment opening and a reduction of approximately 15 % at the sides of the spill edge. Hence, uniformity of temperature across the compartment opening and spill edge is not observed for all simulations and the variation of temperature at the spill edge is greater than at the compartment opening.

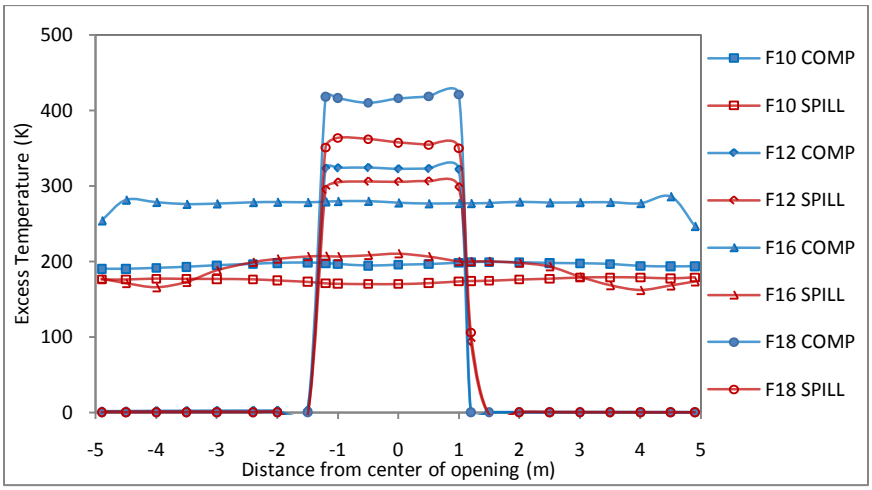

Figure 6.2: Lateral temperature profile across compartment opening and spill edge

Figure 6.3 shows that the velocity across the compartment opening and spill edge is fairly uniform for the simulation with wide compartment opening without downstand

(simulation F1). For a narrow compartment opening without downstand, the variation in the velocity is approximately 10% at the compartment opening and 9% at the spill edge. For simulations with downstand of 0.2 m, the variation in velocity is more significant, with approximately 50 % variation for velocities at the compartment opening and approximately 20 % at the spill edge.

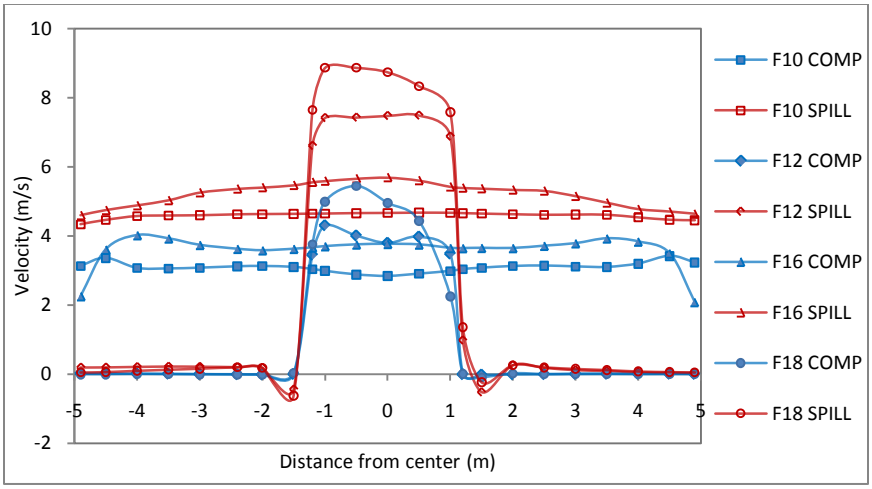

Figure 6.3: Lateral velocity profile across compartment opening and spill edge

From the analysis of the lateral temperature and velocity profiles, it can be concluded that uniformity of flow is not observed for all cases of simulations. Therefore, the mass flow rate predictions would generally be lower than those calculated using Equation 4-1 with experimental values of temperature and velocity taken at the center of the compartment opening and spill edge. Plots of the lateral temperature and velocity profiles for the simulations carried out in this study are shown in Appendix D.

6.3 Temperature and Velocity Profiles

Figure 6.4 and Figure 6.5 show the temperature and velocity profiles, respectively at the compartment opening and spill edge for simulations F10 (10 m wide compartment opening without downstand), F12 (2.4 m wide compartment opening without downstand), F13 (10 m wide compartment opening with 1 m downstand) and F16 (10 m wide compartment opening with 2 m downstand), all with a balcony breadth of 5 m. These profiles represent the typical flow characteristics of all the simulations carried out. Plots of the temperature and velocity profiles for the simulations carried out in this study are shown in Appendix E.

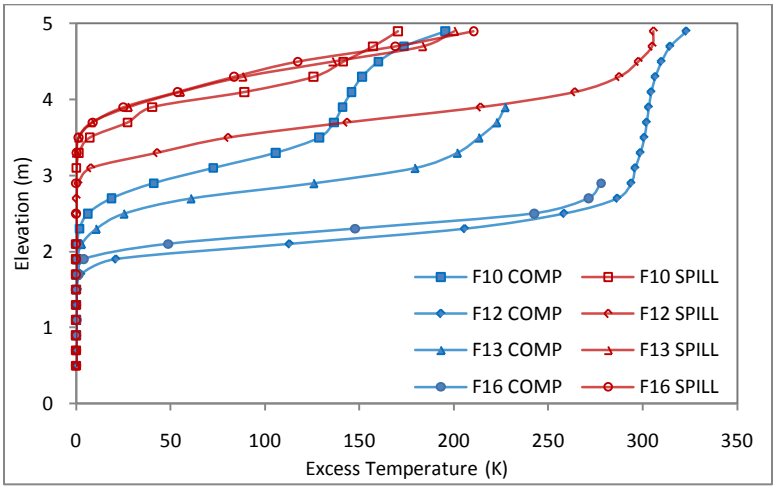

Figure 6.4: Temperature profile at compartment opening and spill edge

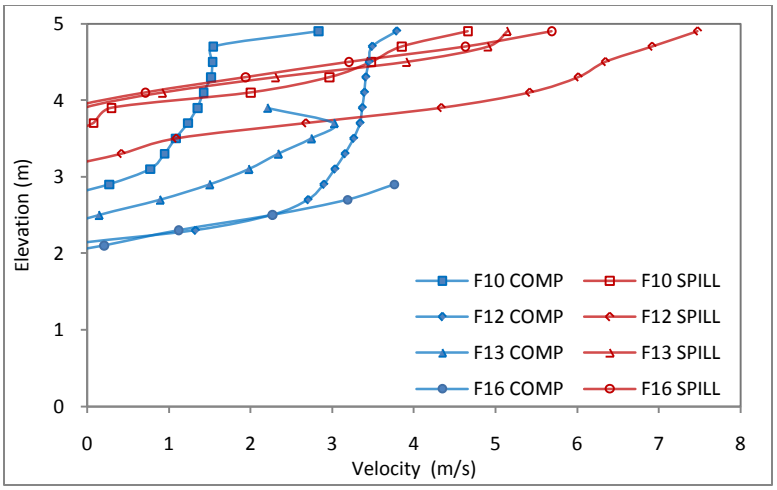

Figure 6.5: Velocity profile at compartment opening and spill edge

6.4 Summary of results

The key results for the series of simulations for fully-channeled flows, partially-channeled flows and unchanneled flows are listed in Table 6-1, Table 6-2 and Table 6-3, respectively.

Table 6-1: Summary of results for series of simulations for fully-channeled flows

Simulation	$\dot{Q}_c$ (kW)	$\dot{m}_w$ (kg/s)	$\dot{m}_s$(kg/s)	$\dot{m}_{p,z=0}$(kg/s)
F1	3882 ± 6.67	26.99 ± 0.028	29.20 ± 0.033	41.78 ± 0.047
F2	3773 ± 5.05	18.40 ± 0.014	20.24 ± 0.022	31.22 ± 0.065
F3	3359 ± 4.97	11.36 ± 0.006	12.69 ± 0.016	22.76 ± 0.059
F4	3764 ± 6.04	21.42 ± 0.023	26.09 ± 0.033	39.79 ± 0.058
F5	3589 ± 6.84	14.74 ± 0.010	17.87 ± 0.025	29.04 ± 0.050
F6	3119 ± 7.40	9.45 ± 0.008	11.45 ± 0.017	21.38 ± 0.045
F7	3486 ± 7.14	15.40 ± 0.019	23.62 ± 0.021	40.02 ± 0.057
F8	3176 ± 6.16	10.74 ± 0.008	14.79 ± 0.013	27.70 ± 0.049
F9	2578 ± 5.88	6.63 ± 0.006	9.38 ± 0.012	19.34 ± 0.044
F10	3854 ± 5.95	26.71 ± 0.027	29.36 ± 0.027	41.97 ± 0.042
F11	3740 ± 4.27	18.11 ± 0.013	20.32 ± 0.015	30.18 ± 0.053
F12	3314 ± 3.31	11.14 ± 0.005	12.68 ± 0.009	21.78 ± 0.039
F13	3737 ± 6.00	21.31 ± 0.026	26.39 ± 0.032	40.55 ± 0.068
F14	3554 ± 6.56	14.56 ± 0.010	18.13 ± 0.022	30.82 ± 0.080

Simulation	$\dot{Q}_c$ (kW)	$\dot{m}_w$ (kg/s)	$\dot{m}_s$(kg/s)	$\dot{m}_{p,z=0}$(kg/s)
F15	3064 ± 8.85	9.29 ± 0.007	11.88 ± 0.025	23.58 ± 0.067
F16	3455 ± 5.03	15.34 ± 0.015	24.36 ± 0.024	39.88 ± 0.049
F17	3142 ± 3.63	10.63 ± 0.007	15.15 ± 0.012	28.46 ± 0.051
F18	2529 ± 4.79	6.57 ± 0.005	9.75 ± 0.014	21.31 ± 0.041
F19	3844 ± 5.18	27.16 ± 0.028	30.36 ± 0.028	43.16 ± 0.045
F20	3711 ± 3.43	18.01 ± 0.013	20.58 ± 0.014	29.50 ± 0.028
F21	3280 ± 2.44	11.11 ± 0.005	12.93 ± 0.007	20.85 ± 0.029
F22	3701 ± 5.59	21.12 ± 0.023	26.73 ± 0.030	39.29 ± 0.047
F23	3518 ± 4.71	14.46 ± 0.010	18.22 ± 0.015	28.39 ± 0.033
F24	3040 ± 6.08	9.26 ± 0.005	12.13 ± 0.020	22.05 ± 0.052
F25	3406 ± 4.50	15.21 ± 0.015	24.89 ± 0.023	38.65 ± 0.045
F26	3140 ± 3.76	10.73 ± 0.006	15.88 ± 0.012	27.91 ± 0.038
F27	2516 ± 4.72	6.61 ± 0.004	10.17 ± 0.015	20.03 ± 0.045
F1R	1928 ± 3.30	19.89 ± 0.024	21.53 ± 0.027	31.11 ± 0.036
F2R	1901 ± 2.78	14.94 ± 0.015	16.27 ± 0.019	24.04 ± 0.036
F3R	1760 ± 2.18	9.66 ± 0.005	10.59 ± 0.012	17.04 ± 0.032
F4R	1825 ± 2.37	14.44 ± 0.014	17.81 ± 0.019	28.29 ± 0.038
F5R	1815 ± 2.92	11.79 ± 0.009	14.14 ± 0.017	22.02 ± 0.033
F6R	1662 ± 4.27	8.08 ± 0.007	9.66 ± 0.017	16.98 ± 0.042
F7R	1709 ± 2.74	11.63 ± 0.014	19.22 ± 0.022	29.15 ± 0.034
F8R	1608 ± 2.72	8.34 ± 0.008	11.71 ± 0.010	21.42 ± 0.040
F9R	1412 ± 2.89	5.65 ± 0.004	7.74 ± 0.007	15.52 ± 0.027
F10R	1911 ± 2.79	19.44 ± 0.028	21.50 ± 0.028	31.28 ± 0.040
F11R	1885 ± 2.26	14.74 ± 0.012	16.28 ± 0.014	23.67 ± 0.029
F12R	1740 ± 1.40	9.50 ± 0.004	10.67 ± 0.006	16.43 ± 0.020
F13R	1817 ± 2.40	14.45 ± 0.016	18.47 ± 0.017	28.68 ± 0.037
F14R	1787 ± 1.60	11.43 ± 0.010	13.89 ± 0.016	22.04 ± 0.041
F15R	1642 ± 3.93	7.96 ± 0.005	9.85 ± 0.015	18.02 ± 0.044
F16R	1725 ± 2.53	11.74 ± 0.010	20.11 ± 0.016	29.58 ± 0.034
F17R	1589 ± 2.48	8.28 ± 0.006	12.07 ± 0.011	21.04 ± 0.037
F18R	1401 ± 2.43	5.66 ± 0.003	8.16 ± 0.010	16.91 ± 0.025
F19R	1908 ± 2.56	20.32 ± 0.024	22.83 ± 0.025	32.47 ± 0.032
F20R	1871 ± 2.06	14.78 ± 0.013	16.65 ± 0.013	23.43 ± 0.019
F21R	1730 ± 1.02	9.50 ± 0.004	10.86 ± 0.005	16.02 ± 0.012
F22R	1780 ± 2.11	13.94 ± 0.012	18.47 ± 0.014	28.59 ± 0.026
F23R	1841 ± 2.41	11.73 ± 0.011	14.83 ± 0.015	22.65 ± 0.025
F24R	1633 ± 2.51	7.98 ± 0.005	10.09 ± 0.011	16.90 ± 0.030
F25R	1664 ± 2.35	11.37 ± 0.009	19.91 ± 0.014	29.29 ± 0.034
F26R	1594 ± 2.24	8.52 ± 0.008	12.78 ± .010	12.78 ± 0.022

Simulation	$\dot{Q}_c$ (kW)	$\dot{m}_w$ (kg/s)	$\dot{m}_s$(kg/s)	$\dot{m}_{p,z=0}$(kg/s)
F27R	1392 ± 2.12	5.70 ± 0.004	8.42 ± 0.009	8.42 ± 0.019
F1RR	750 ± 1.32	12.46 ± 0.015	13.68 ± 0.016	13.68 ± 0.024
F4RR	712 ± 1.28	9.45 ± 0.009	12.33 ± 0.012	20.11 ± 0.022
F6RR	684 ± 0.84	6.48 ± 0.004	7.64 ± 0.007	12.86 ± 0.020
F7RR	660 ± 0.75	8.41 ± 0.008	13.63 ± 0.013	21.27 ± 0.023
F9RR	603 ± 0.72	4.65 ± 0.004	6.21 ± 0.006	11.90 ± 0.019
F10RR	743 ± 1.38	12.50 ± 0.014	13.93 ± 0.016	21.3 ± 0.021
F13RR	698 ± 0.92	9.17 ± 0.009	12.36 ± 0.011	20.14 ± 0.022
F15RR	674 ± 0.83	6.37 ± 0.004	7.70 ± 0.007	13.22 ± 0.026
F16RR	652 ± 1.23	8.19 ± 0.008	13.98 ± 0.013	21.09 ± 0.023
F18RR	595 ± 1.12	4.63 ± 0.003	6.50 ± 0.006	12.16 ± 0.020
F19RR	734 ± 1.35	12.43 ± 0.012	14.23 ± 0.015	21.71 ± 0.022
F22RR	689 ± 0.85	9.27 ± 0.007	12.58 ± 0.010	20.33 ± 0.020
F24RR	670 ± 0.81	6.45 ± 0.003	7.98 ± 0.008	12.45 ± 0.021
F25RR	635 ± 1.46	7.98 ± 0.008	14.20 ± 0.015	21.25 ± 0.022
F27RR	587 ± 1.30	4.65 ± 0.003	6.66 ± 0.007	11.89 ± 0.013

Table 6-2: Summary of results for series of simulations for partially-channeled flows

Simulation	$\dot{Q}_c$ (kW)	$\dot{m}_w$ (kg/s)	$\dot{m}_s$(kg/s)	$\dot{m}_{p,z=0}$(kg/s)
F1F	3880 ± 6.52	27.18 ± 0.032	30.67 ± 0.035	46.98 ± 0.054
F2F	3776 ± 6.27	19.01 ± 0.012	25.01 ± 0.029	46.89 ± 0.086
F3F	3434 ± 7.57	12.57 ± 0.007	19.50 ± 0.026	44.76 ± 0.089
F4F	3733 ± 5.23	21.07 ± 0.022	27.18 ± 0.029	45.49 ± 0.062
F5F	3563 ± 5.66	14.90 ± 0.009	22.33 ± 0.021	43.37 ± 0.062
F6F	3134 ± 5.57	9.77 ± 0.004	18.44 ± 0.017	40.23 ± 0.061
F7F	3466 ± 7.09	15.35 ± 0.014	25.86 ± 0.048	47.01 ± 0.060
F8F	3136 ± 6.60	10.52 ± 0.006	20.36 ± 0.036	42.95 ± 0.053
F9F	2560 ± 4.70	6.59 ± 0.004	17.49 ± 0.036	37.79 ± 0.054

Table 6-3: Summary of results for series of simulations for unchanneled flows

Simulation	$\dot{Q}_c$ (kW)	$\dot{m}_w$ (kg/s)	$\dot{m}_s$(kg/s)	$\dot{m}_{p,z=0}$(kg/s)
F1U	3778 ± 8.92	27.21 ± 0.037	36.21 ± 0.048	57.39 ± 0.066
F2U	3664 ± 8.49	19.04 ± 0.019	30.60 ± 0.036	57.39 ± 0.099
F3U	3260 ± 10.57	12.59 ± 0.009	27.54 ± 0.036	57.05 ± 0.104

7. Discussion

7.1 Flow characteristics for fully-channeled flows

7.1.1 Wide compartment opening without downstand

Figure 7.1 shows the typical predicted flow characteristics as the hot gas flows out of a wide compartment without a downstand, using a temperature isosurface file set at 30 °C. The hot gas flows out of the compartment, beneath the balcony, before projecting from the spill edge. It is observed that the entire flow falls within the computational domain as it rotates around the spill edge. It is also observed that the flow is fully contained by the channeling screens and there seems to be minimal lateral spread as the flow projects from the spill edge.

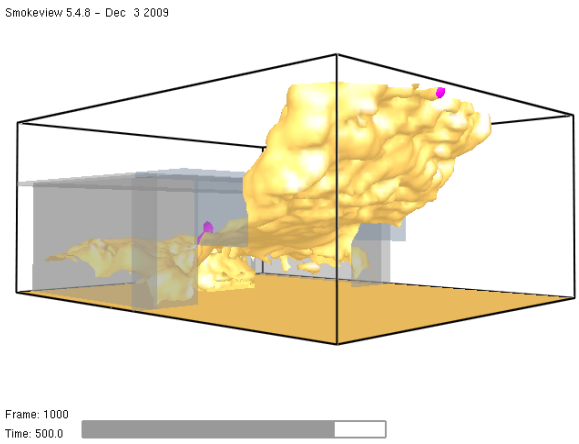

Figure 7.1: Typical flow characteristics for wide compartment opening without downstand (Simulation F1)

Figure 7.2 shows the temperature contours for the hot gas flow. The thickness of the flow layer reduces as it flows from the compartment opening to the spill edge. At the

spill edge, as the flow rotates and discharges as a spill plume, the gas temperature reduces due to the entrainment of ambient air. Figure 7.2 also shows that the entire flow is contained within the computational domain.

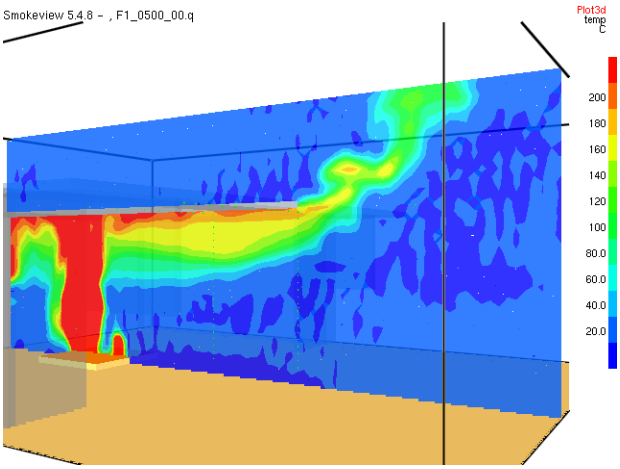

Figure 7.2: Temperature contours for wide compartment opening without downstand (Simulation F1)

Figure 7.3 shows the velocity vectors of the hot gas flow under the balcony and the spill edge. The flow beneath the balcony is predominantly in the horizontal direction and the flow is accelerated as it approaches the spill edge. At the spill edge, the flow rotates and discharges as a spill plume. In this region, there is entrainment at both upper and lower region of the flow layer, indicated by the arrows in Figure 7.3. Away from the spill plume, the air is quiescent, indicated by the zero velocity vectors. This gives further evidence that the entire flow field is within the computational domain.

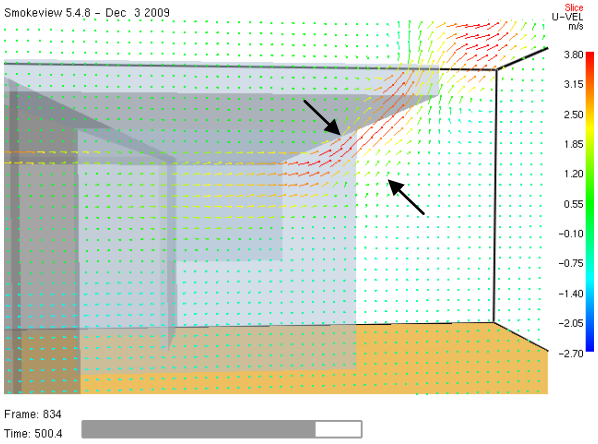

Figure 7.3: Velocity vectors for wide compartment opening without downstand (Simulation F1)

7.1.2 Wide compartment opening with downstand

Figure 7.4(a) and (b) show that the flow characteristics for wide compartment openings with downstand of 1 m and 2 m, respectively. Similar to the previous case, there seems to be minimal lateral spread as the hot gases project from the spill edge. The presence of a downstand creates a smoke reservoir in the fire compartment and this causes the depth of the smoke layer in the compartment to increase.

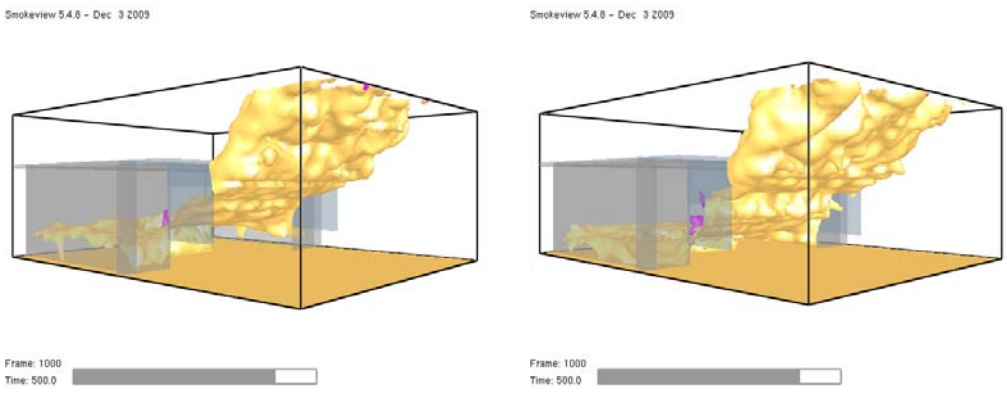

(a) (b)

Figure 7.4: Typical flow characteristics for wide compartment opening with (a) 1 m downstand (Simulation F4) (b) 2 m downstand (Simulation F7)

Figure 7.5 (a) and (b) show that the temperature of the flow layer at the compartment opening increases as the depth of the downstand increase. The presence of a downstand reduces the area of the compartment opening and hence the flow rate of out flow of hot gases, thereby increasing its temperature for a constant fire size.

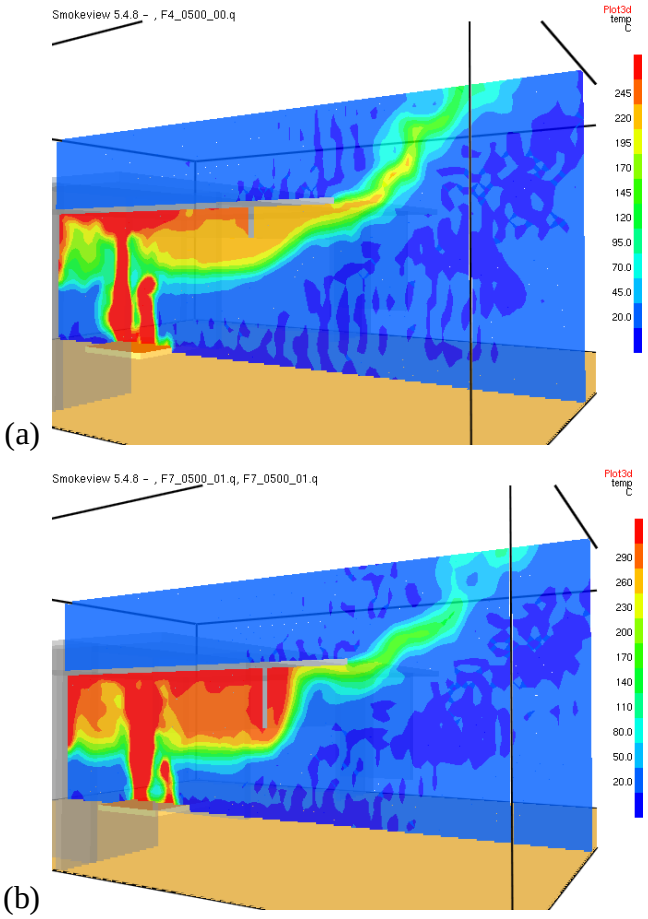

Figure 7.5: Temperature contour for wide compartment opening with (a) 1 m downstand (Simulation F4) (b) 2 m downstand (Simulation F7)

Figure 7.6 (a) and (b) show that the hot gas discharges from beneath the downstand as a jet, impinges on the balcony and moves as a horizontal flow layer. Recirculation is observed at the rear end of the jet, indicated by black arrows, after it impinges the ceiling. For the 1 m downstand, the jet impinges close to the edge of the balcony.

For the deeper downstand, the jet rises at a steeper angle from beneath the downstand. This phenomenon is primarily due to increased buoyancy associated with the higher temperature of the gases.

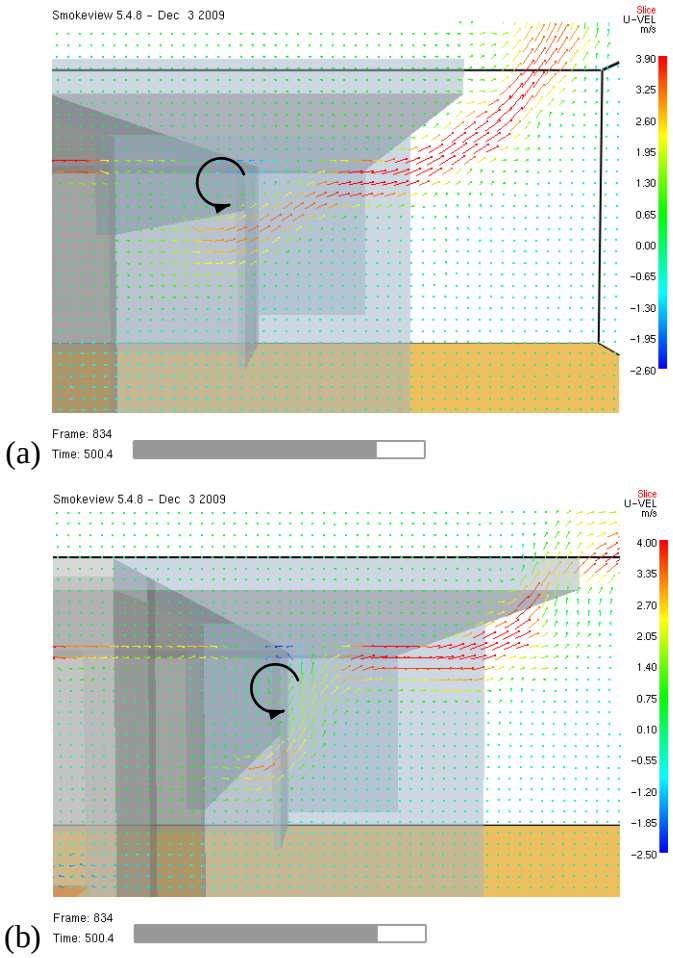

Figure 7.6: Velocity vectors for wide compartment opening with (a) 1 m downstand (Simulation F4) (b) 2 m downstand (Simulation F7)

7.1.3 Narrow compartment opening without downstand

Figure 7.7 shows that for the case of a compartment opening of 2.4 m, the smoke layer in the compartment is almost at the floor level and the flow layer under the balcony is almost as deep as the channeling screens. Similar to the flow from a wide

compartment opening, there is minimal lateral spread as the flow rotates around the spill edge.

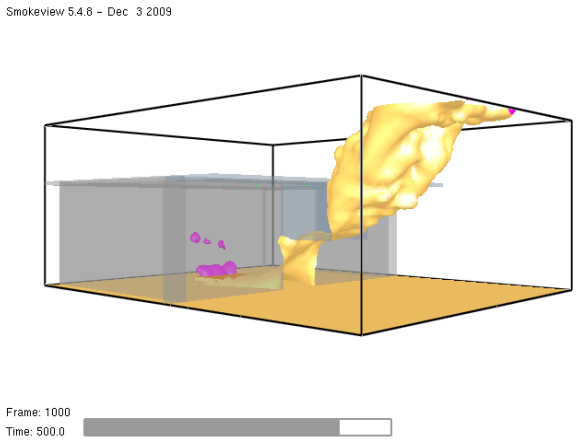

Figure 7.7: Typical flow characteristics for narrow compartment opening without downstand (Simulation F3)

Figure 7.8 shows that the temperature of the hot gas flow from the compartment opening is significantly higher than those from wide compartment openings. The temperature contours show the inflow air causing the plume to tilt towards the rear of the compartment.

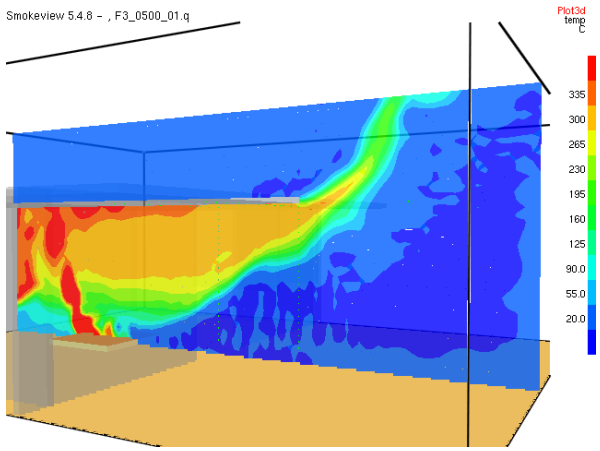

Figure 7.8: Temperature contour for narrow compartment opening without downstand (Simulation F3)

Figure 7.9 shows that the flow layer is thicker and discharges at a higher velocity as compared to those from wide compartment openings. The flow is accelerated considerably as it flows under the balcony, resulting in a reduction of the flow layer depth. Entrainment is also observed at the upper and lower regions of the spill plume as it projects from the spill edge.

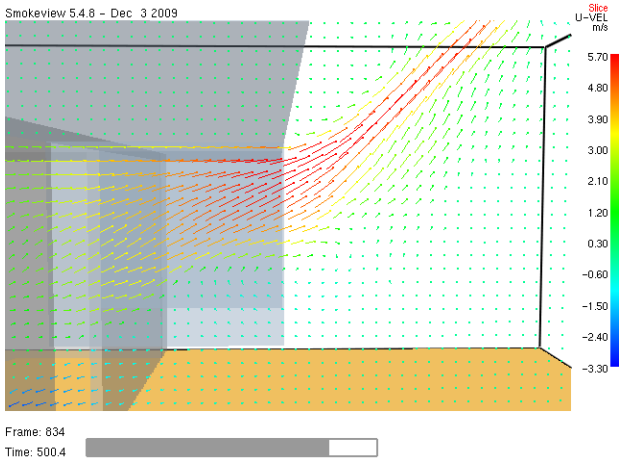

Figure 7.9: Velocity vectors for narrow compartment opening without downstand (Simulation F3)

7.1.4 Narrow compartment opening with downstand

Figure 7.10 shows that the flow characteristics for a narrow compartment with a 1 m downstand. Similar to the case without a downstand, there is minimal lateral spread as the flow rotates around the spill edge. The smoke layer in the compartment is even closer to the floor level and the flow under the balcony is contained by the channeling screen.

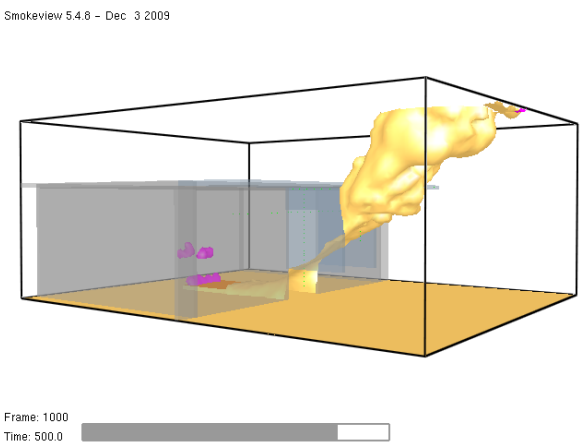

Figure 7.10: Typical flow characteristics for narrow compartment opening with 1 m downstand (Simulation F6)

Figure 7.11 shows that the temperature in the fire compartment and the temperature of the flow out of the compartment are significantly higher than the scenario without a downstand. It is also observed that there is a region of lower gas temperature on the downstream side of the downstand, shown by the arrow in Figure 7.11.

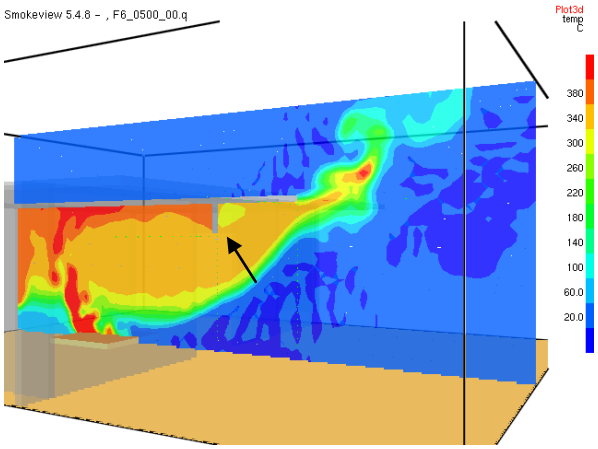

Figure 7.11: Temperature contour for narrow compartment opening with 1 m downstand (Simulation F6)

Figure 7.12 shows that the hot gases project from beneath the downstand directly into the atrium. This phenomenon is also observed for the case with narrow compartment opening and 2 m downstand. For compartment opening widths of 4.8 m with a downstand, only part of the jet impinges on the balcony. Figure 7.13 illustrates the partial impingement for compartment opening width of 4.8 m with a 1 m downstand. For both of these cases, there is recirculation of gases in the space between the downstand, balcony and the jet, shown by the black arrows. It is this recirculation that causes the entrapment of a pocket of lower temperature gas in the space bounded by the downstand, underside of the balcony and the jet.

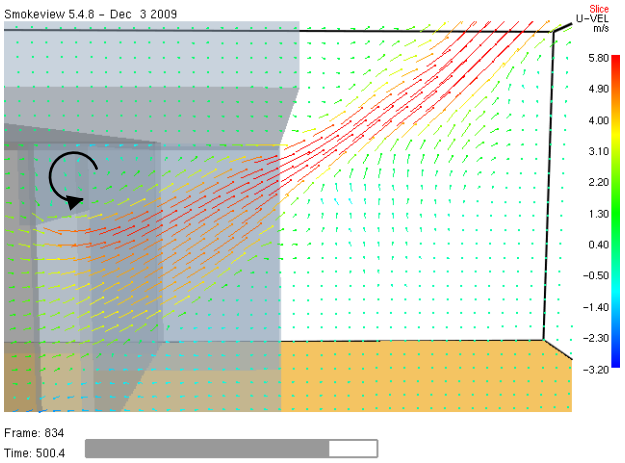

Figure 7.12: Velocity vectors for narrow compartment opening with 1 m downstand (Simulation F6)

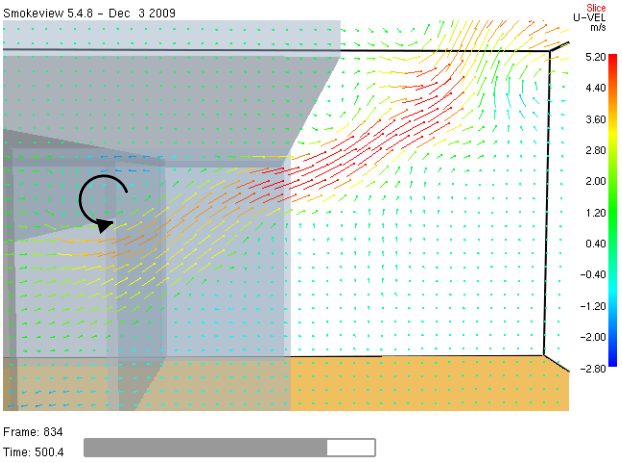

Figure 7.13: Velocity vectors for 4.8 m wide compartment opening with 1 m downstand (Simulation F5)

As these configurations result in flow characteristics that are different from the rest of the simulations, their results are omitted in subsequent sections.

7.1.5 Reduced fire size

Figure 7.14 shows the temperature contours for a wide compartment opening without downstand for a 2.5 MW fire. The temperature in the fire compartment is significantly lower than those with fire size of 5 MW. The temperature of the flow out of the compartment is approximately 25 % lower.

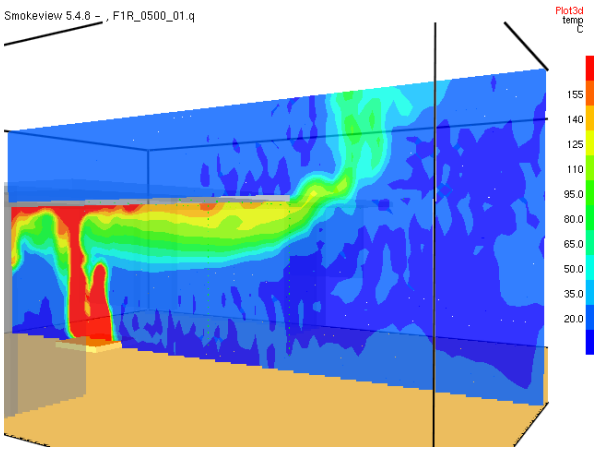

Figure 7.14: Temperature contours for 2.5 MW fire wide compartment opening without downstand (Simulation F1R)

Figure 7.15 shows that the velocity of the flow under the balcony and at the spill edge is about 25 % lower as compared to Figure 7.3. There is also a reduction in the depth of the flow layer under the balcony by about 10 %.

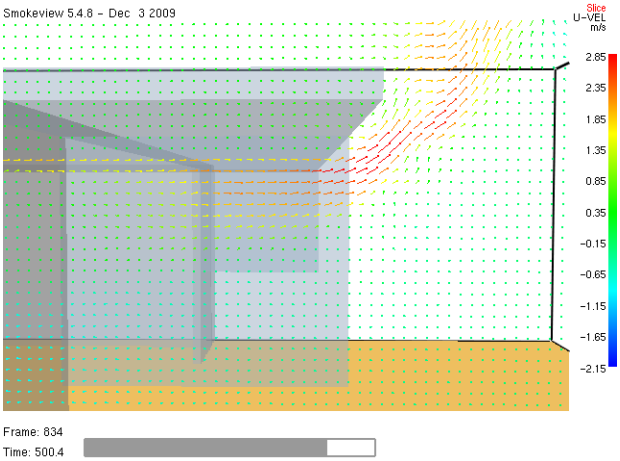

Figure 7.15: Velocity vectors for 2.5 MW fire wide compartment opening without downstand (Simulation F1R)

Figure 7.16 shows the temperature contours for the case of a wide compartment opening with 2 m downstand. The temperature of the flow layer in the balcony is about 40 % lower.

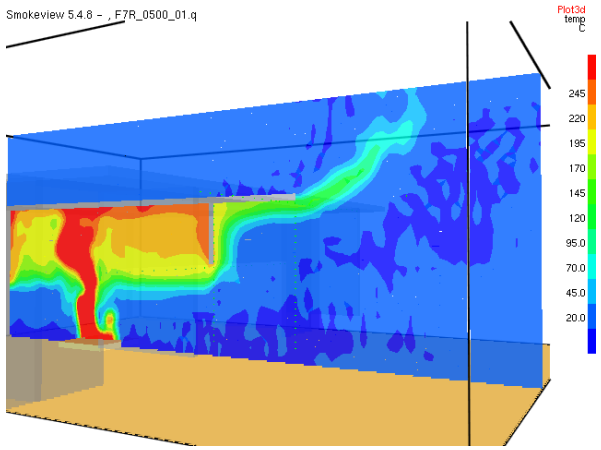

Figure 7.16: Temperature contours for 2.5 MW fire wide compartment opening with 2 m downstand (Simulation F7R)

Figure 7.17 shows that the hot gases rise vertically from beneath the downstand. The velocity at the compartment opening and under the balcony is about 25 % lower compared to the case with a 5 MW fire. The thickness of the flow layer is also reduced by the same margin. Due to the lower flow velocity at the compartment opening, the dominant buoyancy forces cause the gas to rise vertically.

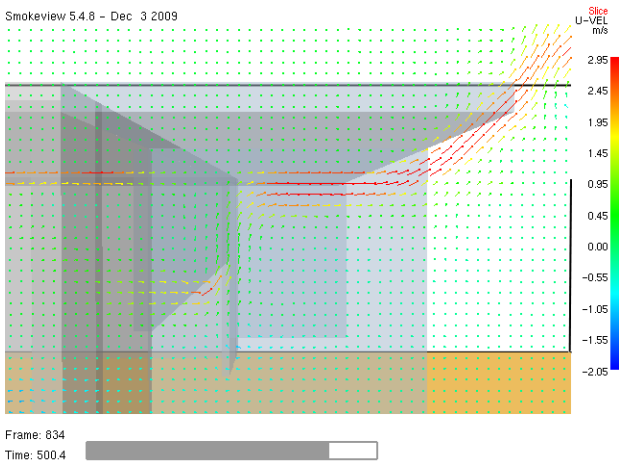

Figure 7.17: Velocity vectors for 2.5 MW fire wide compartment opening with 2 m downstand (Simulation F7R)

7.1.6 Balcony breadth

In general, an increase in the balcony breadth does not cause significant changes to the flow characteristics. The extended balcony allows the jet projecting from beneath the downstand to impinge the balcony and travel horizontally before discharging from the spill edge. Figure 7.18 shows that the temperatures in the compartment and under the balcony are similar to the case with a 3 m balcony. However, the temperature of the flow at the spill edge is approximately 10 % lower.

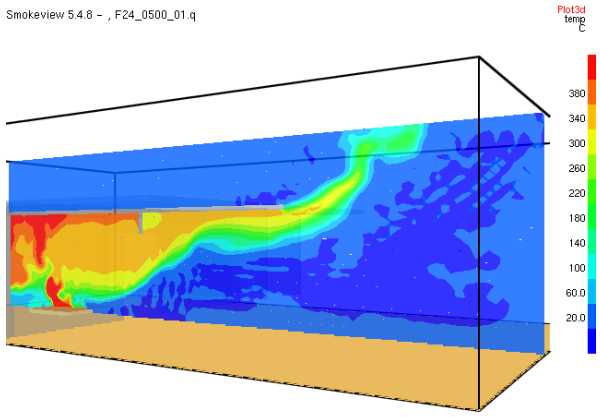

Figure 7.18: Temperature contours for 5 MW fire narrow compartment opening with 1 m downstand (Simulation F24)

Figure 7.19 shows entrainment of air into the flow layer as it moves beneath the balcony, shown by the arrows. The entrainment of air into the flow layer causes the temperature to decrease at the spill edge.

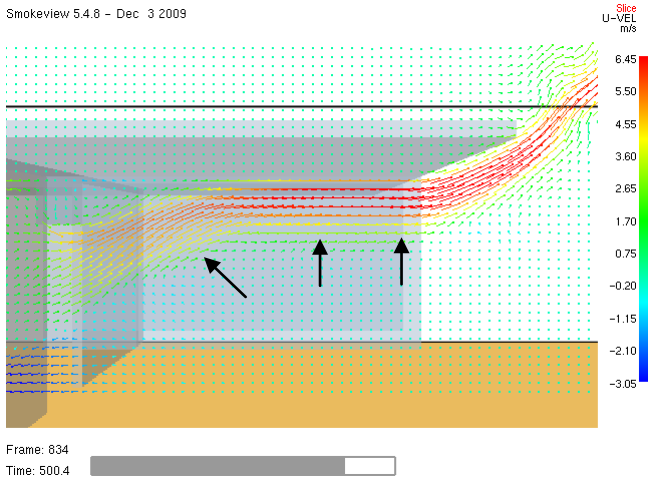

Figure 7.19: Velocity vectors for 5 MW fire narrow compartment opening with 1 m downstand (Simulation F24)

7.2 Temperature and velocity profiles

Figure 7.20 shows the temperature profiles at compartment opening and spill edge for simulations F1 (wide compartment opening without downstand), F3 (narrow compartment opening without downstand), F7 (wide compartment opening with 2 m downstand) and F19 (wide compartment opening with 8 m balcony, without downstand). The longer balcony breadth in simulation F19 impedes the flow of the gases out of the compartment, resulting in marginally higher temperatures as compared to simulation F1. At the spill edge, the predicted temperatures for simulation F19 are lower than simulation F1. This is caused by heat losses and entrainment of air as the gases flow under the extended balcony.

The narrow compartment opening for simulation F3 results in an increase of the smoke layer depth at the compartment opening and spill edge. The smaller compartment opening also causes a reduction in the flow rate of gases from the compartment, thus resulting in significantly higher temperatures. At the spill edge, the temperature is marginally lower, but the depth of the smoke layer is reduced significantly.

The presence of a 2 m downstand in simulation F7 causes a reduction in the flow rate of gases out of the compartment opening, hence an increase in gas temperature compared to simulation F1. The depth of the smoke layer at the compartment opening and spill edge is also reduced due to lower flow rate of gases. There is a greater temperature difference (about 50 °C) between the flow layer at the

compartment opening and the spill edge. This is due to the entrainment of air into the smoke layer as it flows from the underside of the downstand to the balcony.

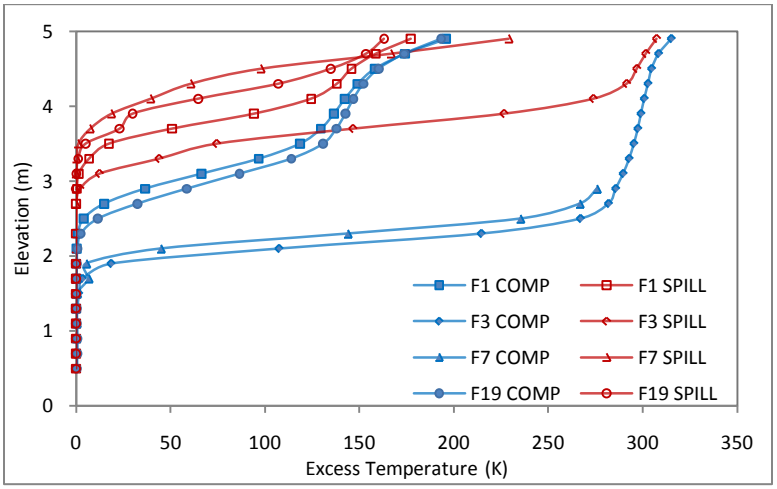

Figure 7.20: Temperature profile at compartment opening and spill edge

Figure 7.21 shows the velocity profiles at the compartment opening and spill edge for the same simulations as in Figure 7.20. Predicted velocities for simulation F19 are marginally lower than F1 due to the impedance caused by the extended balcony. Increased smoke layer depth and velocities are observed for simulation F3 due to the narrow compartment opening. The maximum velocity at the spill edge is almost two times the maximum velocity at the compartment opening, thus the smoke layer depth at the spill edge is significantly reduced. Similar to the observations made from temperature profiles of simulation F7, the depth of the smoke layer is reduced due to lower flow rates of gases. In general, the depth of the smoke layer at the compartment opening obtained from the temperature profiles is marginally lower than that from temperature profile, this is possibly due to mixing of cool incoming air with the hotter out flowing gases.

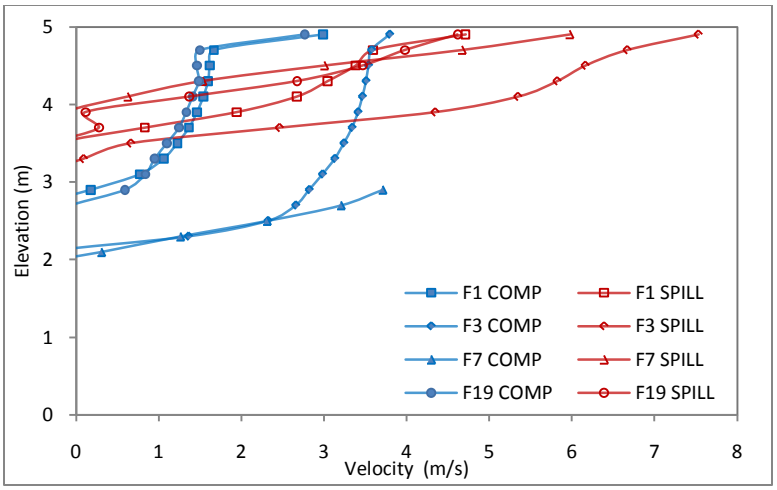

Figure 7.21: Velocity profile at compartment opening and spill edge

7.3 Comparison of FDS predictions with experiment

The temperature and velocity profiles of the FDS predictions are compared with experimental data from NRCC full-scale tests, described in Section 2.2.4. As the geometry of the compartment in the full-scale test is not identical to the modeled geometry in this research, only 2 suitable comparisons are possible for the temperature at compartment opening and temperature and velocity at the spill edge. For both of these cases, the fire size is 5 MW.

Figure 7.22 shows the comparison of the FDS predicted temperature profile at the compartment opening for simulations F10 and F11 with experimental data for Test 42 and 62. The compartment opening widths for Test 42 and 62 are 5 m and 10 m, respectively. The compartment opening widths of the corresponding FDS simulations, F11 and F10 are 4.8 m and 10 m respectively. Both of these tests are conducted with a balcony breadth of 4.2 m and without a downstand at the compartment opening. Simulations F10 and F11 also do not have a downstand, but

the balcony is broader at 5 m. Another difference, the length of compartment in the tests is 5 m, half the value of those in the modeled compartment in this research.

Due to the broader balcony in the simulations, the temperature at the compartment opening should be marginally higher than the experimental data. However, in this case, the predicted temperatures are about 20 % lower than the maximum temperature recorded in the experiments. This could be due to the combined effects of error in the experimental measurements and the shorter length of the compartment, resulting in higher gas temperatures at the compartment opening. At slightly further distances from the ceiling, data from Test 62 and simulation F10 shows very good agreement with about 10 % variation. For Test 42 and simulation F11, there is greater variation in the prediction.

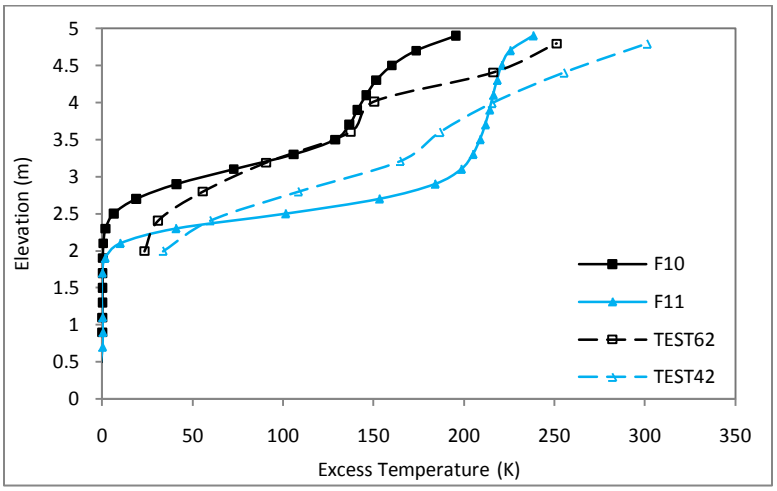

Figure 7.22: Comparison with experimental data at compartment opening

Figure 7.23 and Figure 7.24 show the comparison of temperature and velocity data at the spill edge for simulations F11 and F17 with Test 2 and Test 7. The compartment

opening widths for both tests are 5 m. Test 7 has a downstand of 1.6 m at the compartment opening, while Test 2 does not have a downstand present.

The temperature profiles in Figure 7.23 shows that there is much better agreement between the FDS predictions and experimental data at the spill edge. The variation in the experimental data and FDS predictions are about 10%. A larger variation of about 15 % is noted for Test 2 and simulation F11 for the data point closest to the ceiling.

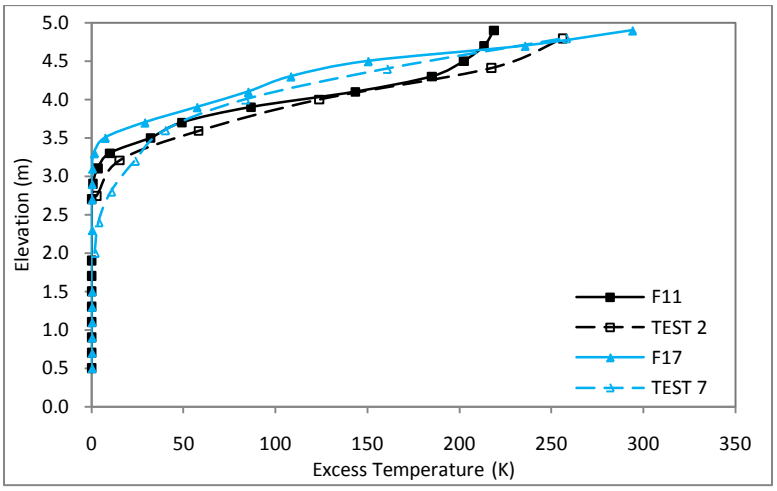

Figure 7.23: Comparison with experimental data at spill edge

Figure 7.24 shows excellent agreement in the velocity data for measurements close to the ceiling, where the variation between experimental data and FDS predictions is about 5 %. The experimental data shows a velocity of 0.5 m/s at a distance of 3 m below the ceiling, indicating that the depth of the smoke layer is greater than 3 m at the spill edge. This is not possible as the temperature data shows that the smoke layer is not more than 2.5 m. Hence it is suspected that the velocity data is for the inflow

of air towards the compartment opening and should be corrected to -0.5 m/s. In this case, it agrees very well with the predicted value of -0.3 m/s.

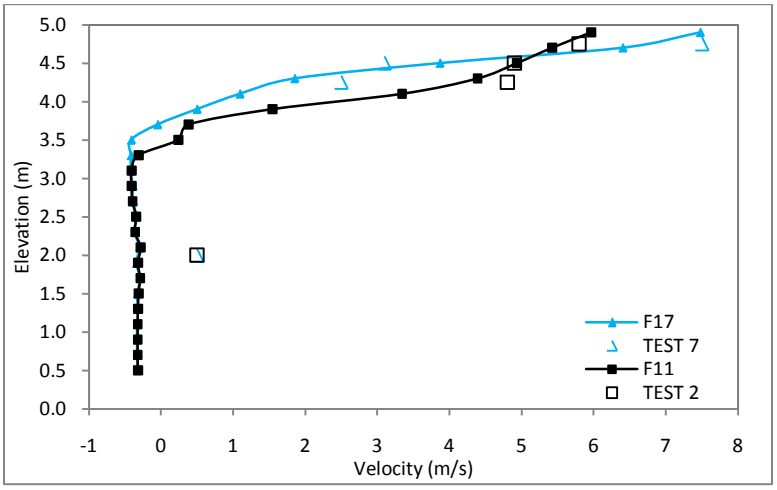

Figure 7.24: Comparison with experimental data at spill edge

7.4 Effect of balcony breadth on entrainment

Figure 7.25 shows the variation in the entrainment between the compartment opening and the spill edge ($\dot{m}_s/\dot{m}_w$) for fire size of 2.5 MW. The entrainment increases as the balcony breadth is increased, corroborating the observations made in Section 7.2. The entrainment is weakly dependent on balcony breadth and seems to obey a weak power law.

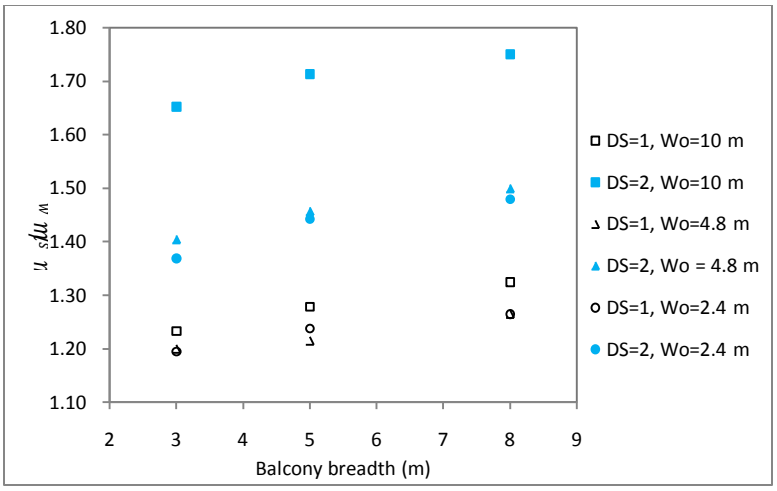

Figure 7.25: Effect of balcony breadth on rate of entrainment between compartment opening and spill edge

7.5 Empirical Correlation for entrainment rate at spill edge

FDS predictions from simulations carried out in this research are compared with the existing correlations. Simulations F5, F6, F8 and F9 are omitted from the comparison as the flow characteristics are different from the rest of the simulations.

Figure 7.26 shows the comparison of FDS predictions with the correlation by Ko (31) given by Equation 2-14. The correlation given by Ko does not address the variation in width of the compartment opening and balcony breadth. It is clear from Figure 7.26 that the correlation is inadequate in addressing the effects from the various compartment opening widths and balcony breadths from the simulations in this research.

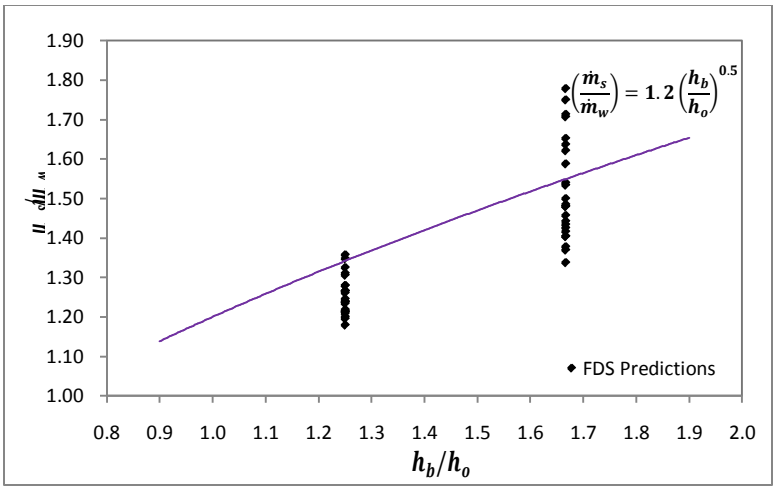

Figure 7.26: Comparison FDS predictions with correlation by Ko

Figure 7.27 shows the comparison of FDS predictions with the correlation by Harrison (29) given by Equation 2-11. The correlation developed by Harrison does not account for the effects of balcony breadth and most of the data used in the development of the correlation is based on a balcony breadth of 0.3 m, i.e. a full-scale equivalent of 3 m. Since the correlation addresses the effects of variation in the compartment opening width on the entrainment, it gives a better agreement with the FDS predictions. However, at smaller compartment opening height to compartment opening width ratios, i.e. $\left(\frac{h_o}{w_o}\right)$, the correlation gives a value of entrainment which is about 30% lower than the FDS predictions. This is possibly due to the combined effects of the broader balcony in the FDS predictions in this research and reduced entrainment into the fire plume in the FDS simulations carried out by Harrison (29), (46) as discussed in Section 4.2.

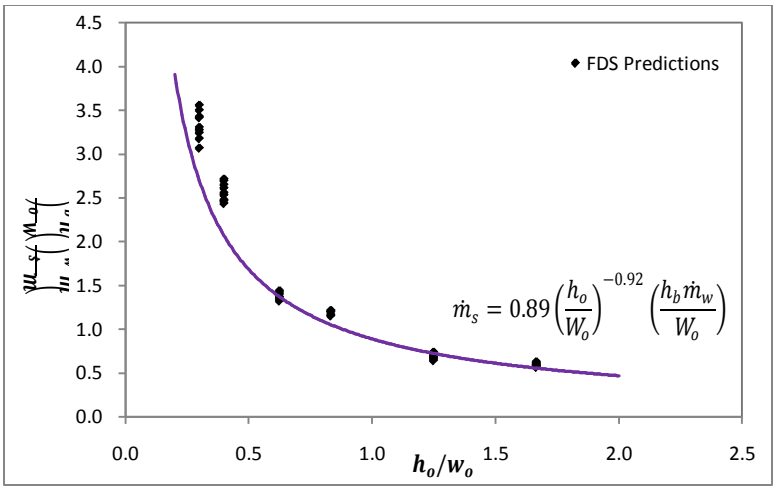

Figure 7.27: Comparison FDS predictions with correlation by Harrison

Due to the relatively large variation between the FDS predictions and the correlation given by Harrison at small compartment opening height to compartment opening width ratios, a new correlation that addresses the effect of balcony is sought. The new correlation would also address the concerns of under prediction of entrainment into the fire plume within the compartment opening.

Since the correlation given by Harrison shows good agreement, a similar approach is taken. With the knowledge that the balcony breadth and entrainment are related by a weak positive power law, $\left(\frac{\dot{m}_s}{\dot{m}_w}\right)\left(\frac{bW_o}{h_b}\right)$ is plotted with respect to $\left(\frac{h_o}{bW_o}\right)$. Figure 7.28 shows that the data falls into a power law relationship. The best fit curve is given by Equation 7-1, which is non-dimensional, as follows,

$$\left(\frac{\dot{m}_s}{\dot{m}_w}\right) = 0.86(bW_o)^{0.05}\frac{h_b}{{h_o}^{1.05}} \qquad (7\text{-}1)$$

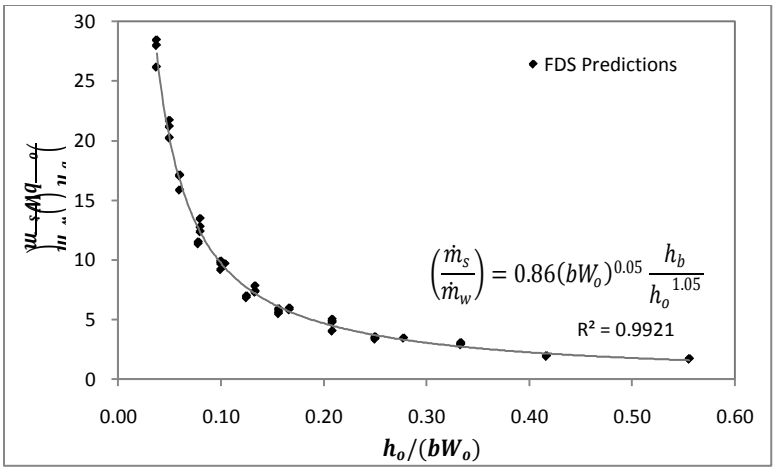

Figure 7.28: Correlated FDS prediction

7.6 Validation of Empirical Correlation

In order to assess the validity of the proposed empirical correlation, comparisons are made with experimental and FDS simulation data from Harrison (29) and Ko (31). Figure 7.29 shows experimental data and FDS predictions from previous work by Harrison (29) plotted in the same manner as Figure 7.28. Both sets of data show very good agreement to the proposed empirical correlation.

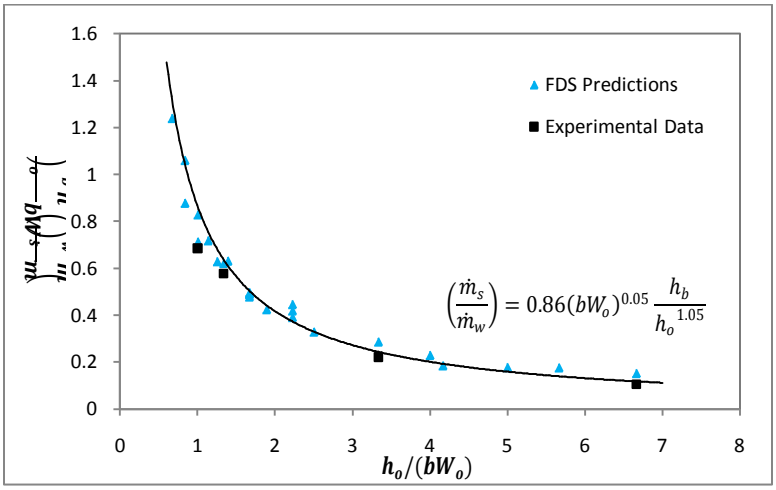

Figure 7.29: Comparison of proposed empirical correlation with data by Harrison (29)

Figure 7.30 shows FDS predictions from previous work by Ko (31) plotted in the same manner as Figure 7.28. The FDS predictions show very good agreement to the proposed empirical correlation.

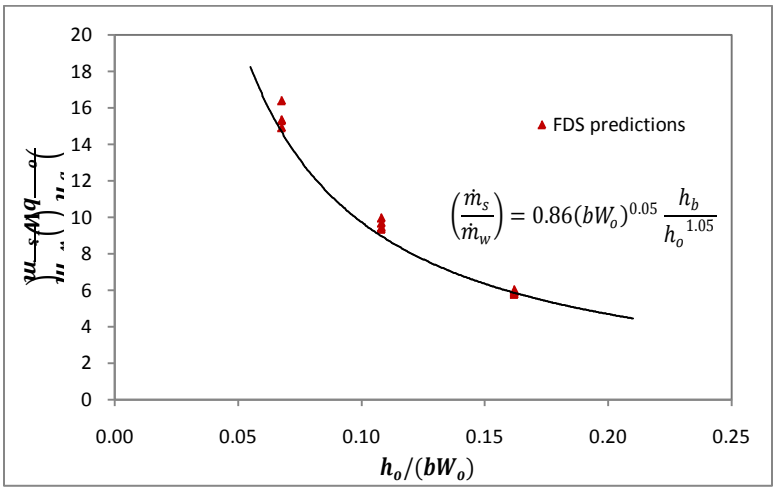

Figure 7.30: Comparison of proposed empirical correlation with data by Ko (31)

7.7 Empirical correlation for design purpose

The good agreement of the experimental data and FDS predictions from different geometry to the empirical correlation gives confidence for its use as a design calculation tool. The correlation can be employed to predict the mass flow rate of the gases at the spill edge as follows,

$$\dot{m}_s = 0.86(bW_o)^{0.05}\frac{h_b}{h_o^{1.05}}\dot{m}_w \qquad (7\text{-}2)$$

Equation 7-2 requires the input of mass flow rate at the compartment opening as well as other physical parameters of the compartment geometry. The mass flow rate of the compartment opening can be determined from well-established methods described in Section 2.1. The correlation only applies to a flow from a compartment with a

downstand at the compartment opening and which is channeled as it flows beneath the ceiling such that the width of the flow at the compartment opening and spill edge are equal.

Given that Equation 7-1 and 7-2 are empirical in nature, the criteria on their use are dependent on the range of conditions from which the correlation was derived. The criterion for the aspect ratio of the compartment opening for which the proposed empirical correlation applies is given by Equation 7-3, a non-dimensional criterion.

$$0.3 \leq \frac{h_o}{W_o} \leq 2.08 \tag{7-3}$$

Another criterion to be met is that the flow from the compartment opening has to impinge the underside of the balcony and travel horizontally before discharging at the spill edge. In this study, only balcony breadth of 5 m or more provides the necessary conditions to allow this criterion to be met for all fire sizes. Hence the criterion is given by the following,

$$\left(\frac{h_b}{h_o}\right)\left(\frac{b}{h_b - h_o}\right) \geq 6.25 \tag{7-4}$$

7.8 Empirical correlation for entrainment at rotated flow

In the analysis of entrainment at the rotation region, an approach consistent with that used by Thomas et al. (45) and Harrison (46) was used. Firstly, data from simulations of balcony spill plumes from compartments without downstand are analyzed. Figure 7.31 shows $\dot{m}_p'/\dot{Q}_c'$ at z = 0, the elevation of the balcony, plotted against $\dot{m}_s'/\dot{Q}_c'$.

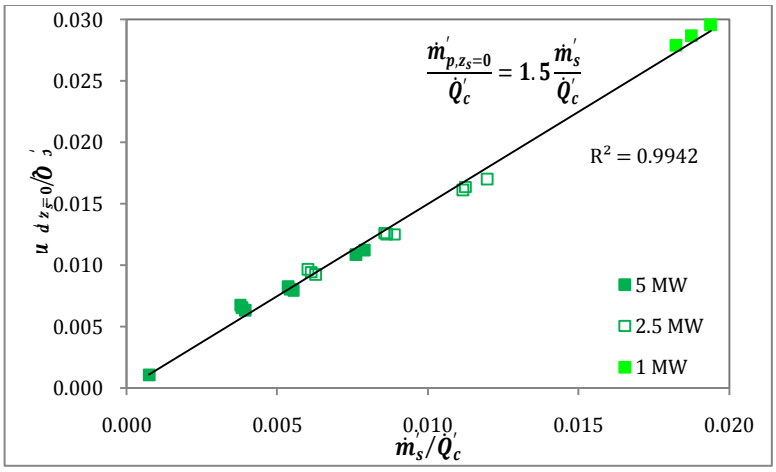

Figure 7.31: Correlation between $\dot{m}'_{p,z_s=0}/\dot{Q}'_c$ and $\dot{m}'_s/\dot{Q}'_c$ for compartments without downstand

The data can be described by a linear relationship given by Equation 7-5.

$$\frac{\dot{m}'_{p,z_s=0}}{\dot{Q}'_c} = 1.5\frac{\dot{m}'_s}{\dot{Q}'_c} \qquad (7\text{-}5)$$

Equation 7-5 suggests that the entrainment in the rotation region is 50 % of the total mass flow rate at the spill edge, which is 10 % and 16 % more than that suggested by Thomas et al. and Harrison, respectively. From the discussion in Section 4.2.5, the mass flow rate at the spill edge derived from experimental data may be at least 5 % higher than FDS predictions, due to the assumption of uniformity of flow properties across the spill edge. Hence, the higher mass flow rate at the spill edge from experimental data, could lead to a reduced entrainment at the rotation region. The mass flow rate of the gases after rotation is measured using a CO_2 tracer gas method and the deviation from FDS predictions is unknown. Thus, the data are not corrected. Figure 7.32 shows a plot of $\dot{m}'_p/\dot{Q}'_c$ against $\dot{m}'_s/\dot{Q}'_c$ at z = 0 with the data for mass flow

rate at the spill edge corrected which exhibits better agreement with Equation 7-5, albeit marginally lower than the FDS predictions.

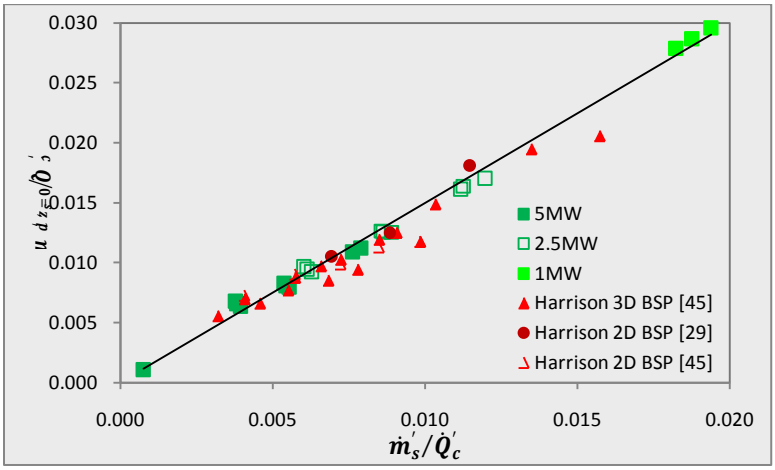

Figure 7.32: Correlation between $\dot{m}'_{p,z_s=0}/\dot{Q}'_c$ *and* $\dot{m}'_s/\dot{Q}'_c$ *for compartments without downstand for FDS predictions and experimental data by Harrison (29), (45)*

Data from simulations of balcony spill plumes from compartments with a downstand at the compartment opening are also analyzed an approach consistent with that used by Thomas et al. (45). Figure 7.33 shows $\dot{m}'_p/\dot{Q}'_c$ plotted against $\dot{m}'_s/\dot{Q}'_c$ at z = 0.

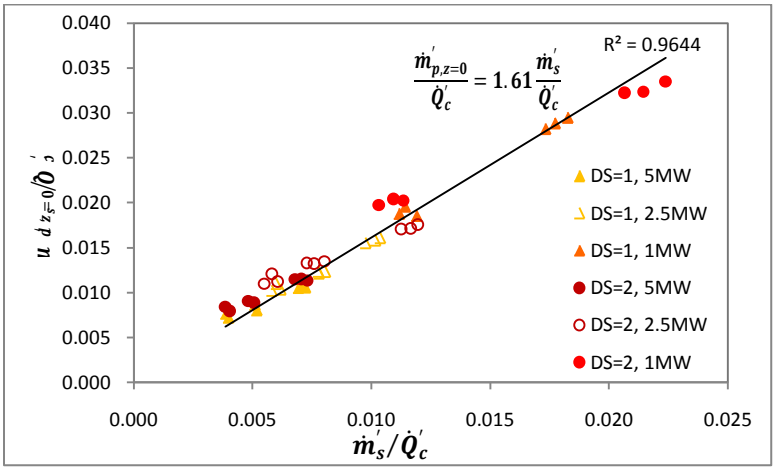

Figure 7.33: Correlation between $\dot{m}'_{p,z_s=0}/\dot{Q}'_c$ *and* $\dot{m}'_s/\dot{Q}'_c$ *for compartments with downstand*

The data can be described by a linear relationship given by Equation 7-6.

$$\frac{\dot{m}'_{p,z=0}}{\dot{Q}'_c} = 1.61\frac{\dot{m}'_s}{\dot{Q}'_c} \tag{7-6}$$

Equation 7-6 suggests that the entrainment in the rotation region is 61 % of the total mass flow rate at the spill edge, which is 11 % more than that for flows from compartments without a downstand at the compartment opening. For both cases, with and without downstand, although the gases flow horizontally under the balcony before discharging at the spill edge, the entrainment in the rotation region is different. This may be due to flows from compartments with downstand being more turbulent in nature and hence there is an increase in entrainment. However, due to the lack of available experimental data for comparison, further analysis and conclusion cannot be made.

In conclusion, the proposed empirical relationship to describe the entrainment in the rotation region for flows from compartments without downstand is as follows,

$$\dot{m}'_{p,z_s=0} = 1.5\dot{m}_s \tag{7-7}$$

The entrainment in the rotation region appears to be higher for flows from compartments with a downstand. The proposed empirical relationship to describe the entrainment in the rotation region for flows from compartments with a downstand of 1 – 2 m at the compartment opening is given by,

$$\dot{m}'_{p,z_s=0} = 1.61\dot{m}_s \tag{7-8}$$

These correlations appear to apply generally for balcony spill plumes that are fully-channeled under the balcony.

7.9 Flow characteristics for partially-channeled flows

7.9.1 Wide compartment opening without downstand

Figure 7.34 shows the flow characteristics for partially-channeled flows with a wide compartment opening and no downstand. The characteristics seem to be similar to the case of fully-channeled flows. The smoke spreads laterally under the balcony towards the channeling screens before discharging at the spill edge. As the smoke rotates around the spill edge, there seems to be minimal lateral spread.

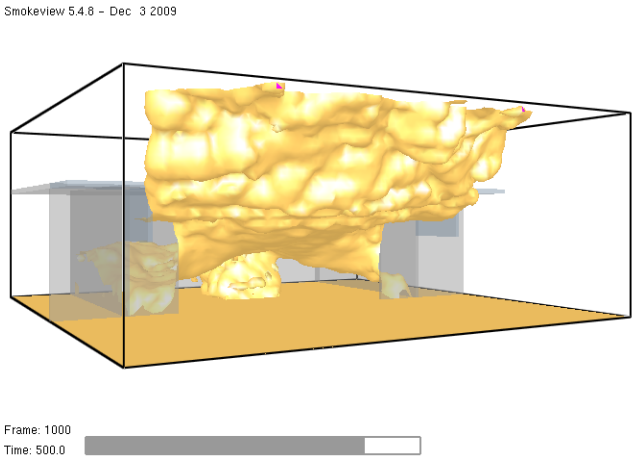

Figure 7.34: Typical flow characteristics for partially-channeled flows with wide compartment opening and no downstand (Simulation F1F)

Figure 7.35 shows a comparison of temperature contours of the smoke flow as it flows from the compartment opening to the spill edge, for both fully-channeled and

partially-channeled flows. There appears to be insignificant differences in temperatures for both cases.

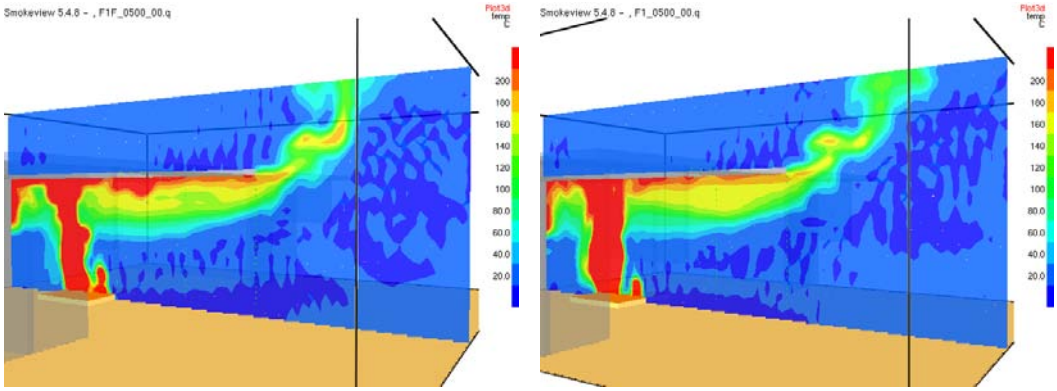

(a) (b)

Figure 7.35: Temperature contours for wide compartment opening without downstand (a) partially-channeled flows (simulation F1F) (b) fully-channeled flows (simulation F1)

Figure 7.36 shows a comparison of the velocity vectors of the smoke flow under balcony and spill edge. There are insignificant differences in the flow velocity.

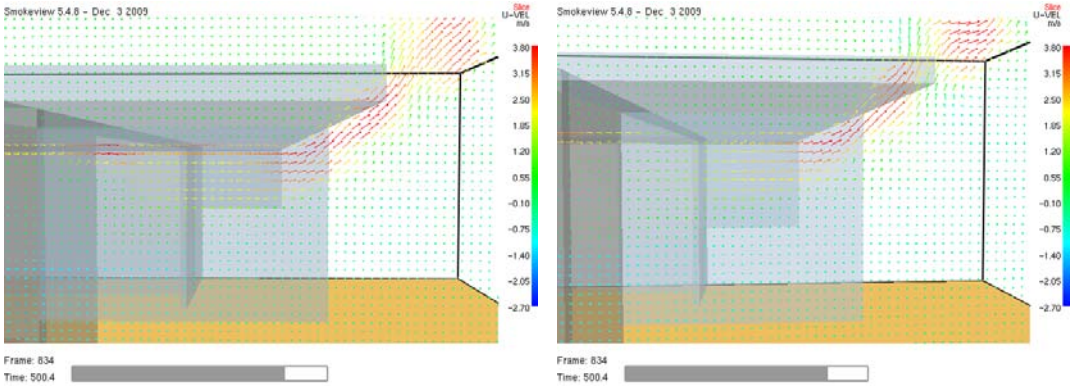

(a) (b)

Figure 7.36: Velocity vectors for wide compartment opening without downstand (a) partially-channeled flows (simulation F1F) (b) fully-channeled flows (simulation F1)

Figure 7.37 shows that the temperature across the spill edge is not uniform. The central section of the spill edge shows the highest temperature and thickest flow layer. The thickness of the flow layer in this region is relatively uniform. The outermost section of the flow layer has a relatively uniform thickness which is about half the thickness of the layer in the central section. The highest temperature in this section is about 30% lower. Between these two sections, the flow layer reduces in thickness and temperature as it moves towards the channeling screens.

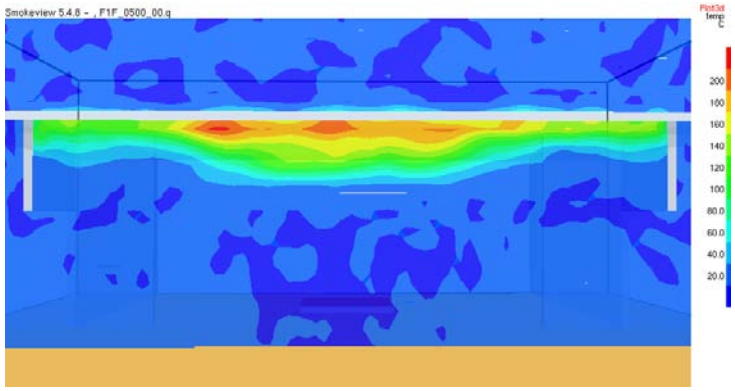

Figure 7.37: Temperature contours across the spill edge for partially-channeled flows with wide compartment opening and no downstand (Simulation F1F)

Figure 7.38 show that the longitudinal velocity across the spill edge exhibits a similar contour profile as the temperature. The flow layer at the central section is thicker and has higher velocity. An interesting phenomenon is observed at the outmost section of the flow where it meets the channeling screen, which is not observed previously in the fully-channeled flows. The flow layer seems to thicken significantly and this is attributed to a rather thick layer of gas with low longitudinal velocity and temperature. This is possibly due to the lateral spread of the gases as it exits the compartment opening, impinges on the channeling screens and rotates downwards.

As it rotates downwards, it mixes with the cool ambient air and causes a reduction in temperature and velocity.

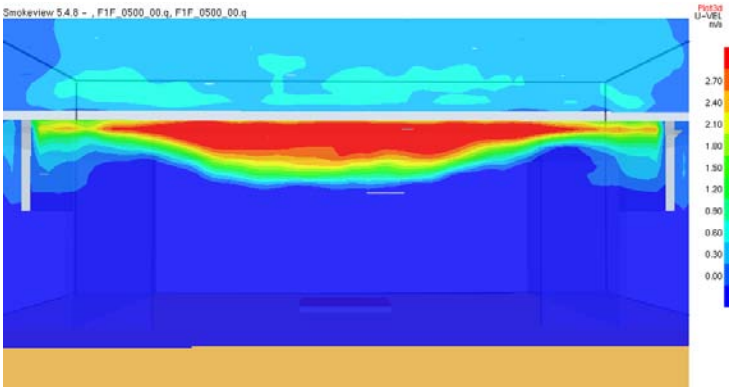

Figure 7.38: Velocity contours across the spill edge for partially-channeled flows with wide compartment opening and no downstand (Simulation F1F)

Figure 7.39 shows the spread of the flow under the balcony as it exits the compartment opening. The outermost section of the flow impinges on the channeling screen before it flows past the spill edge. It is this impingement that causes a thicker flow layer as observed in Figure 7.38. The gas at the region of the interface between the screens and the walls remain relatively stagnant.

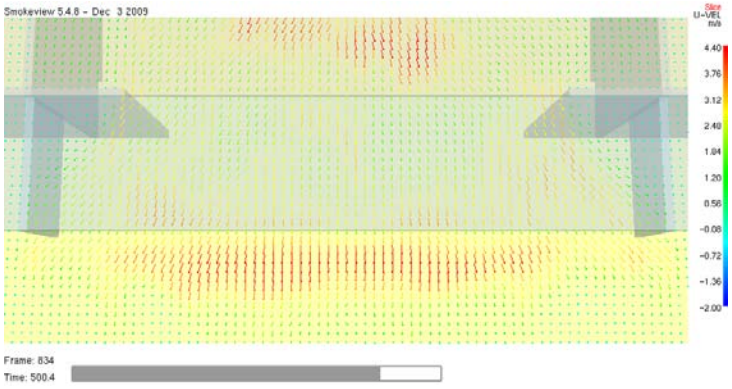

Figure 7.39: Velocity vectors under the balcony for partially-channeled flows from wide compartment opening without downstand (simulation F1F)

7.9.2 Narrow compartment opening without downstand

Figure 7.40 shows the flow characteristics for partially-channeled flow from a narrow compartment opening without a downstand. The smoke spreads laterally under the balcony towards the channeling screens, forming a relatively thin layer before discharging at the spill edge. As the smoke rotates around the spill edge, there appears to be minimal lateral spread.

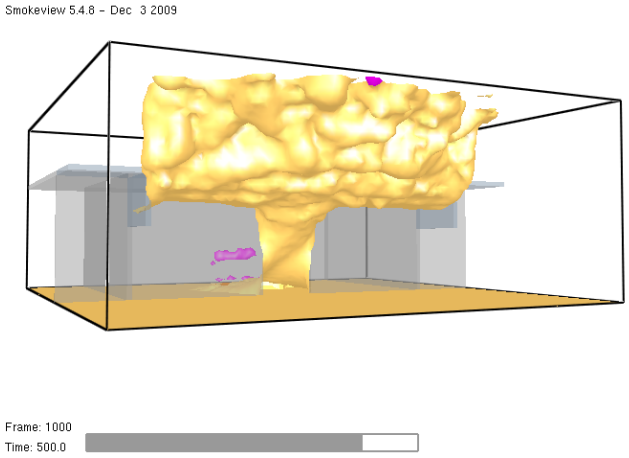

Figure 7.40: Typical flow characteristics for partially-channeled flows from narrow compartment opening without downstand (Simulation F3F)

Figure 7.41 shows a comparison of temperature contours of the smoke flow as it flows from the compartment opening to the spill edge, for partially-channeled flows and fully-channeled flows. For the case of partially-channeled flows, the temperature in the compartment and at the spill edge is significantly lower compared to the case of the fully-channeled flow. At the spill edge, there is a reduction of approximately 30% in the temperature. Beyond the spill edge, the flow appears to have less vertical velocity which is a result of reduced buoyancy due to lower temperature.

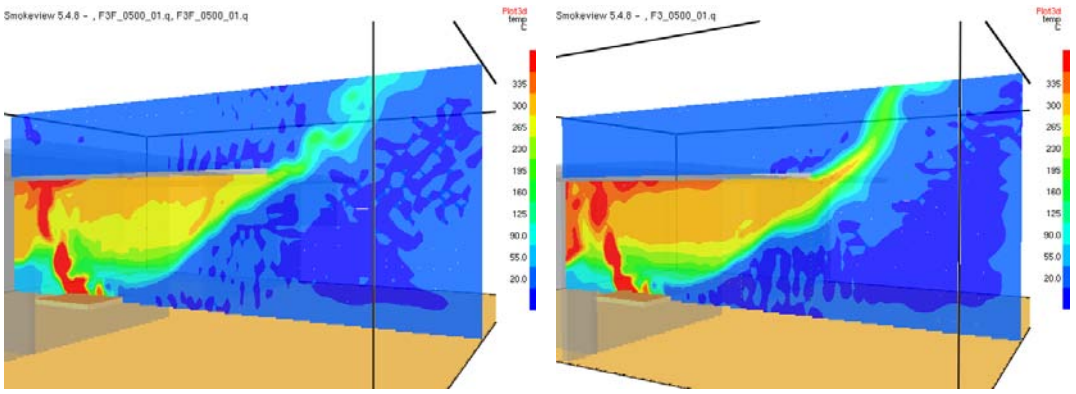

(a) (b)

Figure 7.41: Temperature contours for narrow compartment opening without downstand (a) partially-channeled flows (simulation F3F) (b) fully-channeled flows (simulation F3)

Figure 7.42 shows that the thickness of the flow layer at the spill edge is reduced by about 50 % as the widely-spaced channeling screens allow the lateral spread of smoke. The longitudinal velocity of the flow layer at the spill edge does not show any significant in magnitude. Beyond the spill edge, the velocity reduces rapidly and the effect of a jet-like projection as observed for the fully-channeled flow is absent for the case of partially-channeled flows.

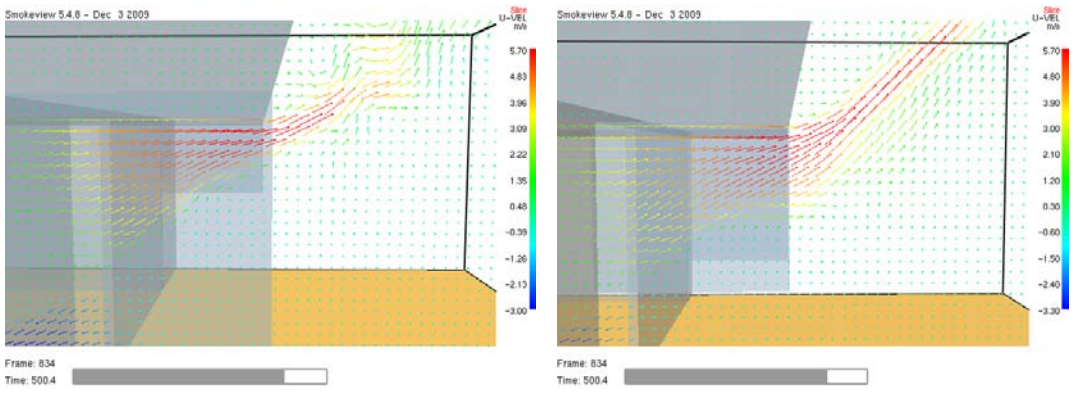

(a) (b)

Figure 7.42: Velocity vectors for narrow compartment opening without downstand (a) partially-channeled flows (simulation F3F) (b) fully-channeled flows (simulation F3)

Figure 7.43 shows that there is less variation in the flow layer thickness across the spill edge as compared to flows from a wide compartment opening. However, the temperatures of the flow layer near the channeling screens are about 50 % lower than the central section. This is possibly due to heat loss and entrainment as the gas travels a longer distance. Near the channeling screens, the layer is marginally thicker due to the downward movement of the gas after it impinges the screens.

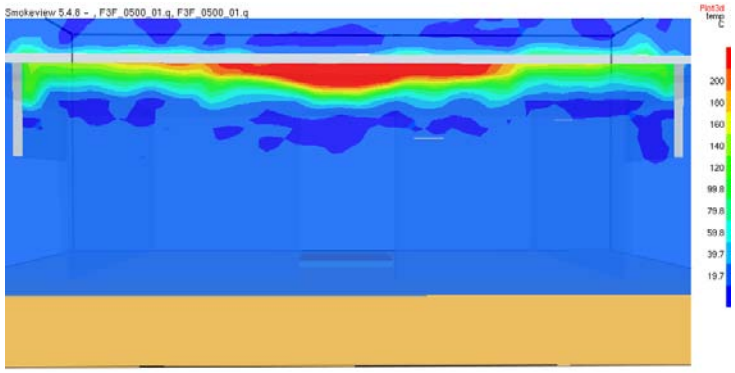

Figure 7.43: Temperature contours across the spill edge for partially-channeled flows from narrow compartment opening without downstand (simulation F3F)

Figure 7.44 shows that the longitudinal velocity across the spill edge exhibits a similar contour profile as the temperature. The variation in velocity across the spill edge is more significant than the case of wide compartment opening, with the velocity in the central section about 2 times the velocity at the outermost section. Again, this is due to the wide lateral spread as the flow exits from the compartment opening. Near the channeling screens, the flow layer is only marginally thicker as compared to that observed in Figure 7.38. This is possibly due to reduced gas impingement onto the screens due to the longer lateral distance that the gas needs to travel.

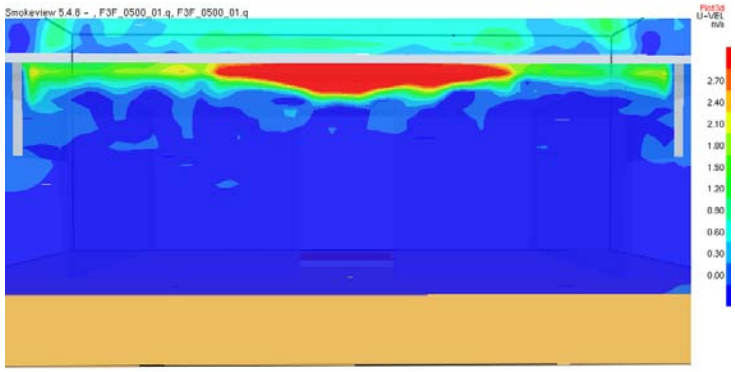

Figure 7.44: Velocity contours across the spill edge for partially-channeled flows from narrow compartment opening without downstand (simulation F3F)

Figure 7.45 shows that the flow spreads at a larger angle as compared to that from a wide compartment opening. The flow impinges the screens very close to the spill edge thus explaining the marginally thicker flow layer in that region. The relatively stagnant region at the interface of the channeling screens and the compartment wall is larger for this case.

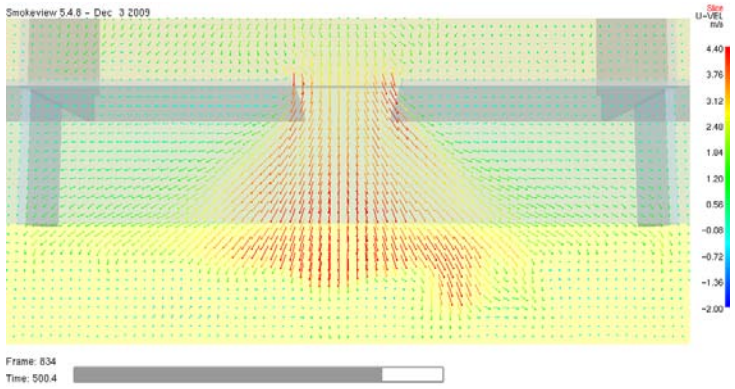

Figure 7.45: Velocity vectors under the balcony for partially-channeled flows from narrow compartment opening without downstand (simulation F3F)

7.10 Flow characteristics for unchanneled flows

7.10.1 Unchanneled flows from wide compartment opening

Figure 7.46 shows that for an unchanneled flow from a wide compartment opening, as the smoke exits the compartment opening, it spreads laterally beneath the balcony until it reaches the extreme ends of the modeled balcony. Although the lateral spread is significant, most of the smoke seems to discharge from the spill edge directly in front of the compartment opening.

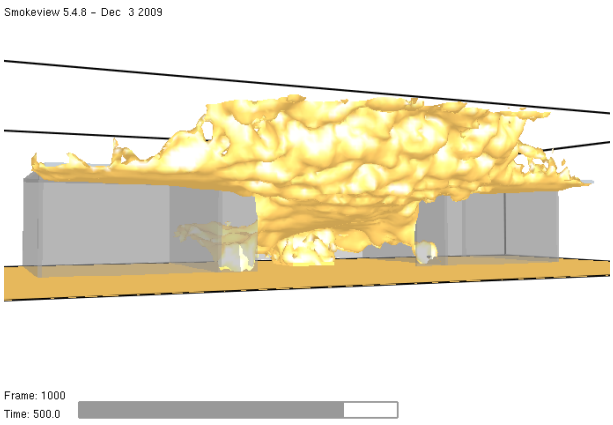

Figure 7.46: Typical flow characteristics for unchanneled flows from wide compartment opening (Simulation F1U)

Figure 7.47 and Figure 7.48 show the temperature and velocity contours at the spill edge. It can be seen that most of the flow seems to be discharging from the spill edge in the section directly in front of the compartment opening. The thickness of the flow layer is largest in the middle of the spill edge and decreases rapidly in the lateral directions. The section of uniform thickness observed in Figure 7.37 is not observed

here. The temperature and velocity of the flow at the outer sections are very low due to heat loss and entrainment of air as it flows under the balcony.

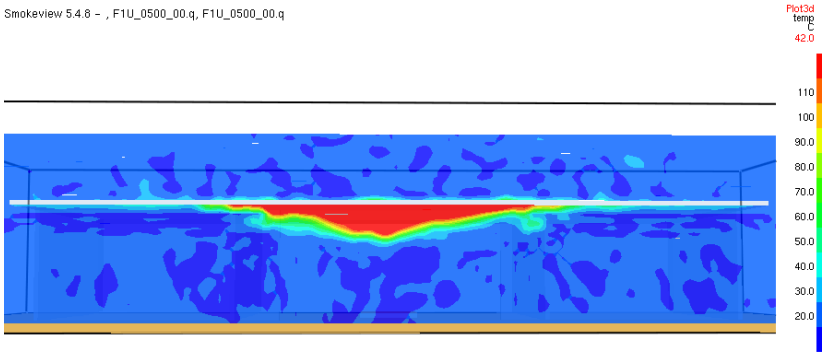

Figure 7.47: Temperature contours across the spill edge for unchanneled flows with wide compartment opening (Simulation F1U)

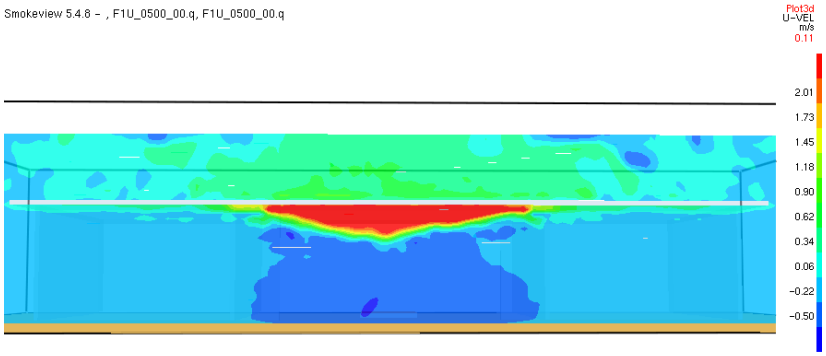

Figure 7.48: Velocity contours across the spill edge for unchanneled flows with wide compartment opening (Simulation F1U)

Figure 7.49 shows that most of the smoke discharges directly in front of the compartment opening with an angle of spread of about 30 °, similar to that observed in Figure 7.39 for partially-channeled flows. Figure 7.50 shows that the lateral spread

of the smoke reaches the extreme ends of the modeled balcony at a much reduced flow velocity.

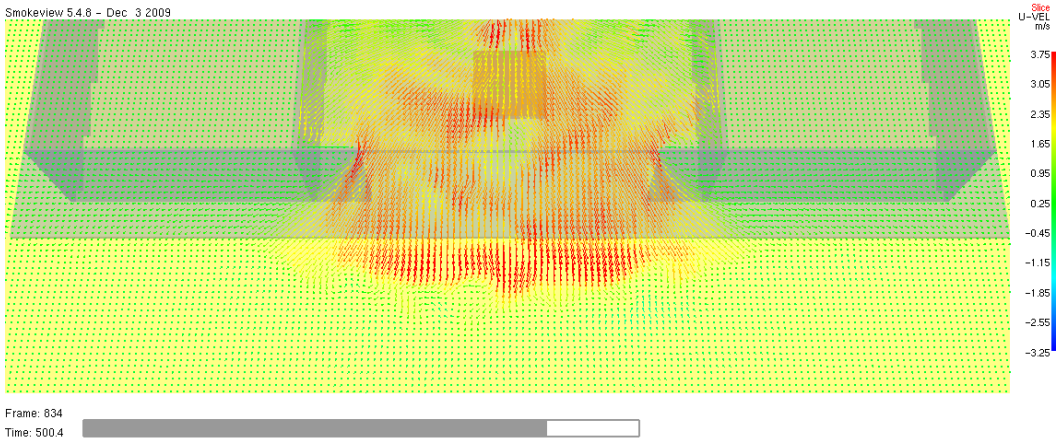

Figure 7.49: Velocity vectors under the balcony for unchanneled flows from wide compartment opening (simulation F1U)

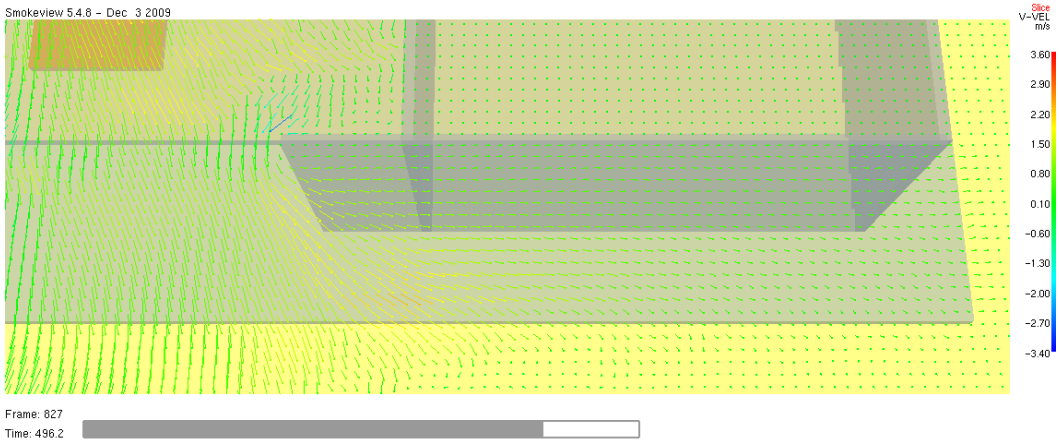

Figure 7.50: Velocity vectors showing lateral spread of smoke under the balcony for wide compartment opening (simulation F1U)

7.10.2 Unchanneled flows from narrow compartment openings

Figure 7.51 shows that the lateral spread of smoke beneath the balcony seems to be more substantial for an unchanneled flow from a narrow compartment opening. Although the lateral spread is increased, a large portion of the smoke appears to discharge from the spill edge directly in front of the compartment opening.

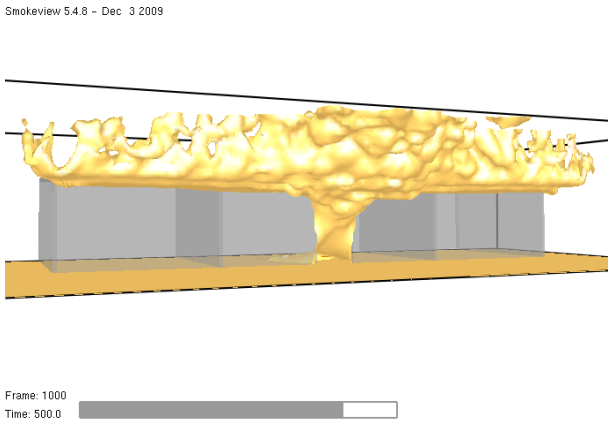

Figure 7.51: Typical flow characteristics for unchanneled flows from narrow compartment opening (Simulation F3U)

Figure 7.52 and Figure 7.53 shows that the majority of the smoke seems to discharge from the spill edge in front of the compartment opening. The layer thickness at the outer sections of the spill edge appears to be thicker than that observed for the case of wide compartment opening. A possible explanation for this observation is that the temperature and velocity of the smoke at the compartment opening is higher due to the narrow compartment opening as discussed for fully-channeled flows in Section 7.2.

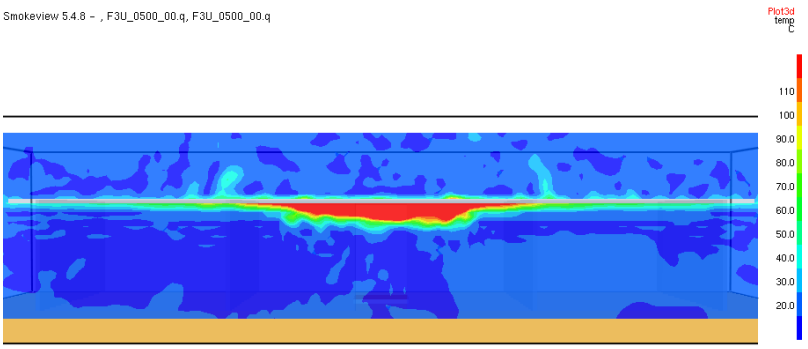

Figure 7.52: Temperature contours across the spill edge for unchanneled flows with narrow compartment opening (Simulation F3U)

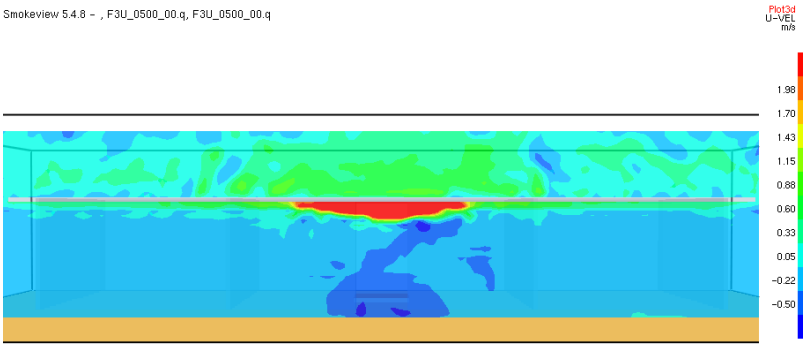

Figure 7.53: Velocity contours across the spill edge for unchanneled flows with narrow compartment opening (Simulation F3U)

Figure 7.54 shows that the angle of spread as the smoke exits the compartment opening is similar to that observed for partially-channeled flows in Figure 7.45. Most of the smoke is discharged at the spill edge in front of the compartment opening. Comparing the longitudinal velocity with the case of wide compartment opening, there is an increase of about 25 %. Figure 7.55 shows that the lateral velocity under the balcony is also higher, thus increasing the lateral spread, resulting in a thicker

flow layer in the outer sections of the spill edge, observed in Figure 7.52 and Figure 7.53.

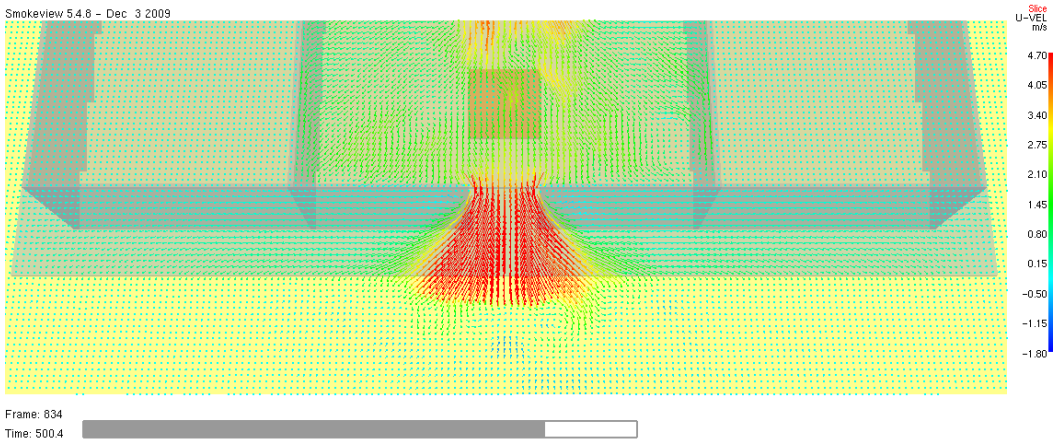

Figure 7.54: Velocity vectors under the balcony for unchanneled flows from narrow compartment opening (simulation F3U)

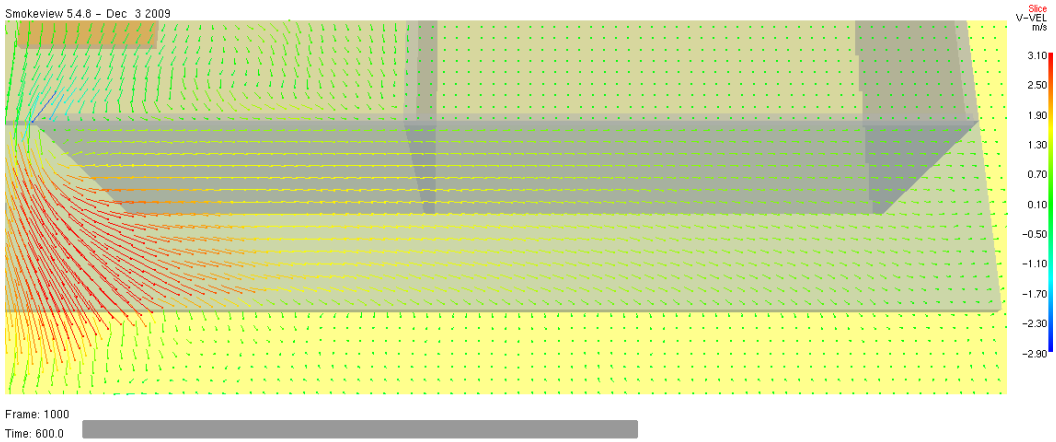

Figure 7.55: Velocity vectors showing lateral spread of smoke under the balcony for narrow compartment opening (simulation F3U)

7.11 Predicted entrainment rates for partially-channeled flows and unchanneled flows

Table 7-1 shows the predicted entrainment rates as the smoke flows from the compartment opening to the spill edge and as the smoke rotates around the spill edge. For unchanneled flows, smoke is observed flowing out from the extreme ends of the balcony in Figure 7.46 and Figure 7.51. The quantity of smoke flowing from these regions is less than 9 % of the total smoke flowing from the front of the spill edge. The entrainment as they rotate around the ends of the balcony is treated in a similar manner as that from the spill edge. It is expected that the loss of accuracy due to this is not significant.

Table 7-1: Predicted entrainment rates for partially-channeled flows and unchanneled flows

Simulation	Configuration	Downstand Height (m)	$\dot{m}_S/\dot{m}_w$	$\dot{m}_{P,z_s=0}/\dot{m}_s$
F1F	Partially-channeled	0	1.13	1.53
F2F	Partially-channeled	0	1.32	1.88
F3F	Partially-channeled	0	1.55	2.30
F4F	Partially-channeled	1	1.29	1.67
F5F	Partially-channeled	1	1.50	1.94
F6F	Partially-channeled	1	1.89	2.18
F7F	Partially-channeled	2	1.69	1.82
F8F	Partially-channeled	2	1.94	2.11
F9F	Partially-channeled	2	2.65	2.16
F1U	Unchanneled	0	1.33	1.58
F2U	Unchanneled	0	1.61	1.88
F3U	Unchanneled	0	2.19	2.07

Figure 7.56 shows the FDS predictions plotted with Equation (7-2).

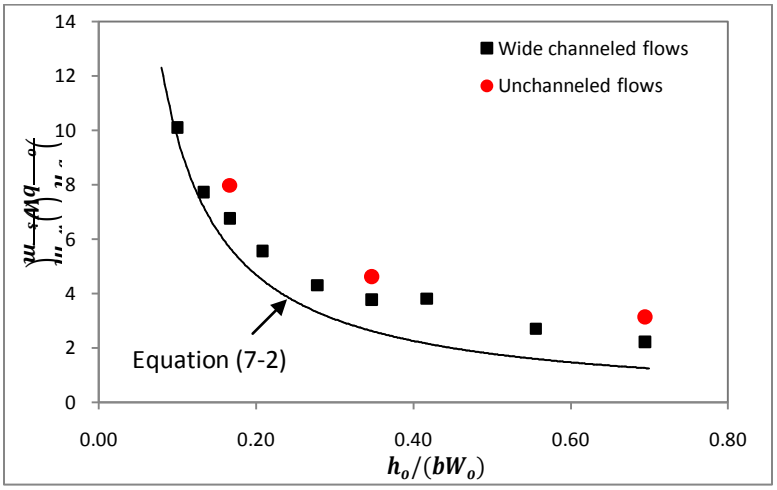

Figure 7.56: Comparison of FDS predictions with Equation (7-2)

Comparing the data in Table 7-1 and Figure 7.56, it can be seen that the entrainment as the smoke flows from the compartment opening to the spill edge, for partially-channeled flows and unchanneled flows is significantly higher than that of fully-channeled flows having the same compartment configurations. The entrainment rate increases as the height of downstand increases and as the compartment opening reduces. For narrow compartment openings, the entrainment under the balcony is predicted to be 165 % and 119% for partially-channeled flows and unchanneled flows respectively. This is greater than the recommendation of 100 % given by BRE in Section 2.2.2. For the cases without downstand at the compartment opening, the entrainment under the balcony is predicted to be as high as 55 %.

For entrainment at the rotation region, a similar trend of increased entrainment is observed from data in Table 7-1. The increase in predicted entrainment compared to fully-channeled flows is the least for wide compartment openings. For wide

compartment openings without downstand, the increase in entrainment is marginal, about 2 % and 5 % for partially-channeled flows and unchanneled flows respectively. When a downstand is present, the increase in predicted entrainment is 4 – 13 % for wide compartment openings. When the compartment opening width is reduced, the increase in predicted entrainment is as high as 53 %.

From these simulations of partially-channeled flows and unchanneled flows, it appears that there is a significant increase in entrainment as compared to fully-channeled flows. It is deduced from the simulations performed in this work that the increase in entrainment is due to the lateral spread of smoke as it travels beneath the balcony. From Figure 7.56, it seems that predictions for partially-channeled flows obey a similar form of power law given by Equation (7-2). Predictions for unchanneled flows seem to exhibit the same trend as well. However, due to the limited number of simulation performed for these configurations, a more definite conclusion cannot be drawn for these cases.

8. Conclusions

This work has characterized the balcony spill plume entrainment in the under balcony and rotation region from FDS simulations, supported by comparisons with experimental data from previous work. The findings of each aspect of this work are summarized in this section.

A rigorous approach is adopted in the determination of the optimum grid cell size for modeling balcony spill plumes in the region of interest. FDS simulations using very small grid cell size of 1 cm are performed to resolve the near wall flow regime of ceiling jets. Using these predictions as reference predictions, they are compared with predictions from larger grid cell sizes to determine the loss of accuracy. The optimum grid cell size is determined to be about 4 % of the ceiling height, which gives predictions that have a deviation of about 10 % from the reference predictions.

Grid sensitivity analysis is then carried out for simulations of balcony spill plumes using the established optimum grid cell size. Analysis of the flow characteristics reveals that experimental data for mass flow rates are generally higher than FDS predictions. This is due to the assumption of uniformity of flow characteristics across the lateral extent of the flow path. Using the same method of calculation and assumptions, FDS predictions for mass flow rates are within 7 % of the experimental data. Scaling laws are applied to these small-scale predictions and experimental data to obtain the full-scale equivalent data. These calculated full-scale data are then compared with FDS predictions made on equivalent full scale models. The

comparison shows that there was excellent agreement of less than 2 % deviation, in the small-scale and full-scale FDS predictions. When compared to the experimental data, there was a deviation of about 7 – 10 %. This deviation is expected to be reduced if the experimental method of calculation and assumptions are adopted. These findings give confidence to the use of FDS for such studies and also verified that the predictions performed with grid cell size of 4 % of the ceiling height gives sufficiently good agreement with experimental data.

A series of 69 simulations are performed to characterize balcony spill plume entrainment in the under balcony and rotation region. These flows are fully channeled such that lateral spread under the balcony is prevented. The fire size, width of compartment opening, downstand height and balcony breadth is varied to produce different flow characteristics. An empirical correlation is proposed to predict the entrainment as the smoke flows from a compartment opening with a downstand to the spill edge, hence the subsequent mass flow rate at the spill edge. This correlation which applies to channeled flows where the smoke does not spread laterally under the balcony is given by,

$$\dot{m}_s = 0.86(bW_o)^{0.05} \frac{h_b}{{h_o}^{1.05}} \dot{m}_w$$

subject to $0.3 \leq \frac{h_o}{W_o} \leq 2.08$ and $\left(\frac{h_b}{h_o}\right)\left(\frac{b}{h_b - h_o}\right) \geq 6.25$

For entrainment at the rotation region, the following empirical correlation is proposed for flow from compartments without downstand,

$$\dot{m}'_{p,z_s=0} = 1.5\dot{m}_s$$

For compartments with a downstand at the compartment opening, the following correlation is proposed,

$$\dot{m}'_{p,z_s=0} = 1.61\dot{m}_s$$

These correlations appear to apply generally for balcony spill plumes that are fully channeled under the balcony.

A series of 3 simulations are carried out for unchanneled flows and 9 simulations for flows where the channeling screens are set at the width of the compartment. The latter case is a closer representation of practical applications where the beam spacing is equal to the compartment width. From the analysis of these predictions, the following are observed,

- Entrainment under the balcony is significantly increased compared to fully-channeled flows.
- Entrainment increases as the height of the downstand increases and as the compartment opening width decreases.
- Entrainment is predicted to be as high as 165 % for partially-channeled flows and 119 % for unchanneled flows.
- Entrainment in the rotation region is significantly increased for flows from narrow compartment openings compared to fully-channeled flows.

- For wide compartment openings, the increase in entrainment in marginal.

Further studies are required to draw a more definite conclusion for these flow scenarios.

9. Further Work

In this work, the entrainment processes under the balcony and in the rotation region has been further characterized for flows that are fully channeled under the balcony. Comparisons of FDS predictions are validated with experimental data to give confidence in the use of FDS for modeling such flow scenarios. In the analysis of small-scale balcony spill plumes, it is discovered that the experimental measurements of mass flow rate using the velocity and temperature profiles with the assumption of uniformity of flow across the lateral extent of the flow path generally result in an overestimation. Further experimental work is suggested to characterize the "errors" associated with such measurements.

For entrainment in the rotation region, there is sufficient experimental data for configurations where there is no downstand at the compartment opening to validate the FDS predictions. However, for configuration with a downstand at the compartment opening, experimental data is not available for validation. Hence, experimental work is suggested to be carried out for such configurations to validate the FDS predictions and draw a more definite conclusion.

The work carried out in this research for partially-channeled flows and unchanneled flows indicate that the entrainment for these flows is significantly higher than fully channeled flows. Further experimental work is suggested for these flow scenarios to characterize the entrainment and develop a correlation that can be used design purposes.

10. Appendices

APPENDIX A: Temperature and velocity profiles for ceiling jet

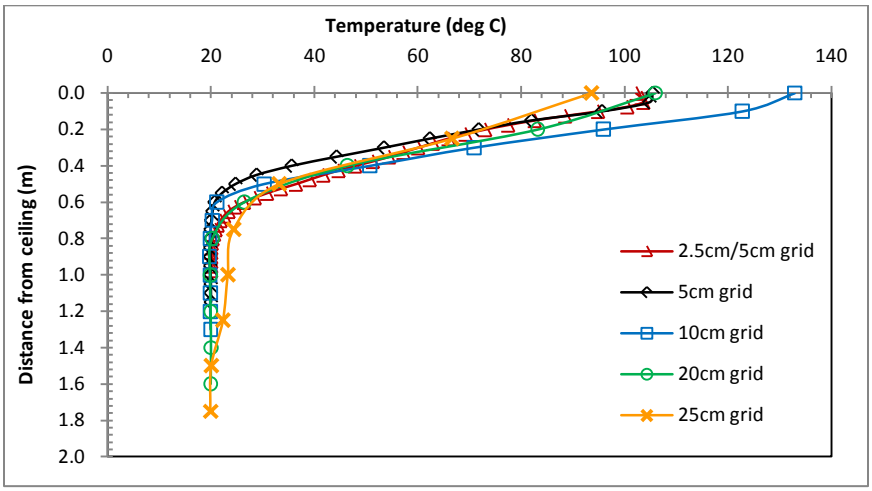

Figure A1: Temperature Profile at r/H = 0.5

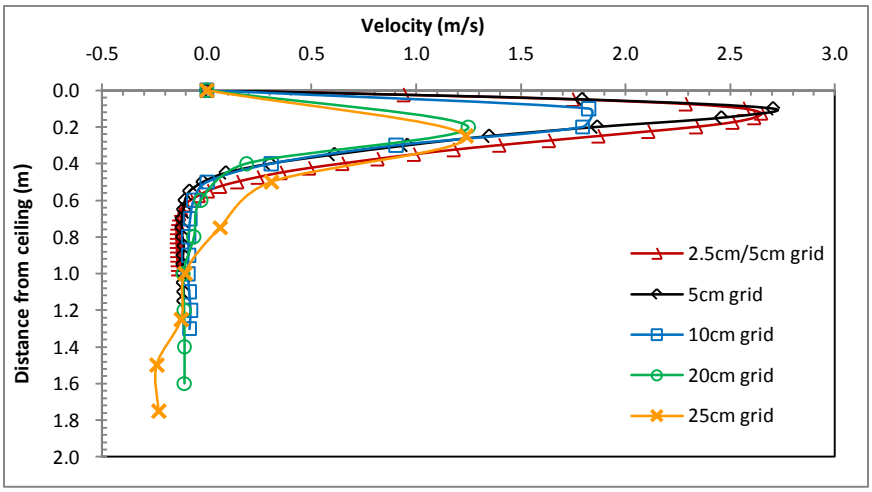

Figure A2: Velocity Profile at r/H = 0.5

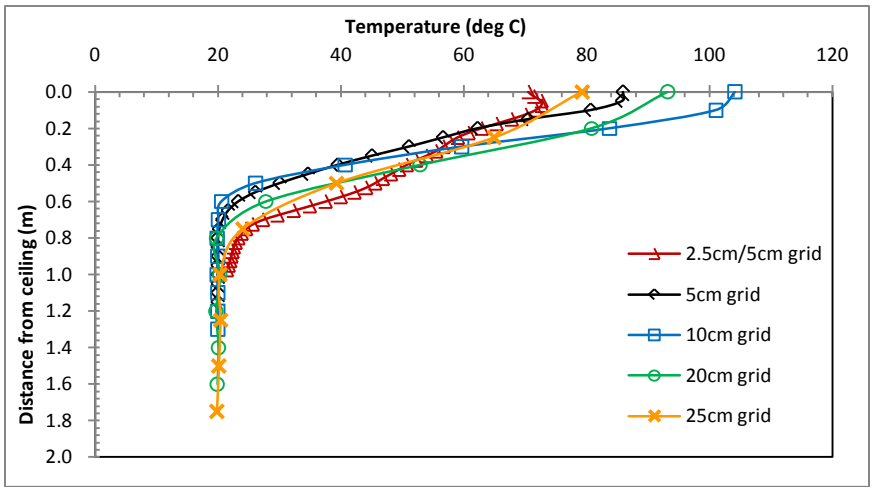

Figure A3: Temperature Profile at r/H = 0.8

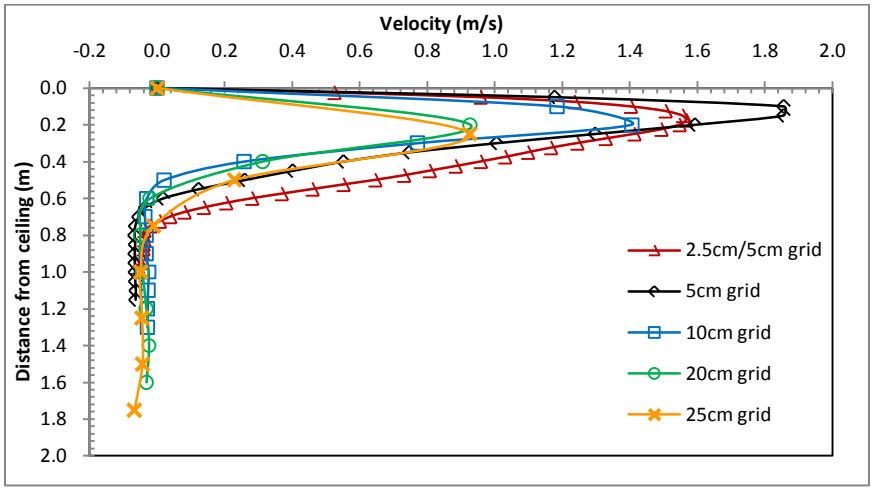

Figure A4: Velocity Profile at r/H = 0.8

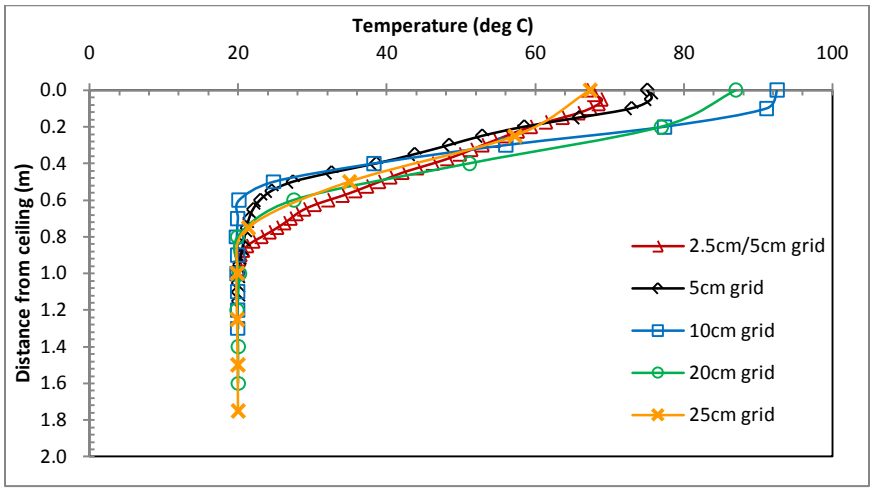

Figure A5: Temperature Profile at r/H = 1

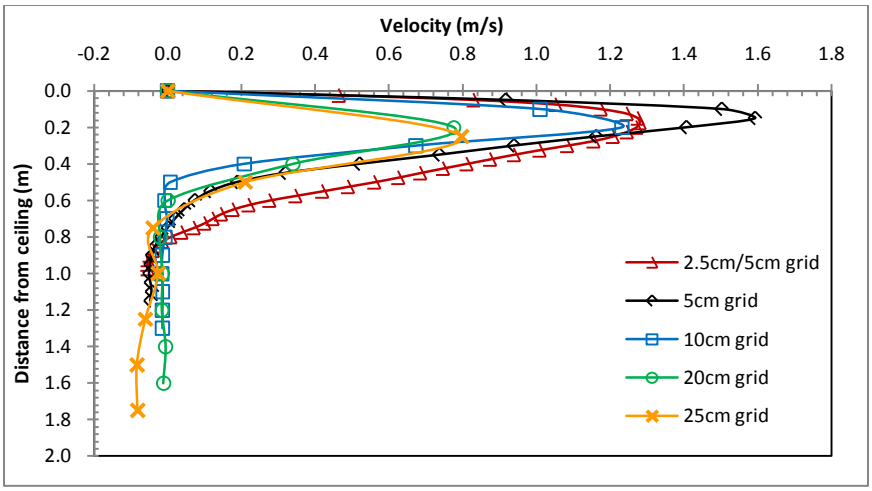

Figure A6: Velocity Profile at r/H = 1.0

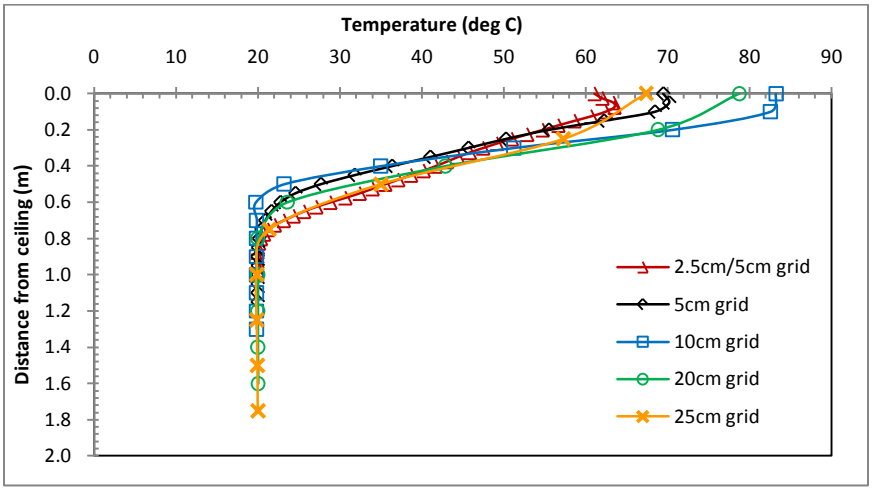

Figure A7: Temperature Profile at r/H = 1.2

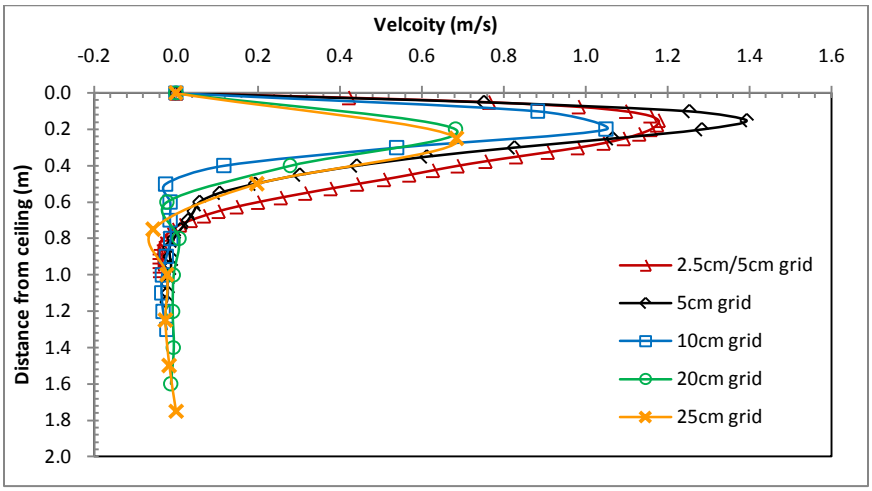

Figure A8: Velocity Profile at r/H = 1.2

APPENDIX B: Temperature and velocity profiles for characterization of boundary layer flow

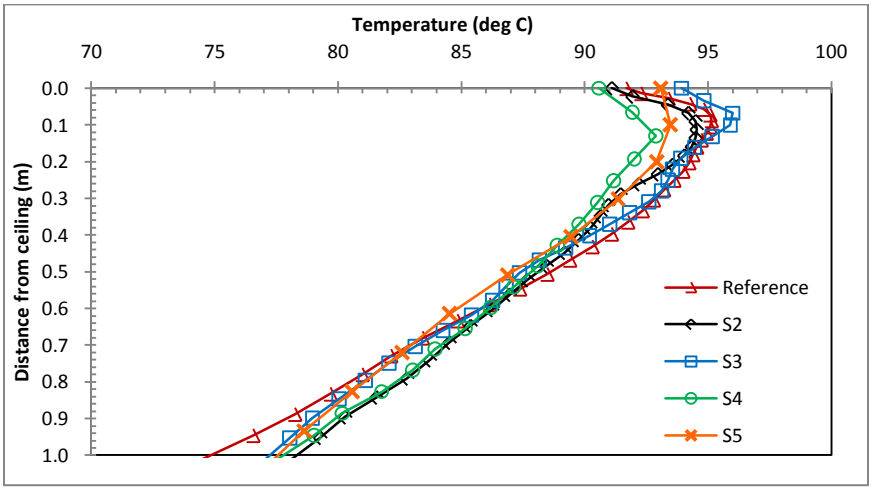

Figure B1: Temperature profile for simulations reference and S2 to S5 at r/H=0.5

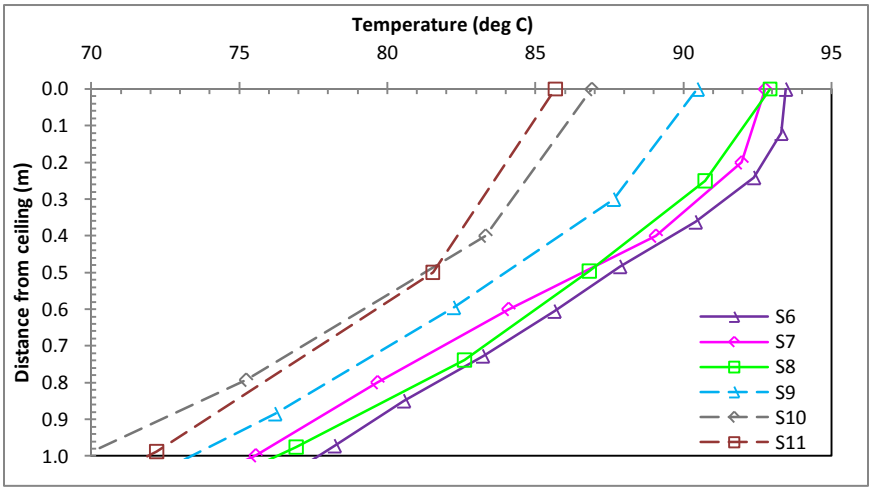

Figure B2: Temperature profile for simulations S6 to S11 at r/H=0.5

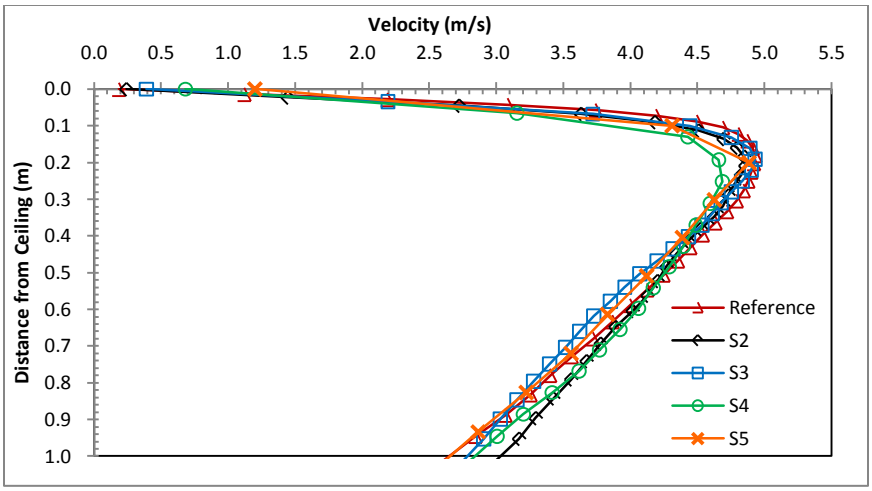

Figure B3: Velocity profile for simulations reference and S2 to S5 at r/H=0.5

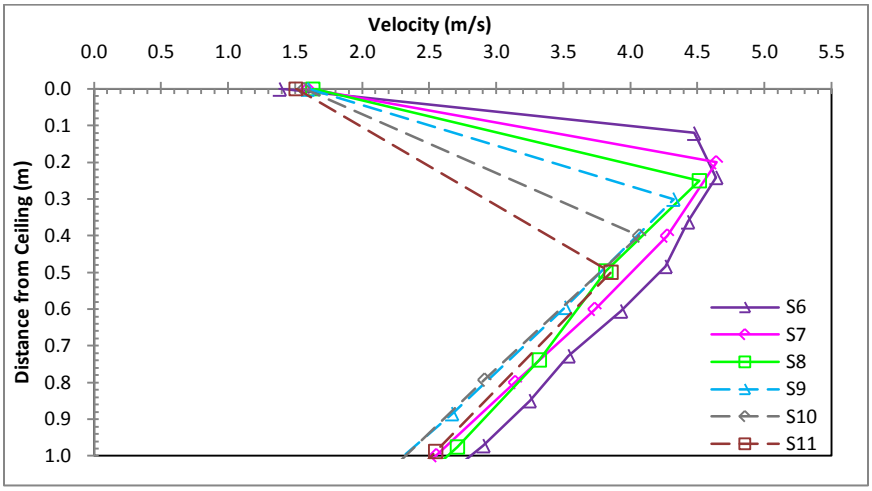

Figure B4: Velocity profile for simulations S6 to S11 at r/H=0.5

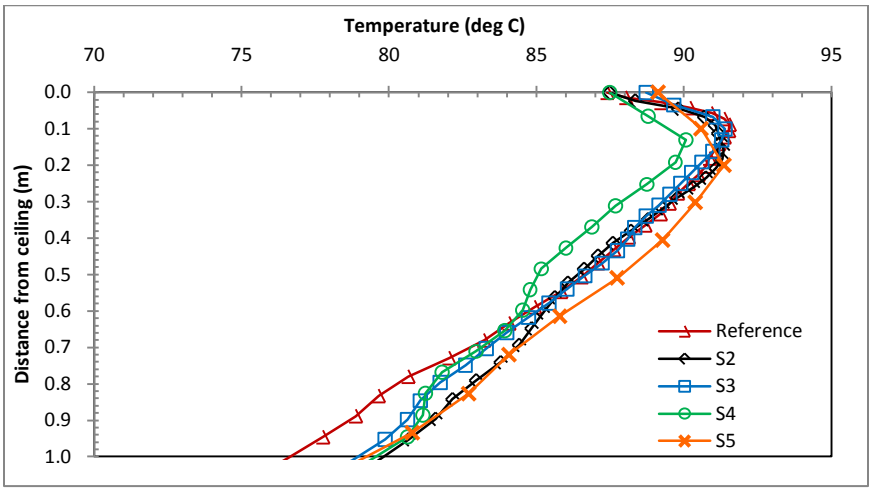

Figure B5: Temperature profile for simulations reference and S2 to S5 at r/H=0.75

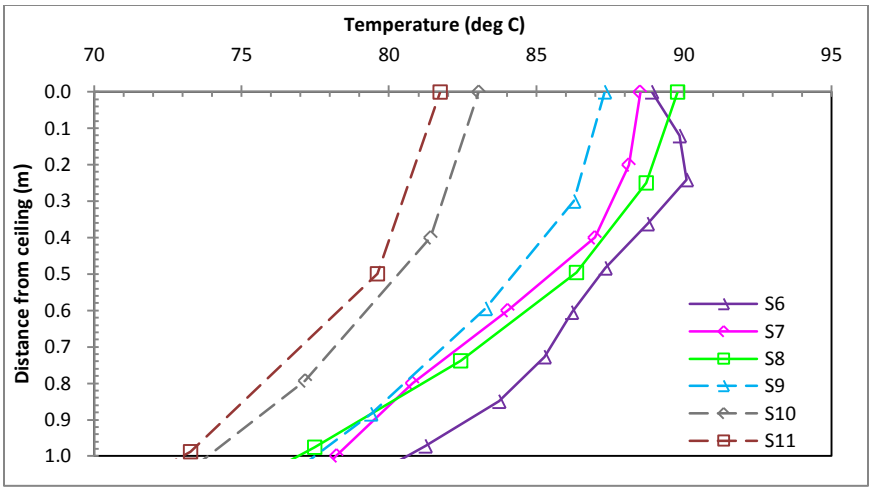

Figure B6: Temperature profile for simulations S6 to S11 at r/H=0.75

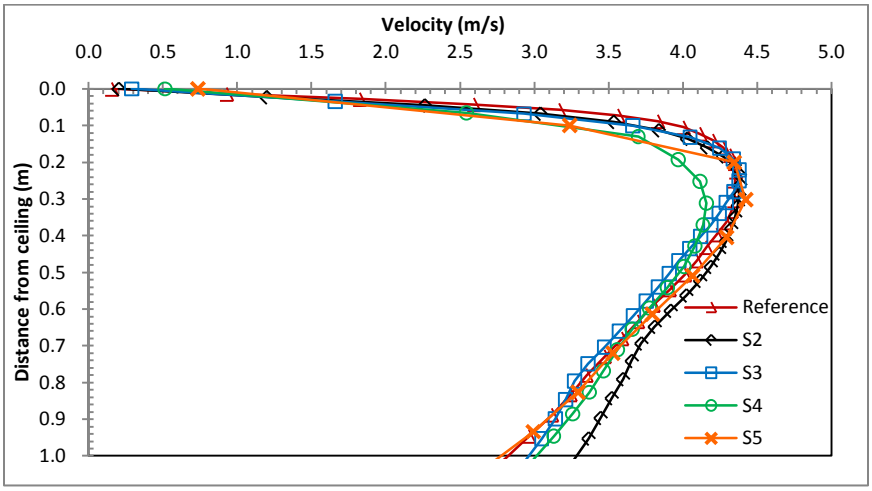

Figure B7: Velocity profile for simulations reference and S2 to S5 at r/H=0.75

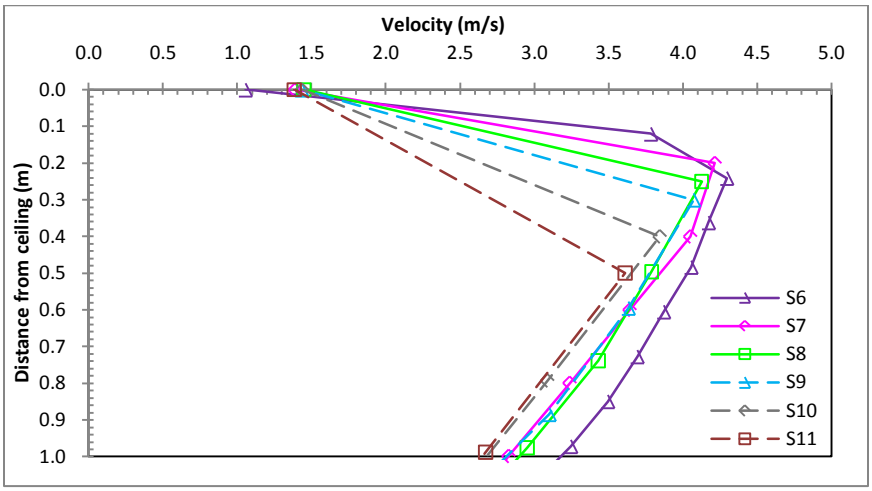

Figure B8: Velocity profile for simulations S6 to S11 at r/H=0.75

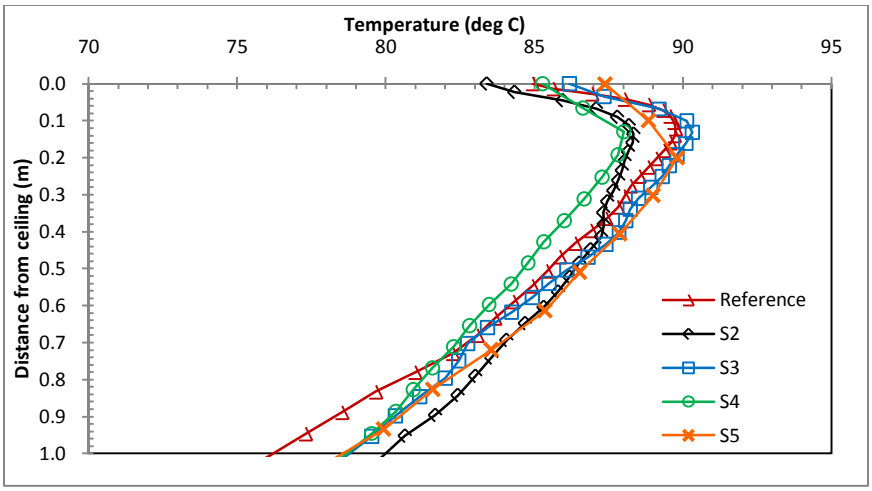

Figure B9: Temperature profile for simulations reference and S2 to S5 at r/H = 1.0

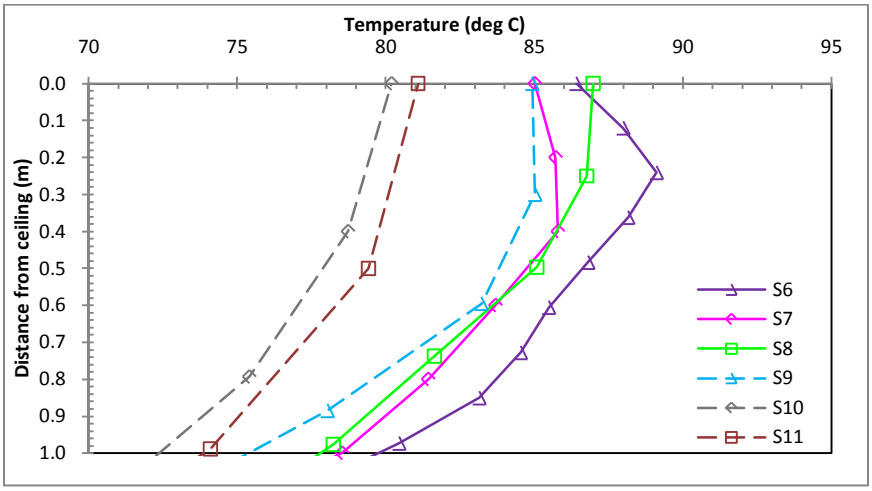

Figure B10: Temperature profile for simulations S6 to S11 at r/H = 1.0

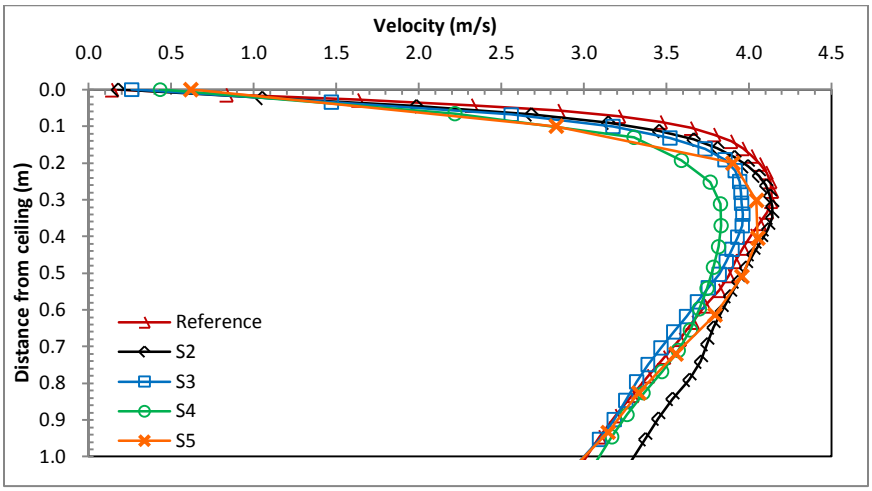

Figure B11: Velocity profile for simulations reference and S2 to S5 at r/H = 1.0

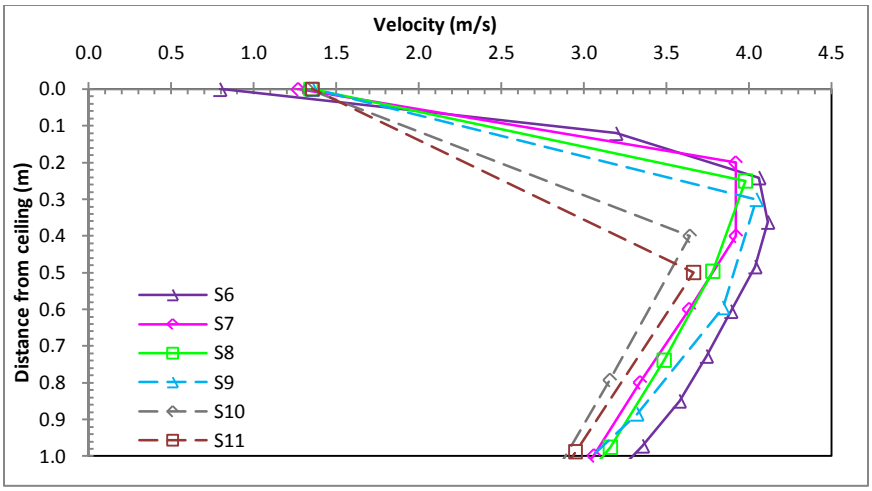

Figure B12: Velocity profile for simulations S6 to S11 at r/H = 1.0

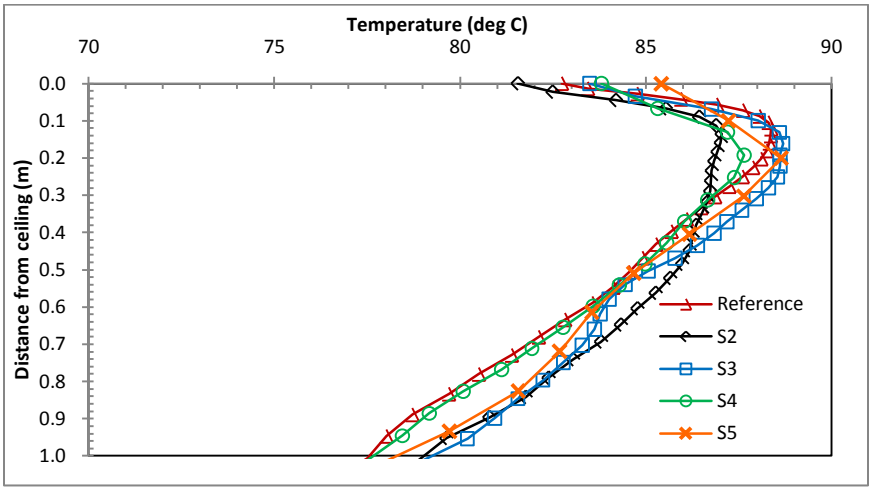

Figure B13: Temperature profile for simulations reference and S2 to S5 at r/H = 1.25

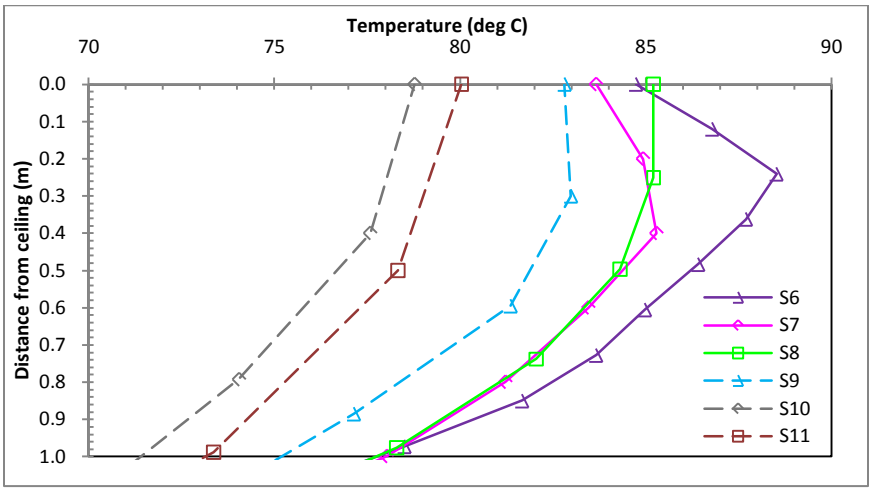

Figure B14: Temperature profile for simulations S6 to S11 at r/H = 1.25

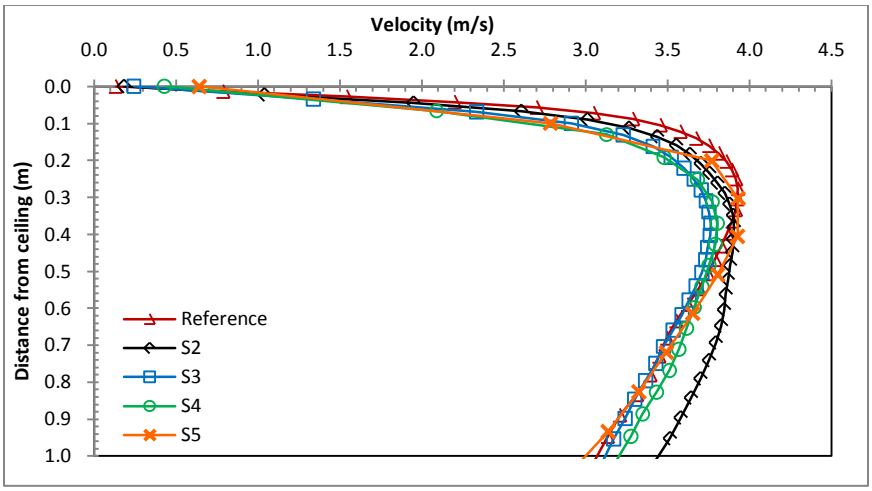

Figure B15: Velocity profile for simulations reference and S2 to S5 at r/H = 1.25

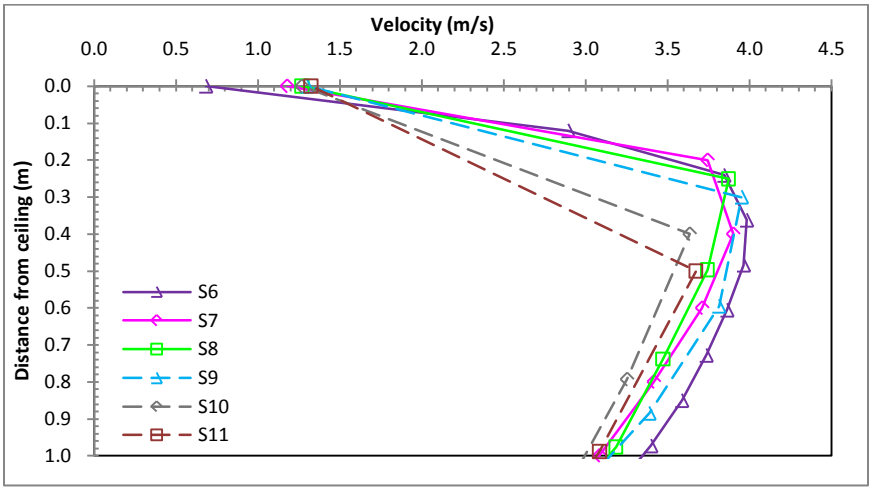

Figure B16: Velocity profile for simulations S6 to S11 at r/H = 1.25

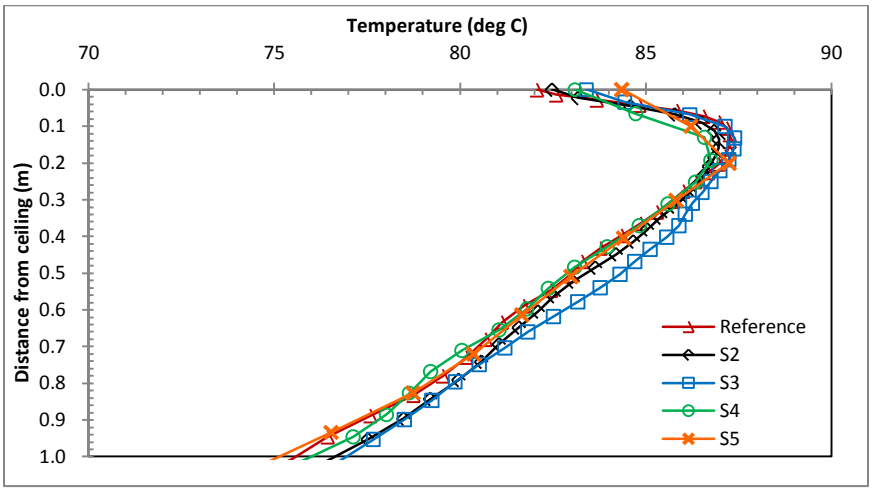

Figure B17: Temperature profile for simulations reference and S2 to S5 at r/H = 1.5

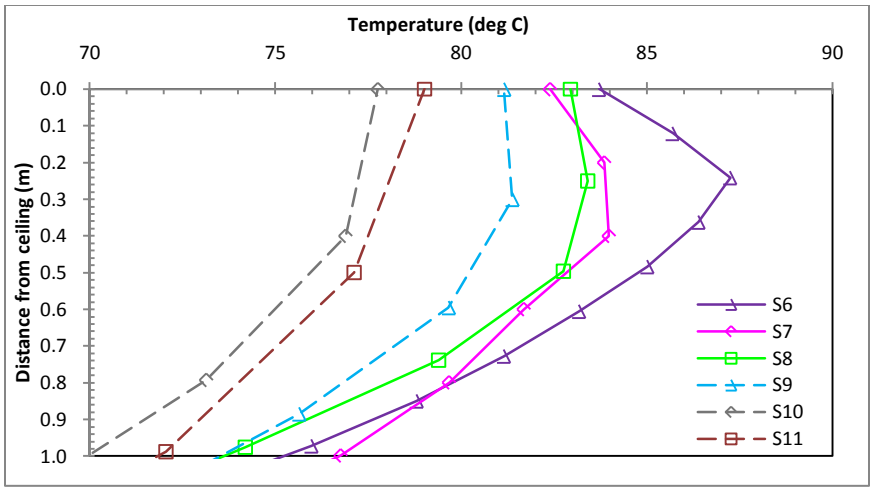

Figure B18: Temperature profile for simulations S6 to S11 at r/H = 1.5

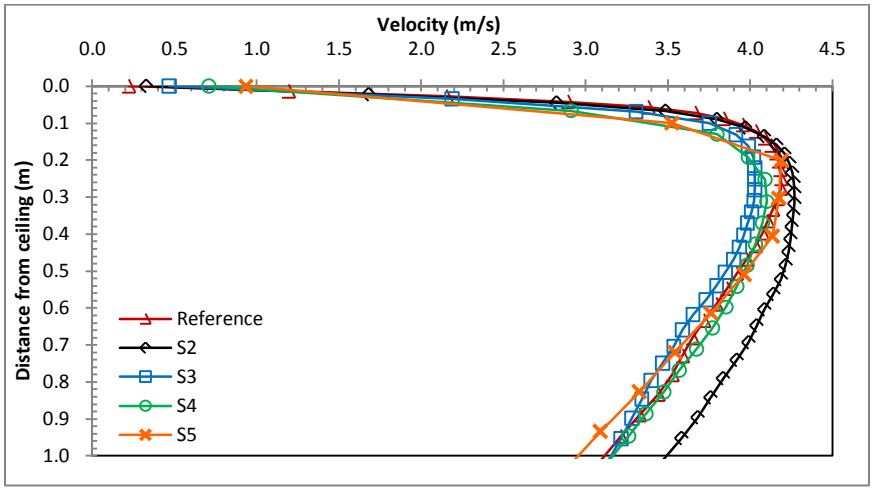

Figure B19: Velocity profile for simulations reference and S2 to S5 at r/H = 1.5

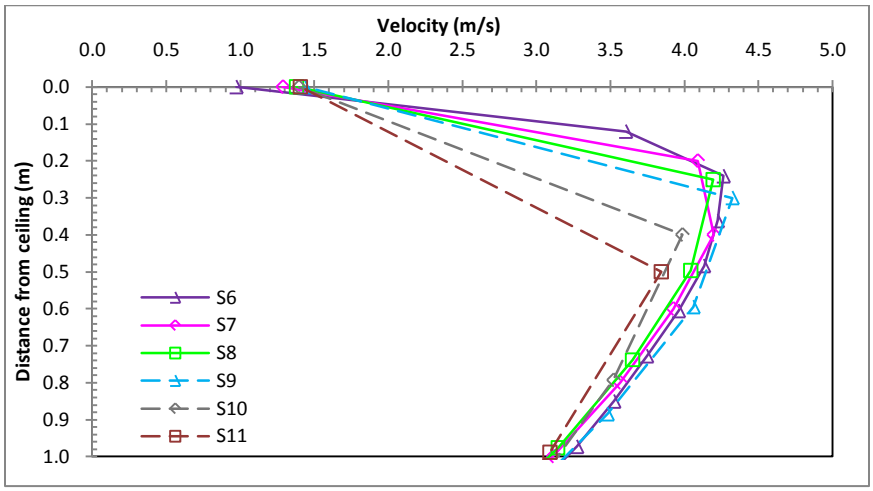

Figure B20: Velocity profile for simulations S6 to S11 at r/H = 1.5

APPENDIX C: Temperature and velocity profiles for simplified case of boundary layer flow

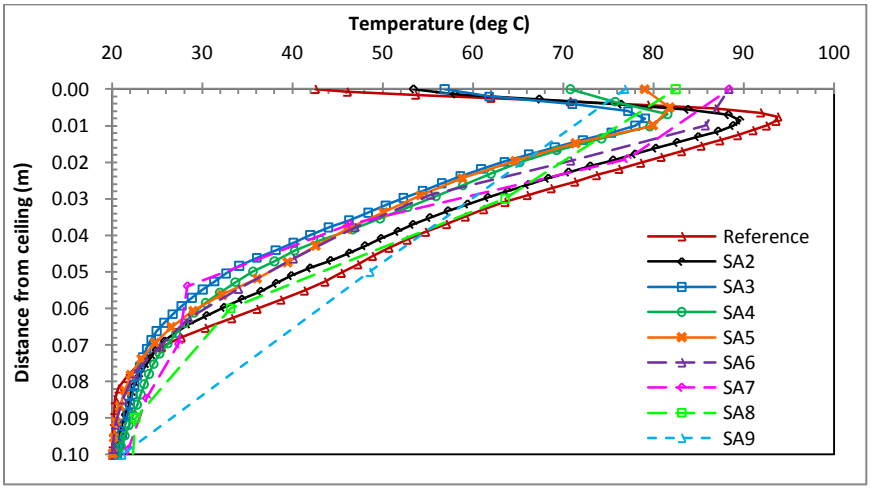

Figure C1: Temperature plot at 0.4m

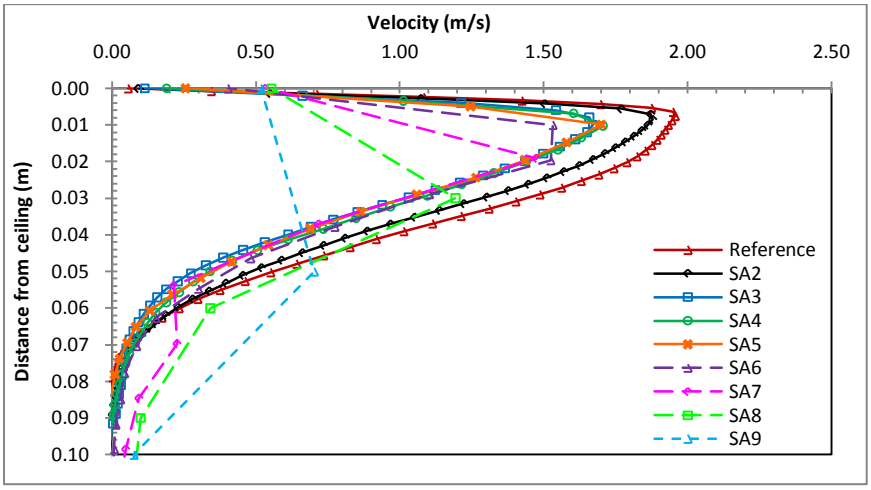

Figure C2: Velocity plot at 0.4m

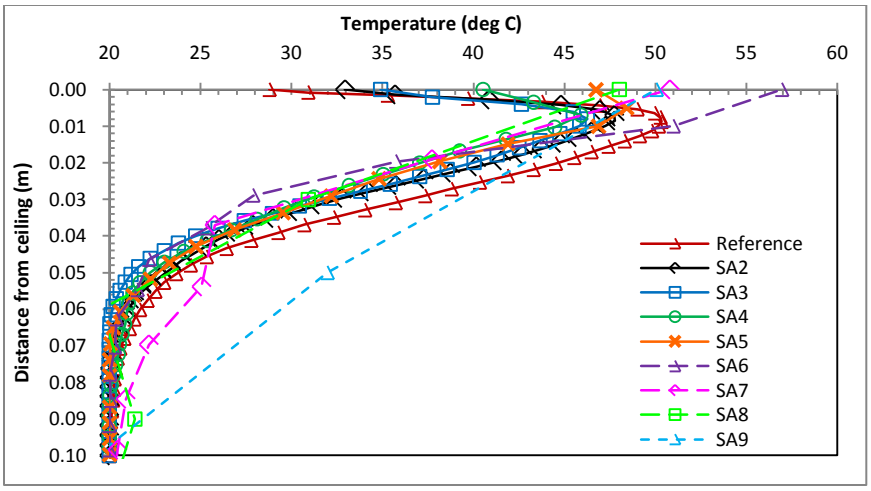

Figure C3: Temperature plot at 0.8m

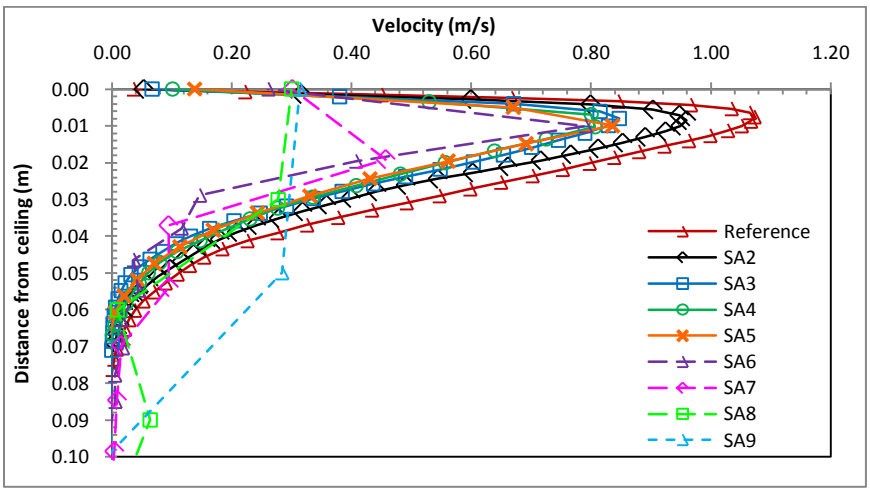

Figure C4: Velocity plot at 0.8m

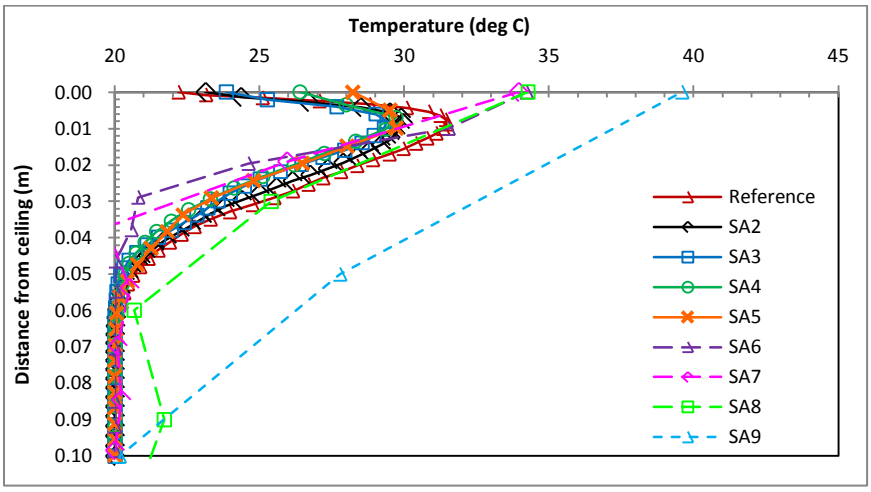

Figure C5: Temperature plot at 1.2m

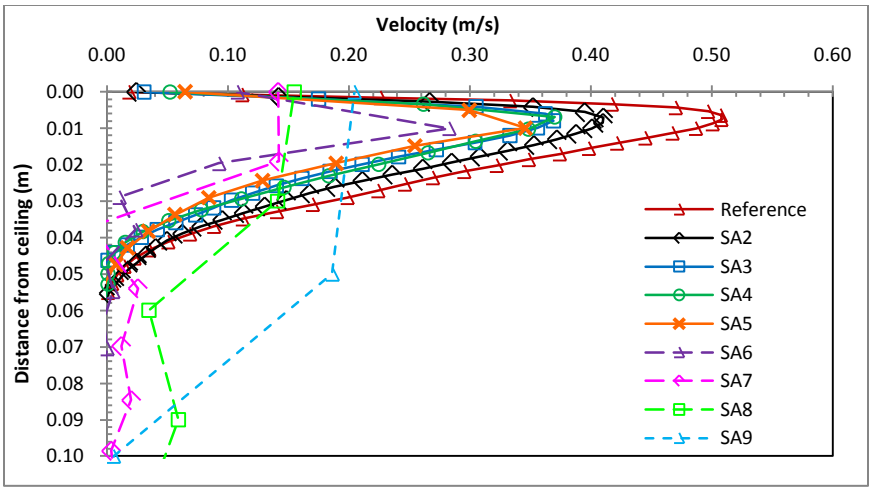

Figure C4: Velocity plot at 1.2m

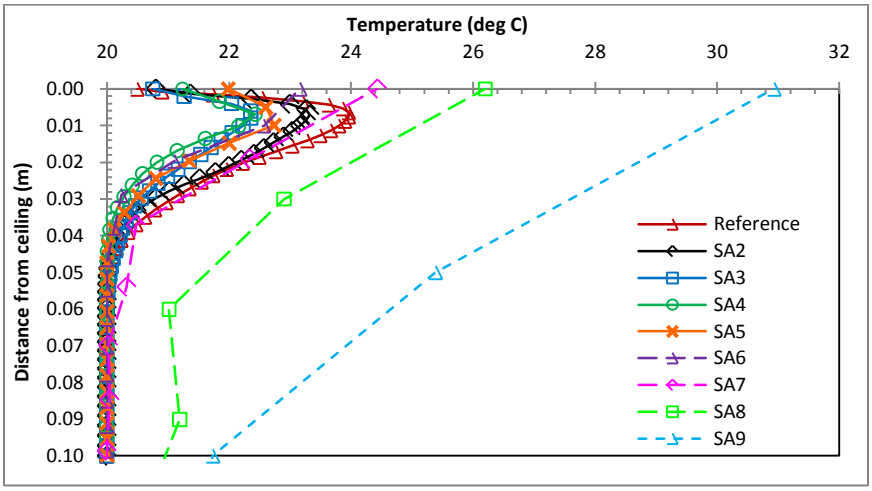

Figure C7: Temperature plot at 1.6m

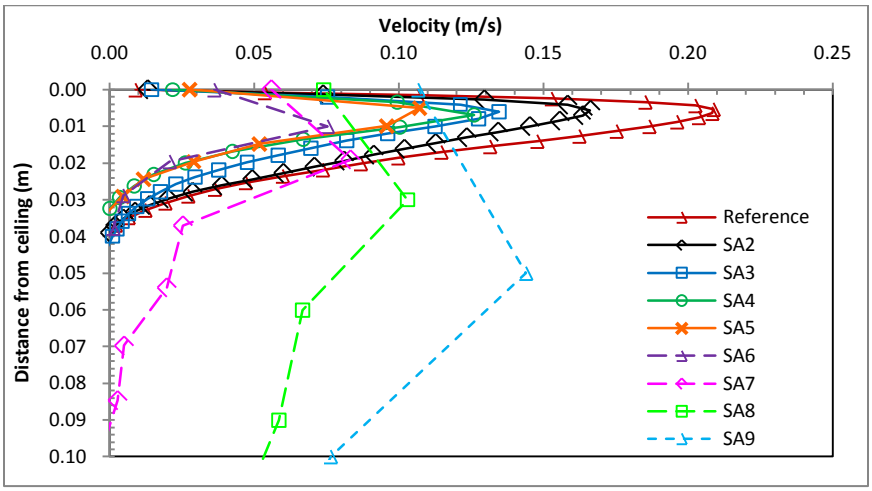

Figure C8: Velocity plot at 1.6m

APPENDIX D: Sample FDS input file for small-scale balcony spill plume

FDS INPUT FILE FOR SIMULATION SC6C

```
&HEAD CHID='SC6C',TITLE='25MM GRID, Q=10.3KW, h=0.5, DS=0, W=0.6' /
&MESH IJK=72,48,24, XB=-1.1,0.7,-0.6,0.6,0,0.6 /

&TIME TWFIN=900.0, SYNCHRONIZE=.TRUE. /
&MISC SUPPRESSION=.FALSE. /
&DUMP DT_PL3D=20., DT_DEVC=0.5, DT_HRR=0.5,
WRITE_XYZ=.TRUE.,
PLOT3D_QUANTITY(1)='U-VELOCITY',
PLOT3D_QUANTITY(2)='V-VELOCITY',
PLOT3D_QUANTITY(3)='W-VELOCITY',
PLOT3D_QUANTITY(4)='TEMPERATURE',
PLOT3D_QUANTITY(5)='MIXTURE_FRACTION' /

*****************************
CHARACTERISTICS OF BURNER FIRE
*****************************
&RADI RADIATIVE_FRACTION=0.25 /
&SURF ID              ='FIRE',
HRRPUA         =527.
COLOR          ='ORANGE'/
&OBST XB=-0.57,-0.43,-0.07,0.07,0,0.025, SURF_IDS='FIRE','INERT','INERT' /

*******************************
CHARACTERISIICS OF THE BOUNDARIES
*******************************
&VENT MB='XMIN' , SURF_ID='OPEN' /Open domain boundary
&VENT MB='XMAX' , SURF_ID='OPEN' /Open domain boundary
&VENT MB='YMIN' , SURF_ID='OPEN' /Open domain boundary
&VENT MB='YMAX' , SURF_ID='OPEN' /Open domain boundary
&VENT MB='ZMAX' , SURF_ID='OPEN' /Open domain boundary

*****************************
MATERIAL AND SURFACE PROPERTIES
*****************************
&MATL   ID                    =FIBER BOARD'
SPECIFIC_HEAT         = 2.090
DENSITY               = 229
CONDUCTIVITY          = 0.041/

&SURF   ID                    ='COMP WALL',
MATL_ID               =’FIBER BOARD',
COLOR                 ='GRAY',
THICKNESS             = 0.025 /FIRE COMPARTMENT WALLS

&SURF ID                      ='BALC WALL',
MATL_ID               =’FIBER BOARD',
COLOR                 ='SLATE GRAY',
THICKNESS             = 0.010 /COLLECTING HOOD WALLS

*******************
COMPARTMENT GEOMETRY
*******************
&OBST XB=-1.0,0.0,-0.525,-0.5,0.0,0.525,SURF_ID='COMP WALL',COLOR ='INVISIBLE' /FIRE
COMP SIDE WALL (FRT)
&OBST XB=-1.0,0.0,0.5,0.525,0.0,0.525,SURF_ID='COMP WALL' /FIRE COMP SIDE WALL (BACK)
&OBST XB=-1.0,-0.975,-0.525,0.525,0.0,0.525,SURF_ID='COMP WALL' /FIRE COMP BACK WALL
&OBST XB=-0.025,0.0,-0.5,-0.3,0.0,0.5,SURF_ID='COMP WALL' /FIRE COMP FRONT 1 (0.6 M
OPENING)
&OBST XB=-0.025,0.0,0.3,0.5,0.0,0.5,SURF_ID='COMP WALL' /FIRE COMP FRONT 2 (0.6 M
OPENING)
&OBST XB=-1.0,0.0,-0.525,0.525,0.5,0.525,SURF_ID='COMP WALL' /FIRE COMP CEILING
```

```
&OBST XB=0.0,0.3,-0.5,0.5,0.5,0.510,SURF_ID='BALC WALL' /0.3 M BALCONY
&OBST XB=0.0,0.3,-0.31,-0.3,0.3,0.5,SURF_ID='BALC WALL',COLOR ='INVISIBLE'
/CHANNELLING SCREEN 1(0.6 M OPENING)
&OBST XB=0.0,0.3,0.3,0.31,0.3,0.5,SURF_ID='BALC WALL' /CHANNELLING SCREEN 2(0.6 M
OPENING)

******************************
INSTRUMENTATION AND MEASUREMENTS
******************************
### MASS FLOW RATE THROUGH OPENING ###
&DEVC XB=0.0,0.0,-0.3,0.3,0.0,0.5, QUANTITY='MASS FLOW +', ID='MFR COMP+'/
&DEVC XB=0.0,0.0,-0.3,0.3,0.0,0.5, QUANTITY='MASS FLOW -', ID='MFR COMP-'/
&DEVC XB=0.3,0.3,-0.3,0.3,0.0,0.5, QUANTITY='MASS FLOW +', ID='MFR SPILL+'/
&DEVC XB=0.3,0.7,-0.5,0.5,0.5,0.5, QUANTITY='MASS FLOW +', ID='MFR ROTATED2+'/

### HEAT FLOW RATE THROUGH OPENING ###
&DEVC XB=0.0,0.0,-0.3,0.3,0.0,0.5, QUANTITY='HEAT FLOW +', ID='MFR COMP+'/
&DEVC XB=0.3,0.3,-0.3,0.3,0.0,0.5, QUANTITY='HEAT FLOW +', ID='MFR SPILL+'/
&DEVC XB=0.3,0.7,-0.5,0.5,0.5,0.5, QUANTITY='HEAT FLOW +', ID='MFR ROTATED2+'/

### TEMPERATURE ACROSS COMPARTMENT OPENING ###
&DEVC XYZ=0.0,-0.30,0.49,QUANTITY='TEMPERATURE',ID='COMP TEMP 0.49(X=-0.30) m' /TEMP
at Compartment Opening, 0.39 m from floor
&DEVC XYZ=0.0,-0.25,0.49,QUANTITY='TEMPERATURE',ID='COMP TEMP 0.49(X=-0.25) m' /TEMP
at Compartment Opening, 0.39 m from floor
&DEVC XYZ=0.0,-0.20,0.49,QUANTITY='TEMPERATURE',ID='COMP TEMP 0.49(X=-0.20) m' /TEMP
at Compartment Opening, 0.39 m from floor
&DEVC XYZ=0.0,-0.15,0.49,QUANTITY='TEMPERATURE',ID='COMP TEMP 0.49(X=-0.15) m' /TEMP
at Compartment Opening, 0.39 m from floor
&DEVC XYZ=0.0,-0.10,0.49,QUANTITY='TEMPERATURE',ID='COMP TEMP 0.49(X=-0.10) m' /TEMP
at Compartment Opening, 0.39 m from floor
&DEVC XYZ=0.0,-0.05,0.49,QUANTITY='TEMPERATURE',ID='COMP TEMP 0.49(X=-0.05) m' /TEMP
at Compartment Opening, 0.39 m from floor
&DEVC XYZ=0.0,0.05,0.49,QUANTITY='TEMPERATURE',ID='COMP TEMP 0.49(X=0.05) m' /TEMP at
Compartment Opening, 0.39 m from floor
&DEVC XYZ=0.0,0.10,0.49,QUANTITY='TEMPERATURE',ID='COMP TEMP 0.49(X=0.10) m' /TEMP at
Compartment Opening, 0.39 m from floor
&DEVC XYZ=0.0,0.15,0.49,QUANTITY='TEMPERATURE',ID='COMP TEMP 0.49(X=0.15) m' /TEMP at
Compartment Opening, 0.39 m from floor
&DEVC XYZ=0.0,0.20,0.49,QUANTITY='TEMPERATURE',ID='COMP TEMP 0.49(X=0.20) m' /TEMP at
Compartment Opening, 0.39 m from floor
&DEVC XYZ=0.0,0.25,0.49,QUANTITY='TEMPERATURE',ID='COMP TEMP 0.49(X=0.25) m' /TEMP at
Compartment Opening, 0.39 m from floor
&DEVC XYZ=0.0,0.30,0.49,QUANTITY='TEMPERATURE',ID='COMP TEMP 0.49(X=0.30) m' /TEMP at
Compartment Opening, 0.39 m from floor

### U-VELOCITY ACROSS COMPARTMENT OPENING ###
&DEVC XYZ=0.0,-0.30,0.49,QUANTITY='U-VELOCITY',ID='COMP U-VEL 0.49(X=-0.30) m' /U-VEL
at Compartment Opening, 0.39 m from floor
&DEVC XYZ=0.0,-0.25,0.49,QUANTITY='U-VELOCITY',ID='COMP U-VEL 0.49(X=-0.25) m' /U-VEL
at Compartment Opening, 0.39 m from floor
&DEVC XYZ=0.0,-0.20,0.49,QUANTITY='U-VELOCITY',ID='COMP U-VEL 0.49(X=-0.20) m' /U-VEL
at Compartment Opening, 0.39 m from floor
&DEVC XYZ=0.0,-0.15,0.49,QUANTITY='U-VELOCITY',ID='COMP U-VEL 0.49(X=-0.15) m' /U-VEL
at Compartment Opening, 0.39 m from floor
&DEVC XYZ=0.0,-0.10,0.49,QUANTITY='U-VELOCITY',ID='COMP U-VEL 0.49(X=-0.10) m' /U-VEL
at Compartment Opening, 0.39 m from floor
&DEVC XYZ=0.0,-0.05,0.49,QUANTITY='U-VELOCITY',ID='COMP U-VEL 0.49(X=-0.05) m' /U-VEL
at Compartment Opening, 0.39 m from floor
&DEVC XYZ=0.0,0.05,0.49,QUANTITY='U-VELOCITY',ID='COMP U-VEL 0.49(X=0.05) m' /U-VEL at
Compartment Opening, 0.39 m from floor
&DEVC XYZ=0.0,0.10,0.49,QUANTITY='U-VELOCITY',ID='COMP U-VEL 0.49(X=0.10) m' /U-VEL at
Compartment Opening, 0.39 m from floor
&DEVC XYZ=0.0,0.15,0.49,QUANTITY='U-VELOCITY',ID='COMP U-VEL 0.49(X=0.15) m' /U-VEL at
Compartment Opening, 0.39 m from floor
&DEVC XYZ=0.0,0.20,0.49,QUANTITY='U-VELOCITY',ID='COMP U-VEL 0.49(X=0.20) m' /U-VEL at
Compartment Opening, 0.39 m from floor
&DEVC XYZ=0.0,0.25,0.49,QUANTITY='U-VELOCITY',ID='COMP U-VEL 0.49(X=0.25) m' /U-VEL at
Compartment Opening, 0.39 m from floor
&DEVC XYZ=0.0,0.30,0.49,QUANTITY='U-VELOCITY',ID='COMP U-VEL 0.49(X=0.30) m' /U-VEL at
Compartment Opening, 0.39 m from floor
```

```
### TEMPERATURE ACROSS SPILL EDGE ###
&DEVC XYZ=0.3,-0.30,0.49,QUANTITY='TEMPERATURE',ID='BALC TEMP 0.49(X=-0.30) m' /TEMP
at Spill Edge, 0.49 m from floor
&DEVC XYZ=0.3,-0.25,0.49,QUANTITY='TEMPERATURE',ID='BALC TEMP 0.49(X=-0.25) m' /TEMP
at Spill Edge, 0.49 m from floor
&DEVC XYZ=0.3,-0.20,0.49,QUANTITY='TEMPERATURE',ID='BALC TEMP 0.49(X=-0.20) m' /TEMP
at Spill Edge, 0.49 m from floor
&DEVC XYZ=0.3,-0.15,0.49,QUANTITY='TEMPERATURE',ID='BALC TEMP 0.49(X=-0.15) m' /TEMP
at Spill Edge, 0.49 m from floor
&DEVC XYZ=0.3,-0.10,0.49,QUANTITY='TEMPERATURE',ID='BALC TEMP 0.49(X=-0.10) m' /TEMP
at Spill Edge, 0.49 m from floor
&DEVC XYZ=0.3,-0.05,0.49,QUANTITY='TEMPERATURE',ID='BALC TEMP 0.49(X=-0.05) m' /TEMP
at Spill Edge, 0.49 m from floor
&DEVC XYZ=0.3,0.05,0.49,QUANTITY='TEMPERATURE',ID='BALC TEMP 0.49(X=0.05) m' /TEMP at
Spill Edge, 0.49 m from floor
&DEVC XYZ=0.3,0.10,0.49,QUANTITY='TEMPERATURE',ID='BALC TEMP 0.49(X=0.10) m' /TEMP at
Spill Edge, 0.49 m from floor
&DEVC XYZ=0.3,0.15,0.49,QUANTITY='TEMPERATURE',ID='BALC TEMP 0.49(X=0.15) m' /TEMP at
Spill Edge, 0.49 m from floor
&DEVC XYZ=0.3,0.20,0.49,QUANTITY='TEMPERATURE',ID='BALC TEMP 0.49(X=0.20) m' /TEMP at
Spill Edge, 0.49 m from floor
&DEVC XYZ=0.3,0.25,0.49,QUANTITY='TEMPERATURE',ID='BALC TEMP 0.49(X=0.25) m' /TEMP at
Spill Edge, 0.49 m from floor
&DEVC XYZ=0.3,0.30,0.49,QUANTITY='TEMPERATURE',ID='BALC TEMP 0.49(X=0.30) m' /TEMP at
Spill Edge, 0.49 m from floor

### U-VELOCITY ACROSS SPILL EDGE ###
&DEVC XYZ=0.3,-0.30,0.49,QUANTITY='U-VELOCITY',ID='BALC U-VEL 0.49(X=-0.30) m' /U-VEL
at Spill Edge, 0.49 m from floor
&DEVC XYZ=0.3,-0.25,0.49,QUANTITY='U-VELOCITY',ID='BALC U-VEL 0.49(X=-0.25) m' /U-VEL
at Spill Edge, 0.49 m from floor
&DEVC XYZ=0.3,-0.20,0.49,QUANTITY='U-VELOCITY',ID='BALC U-VEL 0.49(X=-0.20) m' /U-VEL
at Spill Edge, 0.49 m from floor
&DEVC XYZ=0.3,-0.15,0.49,QUANTITY='U-VELOCITY',ID='BALC U-VEL 0.49(X=-0.15) m' /U-VEL
at Spill Edge, 0.49 m from floor
&DEVC XYZ=0.3,-0.10,0.49,QUANTITY='U-VELOCITY',ID='BALC U-VEL 0.49(X=-0.10) m' /U-VEL
at Spill Edge, 0.49 m from floor
&DEVC XYZ=0.3,-0.05,0.49,QUANTITY='U-VELOCITY',ID='BALC U-VEL 0.49(X=-0.05) m' /U-VEL
at Spill Edge, 0.49 m from floor
&DEVC XYZ=0.3,0.05,0.49,QUANTITY='U-VELOCITY',ID='BALC U-VEL 0.49(X=0.05) m' /U-VEL at
Spill Edge, 0.49 m from floor
&DEVC XYZ=0.3,0.10,0.49,QUANTITY='U-VELOCITY',ID='BALC U-VEL 0.49(X=0.10) m' /U-VEL at
Spill Edge, 0.49 m from floor
&DEVC XYZ=0.3,0.15,0.49,QUANTITY='U-VELOCITY',ID='BALC U-VEL 0.49(X=0.15) m' /U-VEL at
Spill Edge, 0.49 m from floor
&DEVC XYZ=0.3,0.20,0.49,QUANTITY='U-VELOCITY',ID='BALC U-VEL 0.49(X=0.20) m' /U-VEL at
Spill Edge, 0.49 m from floor
&DEVC XYZ=0.3,0.25,0.49,QUANTITY='U-VELOCITY',ID='BALC U-VEL 0.49(X=0.25) m' /U-VEL at
Spill Edge, 0.49 m from floor
&DEVC XYZ=0.3,0.30,0.49,QUANTITY='U-VELOCITY',ID='BALC U-VEL 0.49(X=0.30) m' /U-VEL at
Spill Edge, 0.49 m from floor

#### TEMPERATURE AT CENTER OF COMPARTMENT OPENING ####
&DEVC XYZ=0.0,0.0,0.49,QUANTITY='TEMPERATURE',ID='COMP TEMP 0.49 m' /TEMP at Center of
Compartment Opening, 0.49 m from floor
&DEVC XYZ=0.0,0.0,0.48,QUANTITY='TEMPERATURE',ID='COMP TEMP 0.48 m' /TEMP at Center of
Compartment Opening, 0.48 m from floor
&DEVC XYZ=0.0,0.0,0.47,QUANTITY='TEMPERATURE',ID='COMP TEMP 0.47 m' /TEMP at Center of
Compartment Opening, 0.47 m from floor
&DEVC XYZ=0.0,0.0,0.46,QUANTITY='TEMPERATURE',ID='COMP TEMP 0.46 m' /TEMP at Center of
Compartment Opening, 0.46 m from floor
&DEVC XYZ=0.0,0.0,0.45,QUANTITY='TEMPERATURE',ID='COMP TEMP 0.45 m' /TEMP at Center of
Compartment Opening, 0.45 m from floor
&DEVC XYZ=0.0,0.0,0.44,QUANTITY='TEMPERATURE',ID='COMP TEMP 0.44 m' /TEMP at Center of
Compartment Opening, 0.44 m from floor
&DEVC XYZ=0.0,0.0,0.43,QUANTITY='TEMPERATURE',ID='COMP TEMP 0.43 m' /TEMP at Center of
Compartment Opening, 0.43 m from floor
&DEVC XYZ=0.0,0.0,0.42,QUANTITY='TEMPERATURE',ID='COMP TEMP 0.42 m' /TEMP at Center of
Compartment Opening, 0.42 m from floor
```

```
&DEVC XYZ=0.0,0.0,0.41,QUANTITY='TEMPERATURE',ID='COMP TEMP 0.41 m' /TEMP at Center of
Compartment Opening, 0.41 m from floor
&DEVC XYZ=0.0,0.0,0.40,QUANTITY='TEMPERATURE',ID='COMP TEMP 0.40 m' /TEMP at Center of
Compartment Opening, 0.40 m from floor
&DEVC XYZ=0.0,0.0,0.39,QUANTITY='TEMPERATURE',ID='COMP TEMP 0.39 m' /TEMP at Center of
Compartment Opening, 0.39 m from floor
&DEVC XYZ=0.0,0.0,0.38,QUANTITY='TEMPERATURE',ID='COMP TEMP 0.38 m' /TEMP at Center of
Compartment Opening, 0.38 m from floor
&DEVC XYZ=0.0,0.0,0.37,QUANTITY='TEMPERATURE',ID='COMP TEMP 0.37 m' /TEMP at Center of
Compartment Opening, 0.37 m from floor
&DEVC XYZ=0.0,0.0,0.36,QUANTITY='TEMPERATURE',ID='COMP TEMP 0.36 m' /TEMP at Center of
Compartment Opening, 0.36 m from floor
&DEVC XYZ=0.0,0.0,0.35,QUANTITY='TEMPERATURE',ID='COMP TEMP 0.35 m' /TEMP at Center of
Compartment Opening, 0.35 m from floor
&DEVC XYZ=0.0,0.0,0.34,QUANTITY='TEMPERATURE',ID='COMP TEMP 0.34 m' /TEMP at Center of
Compartment Opening, 0.34 m from floor
&DEVC XYZ=0.0,0.0,0.33,QUANTITY='TEMPERATURE',ID='COMP TEMP 0.33 m' /TEMP at Center of
Compartment Opening, 0.33 m from floor
&DEVC XYZ=0.0,0.0,0.32,QUANTITY='TEMPERATURE',ID='COMP TEMP 0.32 m' /TEMP at Center of
Compartment Opening, 0.32 m from floor
&DEVC XYZ=0.0,0.0,0.31,QUANTITY='TEMPERATURE',ID='COMP TEMP 0.31 m' /TEMP at Center of
Compartment Opening, 0.31 m from floor
&DEVC XYZ=0.0,0.0,0.30,QUANTITY='TEMPERATURE',ID='COMP TEMP 0.30 m' /TEMP at Center of
Compartment Opening, 0.30 m from floor
&DEVC XYZ=0.0,0.0,0.29,QUANTITY='TEMPERATURE',ID='COMP TEMP 0.29 m' /TEMP at Center of
Compartment Opening, 0.29 m from floor
&DEVC XYZ=0.0,0.0,0.28,QUANTITY='TEMPERATURE',ID='COMP TEMP 0.28 m' /TEMP at Center of
Compartment Opening, 0.28 m from floor
&DEVC XYZ=0.0,0.0,0.27,QUANTITY='TEMPERATURE',ID='COMP TEMP 0.27 m' /TEMP at Center of
Compartment Opening, 0.27 m from floor
&DEVC XYZ=0.0,0.0,0.26,QUANTITY='TEMPERATURE',ID='COMP TEMP 0.26 m' /TEMP at Center of
Compartment Opening, 0.26 m from floor
&DEVC XYZ=0.0,0.0,0.25,QUANTITY='TEMPERATURE',ID='COMP TEMP 0.25 m' /TEMP at Center of
Compartment Opening, 0.25 m from floor
&DEVC XYZ=0.0,0.0,0.24,QUANTITY='TEMPERATURE',ID='COMP TEMP 0.24 m' /TEMP at Center of
Compartment Opening, 0.24 m from floor
&DEVC XYZ=0.0,0.0,0.23,QUANTITY='TEMPERATURE',ID='COMP TEMP 0.23 m' /TEMP at Center of
Compartment Opening, 0.23 m from floor
&DEVC XYZ=0.0,0.0,0.22,QUANTITY='TEMPERATURE',ID='COMP TEMP 0.22 m' /TEMP at Center of
Compartment Opening, 0.22 m from floor
&DEVC XYZ=0.0,0.0,0.21,QUANTITY='TEMPERATURE',ID='COMP TEMP 0.21 m' /TEMP at Center of
Compartment Opening, 0.21 m from floor
&DEVC XYZ=0.0,0.0,0.20,QUANTITY='TEMPERATURE',ID='COMP TEMP 0.20 m' /TEMP at Center of
Compartment Opening, 0.20 m from floor
&DEVC XYZ=0.0,0.0,0.11,QUANTITY='TEMPERATURE',ID='COMP TEMP 0.15 m' /TEMP at Center of
Compartment Opening, 0.15 m from floor
&DEVC XYZ=0.0,0.0,0.10,QUANTITY='TEMPERATURE',ID='COMP TEMP 0.10 m' /TEMP at Center of
Compartment Opening, 0.10 m from floor
&DEVC XYZ=0.0,0.0,0.05,QUANTITY='TEMPERATURE',ID='COMP TEMP 0.05 m' /TEMP at Center of
Compartment Opening, 0.05 m from floor

#### U-VELOCITY AT CENTER OF COMPARTMENT OPENING ####
&DEVC XYZ=0.0,0.0,0.49,QUANTITY='U-VELOCITY',ID='COMP U-VEL 0.49 m' /U-VEL at Center
of Compartment Opening, 0.49 m from floor
&DEVC XYZ=0.0,0.0,0.48,QUANTITY='U-VELOCITY',ID='COMP U-VEL 0.48 m' /U-VEL at Center
of Compartment Opening, 0.48 m from floor
&DEVC XYZ=0.0,0.0,0.47,QUANTITY='U-VELOCITY',ID='COMP U-VEL 0.47 m' /U-VEL at Center
of Compartment Opening, 0.47 m from floor
&DEVC XYZ=0.0,0.0,0.46,QUANTITY='U-VELOCITY',ID='COMP U-VEL 0.46 m' /U-VEL at Center
of Compartment Opening, 0.46 m from floor
&DEVC XYZ=0.0,0.0,0.45,QUANTITY='U-VELOCITY',ID='COMP U-VEL 0.45 m' /U-VEL at Center
of Compartment Opening, 0.45 m from floor
&DEVC XYZ=0.0,0.0,0.44,QUANTITY='U-VELOCITY',ID='COMP U-VEL 0.44 m' /U-VEL at Center
of Compartment Opening, 0.44 m from floor
&DEVC XYZ=0.0,0.0,0.43,QUANTITY='U-VELOCITY',ID='COMP U-VEL 0.43 m' /U-VEL at Center
of Compartment Opening, 0.43 m from floor
&DEVC XYZ=0.0,0.0,0.42,QUANTITY='U-VELOCITY',ID='COMP U-VEL 0.32 m' /U-VEL at Center
of Compartment Opening, 0.42 m from floor
&DEVC XYZ=0.0,0.0,0.41,QUANTITY='U-VELOCITY',ID='COMP U-VEL 0.41 m' /U-VEL at Center
of Compartment Opening, 0.41 m from floor
```

```
&DEVC XYZ=0.0,0.0,0.40,QUANTITY='U-VELOCITY',ID='COMP U-VEL 0.40 m' /U-VEL at Center
of Compartment Opening, 0.40 m from floor
&DEVC XYZ=0.0,0.0,0.39,QUANTITY='U-VELOCITY',ID='COMP U-VEL 0.39 m' /U-VEL at Center
of Compartment Opening, 0.39 m from floor
&DEVC XYZ=0.0,0.0,0.38,QUANTITY='U-VELOCITY',ID='COMP U-VEL 0.38 m' /U-VEL at Center
of Compartment Opening, 0.38 m from floor
&DEVC XYZ=0.0,0.0,0.37,QUANTITY='U-VELOCITY',ID='COMP U-VEL 0.37 m' /U-VEL at Center
of Compartment Opening, 0.37 m from floor
&DEVC XYZ=0.0,0.0,0.36,QUANTITY='U-VELOCITY',ID='COMP U-VEL 0.36 m' /U-VEL at Center
of Compartment Opening, 0.36 m from floor
&DEVC XYZ=0.0,0.0,0.35,QUANTITY='U-VELOCITY',ID='COMP U-VEL 0.35 m' /U-VEL at Center
of Compartment Opening, 0.35 m from floor
&DEVC XYZ=0.0,0.0,0.34,QUANTITY='U-VELOCITY',ID='COMP U-VEL 0.34 m' /U-VEL at Center
of Compartment Opening, 0.34 m from floor
&DEVC XYZ=0.0,0.0,0.33,QUANTITY='U-VELOCITY',ID='COMP U-VEL 0.33 m' /U-VEL at Center
of Compartment Opening, 0.33 m from floor
&DEVC XYZ=0.0,0.0,0.32,QUANTITY='U-VELOCITY',ID='COMP U-VEL 0.32 m' /U-VEL at Center
of Compartment Opening, 0.32 m from floor
&DEVC XYZ=0.0,0.0,0.31,QUANTITY='U-VELOCITY',ID='COMP U-VEL 0.31 m' /U-VEL at Center
of Compartment Opening, 0.31 m from floor
&DEVC XYZ=0.0,0.0,0.30,QUANTITY='U-VELOCITY',ID='COMP U-VEL 0.30 m' /U-VEL at Center
of Compartment Opening, 0.30 m from floor
&DEVC XYZ=0.0,0.0,0.29,QUANTITY='U-VELOCITY',ID='COMP U-VEL 0.29 m' /U-VEL at Center
of Compartment Opening, 0.29 m from floor
&DEVC XYZ=0.0,0.0,0.28,QUANTITY='U-VELOCITY',ID='COMP U-VEL 0.28 m' /U-VEL at Center
of Compartment Opening, 0.28 m from floor
&DEVC XYZ=0.0,0.0,0.27,QUANTITY='U-VELOCITY',ID='COMP U-VEL 0.27 m' /U-VEL at Center
of Compartment Opening, 0.27 m from floor
&DEVC XYZ=0.0,0.0,0.26,QUANTITY='U-VELOCITY',ID='COMP U-VEL 0.26 m' /U-VEL at Center
of Compartment Opening, 0.26 m from floor
&DEVC XYZ=0.0,0.0,0.25,QUANTITY='U-VELOCITY',ID='COMP U-VEL 0.25 m' /U-VEL at Center
of Compartment Opening, 0.25 m from floor
&DEVC XYZ=0.0,0.0,0.24,QUANTITY='U-VELOCITY',ID='COMP U-VEL 0.24 m' /U-VEL at Center
of Compartment Opening, 0.24 m from floor
&DEVC XYZ=0.0,0.0,0.23,QUANTITY='U-VELOCITY',ID='COMP U-VEL 0.23 m' /U-VEL at Center
of Compartment Opening, 0.23 m from floor
&DEVC XYZ=0.0,0.0,0.22,QUANTITY='U-VELOCITY',ID='COMP U-VEL 0.22 m' /U-VEL at Center
of Compartment Opening, 0.22 m from floor
&DEVC XYZ=0.0,0.0,0.21,QUANTITY='U-VELOCITY',ID='COMP U-VEL 0.21 m' /U-VEL at Center
of Compartment Opening, 0.21 m from floor
&DEVC XYZ=0.0,0.0,0.20,QUANTITY='U-VELOCITY',ID='COMP U-VEL 0.20 m' /U-VEL at Center
of Compartment Opening, 0.20 m from floor
&DEVC XYZ=0.0,0.0,0.11,QUANTITY='U-VELOCITY',ID='COMP U-VEL 0.15 m' /U-VEL at Center
of Compartment Opening, 0.15 m from floor
&DEVC XYZ=0.0,0.0,0.10,QUANTITY='U-VELOCITY',ID='COMP U-VEL 0.10 m' /U-VEL at Center
of Compartment Opening, 0.10 m from floor
&DEVC XYZ=0.0,0.0,0.05,QUANTITY='U-VELOCITY',ID='COMP U-VEL 0.05 m' /U-VEL at Center
of Compartment Opening, 0.05 m from floor

#### TEMPERATURE AT CENTER OF SPILL EDGE ####
&DEVC XYZ=0.3,0.0,0.49,QUANTITY='TEMPERATURE',ID='BALC TEMP 0.49 m' /TEMP at Center of
Spill Edge, 0.49 m from floor
&DEVC XYZ=0.3,0.0,0.48,QUANTITY='TEMPERATURE',ID='BALC TEMP 0.48 m' /TEMP at Center of
Spill Edge, 0.48 m from floor
&DEVC XYZ=0.3,0.0,0.47,QUANTITY='TEMPERATURE',ID='BALC TEMP 0.47 m' /TEMP at Center of
Spill Edge, 0.47 m from floor
&DEVC XYZ=0.3,0.0,0.46,QUANTITY='TEMPERATURE',ID='BALC TEMP 0.46 m' /TEMP at Center of
Spill Edge, 0.46 m from floor
&DEVC XYZ=0.3,0.0,0.45,QUANTITY='TEMPERATURE',ID='BALC TEMP 0.45 m' /TEMP at Center of
Spill Edge, 0.45 m from floor
&DEVC XYZ=0.3,0.0,0.44,QUANTITY='TEMPERATURE',ID='BALC TEMP 0.44 m' /TEMP at Center of
Spill Edge, 0.44 m from floor
&DEVC XYZ=0.3,0.0,0.43,QUANTITY='TEMPERATURE',ID='BALC TEMP 0.43 m' /TEMP at Center of
Spill Edge, 0.43 m from floor
&DEVC XYZ=0.3,0.0,0.42,QUANTITY='TEMPERATURE',ID='BALC TEMP 0.42 m' /TEMP at Center of
Spill Edge, 0.42 m from floor
&DEVC XYZ=0.3,0.0,0.41,QUANTITY='TEMPERATURE',ID='BALC TEMP 0.41 m' /TEMP at Center of
Spill Edge, 0.41 m from floor
&DEVC XYZ=0.3,0.0,0.40,QUANTITY='TEMPERATURE',ID='BALC TEMP 0.40 m' /TEMP at Center of
Spill Edge, 0.40 m from floor
```

```
&DEVC XYZ=0.3,0.0,0.39,QUANTITY='TEMPERATURE',ID='BALC TEMP 0.39 m' /TEMP at Center of
Spill Edge, 0.39 m from floor
&DEVC XYZ=0.3,0.0,0.38,QUANTITY='TEMPERATURE',ID='BALC TEMP 0.38 m' /TEMP at Center of
Spill Edge, 0.38 m from floor
&DEVC XYZ=0.3,0.0,0.37,QUANTITY='TEMPERATURE',ID='BALC TEMP 0.37 m' /TEMP at Center of
Spill Edge, 0.37 m from floor
&DEVC XYZ=0.3,0.0,0.36,QUANTITY='TEMPERATURE',ID='BALC TEMP 0.36 m' /TEMP at Center of
Spill Edge, 0.36 m from floor
&DEVC XYZ=0.3,0.0,0.35,QUANTITY='TEMPERATURE',ID='BALC TEMP 0.35 m' /TEMP at Center of
Spill Edge, 0.35 m from floor
&DEVC XYZ=0.3,0.0,0.34,QUANTITY='TEMPERATURE',ID='BALC TEMP 0.34 m' /TEMP at Center of
Spill Edge, 0.34 m from floor
&DEVC XYZ=0.3,0.0,0.33,QUANTITY='TEMPERATURE',ID='BALC TEMP 0.33 m' /TEMP at Center of
Spill Edge, 0.33 m from floor
&DEVC XYZ=0.3,0.0,0.32,QUANTITY='TEMPERATURE',ID='BALC TEMP 0.32 m' /TEMP at Center of
Spill Edge, 0.32 m from floor
&DEVC XYZ=0.3,0.0,0.31,QUANTITY='TEMPERATURE',ID='BALC TEMP 0.31 m' /TEMP at Center of
Spill Edge, 0.31 m from floor
&DEVC XYZ=0.3,0.0,0.30,QUANTITY='TEMPERATURE',ID='BALC TEMP 0.30 m' /TEMP at Center of
Spill Edge, 0.30 m from floor
&DEVC XYZ=0.3,0.0,0.28,QUANTITY='TEMPERATURE',ID='BALC TEMP 0.28 m' /TEMP at Center of
Spill Edge, 0.28 m from floor
&DEVC XYZ=0.3,0.0,0.26,QUANTITY='TEMPERATURE',ID='BALC TEMP 0.26 m' /TEMP at Center of
Spill Edge, 0.26 m from floor
&DEVC XYZ=0.3,0.0,0.24,QUANTITY='TEMPERATURE',ID='BALC TEMP 0.24 m' /TEMP at Center of
Spill Edge, 0.24 m from floor
&DEVC XYZ=0.3,0.0,0.22,QUANTITY='TEMPERATURE',ID='BALC TEMP 0.22 m' /TEMP at Center of
Spill Edge, 0.22 m from floor
&DEVC XYZ=0.3,0.0,0.20,QUANTITY='TEMPERATURE',ID='BALC TEMP 0.20 m' /TEMP at Center of
Spill Edge, 0.20 m from floor
&DEVC XYZ=0.3,0.0,0.11,QUANTITY='TEMPERATURE',ID='BALC TEMP 0.15 m' /TEMP at Center of
Spill Edge, 0.15 m from floor
&DEVC XYZ=0.3,0.0,0.10,QUANTITY='TEMPERATURE',ID='BALC TEMP 0.10 m' /TEMP at Center of
Spill Edge, 0.10 m from floor
&DEVC XYZ=0.3,0.0,0.05,QUANTITY='TEMPERATURE',ID='BALC TEMP 0.05 m' /TEMP at Center of
Spill Edge, 0.05 m from floor

#### U-VELOCITY AT CENTER OF SPILL EDGE ####
&DEVC XYZ=0.3,0.0,0.49,QUANTITY='U-VELOCITY',ID='BALC U-VEL 0.49 m' /U-VEL at Center
of Spill Edge, 0.49 m from floor
&DEVC XYZ=0.3,0.0,0.48,QUANTITY='U-VELOCITY',ID='BALC U-VEL 0.48 m' /U-VEL at Center
of Spill Edge, 0.48 m from floor
&DEVC XYZ=0.3,0.0,0.47,QUANTITY='U-VELOCITY',ID='BALC U-VEL 0.47 m' /U-VEL at Center
of Spill Edge, 0.47 m from floor
&DEVC XYZ=0.3,0.0,0.46,QUANTITY='U-VELOCITY',ID='BALC U-VEL 0.46 m' /U-VEL at Center
of Spill Edge, 0.46 m from floor
&DEVC XYZ=0.3,0.0,0.45,QUANTITY='U-VELOCITY',ID='BALC U-VEL 0.45 m' /U-VEL at Center
of Spill Edge, 0.45 m from floor
&DEVC XYZ=0.3,0.0,0.44,QUANTITY='U-VELOCITY',ID='BALC U-VEL 0.44 m' /U-VEL at Center
of Spill Edge, 0.44 m from floor
&DEVC XYZ=0.3,0.0,0.43,QUANTITY='U-VELOCITY',ID='BALC U-VEL 0.43 m' /U-VEL at Center
of Spill Edge, 0.43 m from floor
&DEVC XYZ=0.3,0.0,0.42,QUANTITY='U-VELOCITY',ID='BALC U-VEL 0.42 m' /U-VEL at Center
of Spill Edge, 0.42 m from floor
&DEVC XYZ=0.3,0.0,0.41,QUANTITY='U-VELOCITY',ID='BALC U-VEL 0.41 m' /U-VEL at Center
of Spill Edge, 0.41 m from floor
&DEVC XYZ=0.3,0.0,0.40,QUANTITY='U-VELOCITY',ID='BALC U-VEL 0.40 m' /U-VEL at Center
of Spill Edge, 0.40 m from floor
&DEVC XYZ=0.3,0.0,0.39,QUANTITY='U-VELOCITY',ID='BALC U-VEL 0.39 m' /U-VEL at Center
of Spill Edge, 0.39 m from floor
&DEVC XYZ=0.3,0.0,0.38,QUANTITY='U-VELOCITY',ID='BALC U-VEL 0.38 m' /U-VEL at Center
of Spill Edge, 0.38 m from floor
&DEVC XYZ=0.3,0.0,0.37,QUANTITY='U-VELOCITY',ID='BALC U-VEL 0.37 m' /U-VEL at Center
of Spill Edge, 0.37 m from floor
&DEVC XYZ=0.3,0.0,0.36,QUANTITY='U-VELOCITY',ID='BALC U-VEL 0.36 m' /U-VEL at Center
of Spill Edge, 0.36 m from floor
&DEVC XYZ=0.3,0.0,0.35,QUANTITY='U-VELOCITY',ID='BALC U-VEL 0.35 m' /U-VEL at Center
of Spill Edge, 0.35 m from floor
&DEVC XYZ=0.3,0.0,0.34,QUANTITY='U-VELOCITY',ID='BALC U-VEL 0.34 m' /U-VEL at Center
of Spill Edge, 0.34 m from floor
```

```
&DEVC XYZ=0.3,0.0,0.33,QUANTITY='U-VELOCITY',ID='BALC U-VEL 0.33 m' /U-VEL at Center
of Spill Edge, 0.33 m from floor
&DEVC XYZ=0.3,0.0,0.32,QUANTITY='U-VELOCITY',ID='BALC U-VEL 0.32 m' /U-VEL at Center
of Spill Edge, 0.32 m from floor
&DEVC XYZ=0.3,0.0,0.31,QUANTITY='U-VELOCITY',ID='BALC U-VEL 0.31 m' /U-VEL at Center
of Spill Edge, 0.31 m from floor
&DEVC XYZ=0.3,0.0,0.30,QUANTITY='U-VELOCITY',ID='BALC U-VEL 0.30 m' /U-VEL at Center
of Spill Edge, 0.30 m from floor
&DEVC XYZ=0.3,0.0,0.28,QUANTITY='U-VELOCITY',ID='BALC U-VEL 0.28 m' /U-VEL at Center
of Spill Edge, 0.28 m from floor
&DEVC XYZ=0.3,0.0,0.26,QUANTITY='U-VELOCITY',ID='BALC U-VEL 0.26 m' /U-VEL at Center
of Spill Edge, 0.26 m from floor
&DEVC XYZ=0.3,0.0,0.24,QUANTITY='U-VELOCITY',ID='BALC U-VEL 0.24 m' /U-VEL at Center
of Spill Edge, 0.24 m from floor
&DEVC XYZ=0.3,0.0,0.22,QUANTITY='U-VELOCITY',ID='BALC U-VEL 0.22 m' /U-VEL at Center
of Spill Edge, 0.22 m from floor
&DEVC XYZ=0.3,0.0,0.20,QUANTITY='U-VELOCITY',ID='BALC U-VEL 0.20 m' /U-VEL at Center
of Spill Edge, 0.20 m from floor
&DEVC XYZ=0.3,0.0,0.11,QUANTITY='U-VELOCITY',ID='BALC U-VEL 0.15 m' /U-VEL at Center
of Spill Edge, 0.15 m from floor
&DEVC XYZ=0.3,0.0,0.10,QUANTITY='U-VELOCITY',ID='BALC U-VEL 0.10 m' /U-VEL at Center
of Spill Edge, 0.10 m from floor
&DEVC XYZ=0.3,0.0,0.05,QUANTITY='U-VELOCITY',ID='BALC U-VEL 0.05 m' /U-VEL at Center
of Spill Edge, 0.05 m from floor

&SLCF PBY= 0.0, QUANTITY='TEMPERATURE', /
&SLCF PBY= 0.0, QUANTITY='U-VELOCITY', VECTOR=.TRUE. /
&SLCF PBX= 0.0, QUANTITY='TEMPERATURE', / TEMPERATURE at Compartment Opening
&SLCF PBX= 0.0, QUANTITY='U-VELOCITY', VECTOR=.TRUE. / U-VEL at Compartment Opening
&SLCF PBX= 0.3, QUANTITY='TEMPERATURE', / TEMPERATURE at Spill Edge
&SLCF PBX= 0.3, QUANTITY='U-VELOCITY', VECTOR=.TRUE. / U-VEL at Spill Edge
&SLCF PBZ= 0.5, QUANTITY='TEMPERATURE', / TEMPERATURE at Spill Edge
&SLCF PBZ= 0.5, QUANTITY='U-VELOCITY', VECTOR=.TRUE. / U-VEL at Spill Edge

&TAIL
```

APPENDIX E: Sample FDS input file for full-scale balcony spill plume

FDS INPUT FILE FOR SIMULATION F4

```
&HEAD CHID='F4',TITLE='20CM GRID, HRR=5000KW, h=5, W=10, DS=1, b=3' /
&MESH IJK=100,80,40, XB=-10.0,10.0,-8.0,8.0,0,8.0 /

&TIME T_END=600.0, SYNCHRONIZE=.TRUE. /
&MISC SUPPRESSION=.FALSE. /
&DUMP DT_PL3D=25., DT_DEVC=0.5, DT_HRR=0.5, DT_ISOF=0.5
WRITE_XYZ=.TRUE.,
PLOT3D_QUANTITY(1)='U-VELOCITY',
PLOT3D_QUANTITY(2)='V-VELOCITY',
PLOT3D_QUANTITY(3)='W-VELOCITY',
PLOT3D_QUANTITY(4)='TEMPERATURE',
PLOT3D_QUANTITY(5)='HRRPUV' /

*****************************
CHARACTERISTICS OF BURNER FIRE
*****************************
&RADI RADIATIVE_FRACTION=0.25 /
&SURF ID              ='FIRE',
HRRPUA         =625
COLOR          ='ORANGE'/
&OBST XB=-6.415,-3.585,-1.415,1.415,0,0.20, SURF_IDS='FIRE','INERT','INERT' /

*******************************
CHARACTERISIICS OF THE BOUNDARIES
*******************************
&VENT MB='XMIN' , SURF_ID='OPEN' /Open domain boundary
&VENT MB='XMAX' , SURF_ID='OPEN' /Open domain boundary
&VENT MB='YMIN' , SURF_ID='OPEN' /Open domain boundary
&VENT MB='YMAX' , SURF_ID='OPEN' /Open domain boundary
&VENT MB='ZMAX' , SURF_ID='OPEN' /Open domain boundary

*****************************
MATERIAL AND SURFACE PROPERTIES
*****************************
&MATL   ID            ='FIBER BOARD'
SPECIFIC_HEAT         = 2.090
DENSITY               = 229
CONDUCTIVITY          = 0.041/

&SURF   ID            ='COMP WALL',
MATL_ID               ='FIBER BOARD',
COLOR                 ='GRAY',
TRANSPARENCY          = 0.5,
THICKNESS             = 0.25 /FIRE COMPARTMENT WALLS

&SURF ID              ='BALC WALL',
MATL_ID               =’FIBER BOARD',
COLOR                 ='SLATE GRAY',
TRANSPARENCY          = 0.5,
THICKNESS             = 0.20 /COLLECTING HOOD WALLS

******************
COMPARTMENT GEOMETRY
******************
&OBST XB=-10.00, 0.00, -7.25,-7.00, 0.00,5.25,SURF_ID='COMP WALL' /FIRE COMP SIDE WALL
(FRT)
&OBST XB=-10.00, 0.00,  7.00, 7.25, 0.00,5.25,SURF_ID='COMP WALL' /FIRE COMP SIDE WALL
(BACK)
&OBST XB=-10.00,-9.75, -7.25, 7.25, 0.00,5.25,SURF_ID='COMP WALL' /FIRE COMP BACK WALL
&OBST XB=-10.00, 0.00, -8.00, 8.00, 5.00,5.25,SURF_ID='COMP WALL' /FIRE COMP CEILING
```

```
&OBST XB= -0.25, 0.00, -8.00,-5.00, 0.00,5.00,SURF_ID='COMP WALL' /FIRE COMP FRONT 1
(10M OPENING)
&OBST XB= -0.25, 0.00,  5.00, 8.00, 0.00,5.00,SURF_ID='COMP WALL' /FIRE COMP FRONT 2
(10M OPENING)
&OBST XB= 0.00, 3.00, -8.00, 8.00, 5.00,5.20,SURF_ID='BALC WALL' /BALCONY (3.0M)
&OBST XB= 0.00, 3.00, -5.20,-5.00, 1.40,5.00,SURF_ID='BALC WALL' /CHANNELLING SCREEN
1(10M OPENING)
&OBST XB= 0.00, 3.00,  5.00, 5.20, 1.40,5.00,SURF_ID='BALC WALL' /CHANNELLING SCREEN
2(10M OPENING)
&OBST XB=-0.25, 0.00, -5.00, 5.00, 4.00,5.00,SURF_ID='BALC WALL' /DOWNSTAND (1.0M)

******************************
INSTRUMENTATION AND MEASUREMENTS
******************************
### MASS FLOW RATE THROUGH OPENING ###
&DEVC XB=0.0, 0.0,-5.00,5.00,0.0,4.0, QUANTITY='MASS FLOW +', ID='MFR COMP+'/
&DEVC XB=0.0, 0.0,-5.00,5.00,0.0,4.0, QUANTITY='MASS FLOW -', ID='MFR COMP-'/
&DEVC XB=3.0, 3.0,-5.00,5.00,0.0,5.0, QUANTITY='MASS FLOW +', ID='MFR SPILL+'/
&DEVC XB=3.0,10.0,-6.00,6.00,5.0,5.0, QUANTITY='MASS FLOW +', ID='MFR ROTATED2+'/

### HEAT FLOW RATE THROUGH OPENING ###
&DEVC XB=0.0, 0.0,-5.00,5.00,0.0,4.0, QUANTITY='HEAT FLOW +', ID='MFR COMP+'/
&DEVC XB=3.0, 3.0,-5.00,5.00,0.0,5.0, QUANTITY='HEAT FLOW +', ID='MFR SPILL+'/
&DEVC XB=3.0,10.0,-6.00,6.00,5.0,5.0, QUANTITY='HEAT FLOW +', ID='MFR ROTATED2+'/

### TEMPERATURE ACROSS COMPARTMENT OPENING ###
&DEVC XYZ=0.0,-4.9,3.9,QUANTITY='TEMPERATURE',ID='COMP TEMP 3.9(X=-4.9)m' /TEMP at
Compartment Opening, 0.1m from top
&DEVC XYZ=0.0,-4.5,3.9,QUANTITY='TEMPERATURE',ID='COMP TEMP 3.9(X=-4.5)m' /TEMP at
Compartment Opening, 0.1m from top
&DEVC XYZ=0.0,-4.0,3.9,QUANTITY='TEMPERATURE',ID='COMP TEMP 3.9(X=-4.0)m' /TEMP at
Compartment Opening, 0.1m from top
&DEVC XYZ=0.0,-3.5,3.9,QUANTITY='TEMPERATURE',ID='COMP TEMP 3.9(X=-3.5)m' /TEMP at
Compartment Opening, 0.1m from top
&DEVC XYZ=0.0,-3.0,3.9,QUANTITY='TEMPERATURE',ID='COMP TEMP 3.9(X=-3.0)m' /TEMP at
Compartment Opening, 0.1m from top
&DEVC XYZ=0.0,-2.4,3.9,QUANTITY='TEMPERATURE',ID='COMP TEMP 3.9(X=-2.4)m' /TEMP at
Compartment Opening, 0.1m from top
&DEVC XYZ=0.0,-2.0,3.9,QUANTITY='TEMPERATURE',ID='COMP TEMP 3.9(X=-2.0)m' /TEMP at
Compartment Opening, 0.1m from top
&DEVC XYZ=0.0,-1.5,3.9,QUANTITY='TEMPERATURE',ID='COMP TEMP 3.9(X=-1.5)m' /TEMP at
Compartment Opening, 0.1m from top
&DEVC XYZ=0.0,-1.2,3.9,QUANTITY='TEMPERATURE',ID='COMP TEMP 3.9(X=-1.2)m' /TEMP at
Compartment Opening, 0.1m from top
&DEVC XYZ=0.0,-1.0,3.9,QUANTITY='TEMPERATURE',ID='COMP TEMP 3.9(X=-1.0)m' /TEMP at
Compartment Opening, 0.1m from top
&DEVC XYZ=0.0,-0.5,3.9,QUANTITY='TEMPERATURE',ID='COMP TEMP 3.9(X=-0.5)m' /TEMP at
Compartment Opening, 0.1m from top
&DEVC XYZ=0.0, 0.0,3.9,QUANTITY='TEMPERATURE',ID='COMP TEMP 3.9(X=0.0)m' /TEMP at
Compartment Opening, 0.1m from top
&DEVC XYZ=0.0, 0.5,3.9,QUANTITY='TEMPERATURE',ID='COMP TEMP 3.9(X=0.5)m' /TEMP at
Compartment Opening, 0.1m from top
&DEVC XYZ=0.0, 1.0,3.9,QUANTITY='TEMPERATURE',ID='COMP TEMP 3.9(X=1.0)m' /TEMP at
Compartment Opening, 0.1m from top
&DEVC XYZ=0.0, 1.2,3.9,QUANTITY='TEMPERATURE',ID='COMP TEMP 3.9(X=1.2)m' /TEMP at
Compartment Opening, 0.1m from top
&DEVC XYZ=0.0, 1.5,3.9,QUANTITY='TEMPERATURE',ID='COMP TEMP 3.9(X=1.5)m' /TEMP at
Compartment Opening, 0.1m from top
&DEVC XYZ=0.0, 2.0,3.9,QUANTITY='TEMPERATURE',ID='COMP TEMP 3.9(X=2.0)m' /TEMP at
Compartment Opening, 0.1m from top
&DEVC XYZ=0.0, 2.4,3.9,QUANTITY='TEMPERATURE',ID='COMP TEMP 3.9(X=2.4)m' /TEMP at
Compartment Opening, 0.1m from top
&DEVC XYZ=0.0, 3.0,3.9,QUANTITY='TEMPERATURE',ID='COMP TEMP 3.9(X=3.0)m' /TEMP at
Compartment Opening, 0.1m from top
&DEVC XYZ=0.0, 3.5,3.9,QUANTITY='TEMPERATURE',ID='COMP TEMP 3.9(X=3.5)m' /TEMP at
Compartment Opening, 0.1m from top
&DEVC XYZ=0.0, 4.0,3.9,QUANTITY='TEMPERATURE',ID='COMP TEMP 3.9(X=4.0)m' /TEMP at
Compartment Opening, 0.1m from top
&DEVC XYZ=0.0, 4.5,3.9,QUANTITY='TEMPERATURE',ID='COMP TEMP 3.9(X=4.5)m' /TEMP at
Compartment Opening, 0.1m from top
```

```
&DEVC XYZ=0.0, 4.9,3.9,QUANTITY='TEMPERATURE',ID='COMP TEMP 3.9(X=4.9)m' /TEMP at
Compartment Opening, 0.1m from top

### U-VELOCITY ACROSS COMPARTMENT OPENING ###
&DEVC XYZ=0.0,-4.9,3.9,QUANTITY='U-VELOCITY',ID='COMP U-VEL 3.9(X=-4.9)m' /U-VEL at
Compartment Opening, 0.1m from top
&DEVC XYZ=0.0,-4.5,3.9,QUANTITY='U-VELOCITY',ID='COMP U-VEL 3.9(X=-4.5)m' /U-VEL at
Compartment Opening, 0.1m from top
&DEVC XYZ=0.0,-4.0,3.9,QUANTITY='U-VELOCITY',ID='COMP U-VEL 3.9(X=-4.0)m' /U-VEL at
Compartment Opening, 0.1m from top
&DEVC XYZ=0.0,-3.5,3.9,QUANTITY='U-VELOCITY',ID='COMP U-VEL 3.9(X=-3.5)m' /U-VEL at
Compartment Opening, 0.1m from top
&DEVC XYZ=0.0,-3.0,3.9,QUANTITY='U-VELOCITY',ID='COMP U-VEL 3.9(X=-3.0)m' /U-VEL at
Compartment Opening, 0.1m from top
&DEVC XYZ=0.0,-2.4,3.9,QUANTITY='U-VELOCITY',ID='COMP U-VEL 3.9(X=-2.4)m' /U-VEL at
Compartment Opening, 0.1m from top
&DEVC XYZ=0.0,-2.0,3.9,QUANTITY='U-VELOCITY',ID='COMP U-VEL 3.9(X=-2.0)m' /U-VEL at
Compartment Opening, 0.1m from top
&DEVC XYZ=0.0,-1.5,3.9,QUANTITY='U-VELOCITY',ID='COMP U-VEL 3.9(X=-1.5)m' /U-VEL at
Compartment Opening, 0.1m from top
&DEVC XYZ=0.0,-1.2,3.9,QUANTITY='U-VELOCITY',ID='COMP U-VEL 3.9(X=-1.2)m' /U-VEL at
Compartment Opening, 0.1m from top
&DEVC XYZ=0.0,-1.0,3.9,QUANTITY='U-VELOCITY',ID='COMP U-VEL 3.9(X=-1.0)m' /U-VEL at
Compartment Opening, 0.1m from top
&DEVC XYZ=0.0,-0.5,3.9,QUANTITY='U-VELOCITY',ID='COMP U-VEL 3.9(X=-0.5)m' /U-VEL at
Compartment Opening, 0.1m from top
&DEVC XYZ=0.0, 0.0,3.9,QUANTITY='U-VELOCITY',ID='COMP U-VEL 3.9(X=0.0)m' /U-VEL at
Compartment Opening, 0.1m from top
&DEVC XYZ=0.0, 0.5,3.9,QUANTITY='U-VELOCITY',ID='COMP U-VEL 3.9(X=0.5)m' /U-VEL at
Compartment Opening, 0.1m from top
&DEVC XYZ=0.0, 1.0,3.9,QUANTITY='U-VELOCITY',ID='COMP U-VEL 3.9(X=1.0)m' /U-VEL at
Compartment Opening, 0.1m from top
&DEVC XYZ=0.0, 1.2,3.9,QUANTITY='U-VELOCITY',ID='COMP U-VEL 3.9(X=1.2)m' /U-VEL at
Compartment Opening, 0.1m from top
&DEVC XYZ=0.0, 1.5,3.9,QUANTITY='U-VELOCITY',ID='COMP U-VEL 3.9(X=1.5)m' /U-VEL at
Compartment Opening, 0.1m from top
&DEVC XYZ=0.0, 2.0,3.9,QUANTITY='U-VELOCITY',ID='COMP U-VEL 3.9(X=2.0)m' /U-VEL at
Compartment Opening, 0.1m from top
&DEVC XYZ=0.0, 2.4,3.9,QUANTITY='U-VELOCITY',ID='COMP U-VEL 3.9(X=2.4)m' /U-VEL at
Compartment Opening, 0.1m from top
&DEVC XYZ=0.0, 3.0,3.9,QUANTITY='U-VELOCITY',ID='COMP U-VEL 3.9(X=3.0)m' /U-VEL at
Compartment Opening, 0.1m from top
&DEVC XYZ=0.0, 3.5,3.9,QUANTITY='U-VELOCITY',ID='COMP U-VEL 3.9(X=3.5)m' /U-VEL at
Compartment Opening, 0.1m from top
&DEVC XYZ=0.0, 4.0,3.9,QUANTITY='U-VELOCITY',ID='COMP U-VEL 3.9(X=4.0)m' /U-VEL at
Compartment Opening, 0.1m from top
&DEVC XYZ=0.0, 4.5,3.9,QUANTITY='U-VELOCITY',ID='COMP U-VEL 3.9(X=4.5)m' /U-VEL at
Compartment Opening, 0.1m from top
&DEVC XYZ=0.0, 4.9,3.9,QUANTITY='U-VELOCITY',ID='COMP U-VEL 3.9(X=4.9)m' /U-VEL at
Compartment Opening, 0.1m from top

### TEMPERATURE ACROSS SPILL EDGE ###
&DEVC XYZ=3.0,-4.9,4.9,QUANTITY='TEMPERATURE',ID='SPILL TEMP 4.9(X=-5.0) m' /TEMP at
Spill Edge, 4.9 m from floor
&DEVC XYZ=3.0,-4.5,4.9,QUANTITY='TEMPERATURE',ID='SPILL TEMP 4.9(X=-4.5) m' /TEMP at
Spill Edge, 4.9 m from floor
&DEVC XYZ=3.0,-4.0,4.9,QUANTITY='TEMPERATURE',ID='SPILL TEMP 4.9(X=-4.0) m' /TEMP at
Spill Edge, 4.9 m from floor
&DEVC XYZ=3.0,-3.5,4.9,QUANTITY='TEMPERATURE',ID='SPILL TEMP 4.9(X=-3.5) m' /TEMP at
Spill Edge, 4.9 m from floor
&DEVC XYZ=3.0,-3.0,4.9,QUANTITY='TEMPERATURE',ID='SPILL TEMP 4.9(X=-3.0) m' /TEMP at
Spill Edge, 4.9 m from floor
&DEVC XYZ=3.0,-2.4,4.9,QUANTITY='TEMPERATURE',ID='SPILL TEMP 4.9(X=-2.4) m' /TEMP at
Spill Edge, 4.9 m from floor
&DEVC XYZ=3.0,-2.0,4.9,QUANTITY='TEMPERATURE',ID='SPILL TEMP 4.9(X=-2.0) m' /TEMP at
Spill Edge, 4.9 m from floor
&DEVC XYZ=3.0,-1.5,4.9,QUANTITY='TEMPERATURE',ID='SPILL TEMP 4.9(X=-1.5) m' /TEMP at
Spill Edge, 4.9 m from floor
&DEVC XYZ=3.0,-1.2,4.9,QUANTITY='TEMPERATURE',ID='SPILL TEMP 4.9(X=-1.2) m' /TEMP at
Spill Edge, 4.9 m from floor
```

```
&DEVC XYZ=3.0,-1.0,4.9,QUANTITY='TEMPERATURE',ID='SPILL TEMP 4.9(X=-1.0) m' /TEMP at
Spill Edge, 4.9 m from floor
&DEVC XYZ=3.0,-0.5,4.9,QUANTITY='TEMPERATURE',ID='SPILL TEMP 4.9(X=-0.5) m' /TEMP at
Spill Edge, 4.9 m from floor
&DEVC XYZ=3.0, 0.0,4.9,QUANTITY='TEMPERATURE',ID='SPILL TEMP 4.9(X=0.0) m' /TEMP at
Spill Edge, 4.9 m from floor
&DEVC XYZ=3.0, 0.5,4.9,QUANTITY='TEMPERATURE',ID='SPILL TEMP 4.9(X=0.5) m' /TEMP at
Spill Edge, 4.9 m from floor
&DEVC XYZ=3.0, 1.0,4.9,QUANTITY='TEMPERATURE',ID='SPILL TEMP 4.9(X=1.0) m' /TEMP at
Spill Edge, 4.9 m from floor
&DEVC XYZ=3.0, 1.2,4.9,QUANTITY='TEMPERATURE',ID='SPILL TEMP 4.9(X=1.2) m' /TEMP at
Spill Edge, 4.9 m from floor
&DEVC XYZ=3.0, 1.5,4.9,QUANTITY='TEMPERATURE',ID='SPILL TEMP 4.9(X=1.5) m' /TEMP at
Spill Edge, 4.9 m from floor
&DEVC XYZ=3.0, 2.0,4.9,QUANTITY='TEMPERATURE',ID='SPILL TEMP 4.9(X=2.0) m' /TEMP at
Spill Edge, 4.9 m from floor
&DEVC XYZ=3.0, 2.4,4.9,QUANTITY='TEMPERATURE',ID='SPILL TEMP 4.9(X=2.4) m' /TEMP at
Spill Edge, 4.9 m from floor
&DEVC XYZ=3.0, 3.0,4.9,QUANTITY='TEMPERATURE',ID='SPILL TEMP 4.9(X=3.0) m' /TEMP at
Spill Edge, 4.9 m from floor
&DEVC XYZ=3.0, 3.5,4.9,QUANTITY='TEMPERATURE',ID='SPILL TEMP 4.9(X=3.5) m' /TEMP at
Spill Edge, 4.9 m from floor
&DEVC XYZ=3.0, 4.0,4.9,QUANTITY='TEMPERATURE',ID='SPILL TEMP 4.9(X=4.0) m' /TEMP at
Spill Edge, 4.9 m from floor
&DEVC XYZ=3.0, 4.5,4.9,QUANTITY='TEMPERATURE',ID='SPILL TEMP 4.9(X=4.5) m' /TEMP at
Spill Edge, 4.9 m from floor
&DEVC XYZ=3.0, 4.9,4.9,QUANTITY='TEMPERATURE',ID='SPILL TEMP 4.9(X=5.0) m' /TEMP at
Spill Edge, 4.9 m from floor

### U-VELOCITY ACROSS SPILL EDGE ###
&DEVC XYZ=3.0,-4.9,4.9,QUANTITY='U-VELOCITY',ID='SPILL U-VEL 4.9(X=-5.0) m' /U-VEL at
Spill Edge, 4.9 m from floor
&DEVC XYZ=3.0,-4.5,4.9,QUANTITY='U-VELOCITY',ID='SPILL U-VEL 4.9(X=-4.5) m' /U-VEL at
Spill Edge, 4.9 m from floor
&DEVC XYZ=3.0,-4.0,4.9,QUANTITY='U-VELOCITY',ID='SPILL U-VEL 4.9(X=-4.0) m' /U-VEL at
Spill Edge, 4.9 m from floor
&DEVC XYZ=3.0,-3.5,4.9,QUANTITY='U-VELOCITY',ID='SPILL U-VEL 4.9(X=-3.5) m' /U-VEL at
Spill Edge, 4.9 m from floor
&DEVC XYZ=3.0,-3.0,4.9,QUANTITY='U-VELOCITY',ID='SPILL U-VEL 4.9(X=-3.0) m' /U-VEL at
Spill Edge, 4.9 m from floor
&DEVC XYZ=3.0,-2.4,4.9,QUANTITY='U-VELOCITY',ID='SPILL U-VEL 4.9(X=-2.4) m' /U-VEL at
Spill Edge, 4.9 m from floor
&DEVC XYZ=3.0,-2.0,4.9,QUANTITY='U-VELOCITY',ID='SPILL U-VEL 4.9(X=-2.0) m' /U-VEL at
Spill Edge, 4.9 m from floor
&DEVC XYZ=3.0,-1.5,4.9,QUANTITY='U-VELOCITY',ID='SPILL U-VEL 4.9(X=-1.5) m' /U-VEL at
Spill Edge, 4.9 m from floor
&DEVC XYZ=3.0,-1.2,4.9,QUANTITY='U-VELOCITY',ID='SPILL U-VEL 4.9(X=-1.2) m' /U-VEL at
Spill Edge, 4.9 m from floor
&DEVC XYZ=3.0,-1.0,4.9,QUANTITY='U-VELOCITY',ID='SPILL U-VEL 4.9(X=-1.0) m' /U-VEL at
Spill Edge, 4.9 m from floor
&DEVC XYZ=3.0,-0.5,4.9,QUANTITY='U-VELOCITY',ID='SPILL U-VEL 4.9(X=-0.5) m' /U-VEL at
Spill Edge, 4.9 m from floor
&DEVC XYZ=3.0, 0.0,4.9,QUANTITY='U-VELOCITY',ID='SPILL U-VEL 4.9(X=0.0) m' /U-VEL at
Spill Edge, 4.9 m from floor
&DEVC XYZ=3.0, 0.5,4.9,QUANTITY='U-VELOCITY',ID='SPILL U-VEL 4.9(X=0.5) m' /U-VEL at
Spill Edge, 4.9 m from floor
&DEVC XYZ=3.0, 1.0,4.9,QUANTITY='U-VELOCITY',ID='SPILL U-VEL 4.9(X=1.0) m' /U-VEL at
Spill Edge, 4.9 m from floor
&DEVC XYZ=3.0, 1.2,4.9,QUANTITY='U-VELOCITY',ID='SPILL U-VEL 4.9(X=1.2) m' /U-VEL at
Spill Edge, 4.9 m from floor
&DEVC XYZ=3.0, 1.5,4.9,QUANTITY='U-VELOCITY',ID='SPILL U-VEL 4.9(X=1.5) m' /U-VEL at
Spill Edge, 4.9 m from floor
&DEVC XYZ=3.0, 2.0,4.9,QUANTITY='U-VELOCITY',ID='SPILL U-VEL 4.9(X=2.0) m' /U-VEL at
Spill Edge, 4.9 m from floor
&DEVC XYZ=3.0, 2.4,4.9,QUANTITY='U-VELOCITY',ID='SPILL U-VEL 4.9(X=2.4) m' /U-VEL at
Spill Edge, 4.9 m from floor
&DEVC XYZ=3.0, 3.0,4.9,QUANTITY='U-VELOCITY',ID='SPILL U-VEL 4.9(X=3.0) m' /U-VEL at
Spill Edge, 4.9 m from floor
&DEVC XYZ=3.0, 3.5,4.9,QUANTITY='U-VELOCITY',ID='SPILL U-VEL 4.9(X=3.5) m' /U-VEL at
Spill Edge, 4.9 m from floor
```

```
&DEVC XYZ=3.0, 4.0,4.9,QUANTITY='U-VELOCITY',ID='SPILL U-VEL 4.9(X=4.0) m' /U-VEL at
Spill Edge, 4.9 m from floor
&DEVC XYZ=3.0, 4.5,4.9,QUANTITY='U-VELOCITY',ID='SPILL U-VEL 4.9(X=4.5) m' /U-VEL at
Spill Edge, 4.9 m from floor
&DEVC XYZ=3.0, 4.9,4.9,QUANTITY='U-VELOCITY',ID='SPILL U-VEL 4.9(X=5.0) m' /U-VEL at
Spill Edge, 4.9 m from floor

#### TEMPERATURE AT CENTER AT COMPARTMENT OPENING ####
&DEVC XYZ=0.0,0.0,4.9,QUANTITY='TEMPERATURE',ID='COMP TEMP 4.9 m' /TEMP at Center of
Compartment Opening, 4.9 m from floor
&DEVC XYZ=0.0,0.0,4.7,QUANTITY='TEMPERATURE',ID='COMP TEMP 4.7 m' /TEMP at Center of
Compartment Opening, 4.7 m from floor
&DEVC XYZ=0.0,0.0,4.5,QUANTITY='TEMPERATURE',ID='COMP TEMP 4.5 m' /TEMP at Center of
Compartment Opening, 4.5 m from floor
&DEVC XYZ=0.0,0.0,4.3,QUANTITY='TEMPERATURE',ID='COMP TEMP 4.3 m' /TEMP at Center of
Compartment Opening, 4.3 m from floor
&DEVC XYZ=0.0,0.0,4.1,QUANTITY='TEMPERATURE',ID='COMP TEMP 4.1 m' /TEMP at Center of
Compartment Opening, 4.1 m from floor
&DEVC XYZ=0.0,0.0,3.9,QUANTITY='TEMPERATURE',ID='COMP TEMP 3.9 m' /TEMP at Center of
Compartment Opening, 3.9 m from floor
&DEVC XYZ=0.0,0.0,3.7,QUANTITY='TEMPERATURE',ID='COMP TEMP 3.7 m' /TEMP at Center of
Compartment Opening, 3.7 m from floor
&DEVC XYZ=0.0,0.0,3.5,QUANTITY='TEMPERATURE',ID='COMP TEMP 3.5 m' /TEMP at Center of
Compartment Opening, 3.5 m from floor
&DEVC XYZ=0.0,0.0,3.3,QUANTITY='TEMPERATURE',ID='COMP TEMP 3.3 m' /TEMP at Center of
Compartment Opening, 3.3 m from floor
&DEVC XYZ=0.0,0.0,3.1,QUANTITY='TEMPERATURE',ID='COMP TEMP 3.1 m' /TEMP at Center of
Compartment Opening, 3.1 m from floor
&DEVC XYZ=0.0,0.0,2.9,QUANTITY='TEMPERATURE',ID='COMP TEMP 2.9 m' /TEMP at Center of
Compartment Opening, 2.9 m from floor
&DEVC XYZ=0.0,0.0,2.7,QUANTITY='TEMPERATURE',ID='COMP TEMP 2.7 m' /TEMP at Center of
Compartment Opening, 2.7 m from floor
&DEVC XYZ=0.0,0.0,2.5,QUANTITY='TEMPERATURE',ID='COMP TEMP 2.5 m' /TEMP at Center of
Compartment Opening, 2.5 m from floor
&DEVC XYZ=0.0,0.0,2.3,QUANTITY='TEMPERATURE',ID='COMP TEMP 2.3 m' /TEMP at Center of
Compartment Opening, 2.3 m from floor
&DEVC XYZ=0.0,0.0,2.1,QUANTITY='TEMPERATURE',ID='COMP TEMP 2.1 m' /TEMP at Center of
Compartment Opening, 2.1 m from floor
&DEVC XYZ=0.0,0.0,1.9,QUANTITY='TEMPERATURE',ID='COMP TEMP 1.9 m' /TEMP at Center of
Compartment Opening, 1.9 m from floor
&DEVC XYZ=0.0,0.0,1.7,QUANTITY='TEMPERATURE',ID='COMP TEMP 1.7 m' /TEMP at Center of
Compartment Opening, 1.7 m from floor
&DEVC XYZ=0.0,0.0,1.5,QUANTITY='TEMPERATURE',ID='COMP TEMP 1.5 m' /TEMP at Center of
Compartment Opening, 1.5 m from floor
&DEVC XYZ=0.0,0.0,1.3,QUANTITY='TEMPERATURE',ID='COMP TEMP 1.3 m' /TEMP at Center of
Compartment Opening, 1.3 m from floor
&DEVC XYZ=0.0,0.0,1.1,QUANTITY='TEMPERATURE',ID='COMP TEMP 1.1 m' /TEMP at Center of
Compartment Opening, 1.1 m from floor
&DEVC XYZ=0.0,0.0,0.9,QUANTITY='TEMPERATURE',ID='COMP TEMP 0.9 m' /TEMP at Center of
Compartment Opening, 0.9 m from floor
&DEVC XYZ=0.0,0.0,0.7,QUANTITY='TEMPERATURE',ID='COMP TEMP 0.7 m' /TEMP at Center of
Compartment Opening, 0.7 m from floor
&DEVC XYZ=0.0,0.0,0.5,QUANTITY='TEMPERATURE',ID='COMP TEMP 0.5 m' /TEMP at Center of
Compartment Opening, 0.5 m from floor

#### U-VELOCITY AT CENTER OF COMPARTMENT OPENING ####
&DEVC XYZ=0.0,0.0,4.9,QUANTITY='U-VELOCITY',ID='COMP U-VEL 4.9 m' /U-VEL at Center of
Compartment Opening, 4.9 m from floor
&DEVC XYZ=0.0,0.0,4.7,QUANTITY='U-VELOCITY',ID='COMP U-VEL 4.7 m' /U-VEL at Center of
Compartment Opening, 4.7 m from floor
&DEVC XYZ=0.0,0.0,4.5,QUANTITY='U-VELOCITY',ID='COMP U-VEL 4.5 m' /U-VEL at Center of
Compartment Opening, 4.5 m from floor
&DEVC XYZ=0.0,0.0,4.3,QUANTITY='U-VELOCITY',ID='COMP U-VEL 4.3 m' /U-VEL at Center of
Compartment Opening, 4.3 m from floor
&DEVC XYZ=0.0,0.0,4.1,QUANTITY='U-VELOCITY',ID='COMP U-VEL 4.1 m' /U-VEL at Center of
Compartment Opening, 4.1 m from floor
&DEVC XYZ=0.0,0.0,3.9,QUANTITY='U-VELOCITY',ID='COMP U-VEL 3.9 m' /U-VEL at Center of
Compartment Opening, 3.9 m from floor
&DEVC XYZ=0.0,0.0,3.7,QUANTITY='U-VELOCITY',ID='COMP U-VEL 3.7 m' /U-VEL at Center of
Compartment Opening, 3.7 m from floor
```

```
&DEVC XYZ=0.0,0.0,3.5,QUANTITY='U-VELOCITY',ID='COMP U-VEL 3.5 m' /U-VEL at Center of
Compartment Opening, 3.5 m from floor
&DEVC XYZ=0.0,0.0,3.3,QUANTITY='U-VELOCITY',ID='COMP U-VEL 3.3 m' /U-VEL at Center of
Compartment Opening, 3.3 m from floor
&DEVC XYZ=0.0,0.0,3.1,QUANTITY='U-VELOCITY',ID='COMP U-VEL 3.1 m' /U-VEL at Center of
Compartment Opening, 3.1 m from floor
&DEVC XYZ=0.0,0.0,2.9,QUANTITY='U-VELOCITY',ID='COMP U-VEL 2.9 m' /U-VEL at Center of
Compartment Opening, 2.9 m from floor
&DEVC XYZ=0.0,0.0,2.7,QUANTITY='U-VELOCITY',ID='COMP U-VEL 2.7 m' /U-VEL at Center of
Compartment Opening, 2.7 m from floor
&DEVC XYZ=0.0,0.0,2.5,QUANTITY='U-VELOCITY',ID='COMP U-VEL 2.5 m' /U-VEL at Center of
Compartment Opening, 2.5 m from floor
&DEVC XYZ=0.0,0.0,2.3,QUANTITY='U-VELOCITY',ID='COMP U-VEL 2.3 m' /U-VEL at Center of
Compartment Opening, 2.3 m from floor
&DEVC XYZ=0.0,0.0,2.1,QUANTITY='U-VELOCITY',ID='COMP U-VEL 2.1 m' /U-VEL at Center of
Compartment Opening, 2.1 m from floor
&DEVC XYZ=0.0,0.0,1.9,QUANTITY='U-VELOCITY',ID='COMP U-VEL 1.9 m' /U-VEL at Center of
Compartment Opening, 1.9 m from floor
&DEVC XYZ=0.0,0.0,1.7,QUANTITY='U-VELOCITY',ID='COMP U-VEL 1.7 m' /U-VEL at Center of
Compartment Opening, 1.7 m from floor
&DEVC XYZ=0.0,0.0,1.5,QUANTITY='U-VELOCITY',ID='COMP U-VEL 1.5 m' /U-VEL at Center of
Compartment Opening, 1.5 m from floor
&DEVC XYZ=0.0,0.0,1.3,QUANTITY='U-VELOCITY',ID='COMP U-VEL 1.3 m' /U-VEL at Center of
Compartment Opening, 1.3 m from floor
&DEVC XYZ=0.0,0.0,1.1,QUANTITY='U-VELOCITY',ID='COMP U-VEL 1.1 m' /U-VEL at Center of
Compartment Opening, 1.1 m from floor
&DEVC XYZ=0.0,0.0,0.9,QUANTITY='U-VELOCITY',ID='COMP U-VEL 0.9 m' /U-VEL at Center of
Compartment Opening, 0.9 m from floor
&DEVC XYZ=0.0,0.0,0.7,QUANTITY='U-VELOCITY',ID='COMP U-VEL 0.7 m' /U-VEL at Center of
Compartment Opening, 0.7 m from floor
&DEVC XYZ=0.0,0.0,0.5,QUANTITY='U-VELOCITY',ID='COMP U-VEL 0.5 m' /U-VEL at Center of
Compartment Opening, 0.5 m from floor

#### TEMPERATURE AT CENTER OF SPILL EDGE ####
&DEVC XYZ=3.0,0.0,4.9,QUANTITY='TEMPERATURE',ID='SPILL TEMP 4.9 m' /TEMP at Center of
Spill Edge, 4.9 m from floor
&DEVC XYZ=3.0,0.0,4.7,QUANTITY='TEMPERATURE',ID='SPILL TEMP 4.7 m' /TEMP at Center of
Spill Edge, 4.7 m from floor
&DEVC XYZ=3.0,0.0,4.5,QUANTITY='TEMPERATURE',ID='SPILL TEMP 4.5 m' /TEMP at Center of
Spill Edge, 4.5 m from floor
&DEVC XYZ=3.0,0.0,4.3,QUANTITY='TEMPERATURE',ID='SPILL TEMP 4.3 m' /TEMP at Center of
Spill Edge, 4.3 m from floor
&DEVC XYZ=3.0,0.0,4.1,QUANTITY='TEMPERATURE',ID='SPILL TEMP 4.1 m' /TEMP at Center of
Spill Edge, 4.1 m from floor
&DEVC XYZ=3.0,0.0,3.9,QUANTITY='TEMPERATURE',ID='SPILL TEMP 3.9 m' /TEMP at Center of
Spill Edge, 3.9 m from floor
&DEVC XYZ=3.0,0.0,3.7,QUANTITY='TEMPERATURE',ID='SPILL TEMP 3.7 m' /TEMP at Center of
Spill Edge, 3.7 m from floor
&DEVC XYZ=3.0,0.0,3.5,QUANTITY='TEMPERATURE',ID='SPILL TEMP 3.5 m' /TEMP at Center of
Spill Edge, 3.5 m from floor
&DEVC XYZ=3.0,0.0,3.3,QUANTITY='TEMPERATURE',ID='SPILL TEMP 3.3 m' /TEMP at Center of
Spill Edge, 3.3 m from floor
&DEVC XYZ=3.0,0.0,3.1,QUANTITY='TEMPERATURE',ID='SPILL TEMP 3.1 m' /TEMP at Center of
Spill Edge, 3.1 m from floor
&DEVC XYZ=3.0,0.0,2.9,QUANTITY='TEMPERATURE',ID='SPILL TEMP 2.9 m' /TEMP at Center of
Spill Edge, 2.9 m from floor
&DEVC XYZ=3.0,0.0,2.7,QUANTITY='TEMPERATURE',ID='SPILL TEMP 2.7 m' /TEMP at Center of
Spill Edge, 2.7 m from floor
&DEVC XYZ=3.0,0.0,2.5,QUANTITY='TEMPERATURE',ID='SPILL TEMP 2.5 m' /TEMP at Center of
Spill Edge, 2.5 m from floor
&DEVC XYZ=3.0,0.0,2.3,QUANTITY='TEMPERATURE',ID='SPILL TEMP 2.3 m' /TEMP at Center of
Spill Edge, 2.3 m from floor
&DEVC XYZ=3.0,0.0,2.1,QUANTITY='TEMPERATURE',ID='SPILL TEMP 2.1 m' /TEMP at Center of
Spill Edge, 2.1 m from floor
&DEVC XYZ=3.0,0.0,1.9,QUANTITY='TEMPERATURE',ID='SPILL TEMP 1.9 m' /TEMP at Center of
Spill Edge, 1.9 m from floor
&DEVC XYZ=3.0,0.0,1.7,QUANTITY='TEMPERATURE',ID='SPILL TEMP 1.7 m' /TEMP at Center of
Spill Edge, 1.7 m from floor
&DEVC XYZ=3.0,0.0,1.5,QUANTITY='TEMPERATURE',ID='SPILL TEMP 1.5 m' /TEMP at Center of
Spill Edge, 1.5 m from floor
```

```
&DEVC XYZ=3.0,0.0,1.3,QUANTITY='TEMPERATURE',ID='SPILL TEMP 1.3 m' /TEMP at Center of
Spill Edge, 1.3 m from floor
&DEVC XYZ=3.0,0.0,1.1,QUANTITY='TEMPERATURE',ID='SPILL TEMP 1.1 m' /TEMP at Center of
Spill Edge, 1.1 m from floor
&DEVC XYZ=3.0,0.0,0.9,QUANTITY='TEMPERATURE',ID='SPILL TEMP 0.9 m' /TEMP at Center of
Spill Edge, 0.9 m from floor
&DEVC XYZ=3.0,0.0,0.7,QUANTITY='TEMPERATURE',ID='SPILL TEMP 0.7 m' /TEMP at Center of
Spill Edge, 0.7 m from floor
&DEVC XYZ=3.0,0.0,0.5,QUANTITY='TEMPERATURE',ID='SPILL TEMP 0.5 m' /TEMP at Center of
Spill Edge, 0.5 m from floor

#### U-VELOCITY AT CENTER OF SPILL EDGE ####
&DEVC XYZ=3.0,0.0,4.9,QUANTITY='U-VELOCITY',ID='SPILL U-VEL 4.9 m' /U-VEL at Center of
Spill Edge, 4.9 m from floor
&DEVC XYZ=3.0,0.0,4.7,QUANTITY='U-VELOCITY',ID='SPILL U-VEL 4.7 m' /U-VEL at Center of
Spill Edge, 4.7 m from floor
&DEVC XYZ=3.0,0.0,4.5,QUANTITY='U-VELOCITY',ID='SPILL U-VEL 4.5 m' /U-VEL at Center of
Spill Edge, 4.5 m from floor
&DEVC XYZ=3.0,0.0,4.3,QUANTITY='U-VELOCITY',ID='SPILL U-VEL 4.3 m' /U-VEL at Center of
Spill Edge, 4.3 m from floor
&DEVC XYZ=3.0,0.0,4.1,QUANTITY='U-VELOCITY',ID='SPILL U-VEL 4.1 m' /U-VEL at Center of
Spill Edge, 4.1 m from floor
&DEVC XYZ=3.0,0.0,3.9,QUANTITY='U-VELOCITY',ID='SPILL U-VEL 3.9 m' /U-VEL at Center of
Spill Edge, 3.9 m from floor
&DEVC XYZ=3.0,0.0,3.7,QUANTITY='U-VELOCITY',ID='SPILL U-VEL 3.7 m' /U-VEL at Center of
Spill Edge, 3.7 m from floor
&DEVC XYZ=3.0,0.0,3.5,QUANTITY='U-VELOCITY',ID='SPILL U-VEL 3.5 m' /U-VEL at Center of
Spill Edge, 3.5 m from floor
&DEVC XYZ=3.0,0.0,3.3,QUANTITY='U-VELOCITY',ID='SPILL U-VEL 3.3 m' /U-VEL at Center of
Spill Edge, 3.3 m from floor
&DEVC XYZ=3.0,0.0,3.1,QUANTITY='U-VELOCITY',ID='SPILL U-VEL 3.1 m' /U-VEL at Center of
Spill Edge, 3.1 m from floor
&DEVC XYZ=3.0,0.0,2.9,QUANTITY='U-VELOCITY',ID='SPILL U-VEL 2.9 m' /U-VEL at Center of
Spill Edge, 2.9 m from floor
&DEVC XYZ=3.0,0.0,2.7,QUANTITY='U-VELOCITY',ID='SPILL U-VEL 2.7 m' /U-VEL at Center of
Spill Edge, 2.7 m from floor
&DEVC XYZ=3.0,0.0,2.5,QUANTITY='U-VELOCITY',ID='SPILL U-VEL 2.5 m' /U-VEL at Center of
Spill Edge, 2.5 m from floor
&DEVC XYZ=3.0,0.0,2.3,QUANTITY='U-VELOCITY',ID='SPILL U-VEL 2.3 m' /U-VEL at Center of
Spill Edge, 2.3 m from floor
&DEVC XYZ=3.0,0.0,2.1,QUANTITY='U-VELOCITY',ID='SPILL U-VEL 2.1 m' /U-VEL at Center of
Spill Edge, 2.1 m from floor
&DEVC XYZ=3.0,0.0,1.9,QUANTITY='U-VELOCITY',ID='SPILL U-VEL 1.9 m' /U-VEL at Center of
Spill Edge, 1.9 m from floor
&DEVC XYZ=3.0,0.0,1.7,QUANTITY='U-VELOCITY',ID='SPILL U-VEL 1.7 m' /U-VEL at Center of
Spill Edge, 1.7 m from floor
&DEVC XYZ=3.0,0.0,1.5,QUANTITY='U-VELOCITY',ID='SPILL U-VEL 1.5 m' /U-VEL at Center of
Spill Edge, 1.5 m from floor
&DEVC XYZ=3.0,0.0,1.3,QUANTITY='U-VELOCITY',ID='SPILL U-VEL 1.3 m' /U-VEL at Center of
Spill Edge, 1.3 m from floor
&DEVC XYZ=3.0,0.0,1.1,QUANTITY='U-VELOCITY',ID='SPILL U-VEL 1.1 m' /U-VEL at Center of
Spill Edge, 1.1 m from floor
&DEVC XYZ=3.0,0.0,0.9,QUANTITY='U-VELOCITY',ID='SPILL U-VEL 0.9 m' /U-VEL at Center of
Spill Edge, 0.9 m from floor
&DEVC XYZ=3.0,0.0,0.7,QUANTITY='U-VELOCITY',ID='SPILL U-VEL 0.7 m' /U-VEL at Center of
Spill Edge, 0.7 m from floor
&DEVC XYZ=3.0,0.0,0.5,QUANTITY='U-VELOCITY',ID='SPILL U-VEL 0.5 m' /U-VEL at Center of
Spill Edge, 0.5 m from floor

**** SLICE FILES ****
&SLCF PBY= 0.0, QUANTITY='TEMPERATURE', /
&SLCF PBY= 0.0, QUANTITY='U-VELOCITY', VECTOR=.TRUE. /
&SLCF PBZ= 5.0, QUANTITY='TEMPERATURE', / TEMPERATURE AT SPILL EDGE
&SLCF PBZ= 5.0, QUANTITY='U-VELOCITY', VECTOR=.TRUE. / VELOCITY AT SPILL EDGE
&ISOF QUANTITY='TEMPERATURE', VALUE(1)=30., VALUE(2)=800./


&TAIL
```

APPENDIX F: Lateral temperature and velocity profiles for full-scale balcony spill plume simulations

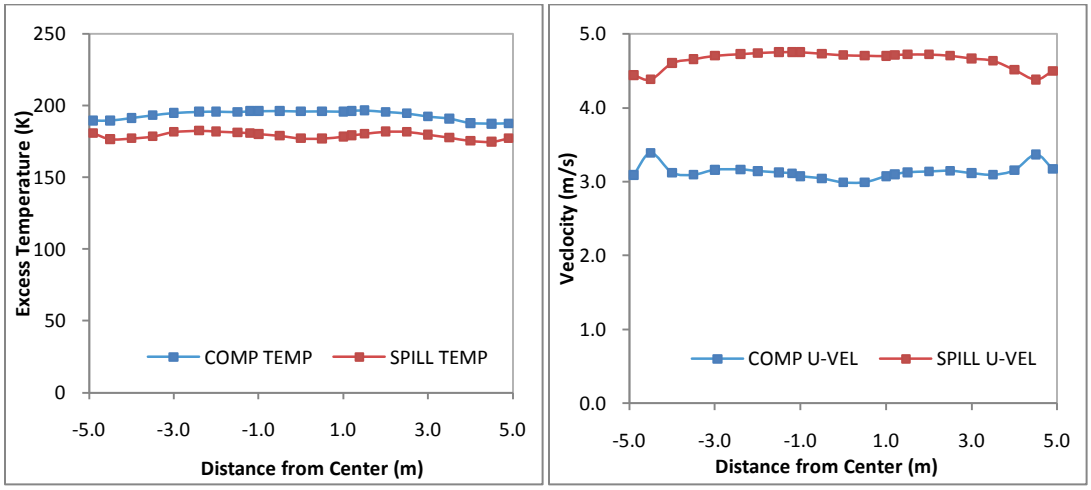

Figure F1: Lateral temperature and velocity profiles for simulation F1

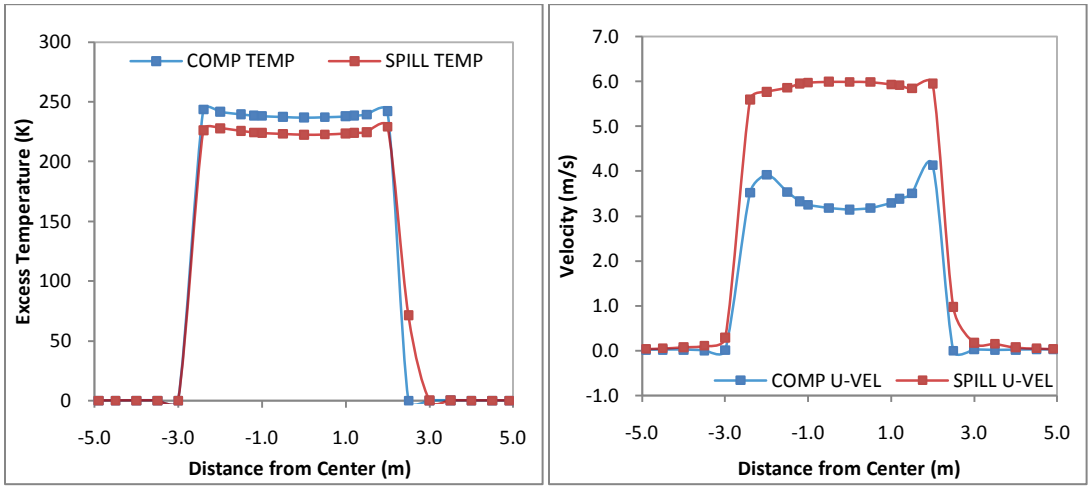

Figure F2: Lateral temperature and velocity profiles for simulation F2

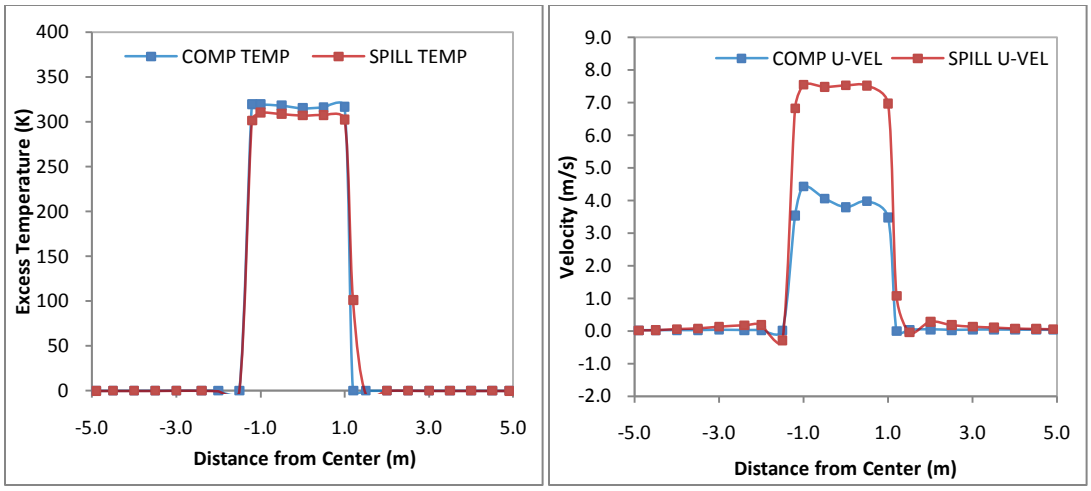

Figure F3: Lateral temperature and velocity profiles for simulation F3

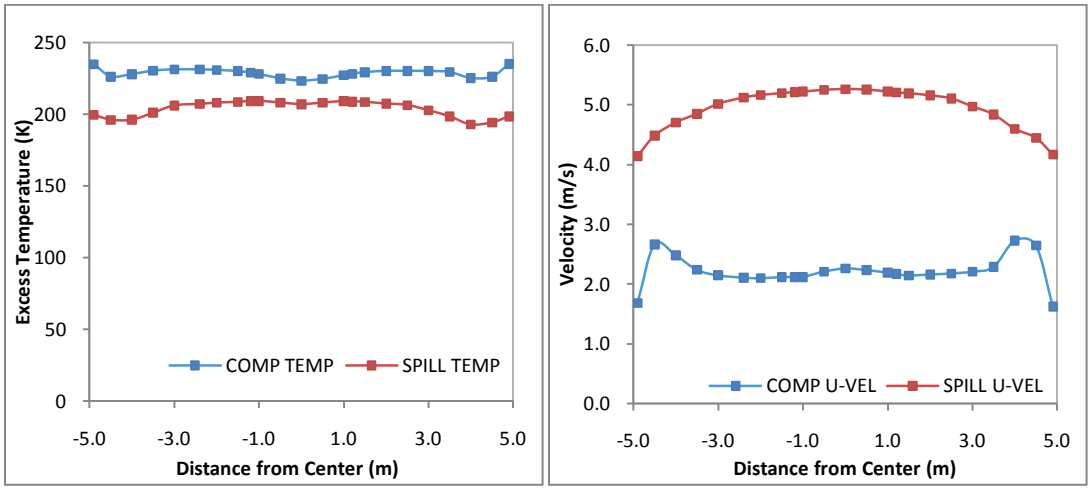

Figure F4: Lateral temperature and velocity profiles for simulation F4

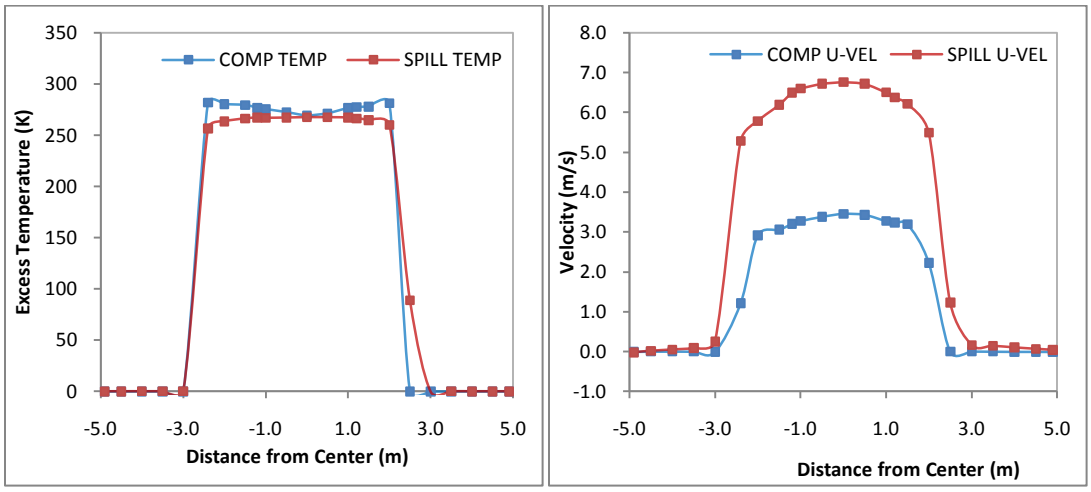

Figure F5: Lateral temperature and velocity profiles for simulation F5

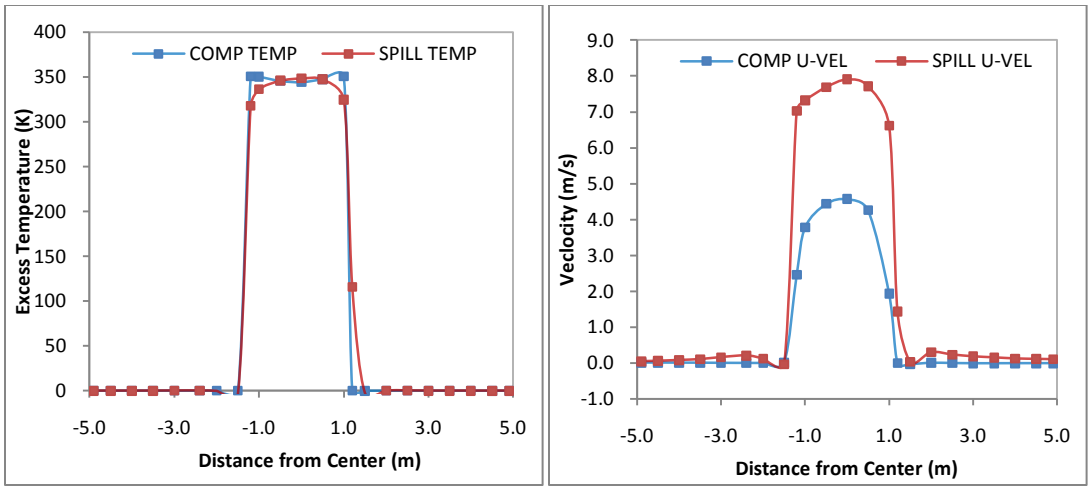

Figure F6: Lateral temperature and velocity profiles for simulation F6

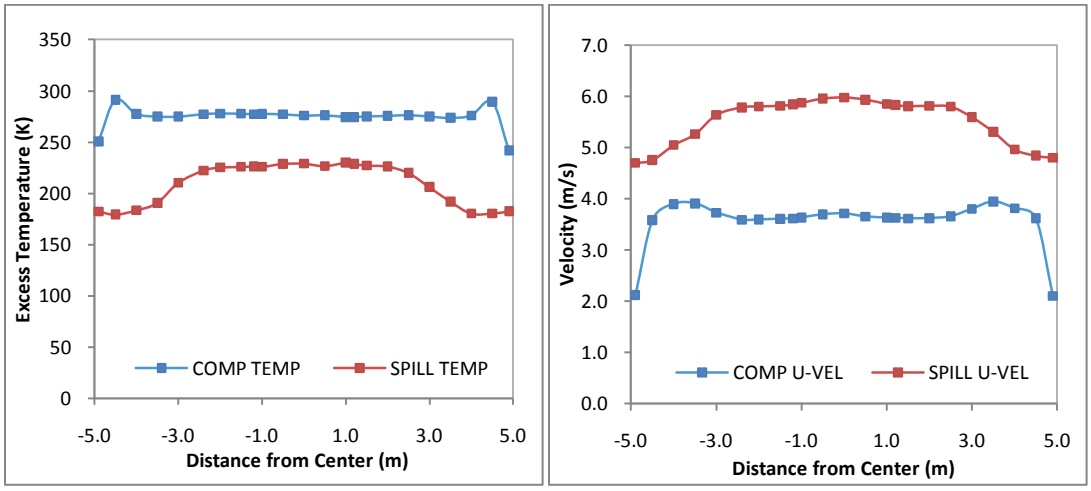

Figure F7: Lateral temperature and velocity profiles for simulation F7

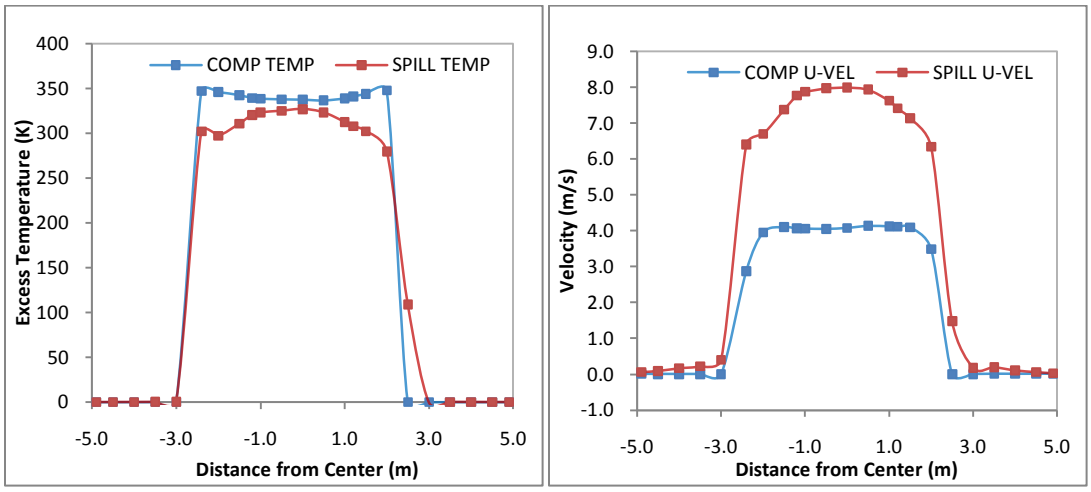

Figure F8: Lateral temperature and velocity profiles for simulation F8

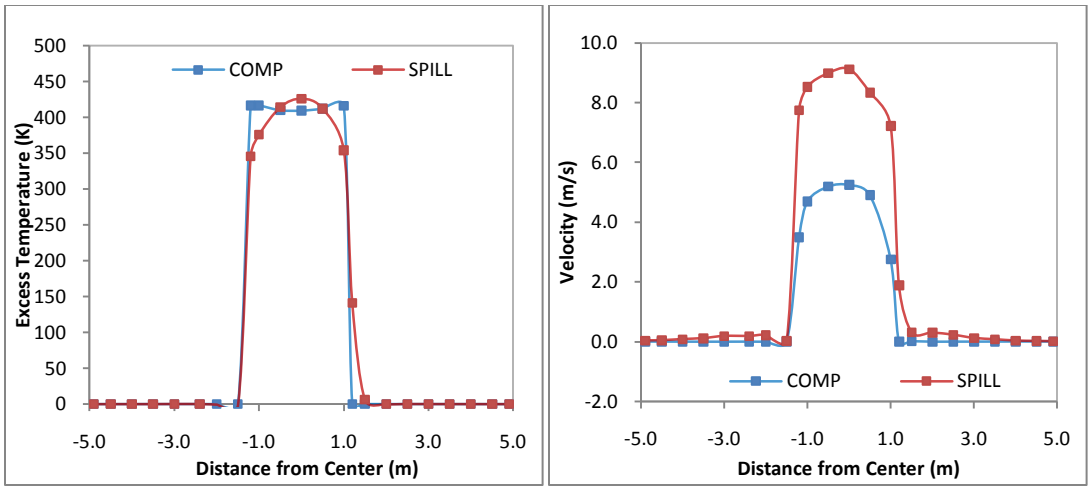

Figure F9: Lateral temperature and velocity profiles for simulation F9

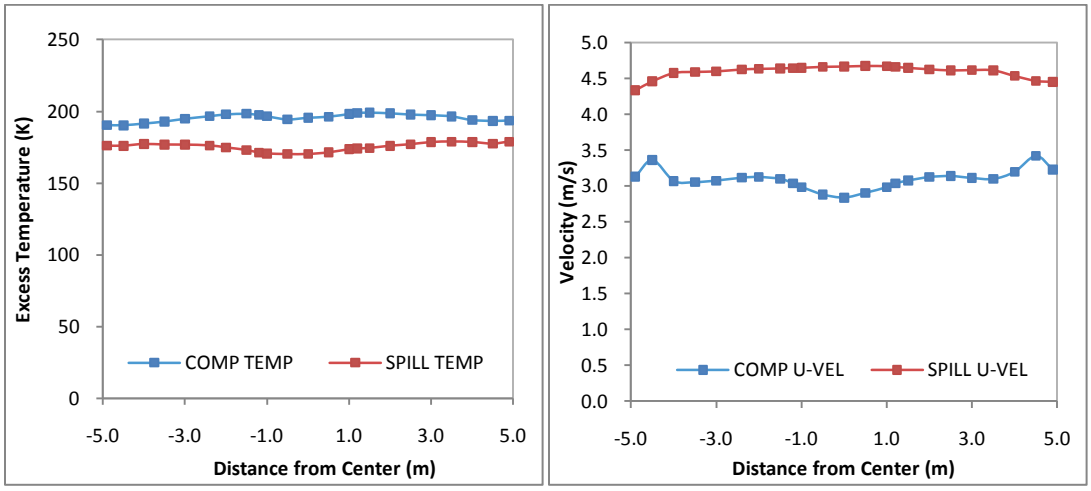

Figure F10: Lateral temperature and velocity profiles for simulation F10

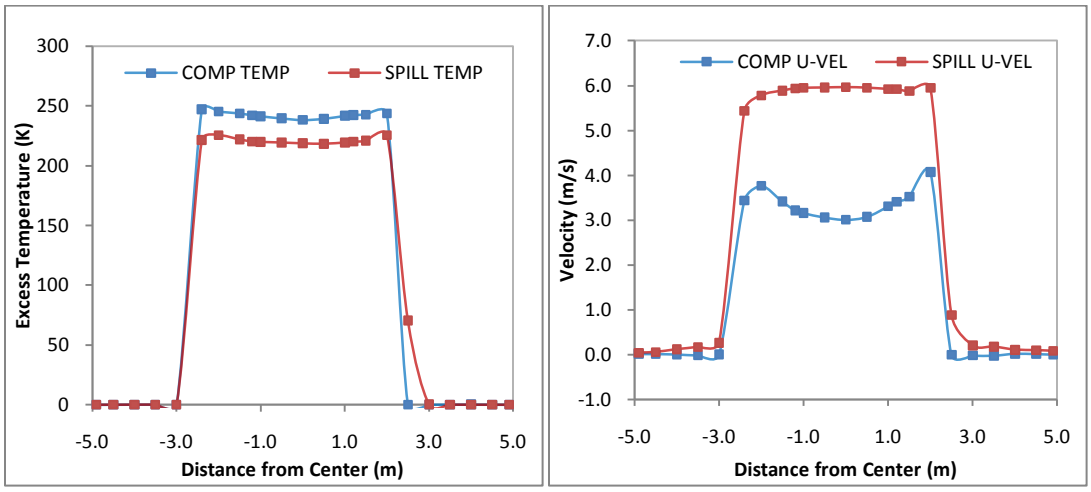

Figure F11: Lateral temperature and velocity profiles for simulation F11

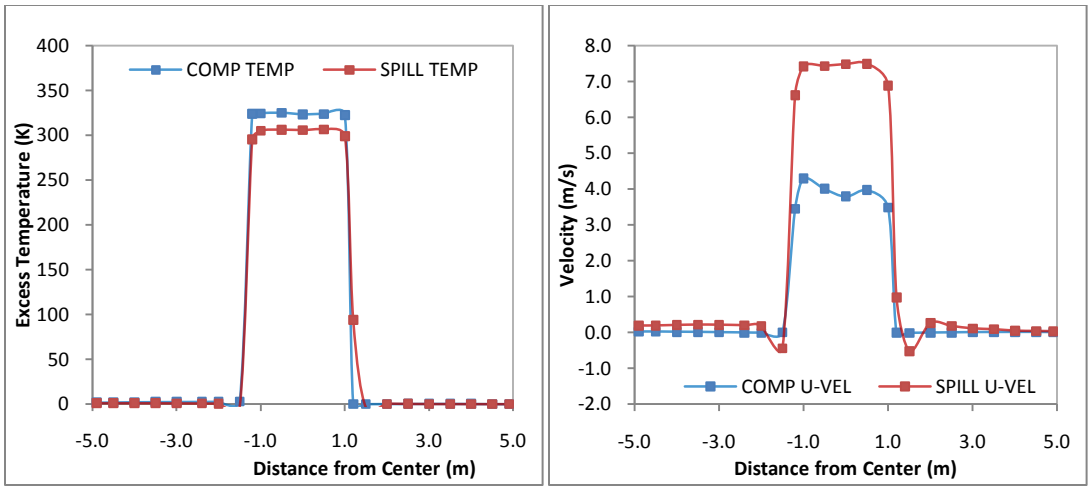

Figure F12: Lateral temperature and velocity profiles for simulation F12

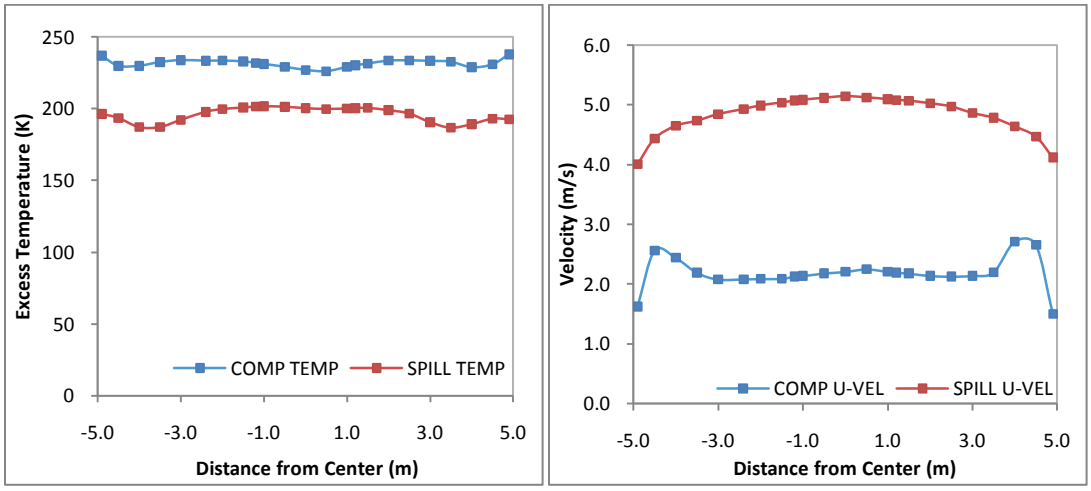

Figure F13: Lateral temperature and velocity profiles for simulation F13

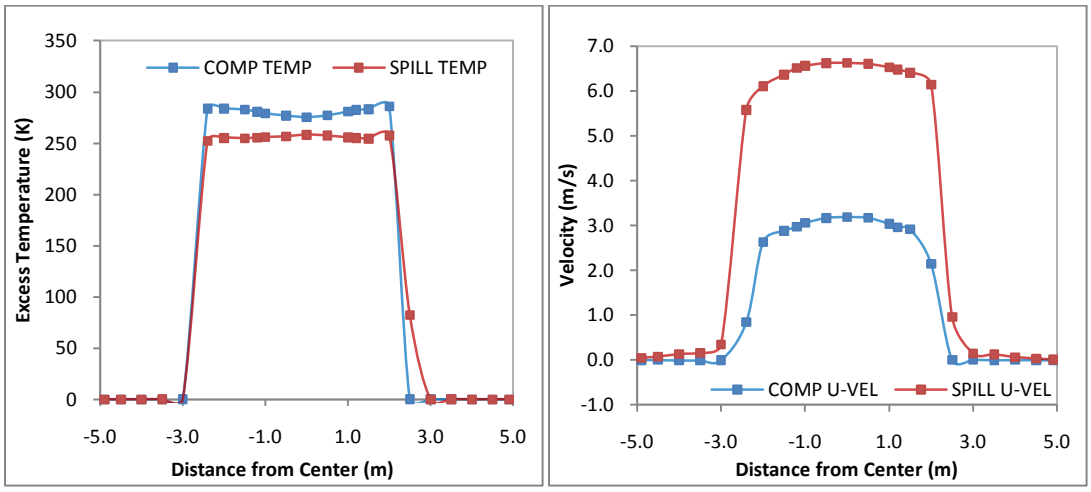

Figure F14: Lateral temperature and velocity profiles for simulation F14

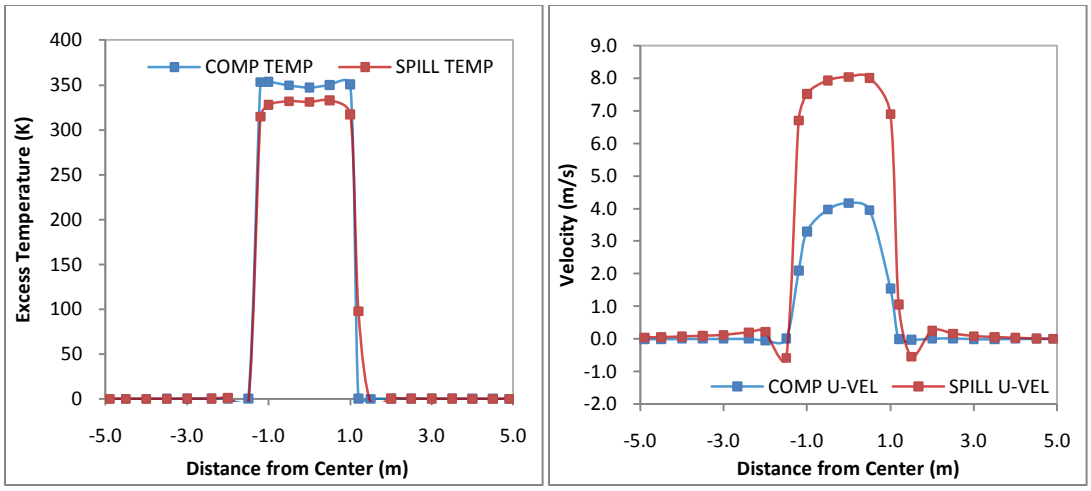

Figure F15: Lateral temperature and velocity profiles for simulation F15

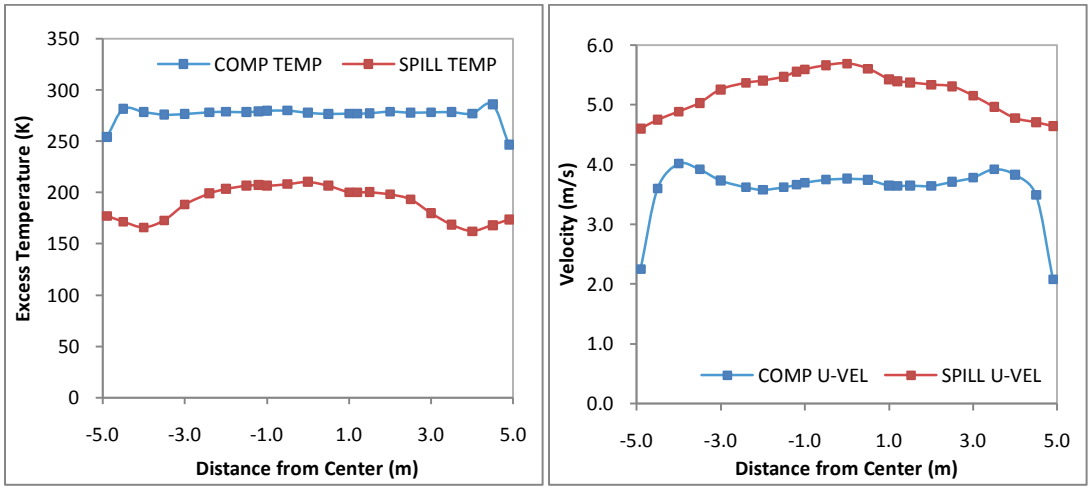

Figure F16: Lateral temperature and velocity profiles for simulation F16

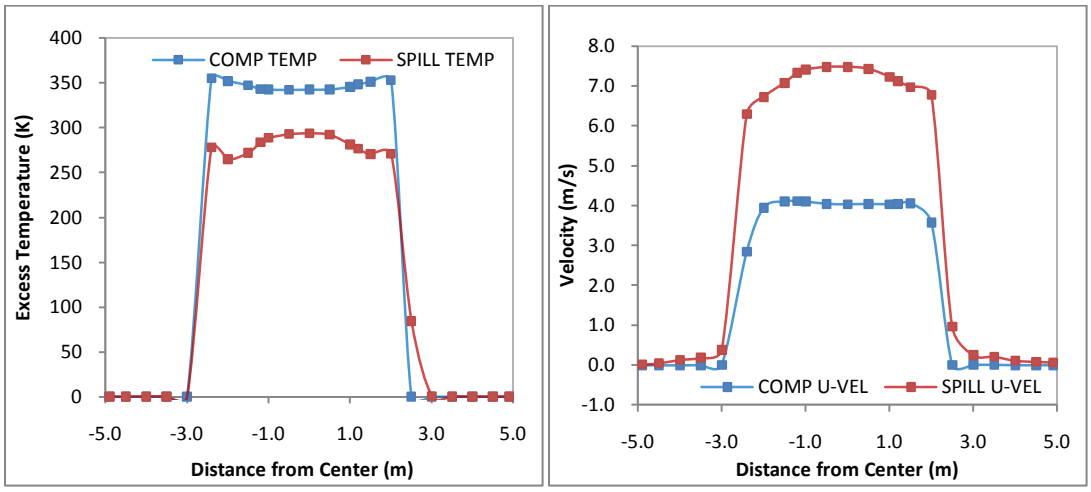

Figure F17: Lateral temperature and velocity profiles for simulation F17

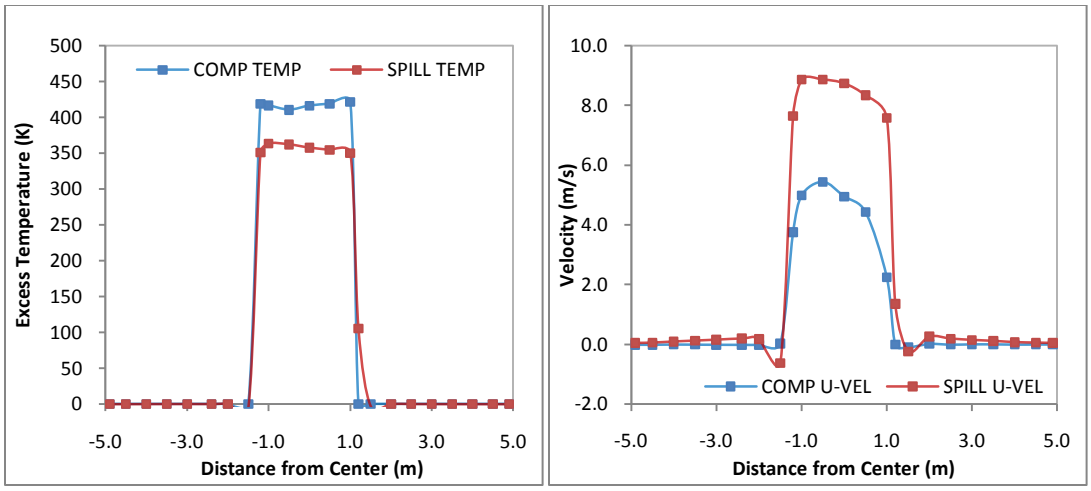

Figure F18: Lateral temperature and velocity profiles for simulation F18

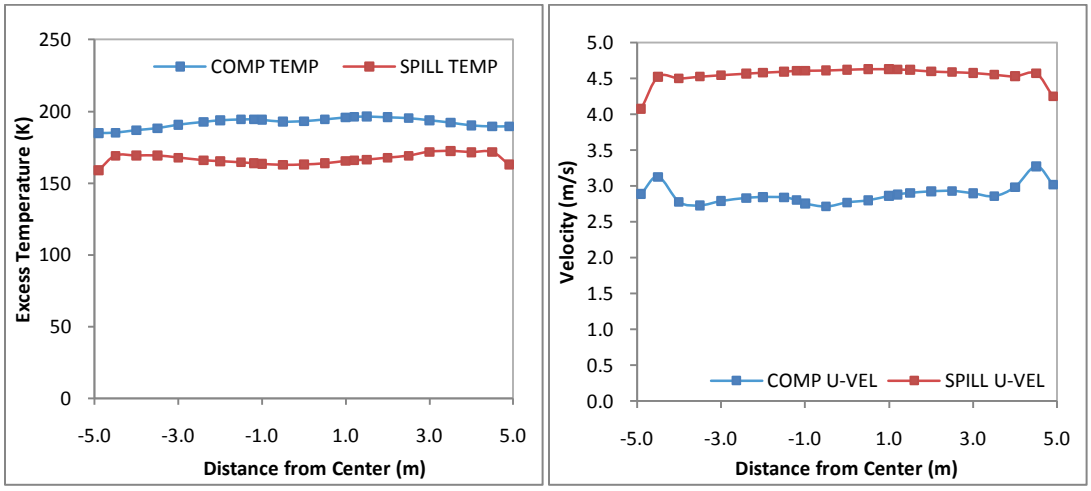

Figure F19: Lateral temperature and velocity profiles for simulation F19

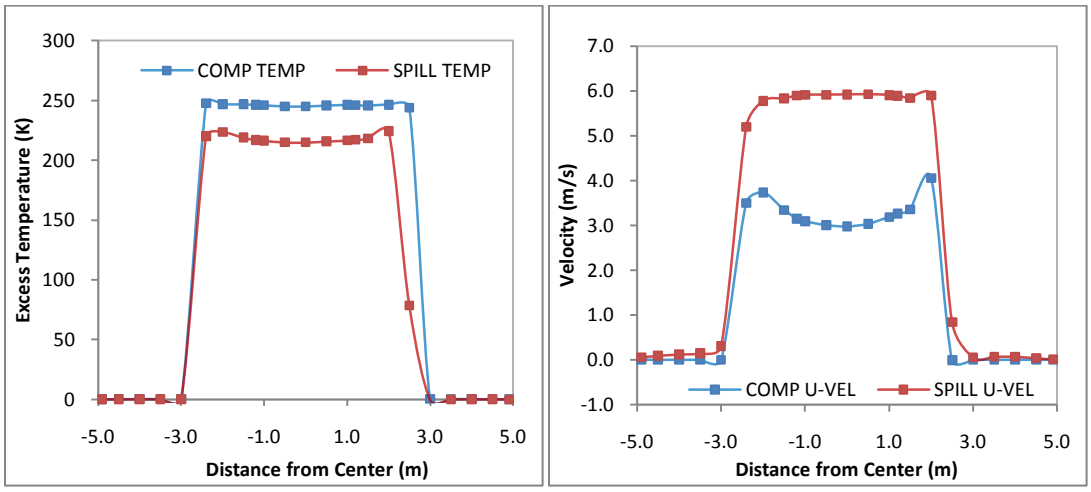

Figure F20: Lateral temperature and velocity profiles for simulation F20

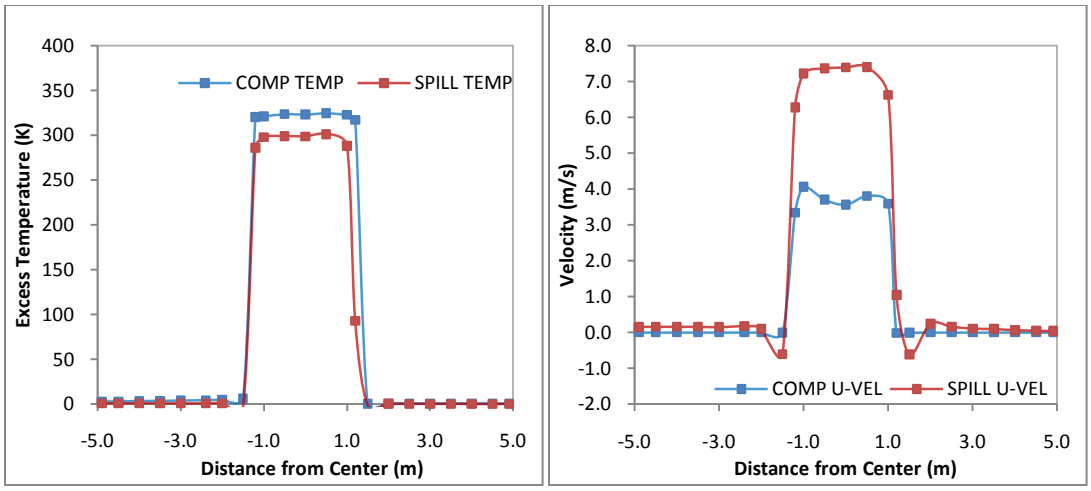

Figure F21: Lateral temperature and velocity profiles for simulation F21

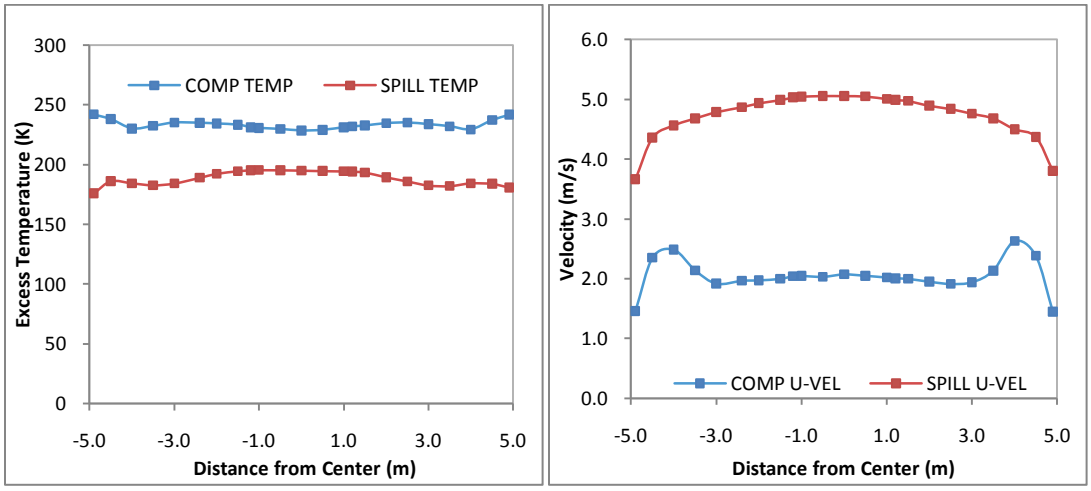

Figure F22: Lateral temperature and velocity profiles for simulation F22

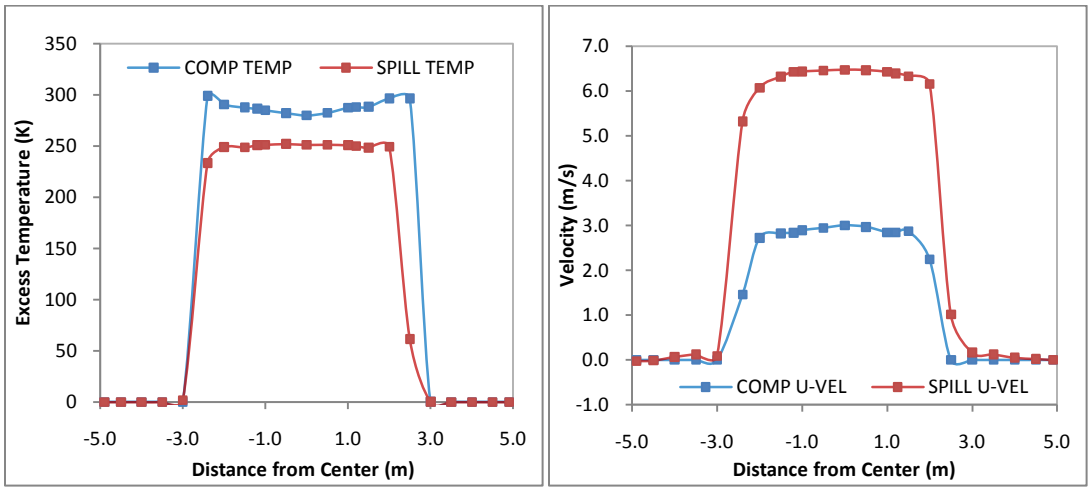

Figure F23: Lateral temperature and velocity profiles for simulation F23

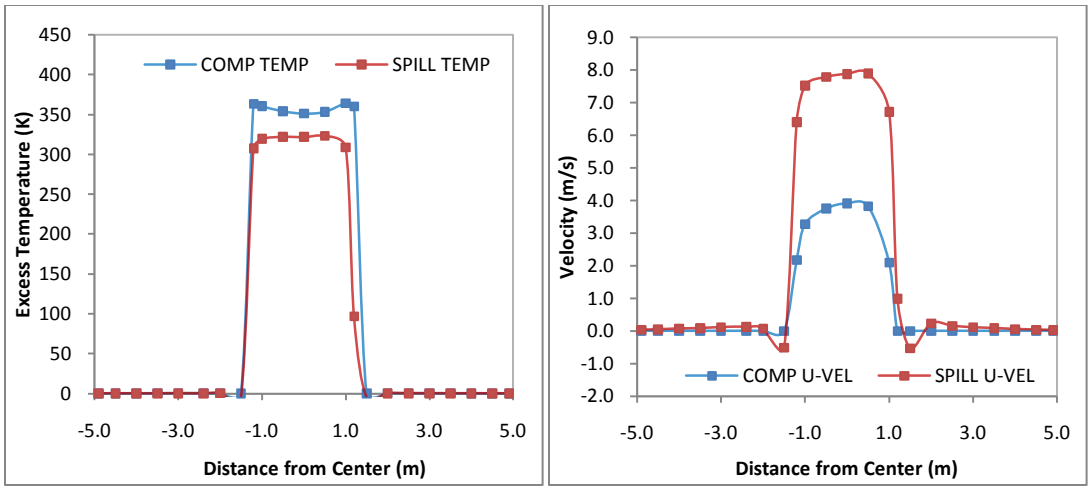

Figure F24: Lateral temperature and velocity profiles for simulation F24

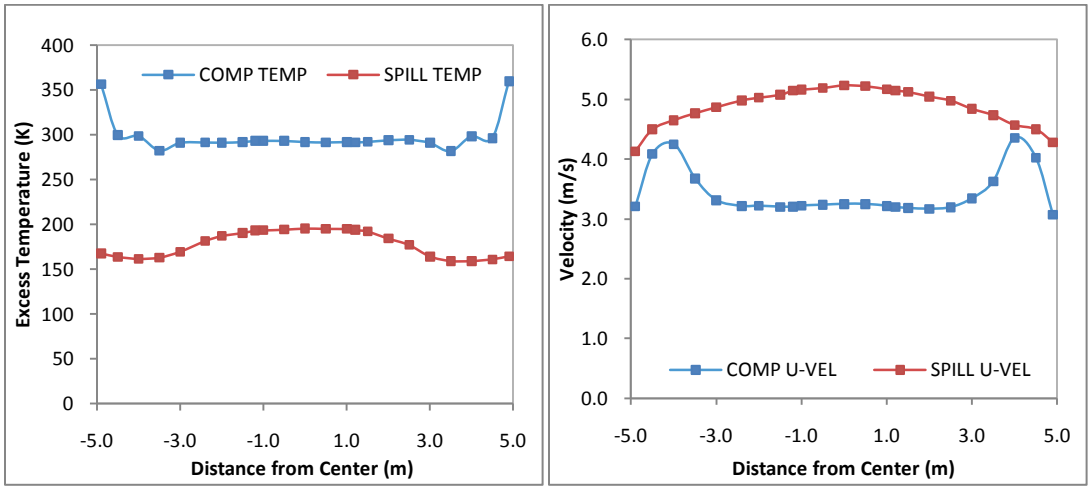

Figure F25: Lateral temperature and velocity profiles for simulation F25

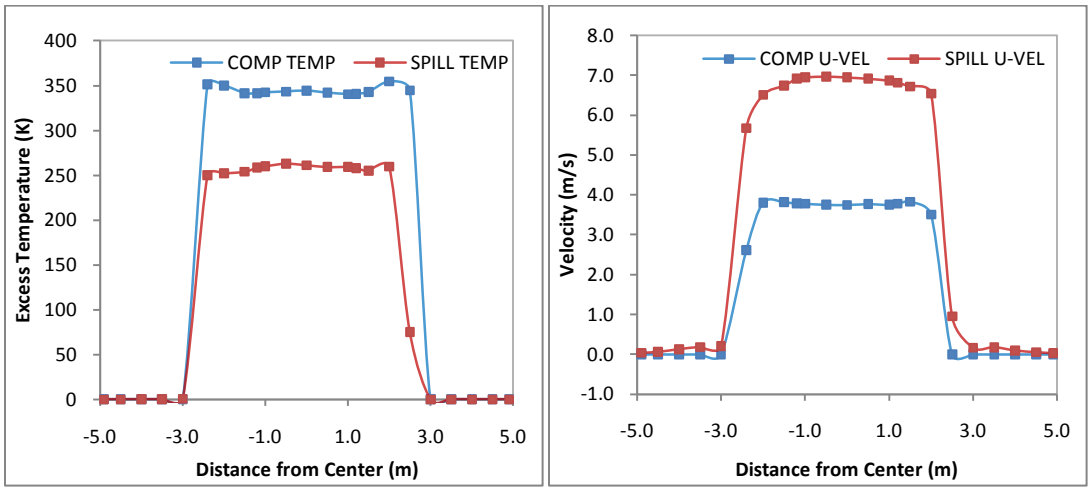

Figure F26: Lateral temperature and velocity profiles for simulation F26

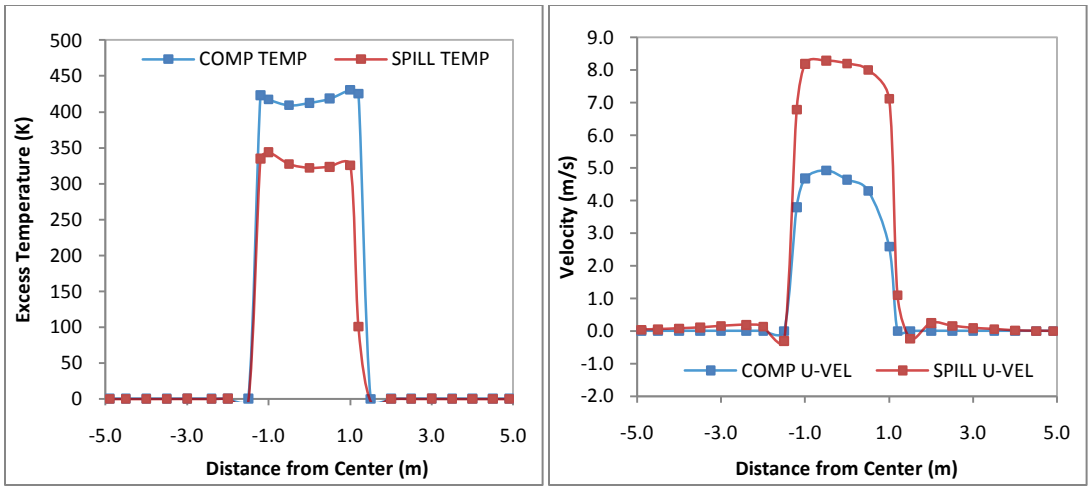

Figure F27: Lateral temperature and velocity profiles for simulation F27

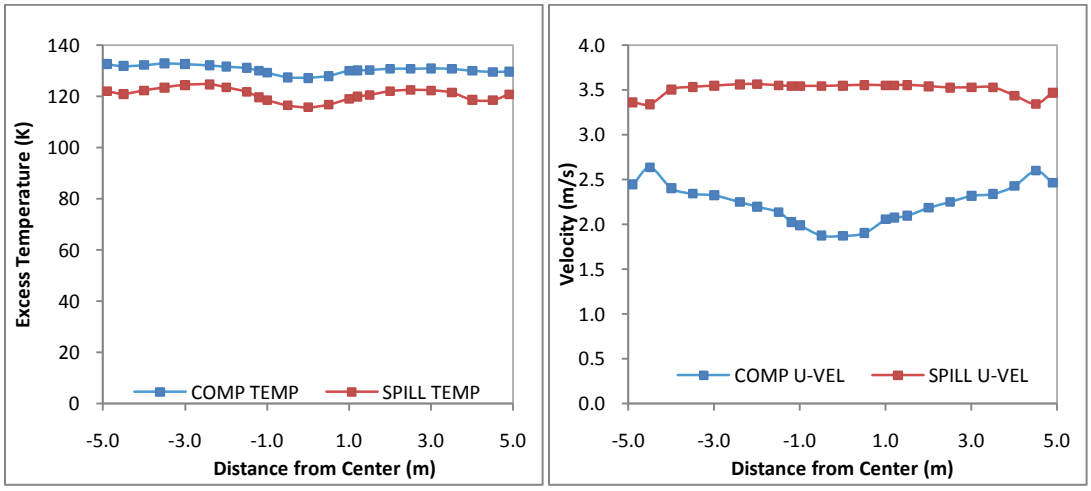

Figure F28: Lateral temperature and velocity profiles for simulation F1R

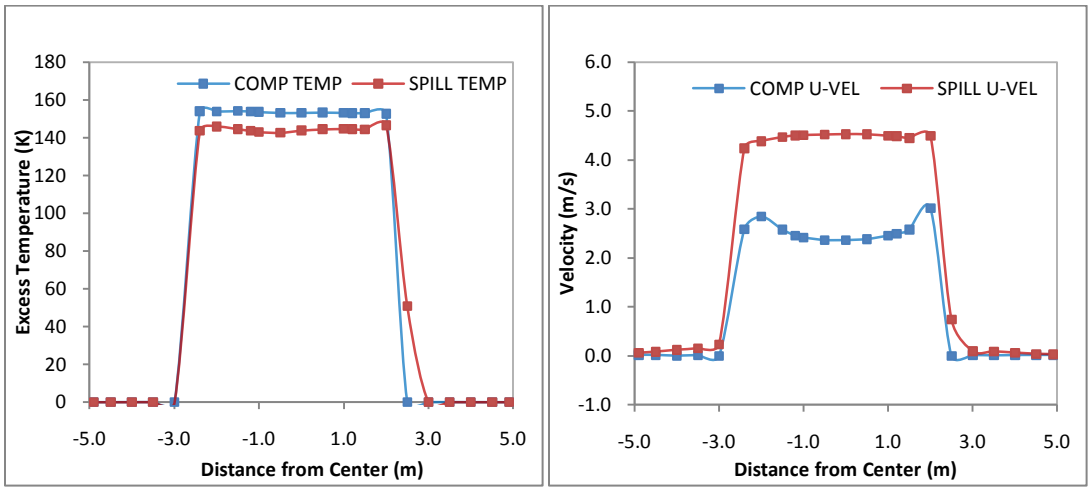

Figure F29: Lateral temperature and velocity profiles for simulation F2R

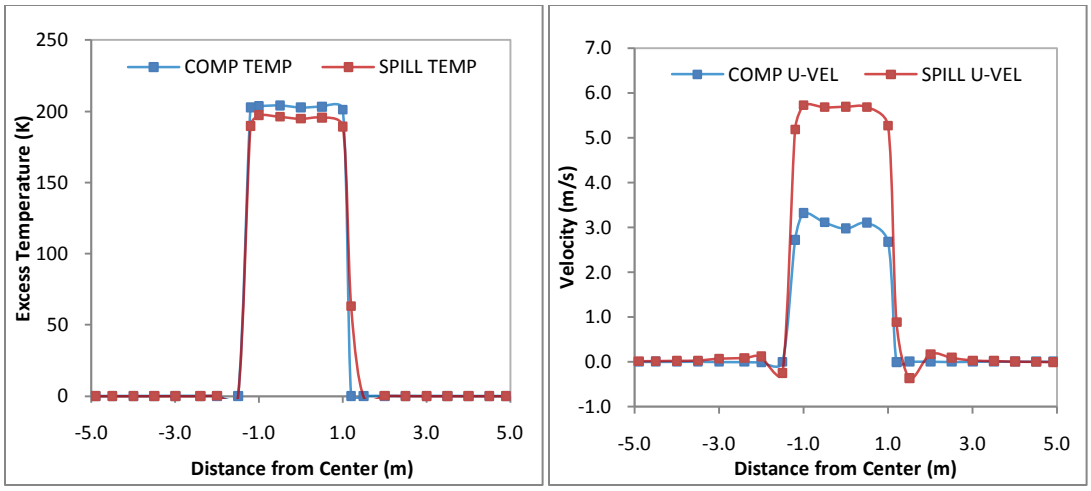

Figure F30: Lateral temperature and velocity profiles for simulation F3R

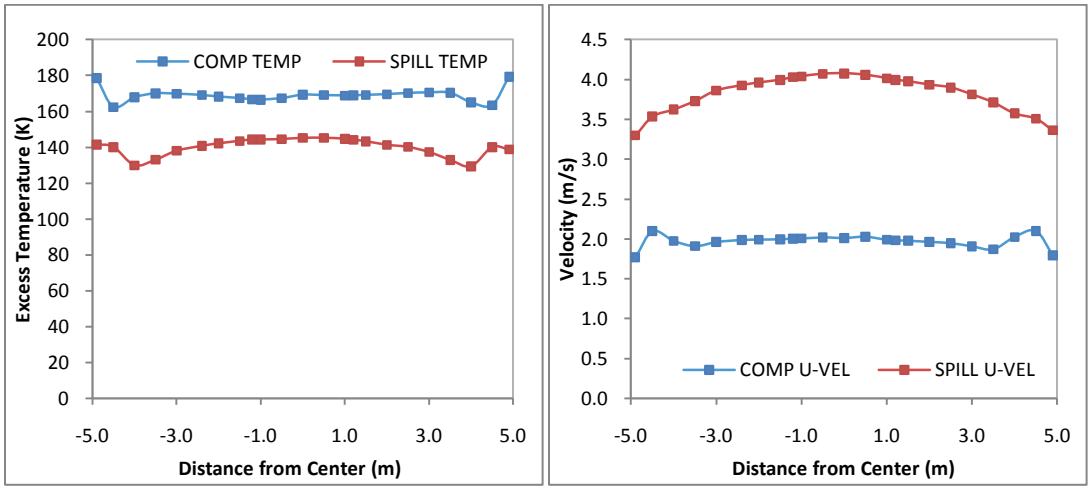

Figure F31: Lateral temperature and velocity profiles for simulation F4R

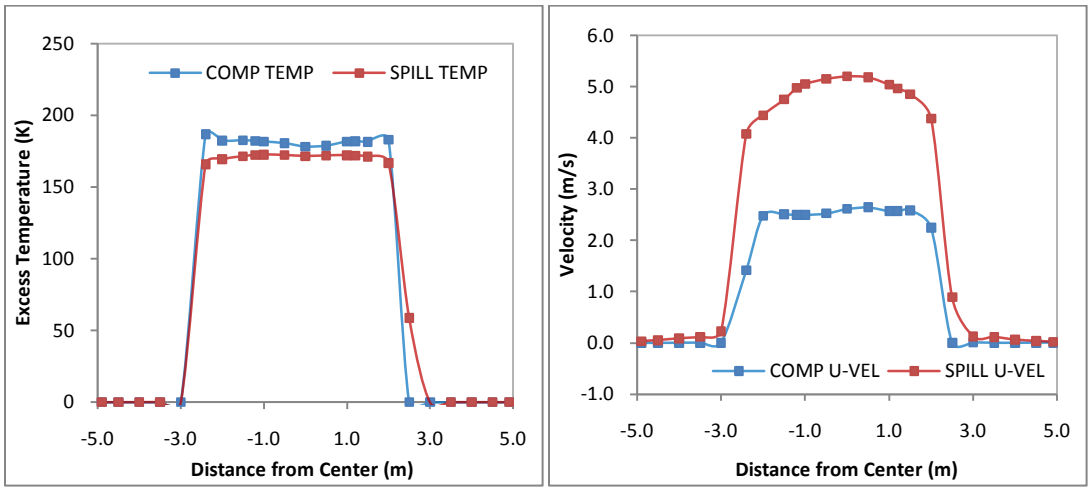

Figure F32: Lateral temperature and velocity profiles for simulation F5R

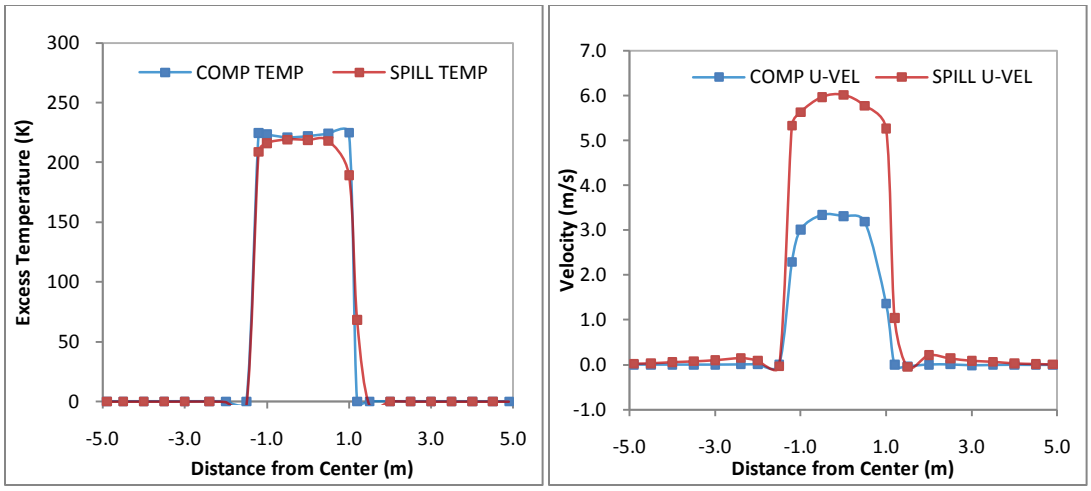

Figure F33: Lateral temperature and velocity profiles for simulation F6R

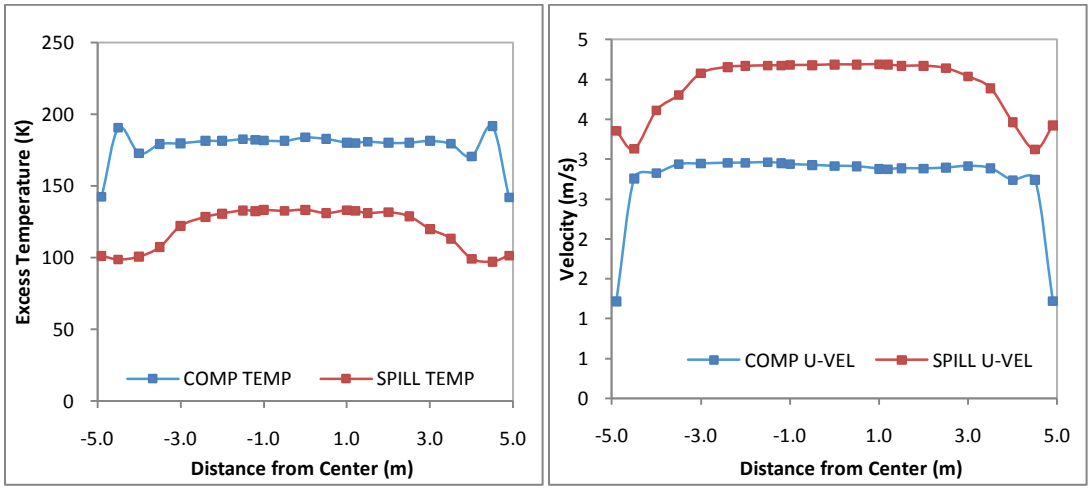

Figure F34: Lateral temperature and velocity profiles for simulation F7R

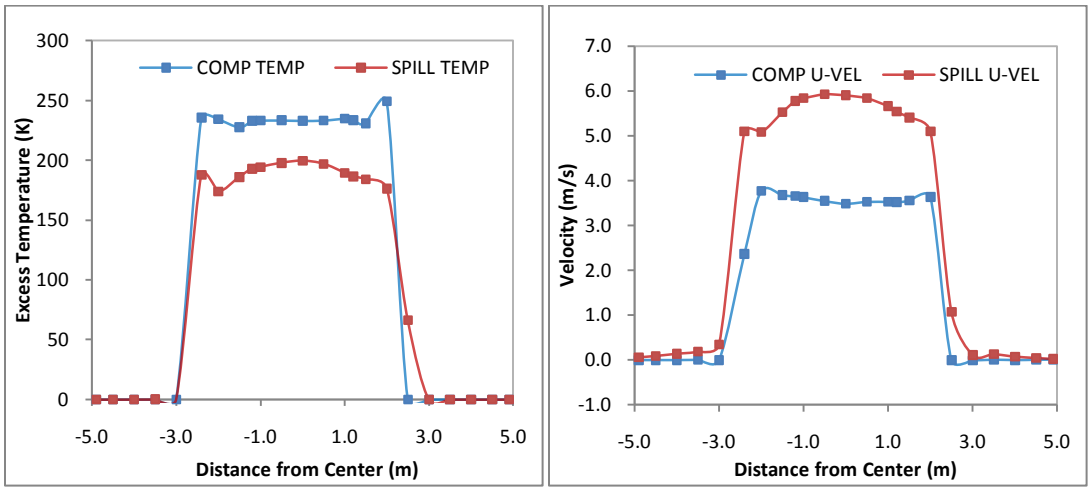

Figure F35: Lateral temperature and velocity profiles for simulation F8R

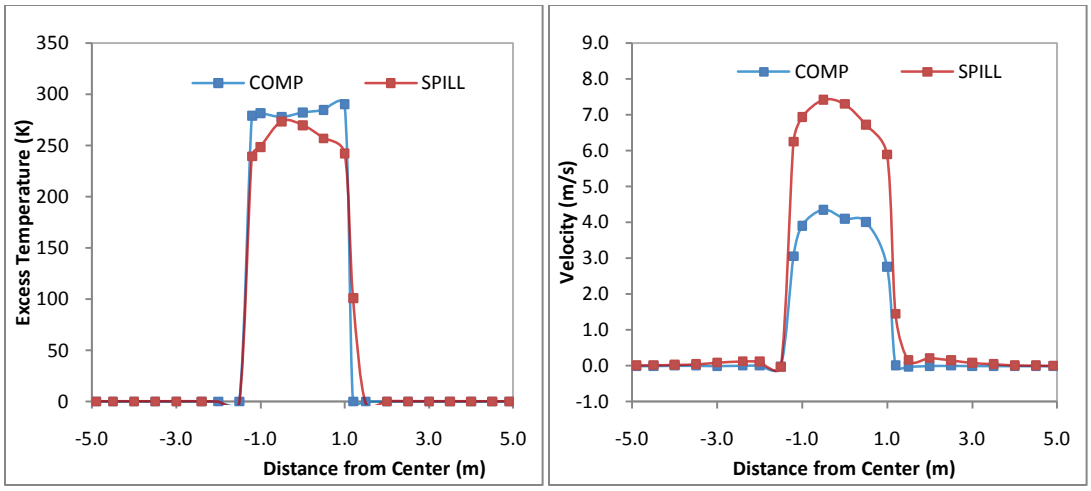

Figure F36: Lateral temperature and velocity profiles for simulation F9R

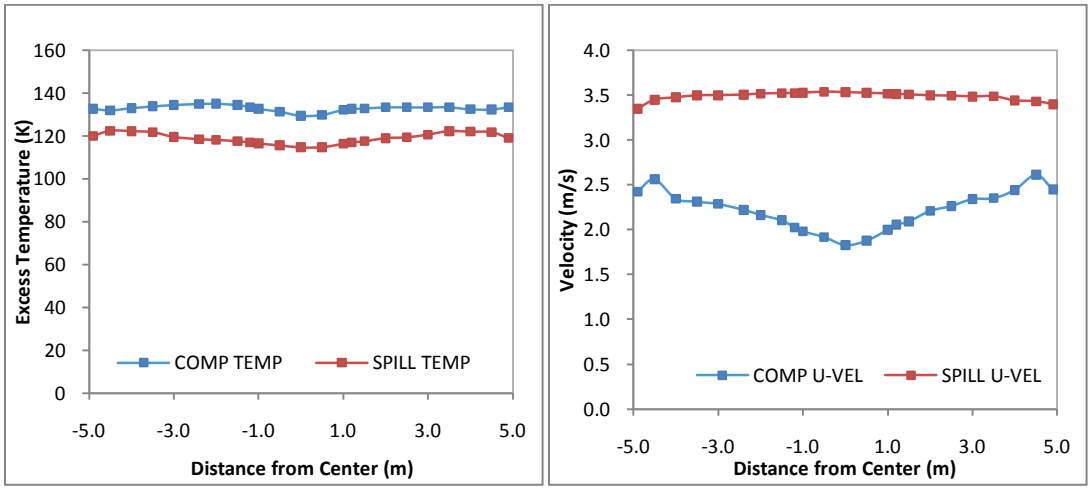

Figure F37: Lateral temperature and velocity profiles for simulation F10R

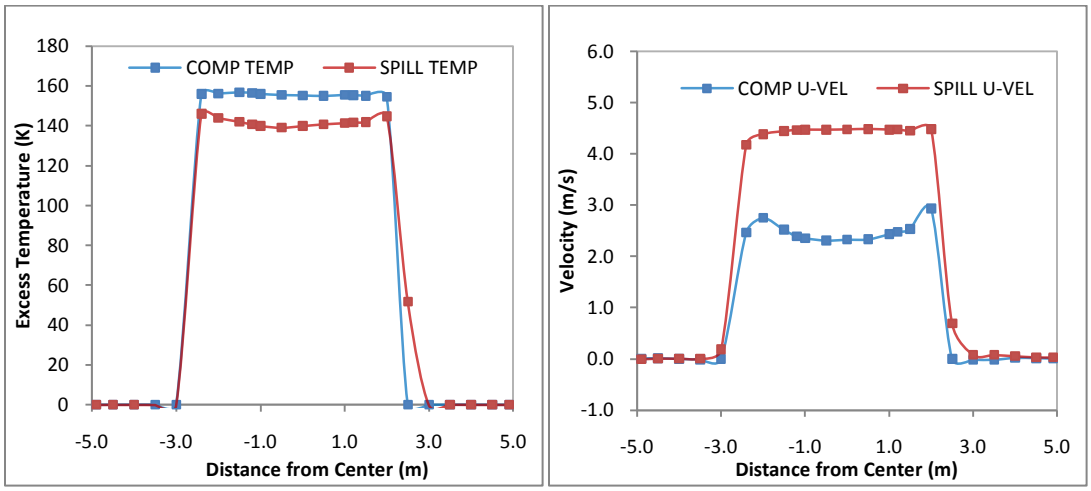

Figure F38: Lateral temperature and velocity profiles for simulation F11R

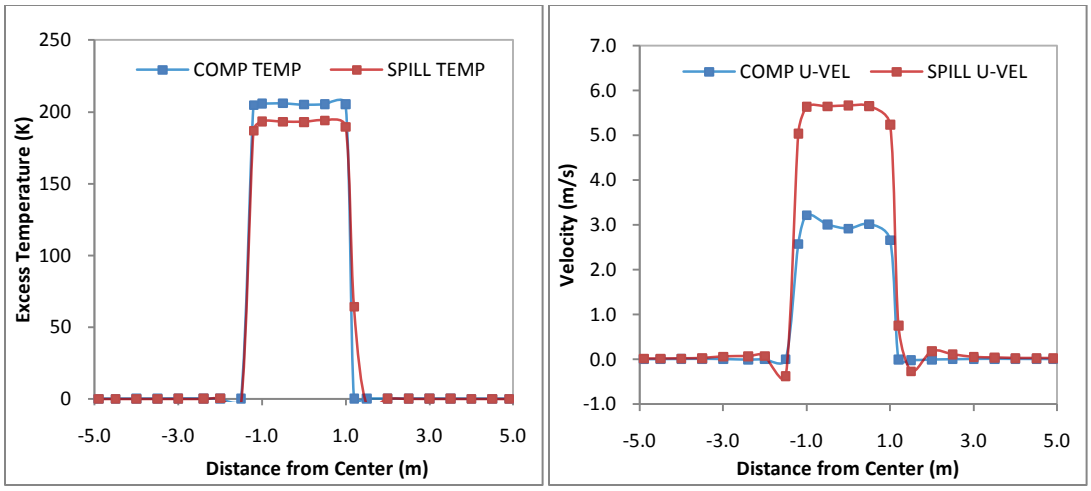

Figure F39: Lateral temperature and velocity profiles for simulation F12R

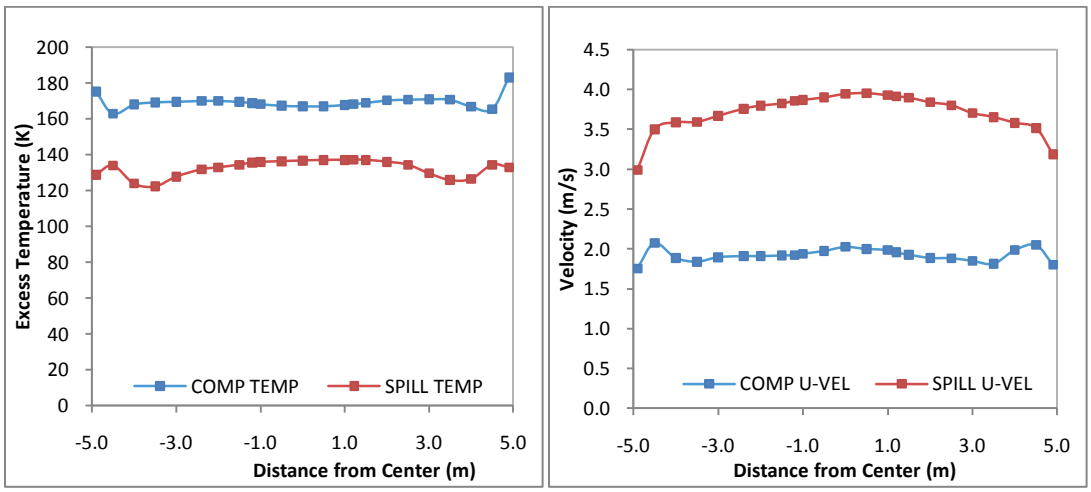

Figure F40: Lateral temperature and velocity profiles for simulation F13R

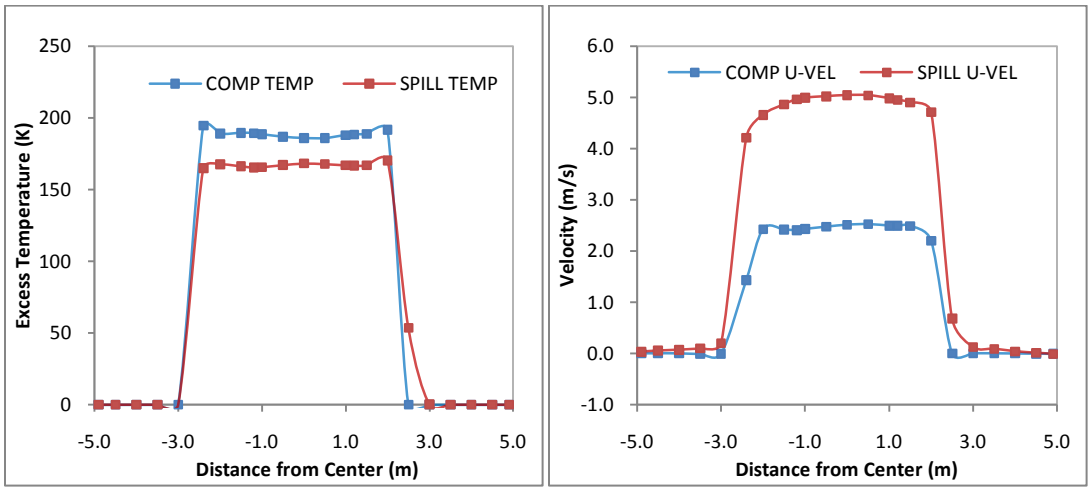

Figure F41: Lateral temperature and velocity profiles for simulation F14R

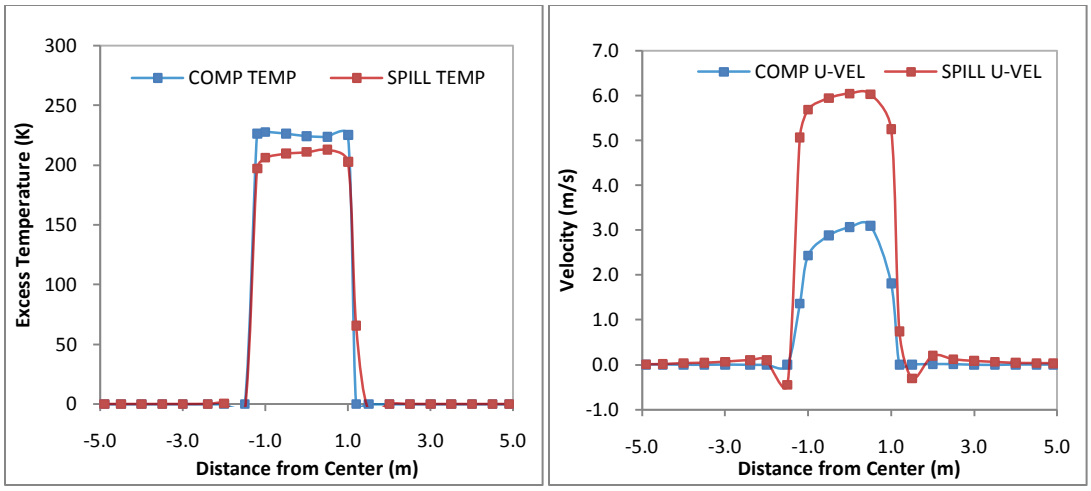

Figure F42: Lateral temperature and velocity profiles for simulation F15R

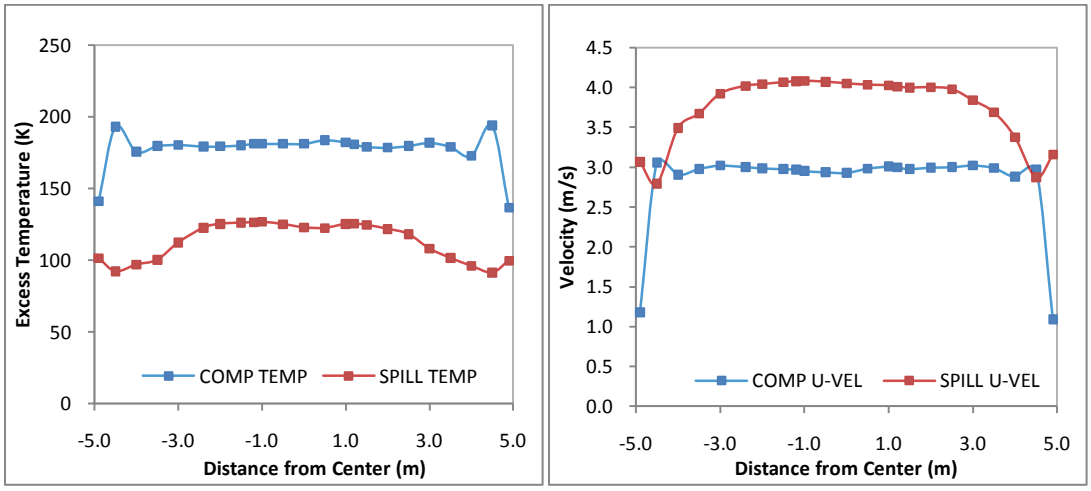

Figure F43: Lateral temperature and velocity profiles for simulation F16R

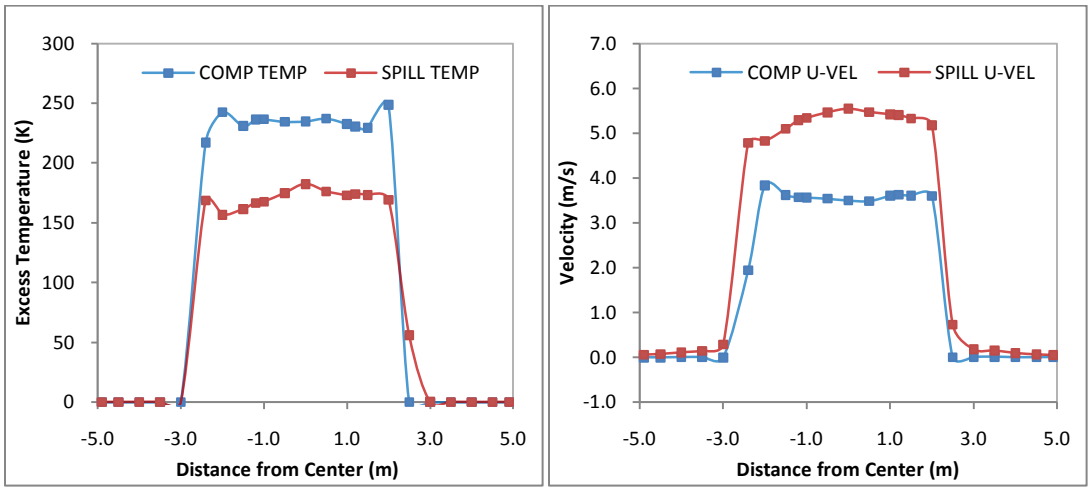

Figure F44: Lateral temperature and velocity profiles for simulation F17R

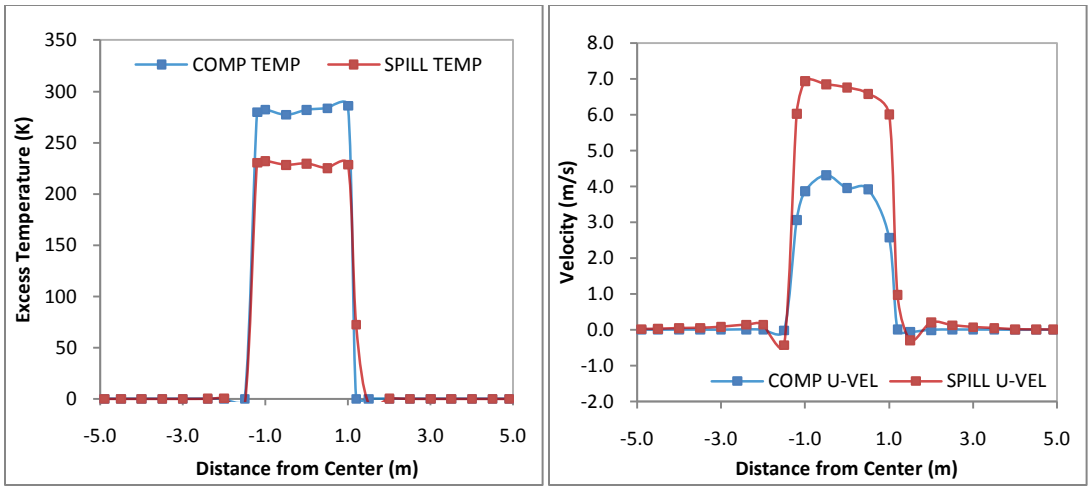

Figure F45: Lateral temperature and velocity profiles for simulation F18R

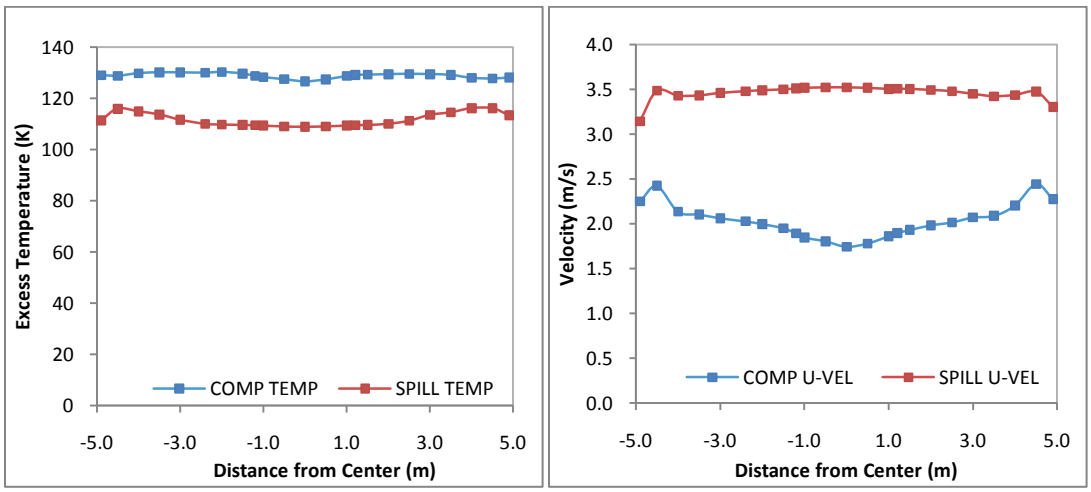

Figure F46: Lateral temperature and velocity profiles for simulation F19R

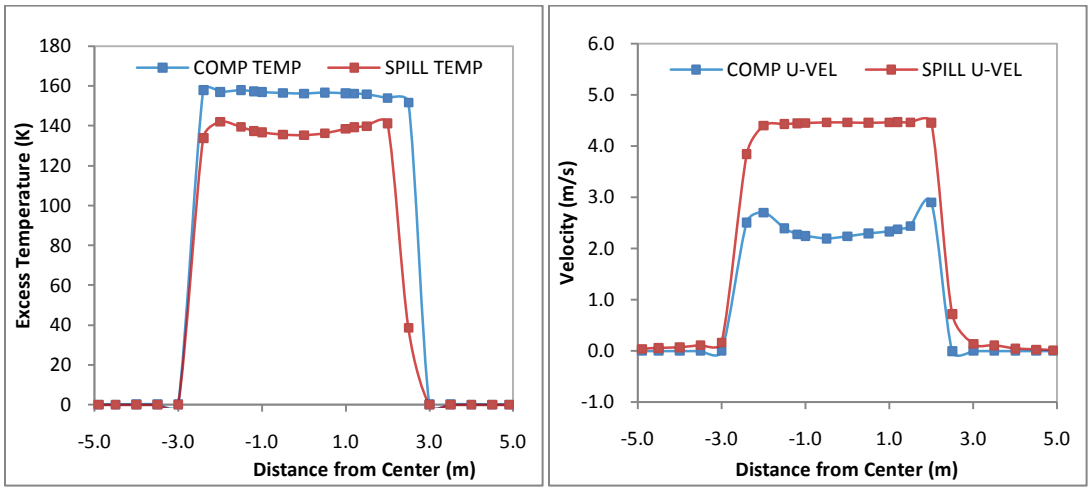

Figure F47: Lateral temperature and velocity profiles for simulation F20R

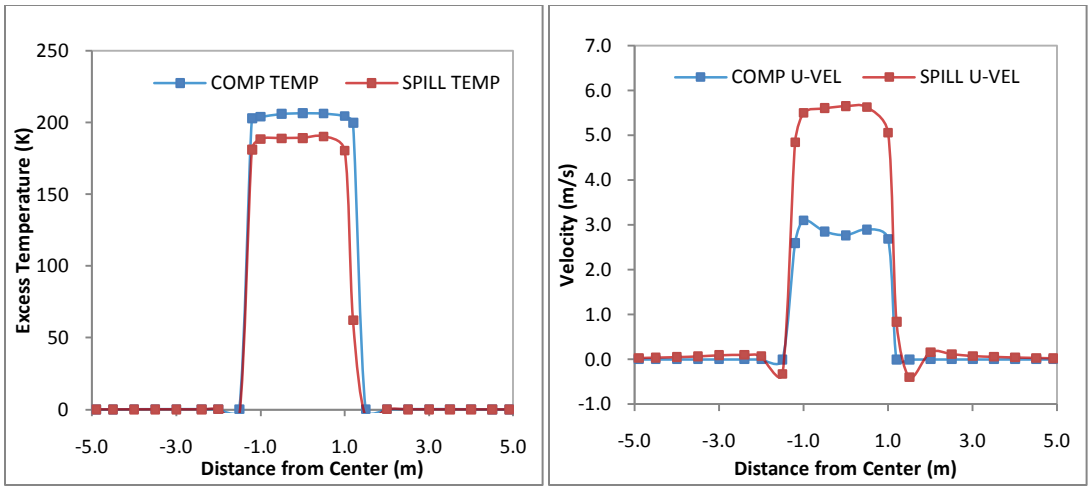

Figure F48: Lateral temperature and velocity profiles for simulation F21R

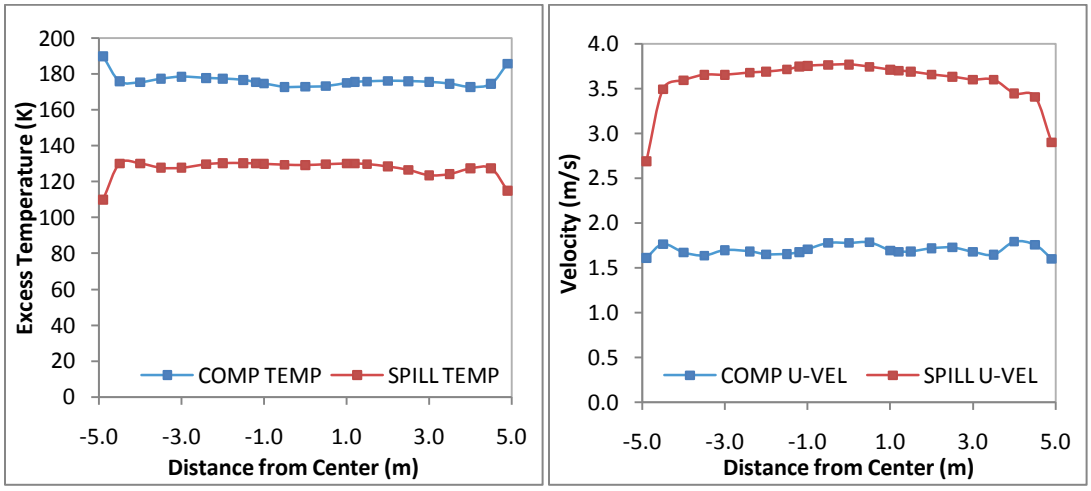

Figure F49: Lateral temperature and velocity profiles for simulation F22R

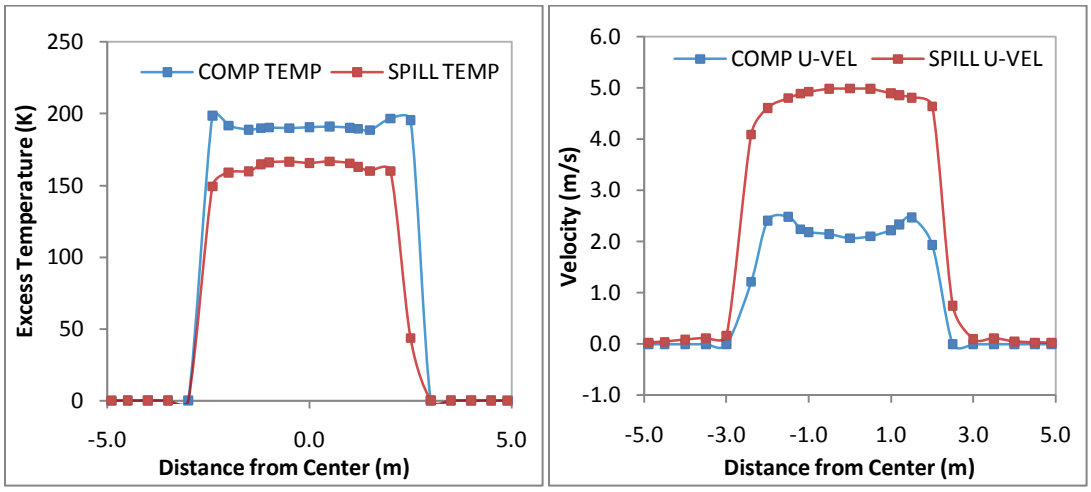

Figure F50: Lateral temperature and velocity profiles for simulation F23R

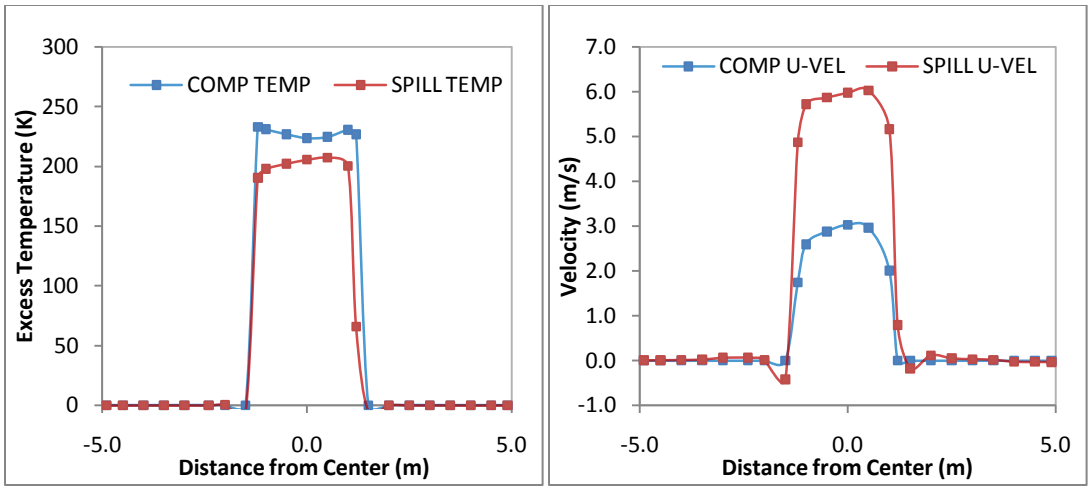

Figure F51: Lateral temperature and velocity profiles for simulation F24R

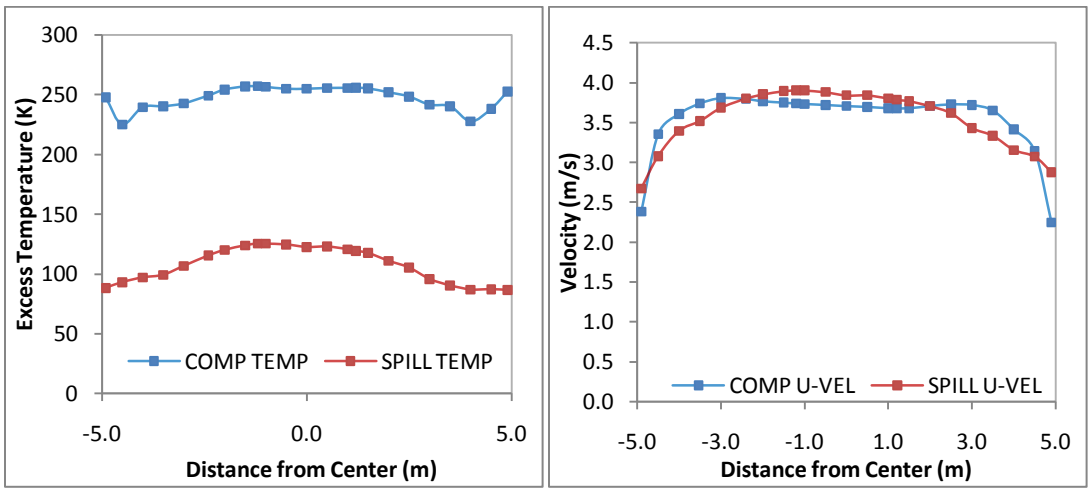

Figure F52: Lateral temperature and velocity profiles for simulation F25R

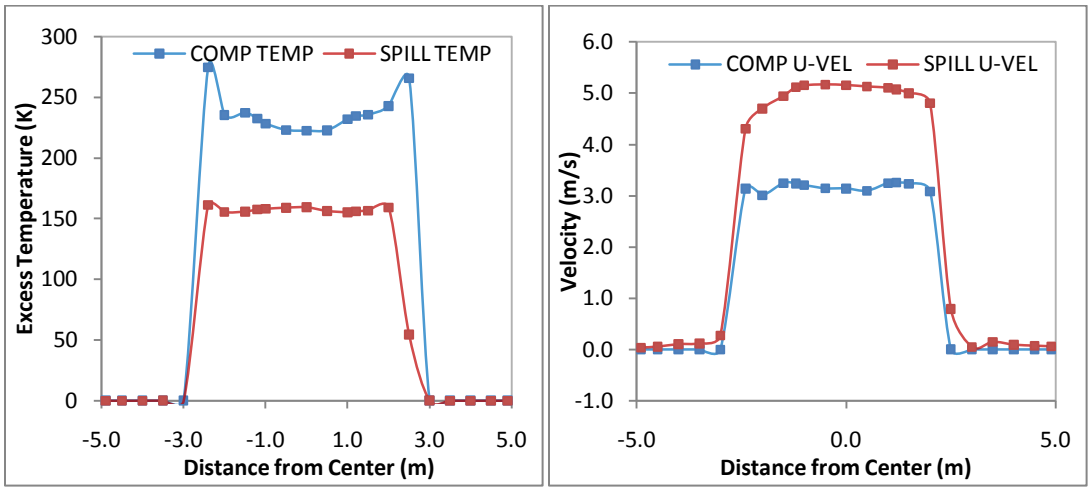

Figure F53: Lateral temperature and velocity profiles for simulation F26R

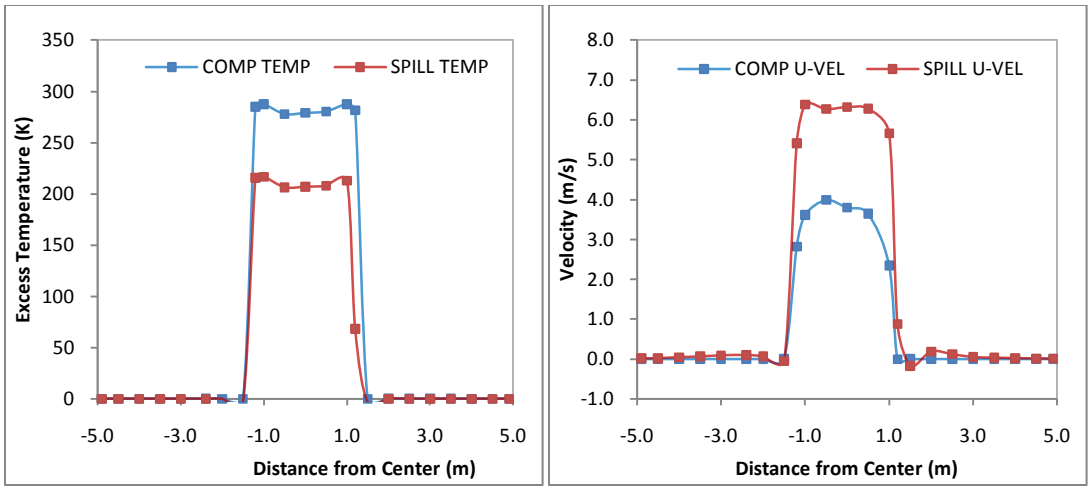

Figure F54: Lateral temperature and velocity profiles for simulation F27R

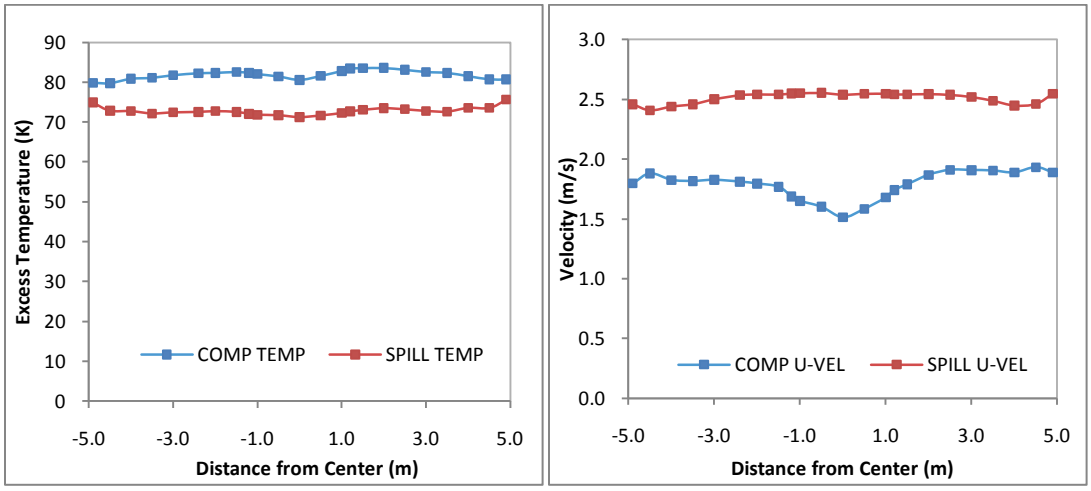

Figure F55: Lateral temperature and velocity profiles for simulation F1RR

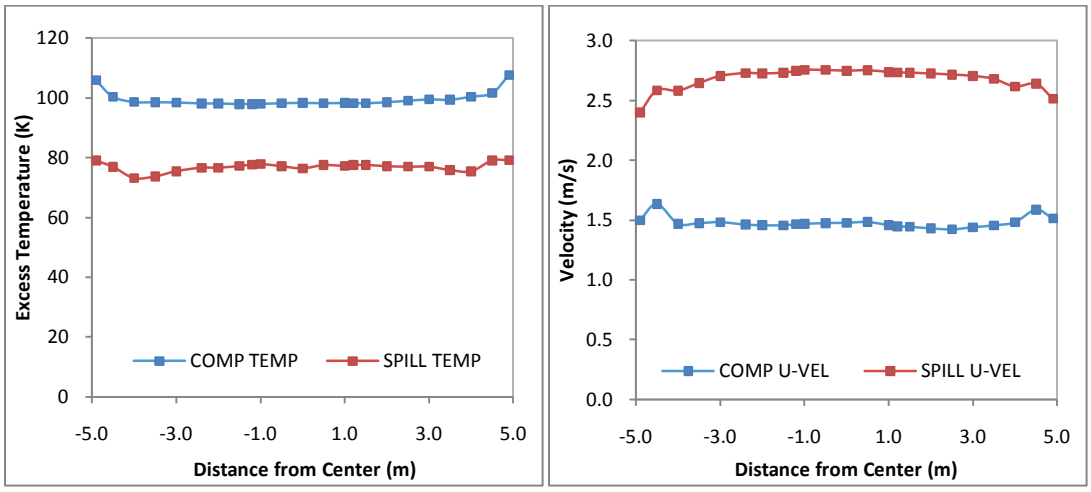

Figure F56: Lateral temperature and velocity profiles for simulation F4RR

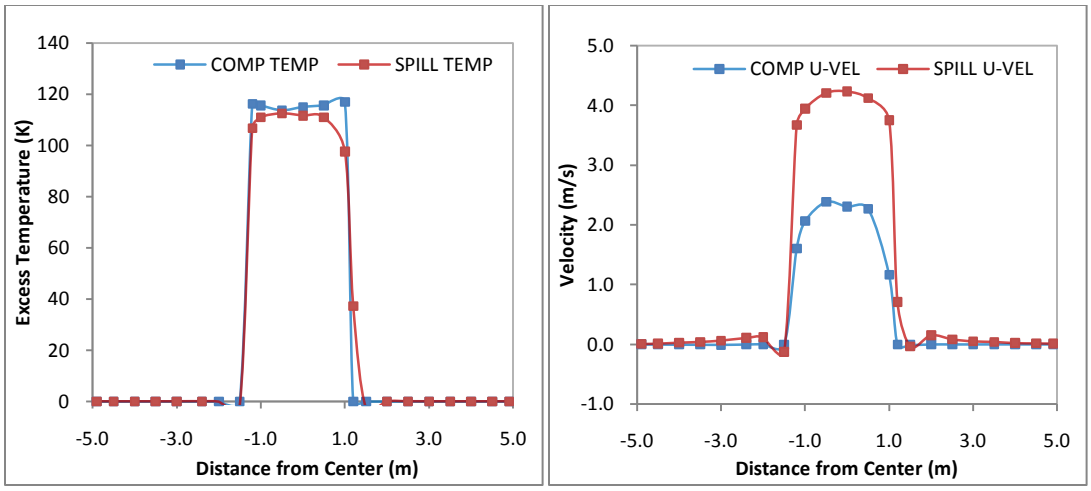

Figure F57: Lateral temperature and velocity profiles for simulation F6RR

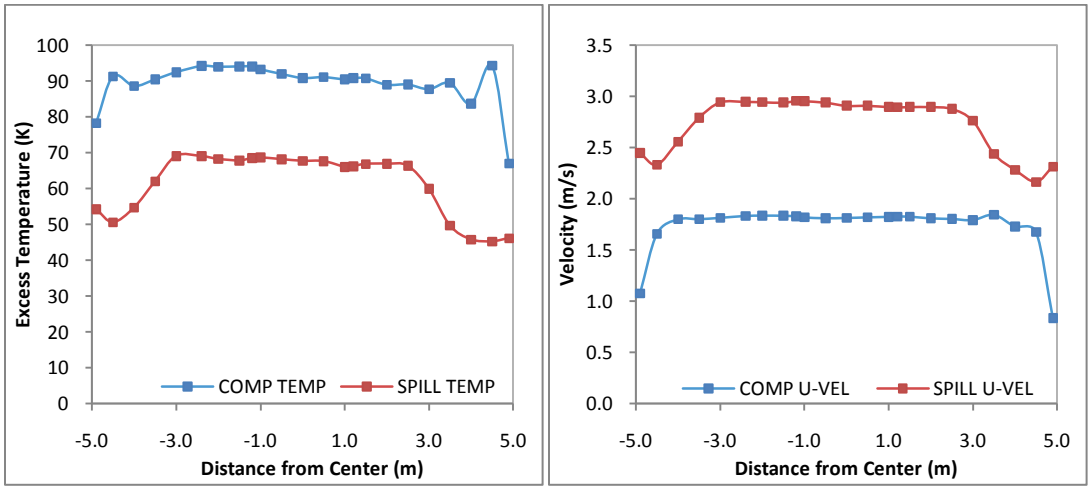

Figure F58: Lateral temperature and velocity profiles for simulation F7RR

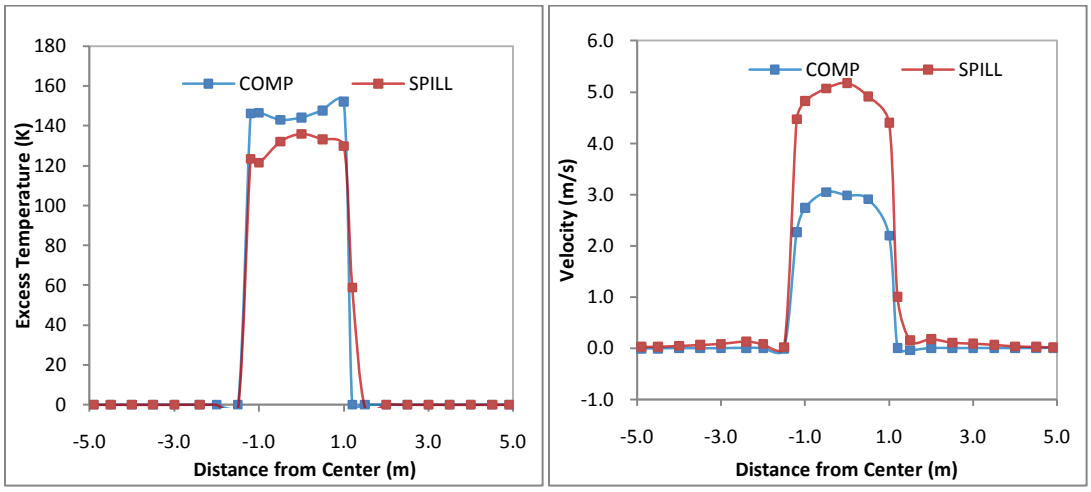

Figure F59: Lateral temperature and velocity profiles for simulation F9RR

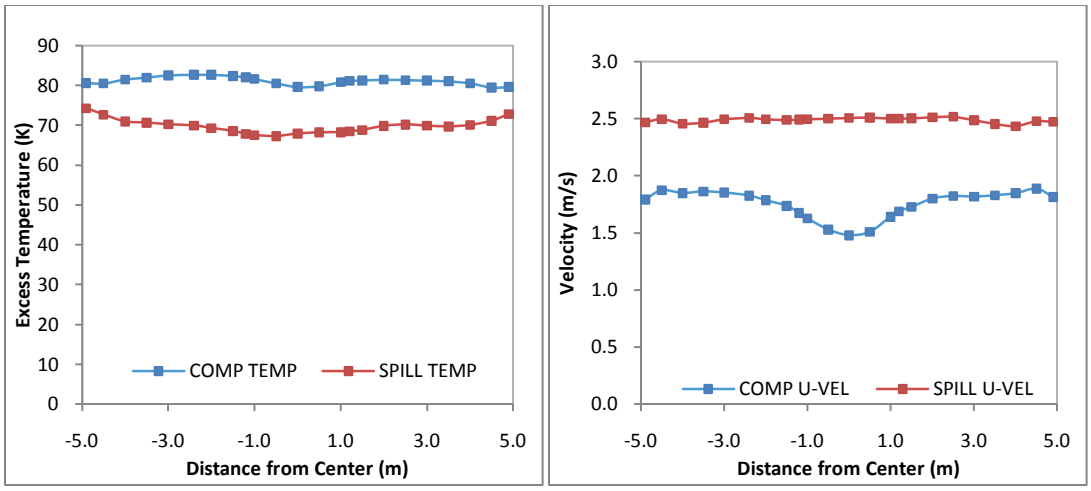

Figure F60: Lateral temperature and velocity profiles for simulation F10RR

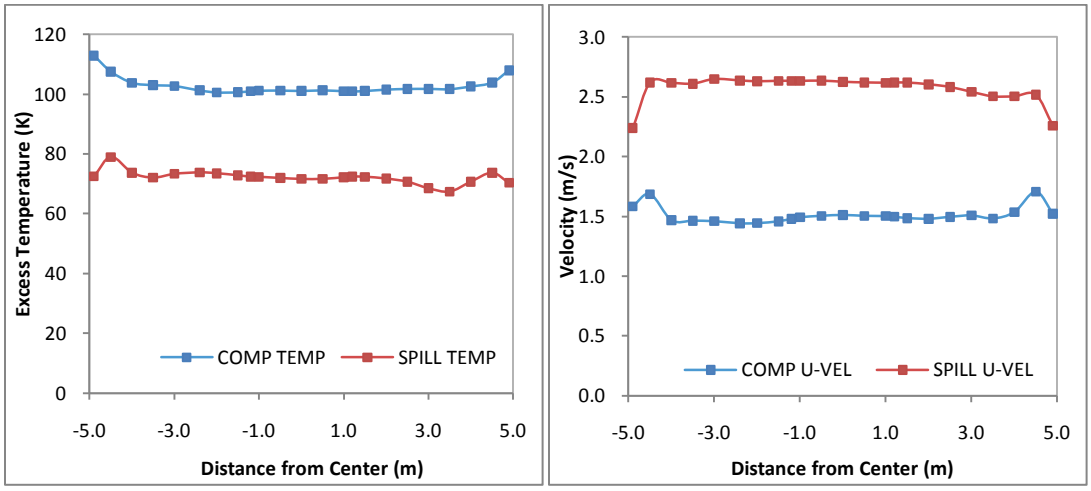

Figure F61: Lateral temperature and velocity profiles for simulation F13RR

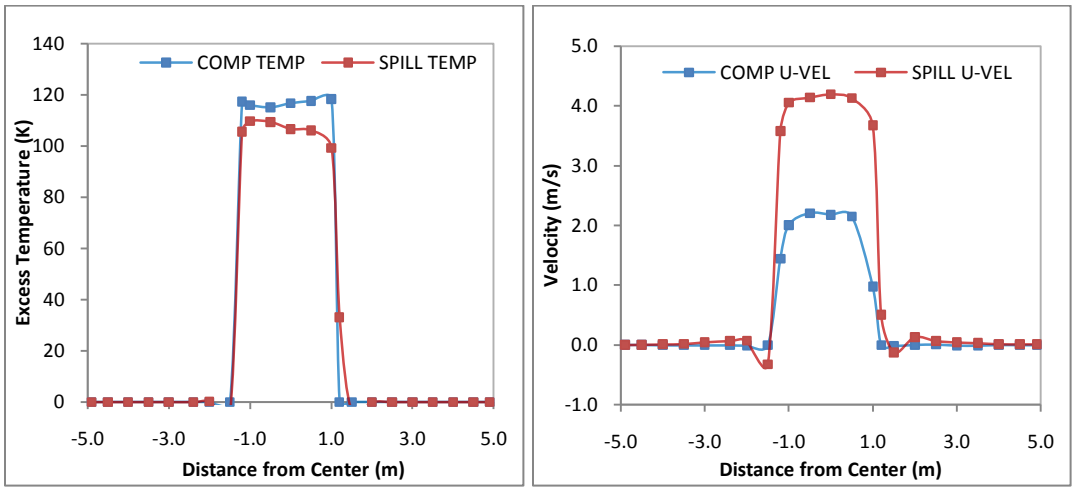

Figure F62: Lateral temperature and velocity profiles for simulation F15RR

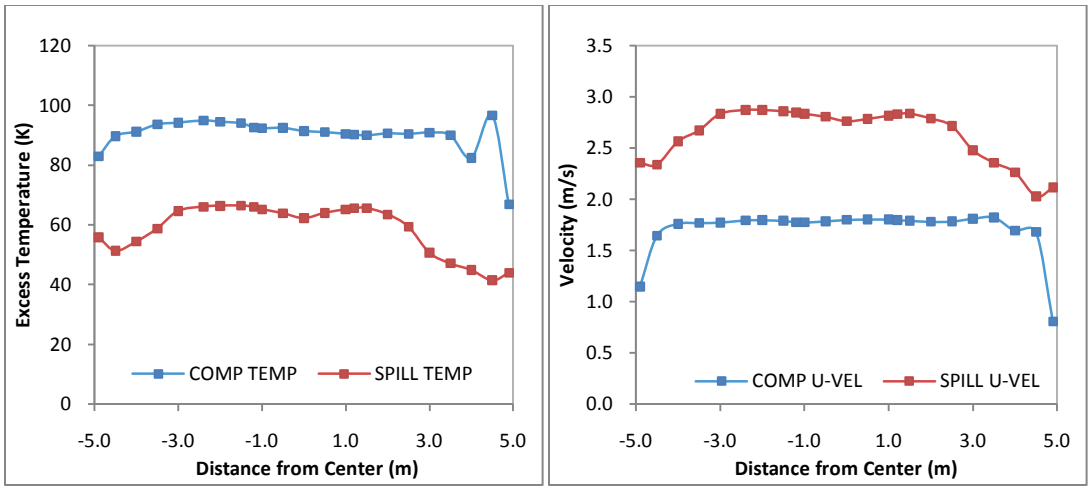

Figure F63: Lateral temperature and velocity profiles for simulation F16RR

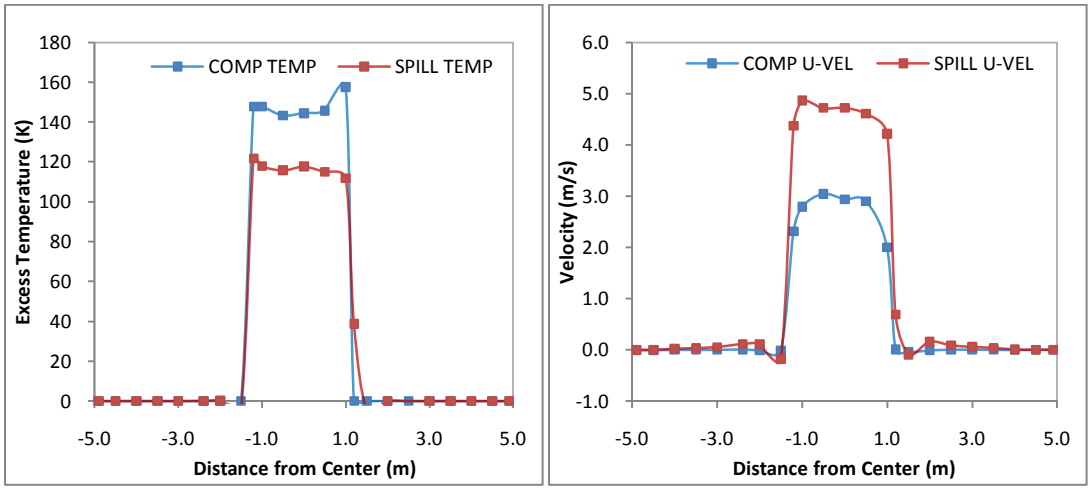

Figure F64: Lateral temperature and velocity profiles for simulation F18RR

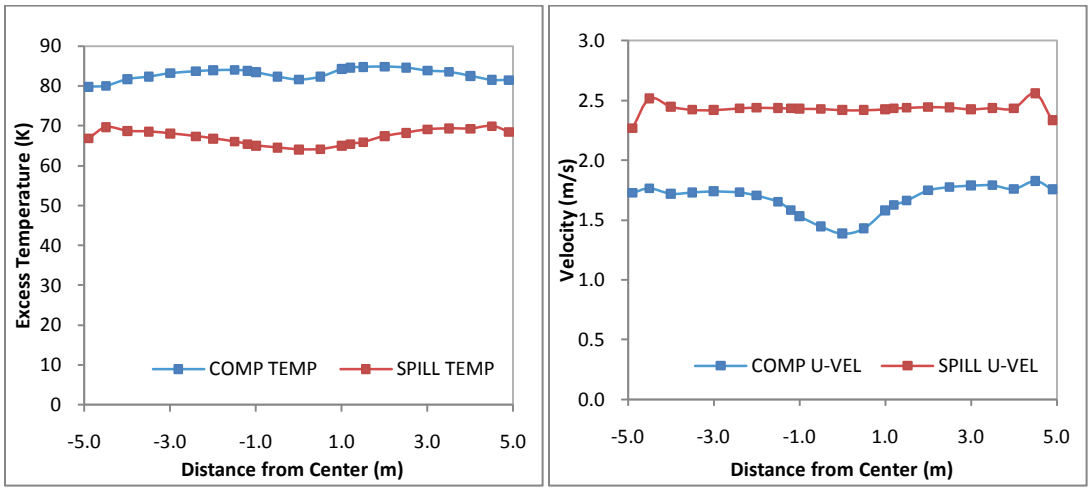

Figure F65: Lateral temperature and velocity profiles for simulation F19RR

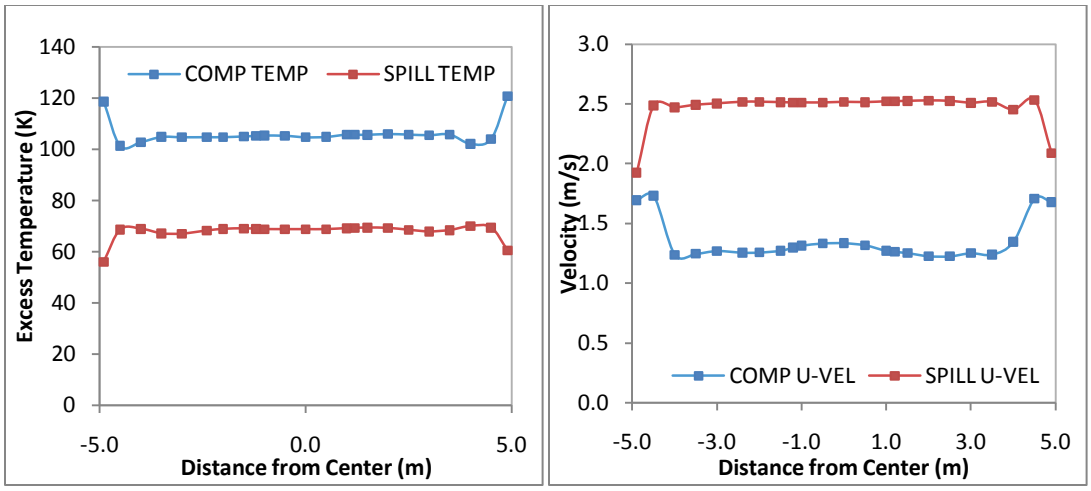

Figure F66: Lateral temperature and velocity profiles for simulation F22RR

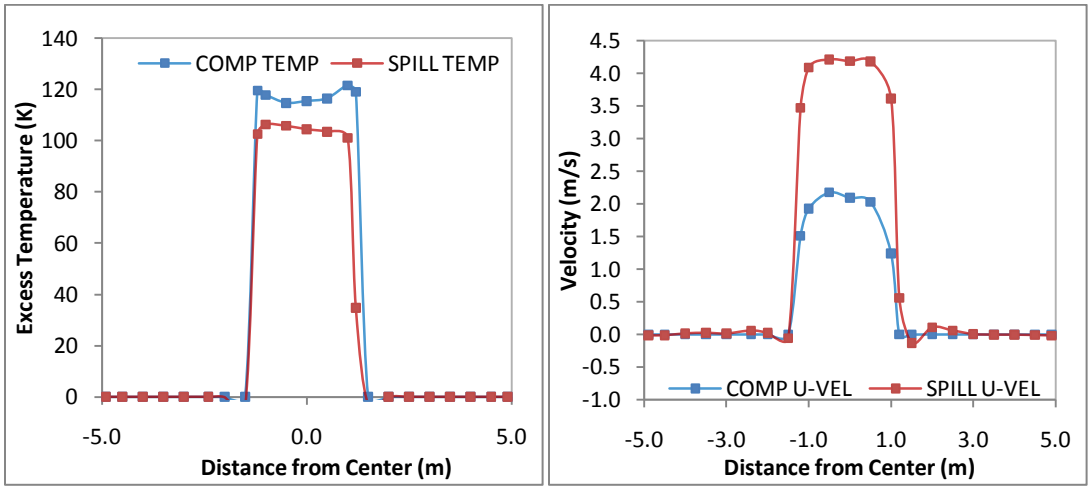

Figure F67: Lateral temperature and velocity profiles for simulation F24RR

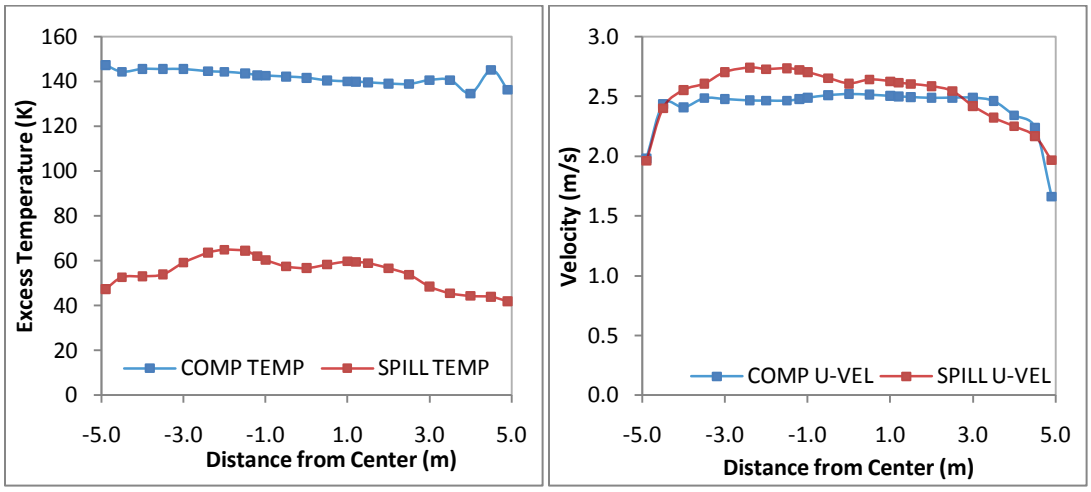

Figure F68: Lateral temperature and velocity profiles for simulation F25RR

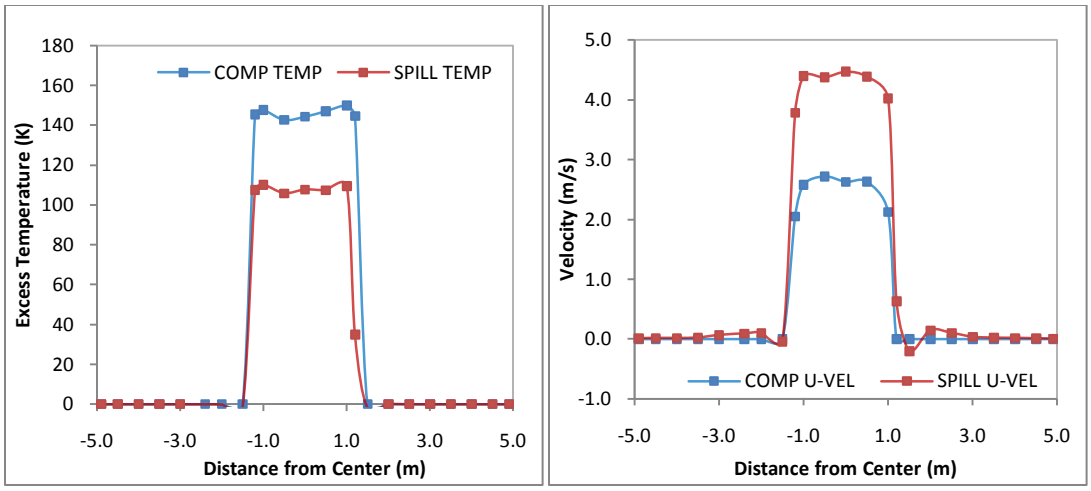

Figure F69: Lateral temperature and velocity profiles for simulation F27RR

APPENDIX G: Vertical temperature and velocity profiles for full-scale balcony spill plume simulations

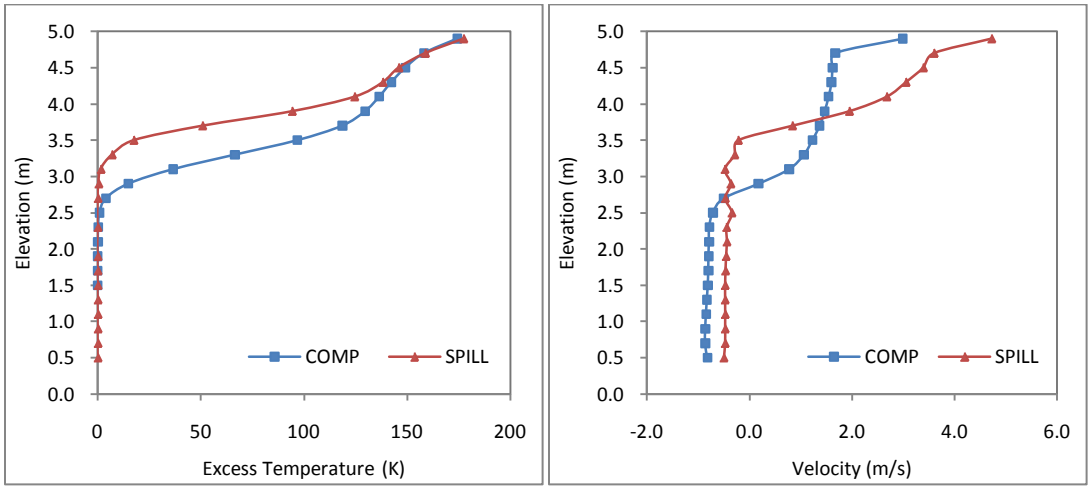

Figure G1: Vertical temperature and velocity profiles for simulation F1

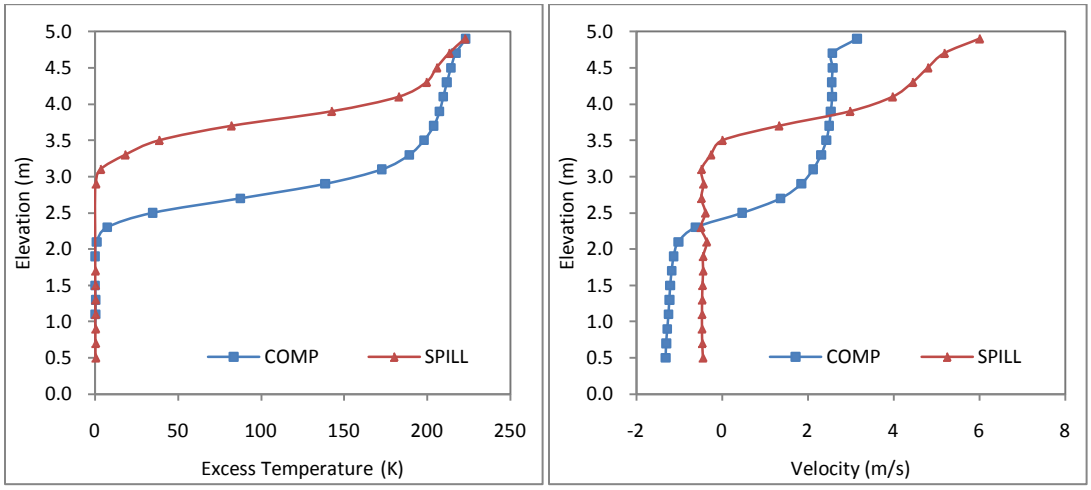

Figure G2: Vertical temperature and velocity profiles for simulation F2

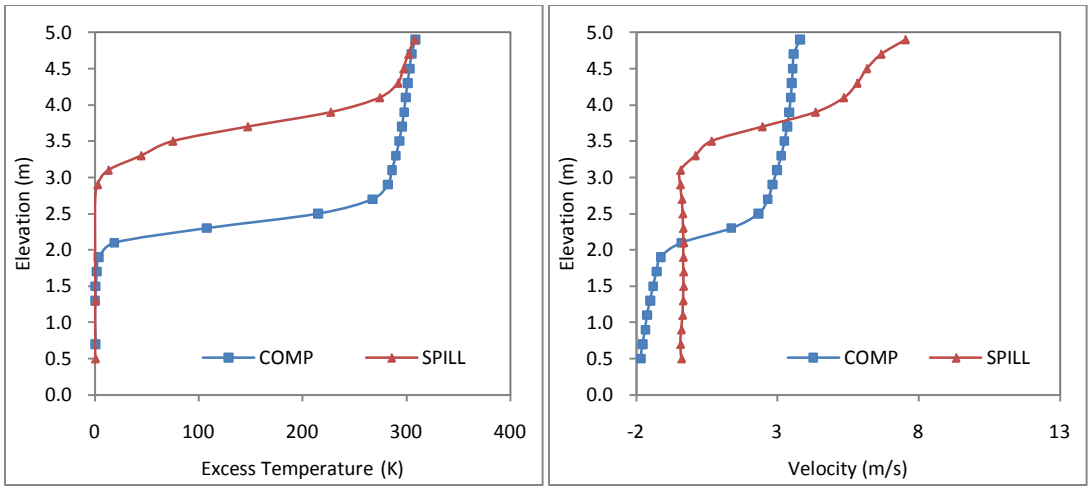

Figure G3: Vertical temperature and velocity profiles for simulation F3

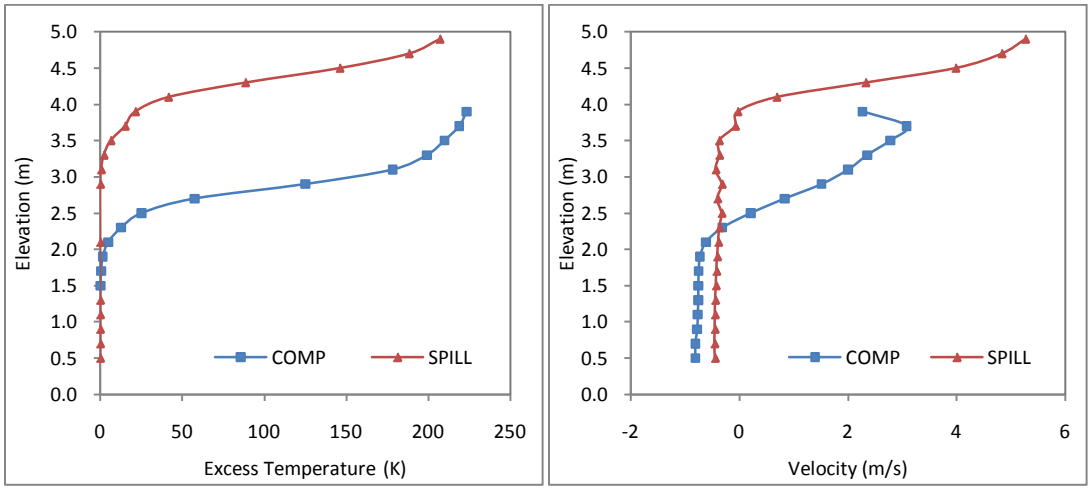

Figure G4: Vertical temperature and velocity profiles for simulation F4

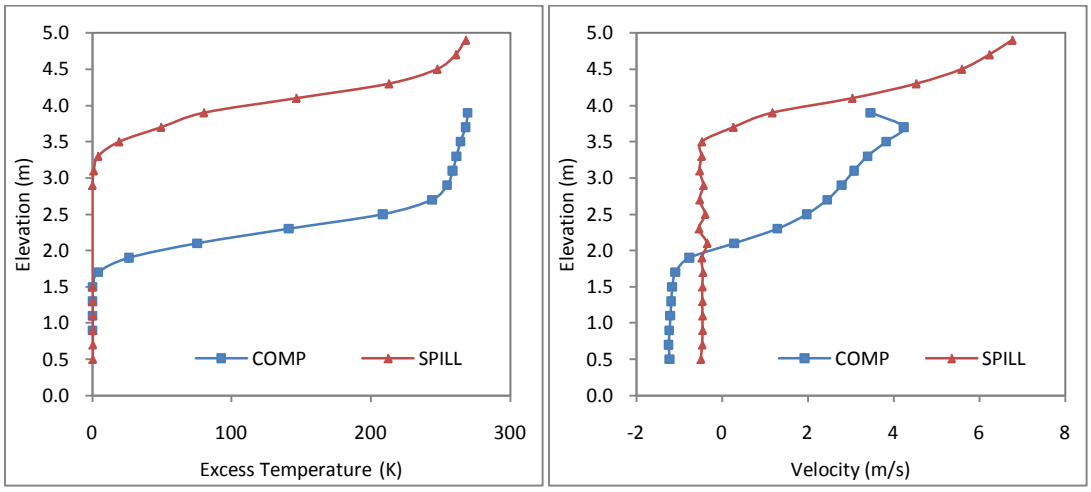

Figure G5: Vertical temperature and velocity profiles for simulation F5

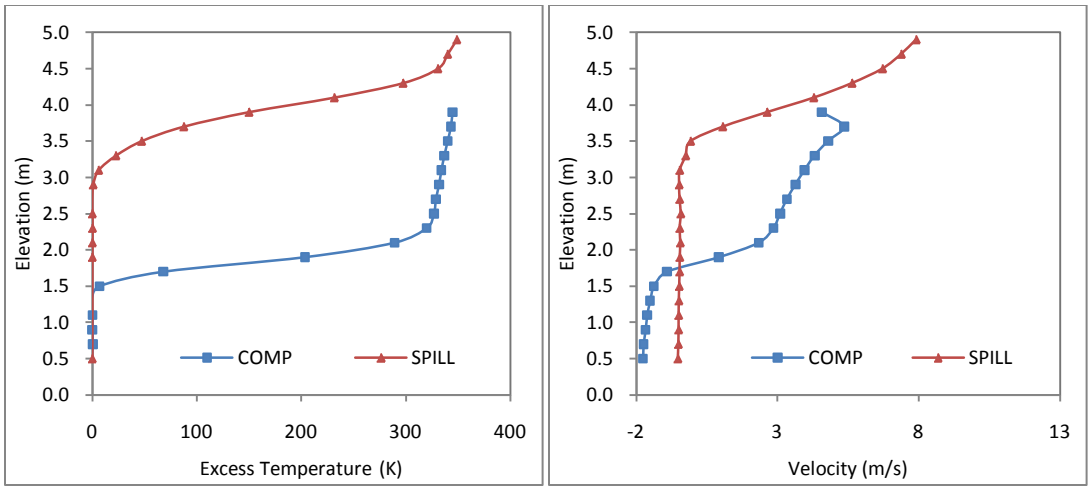

Figure G6: Vertical temperature and velocity profiles for simulation F6

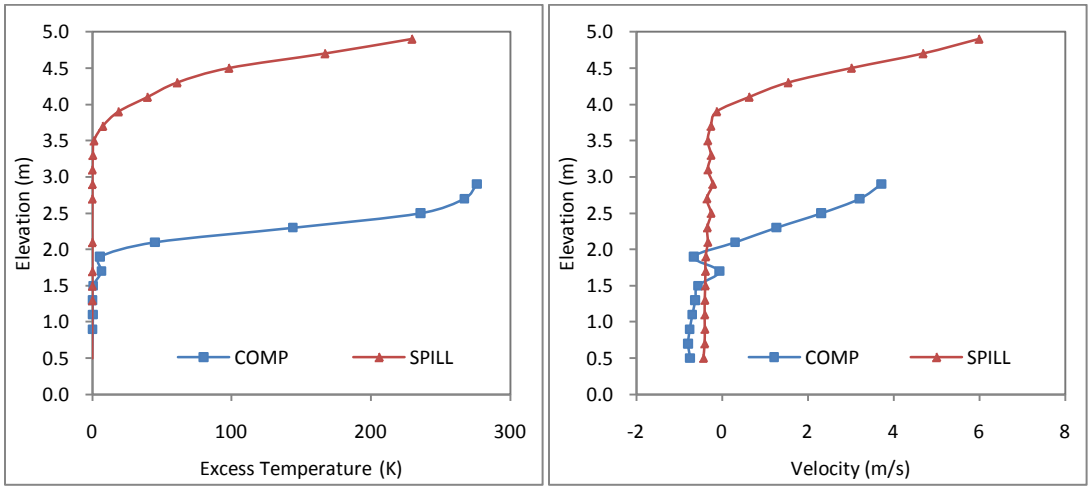

Figure G7: Vertical temperature and velocity profiles for simulation F7

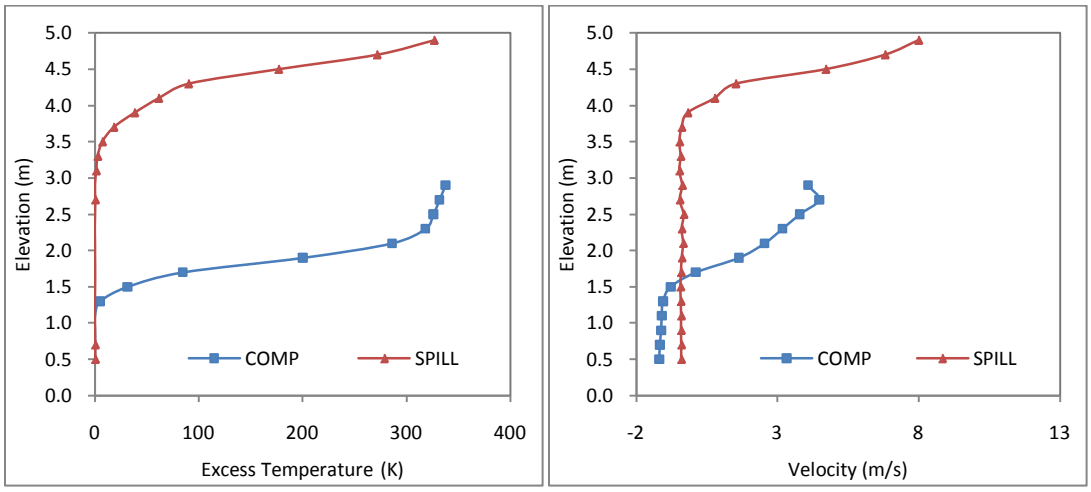

Figure G8: Vertical temperature and velocity profiles for simulation F8

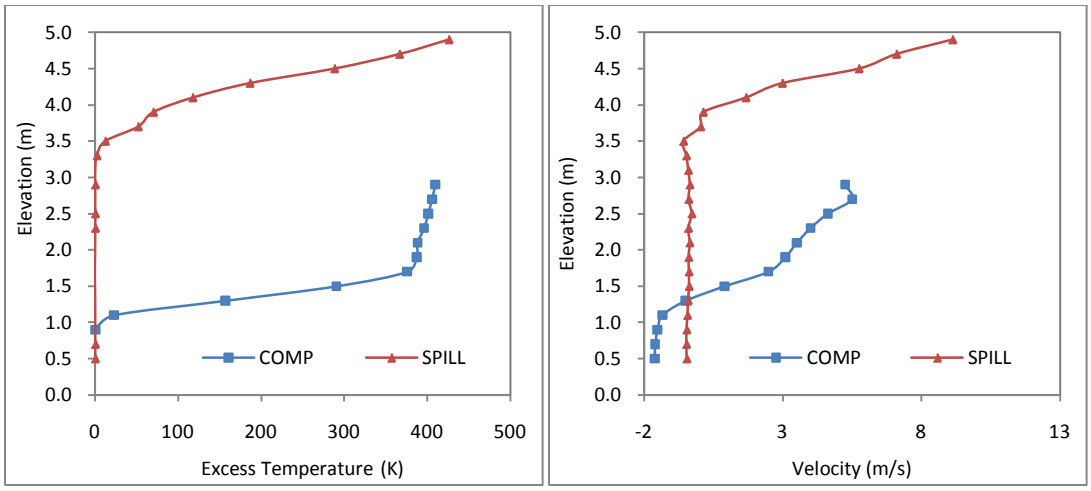

Figure G9: Vertical temperature and velocity profiles for simulation F9

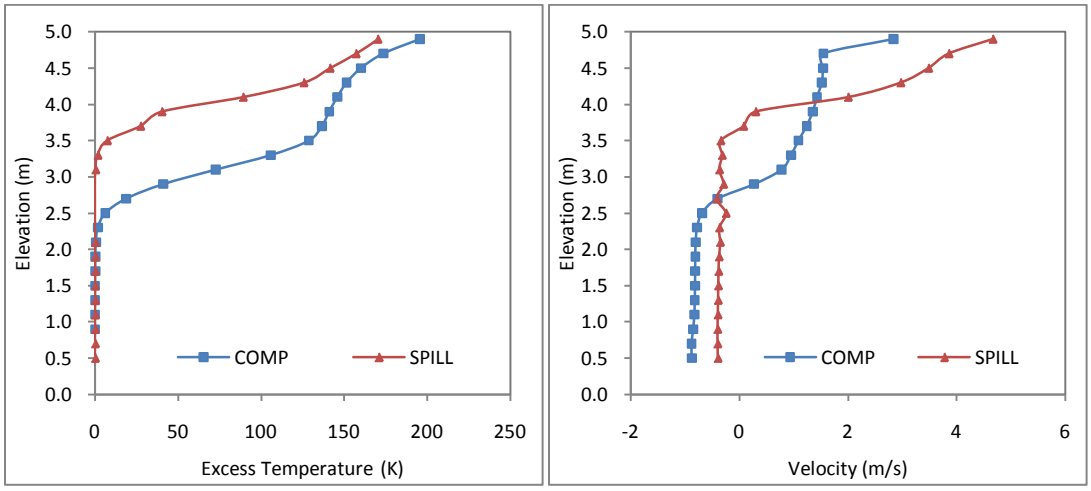

Figure G10: Vertical temperature and velocity profiles for simulation F10

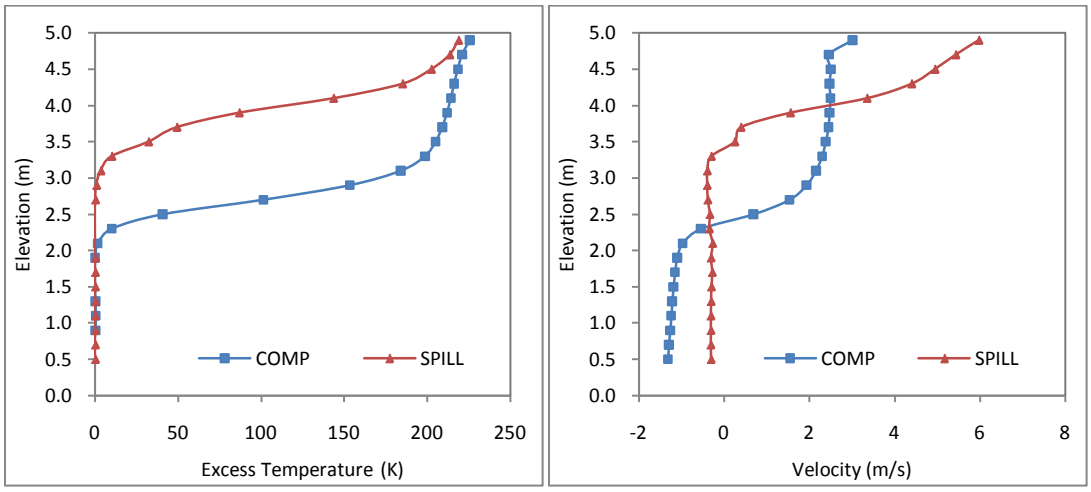

Figure G11: Vertical temperature and velocity profiles for simulation F11

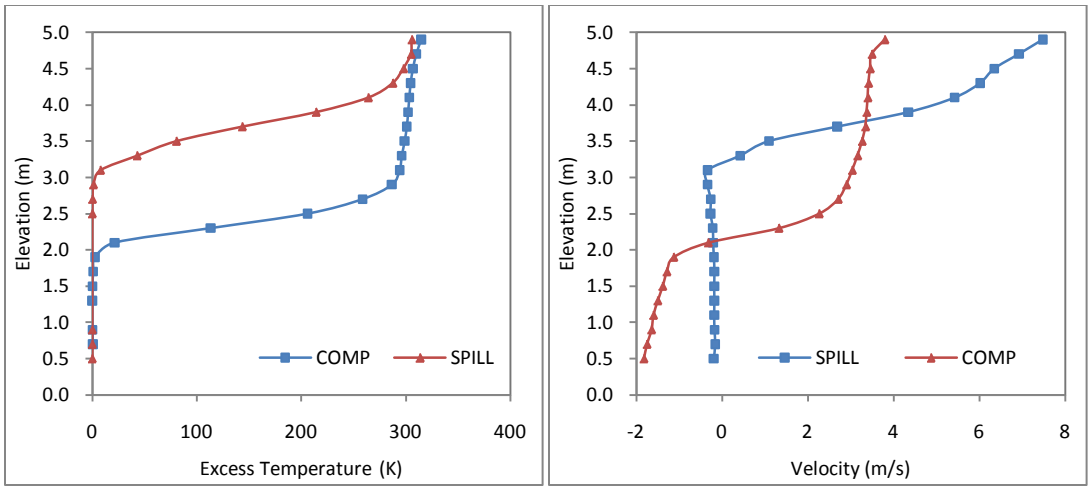

Figure G12: Vertical temperature and velocity profiles for simulation F12

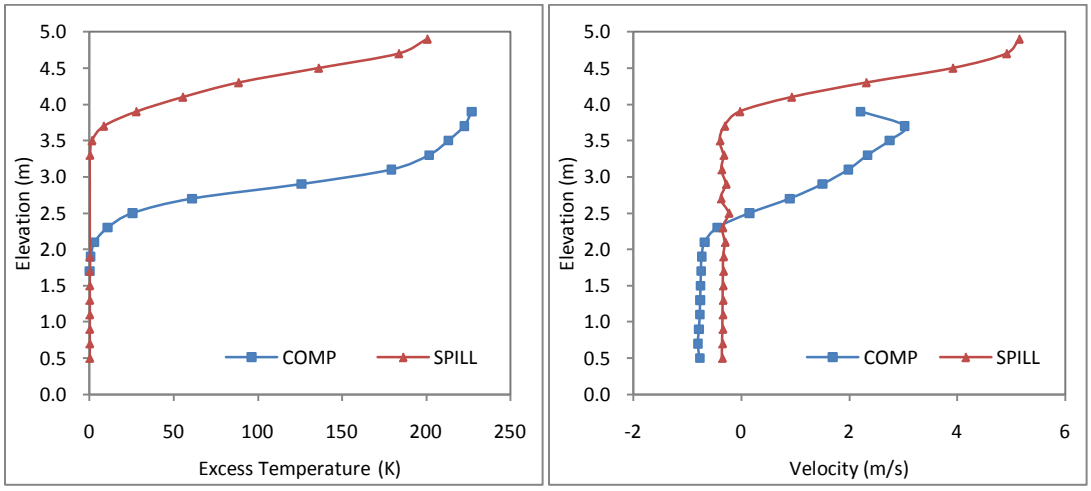

Figure G13: Vertical temperature and velocity profiles for simulation F13

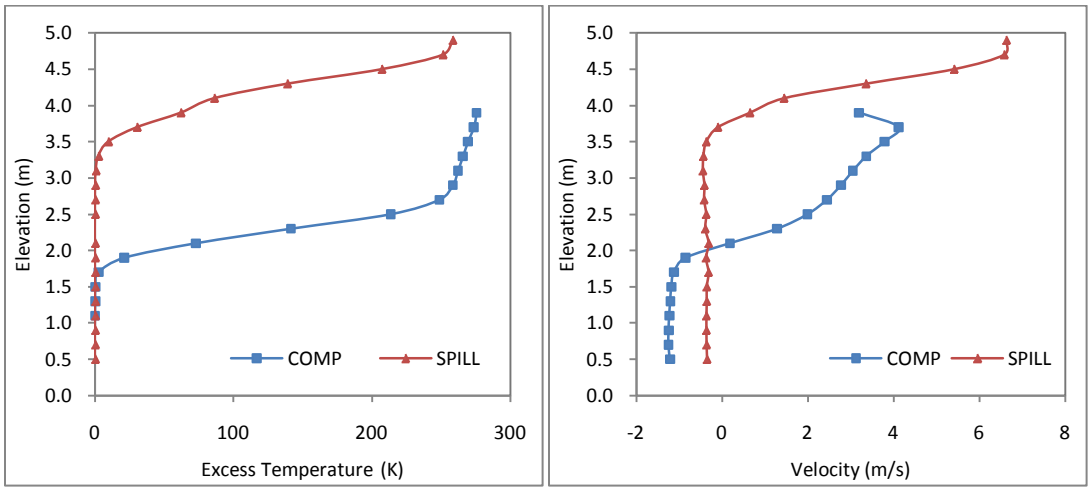

Figure G14: Vertical temperature and velocity profiles for simulation F14

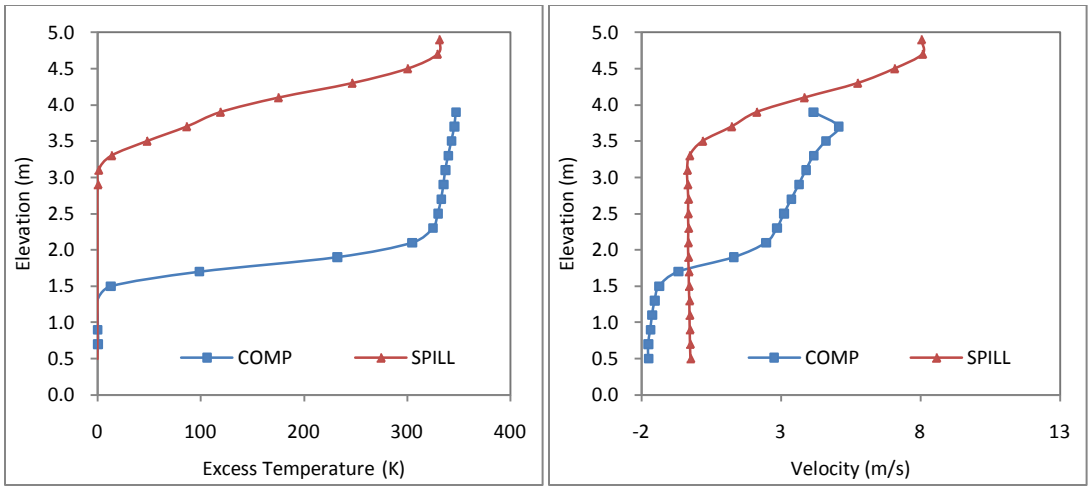

Figure G15: Vertical temperature and velocity profiles for simulation F15

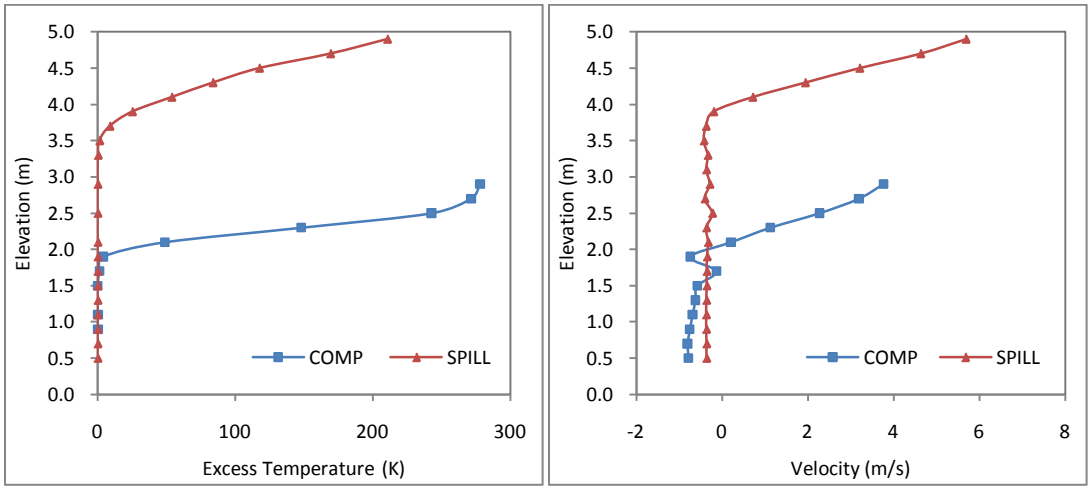

Figure G16: Vertical temperature and velocity profiles for simulation F16

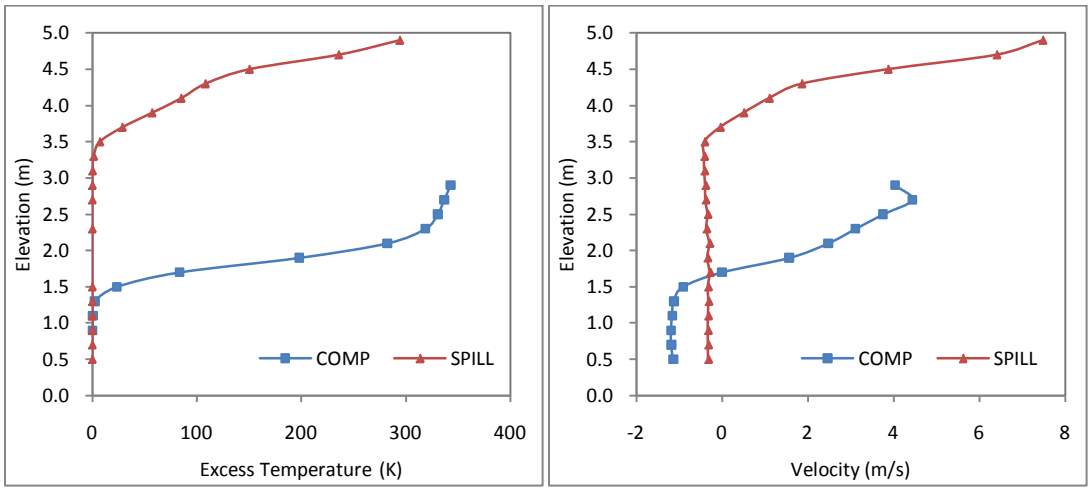

Figure G17: Vertical temperature and velocity profiles for simulation F17

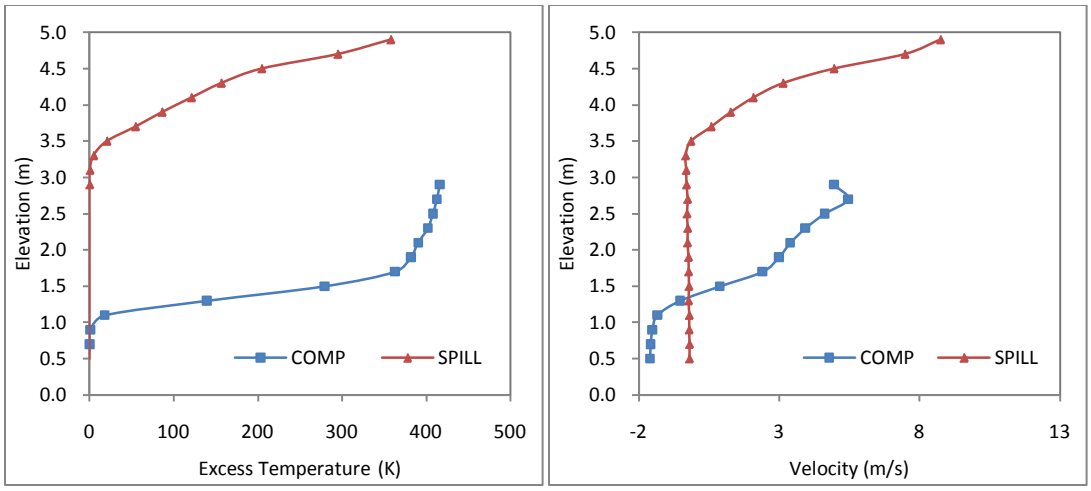

Figure G18: Vertical temperature and velocity profiles for simulation F18

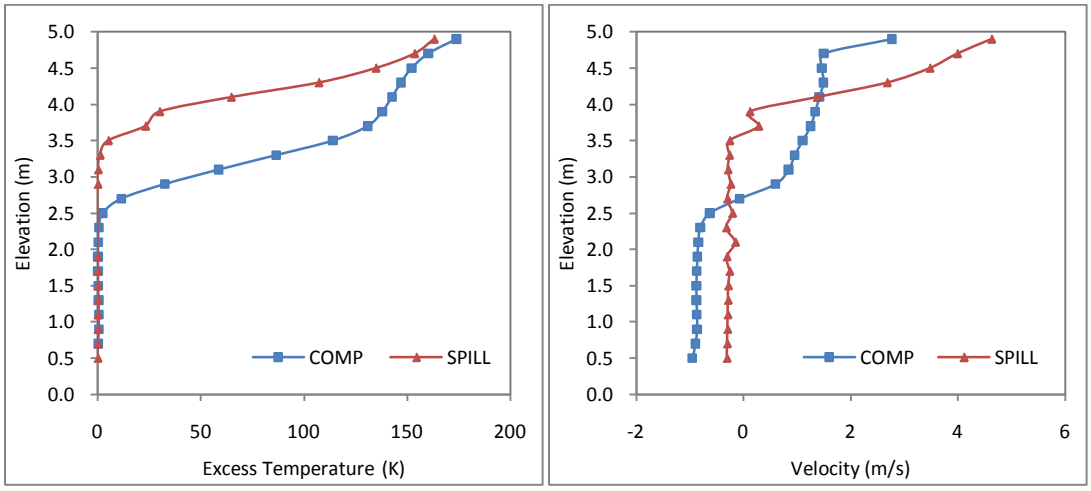

Figure G19: Vertical temperature and velocity profiles for simulation F19

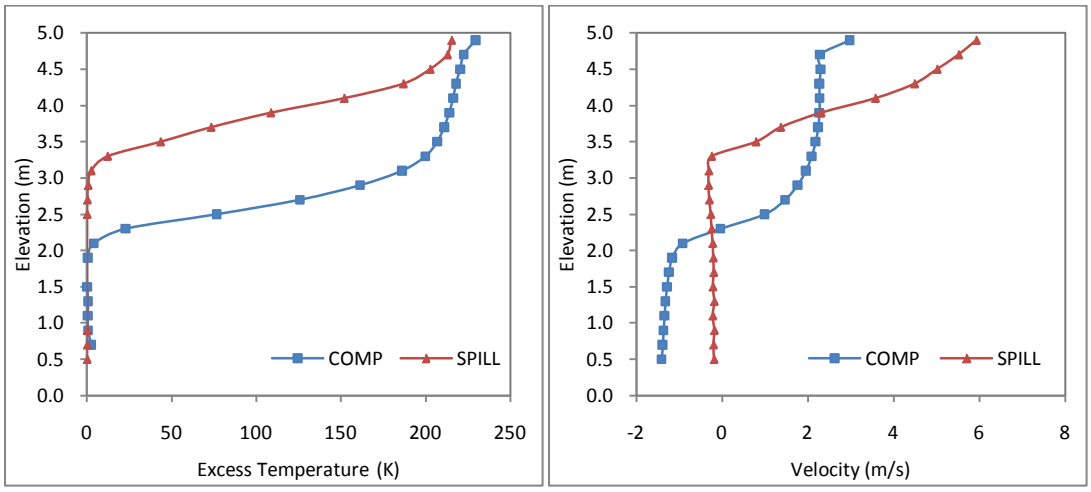

Figure G20: Vertical temperature and velocity profiles for simulation F20

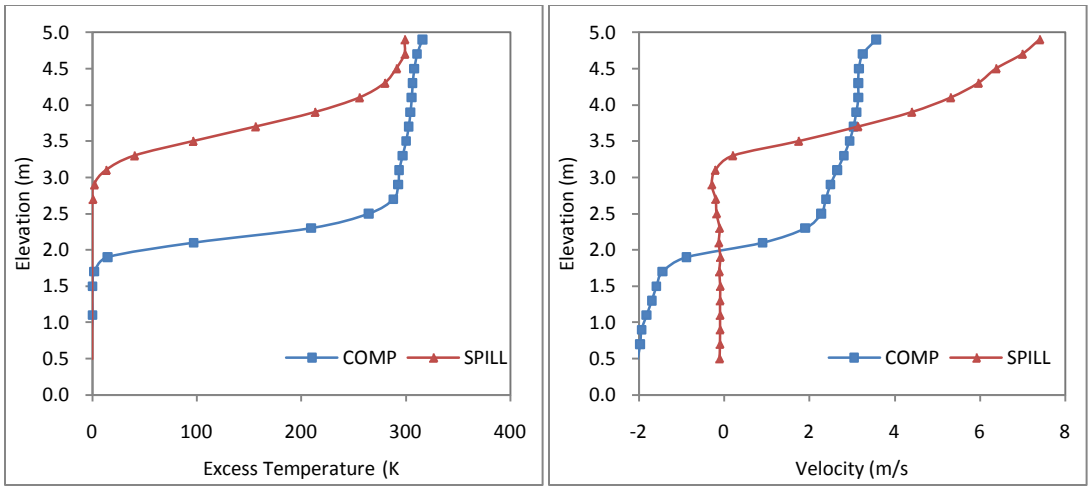

Figure G21: Vertical temperature and velocity profiles for simulation F21

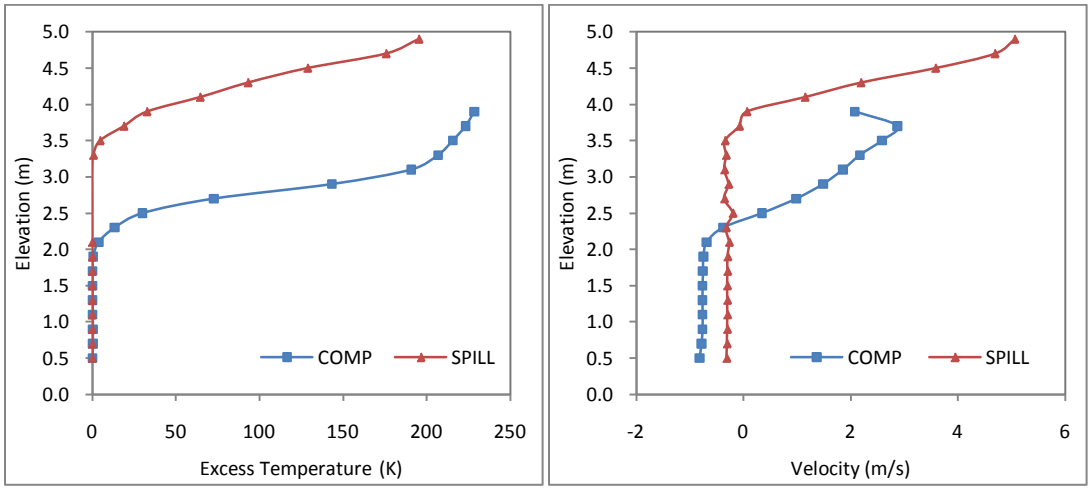

Figure G22: Vertical temperature and velocity profiles for simulation F22

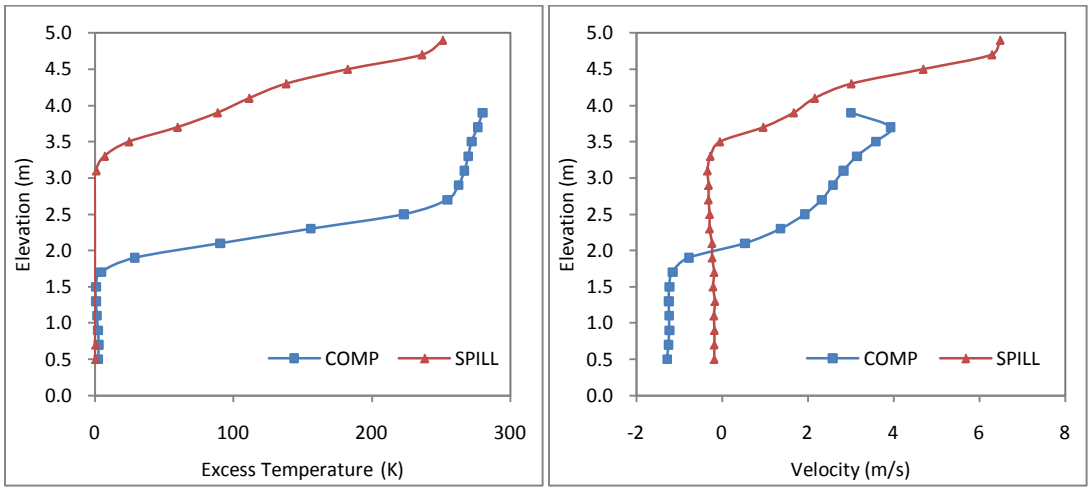

Figure G23: Vertical temperature and velocity profiles for simulation F23

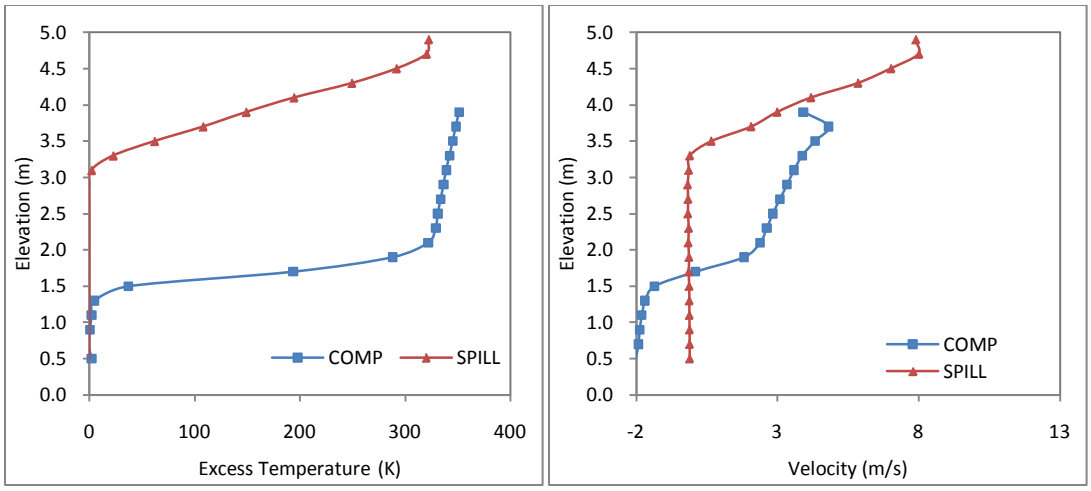

Figure G24: Vertical temperature and velocity profiles for simulation F24

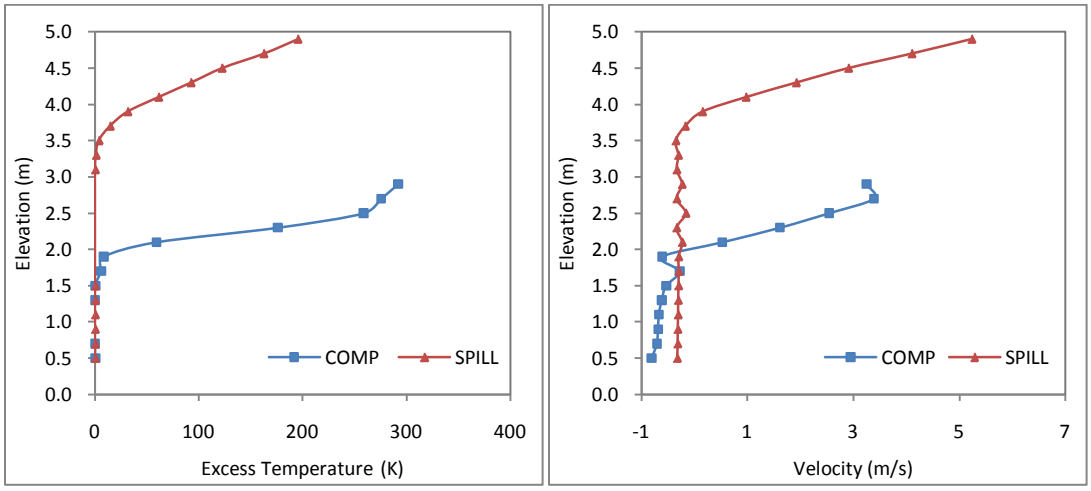

Figure G25: Vertical temperature and velocity profiles for simulation F25

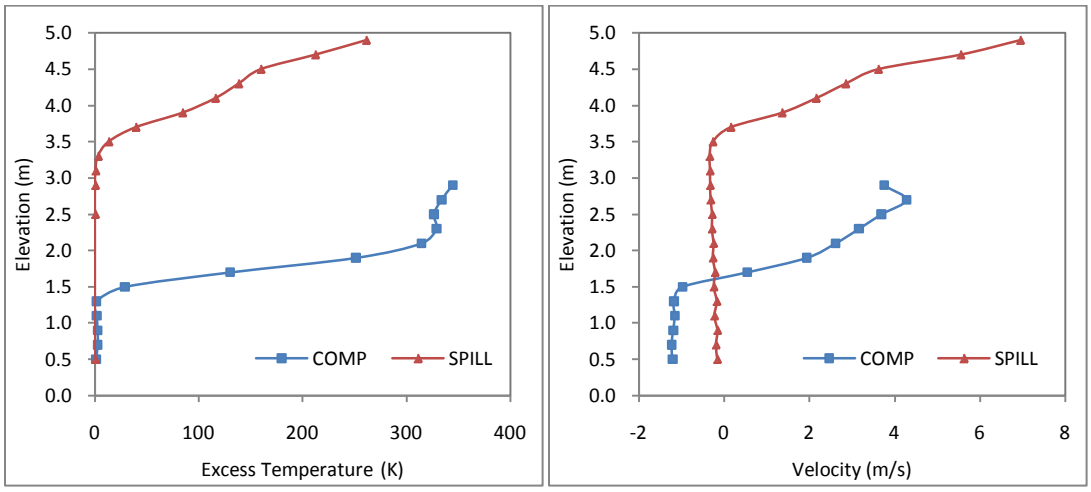

Figure G26: Vertical temperature and velocity profiles for simulation F26

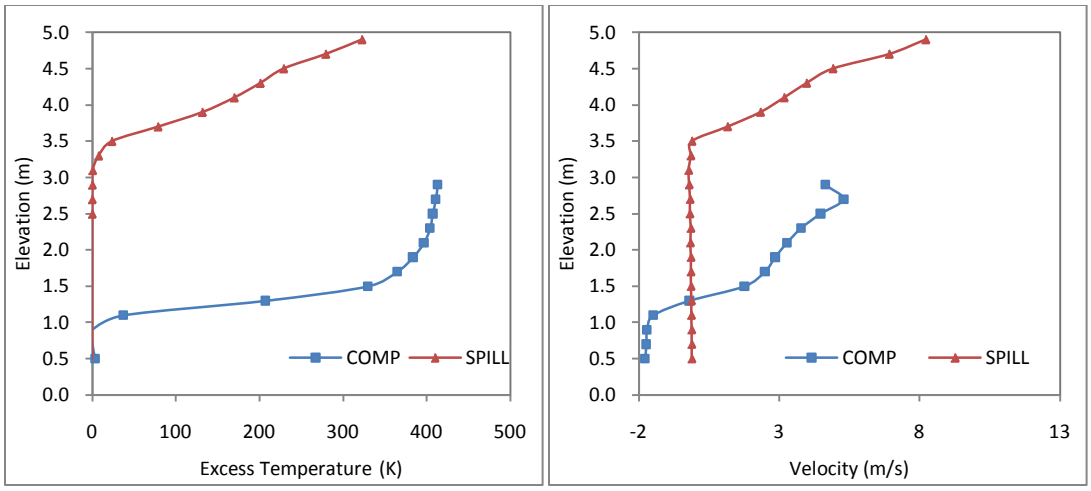

Figure G27: Vertical temperature and velocity profiles for simulation F27

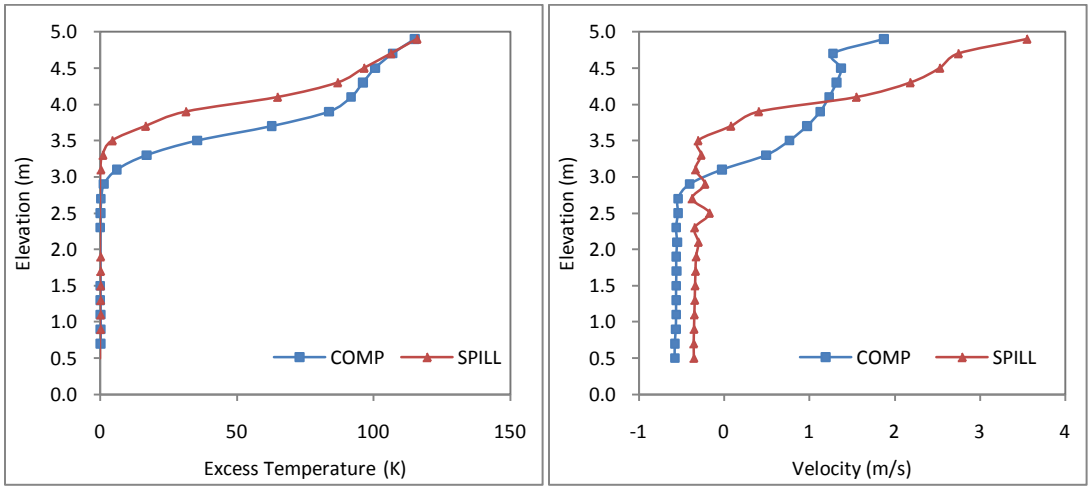

Figure G28: Vertical temperature and velocity profiles for simulation F1R

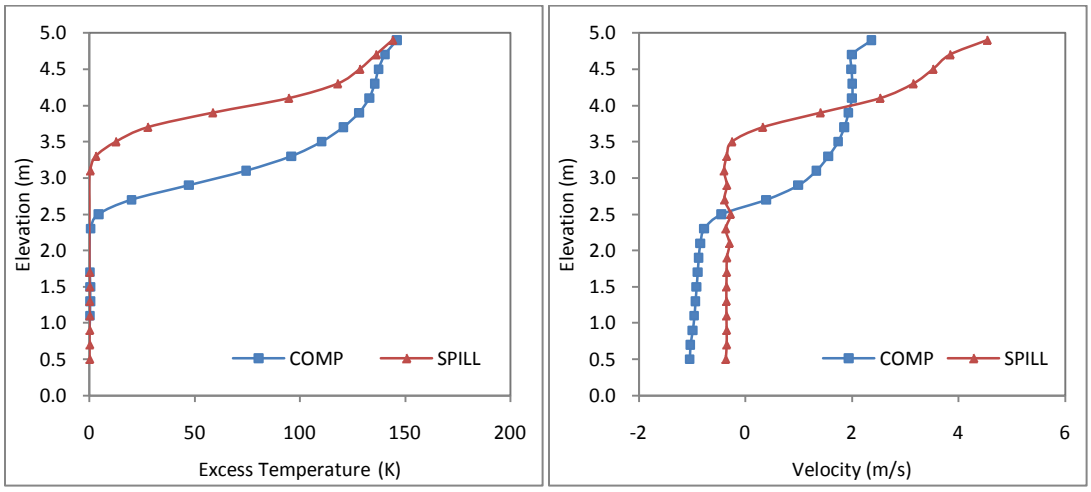

Figure G29: Vertical temperature and velocity profiles for simulation F2R

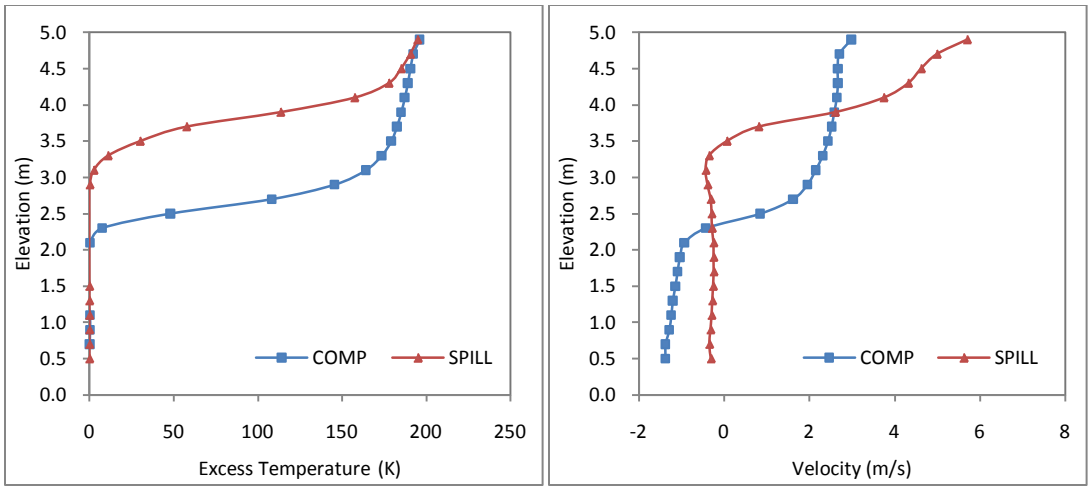

Figure G30: Vertical temperature and velocity profiles for simulation F3R

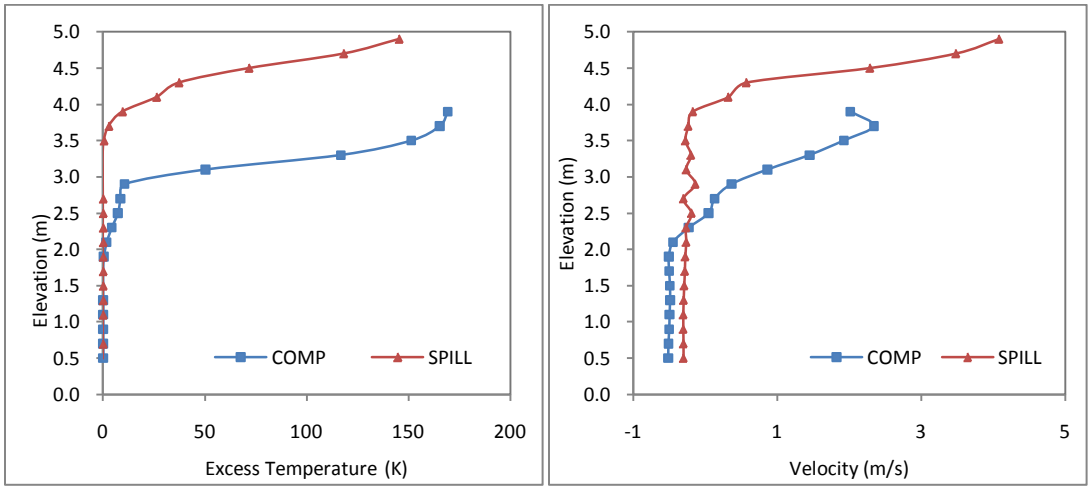

Figure G31: Vertical temperature and velocity profiles for simulation F4R

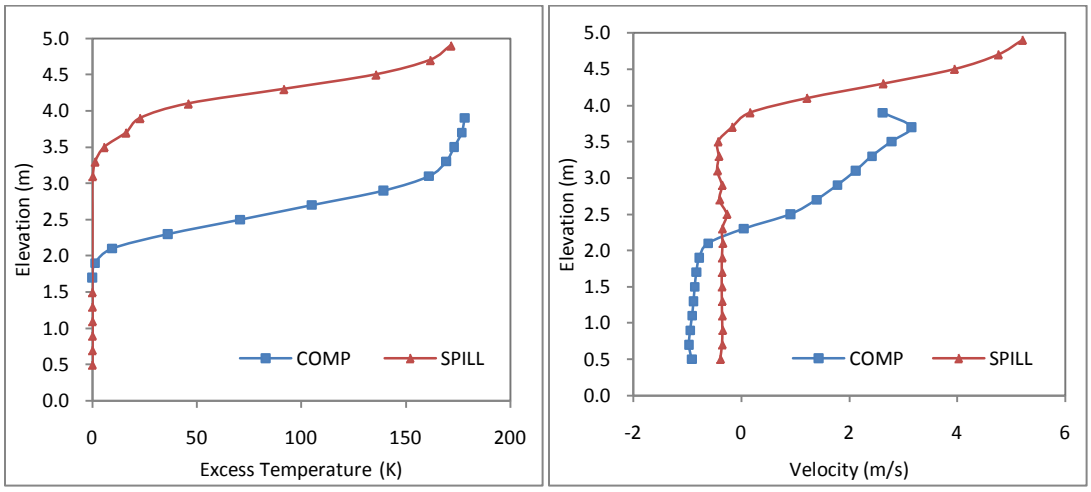

Figure G32: Vertical temperature and velocity profiles for simulation F5R

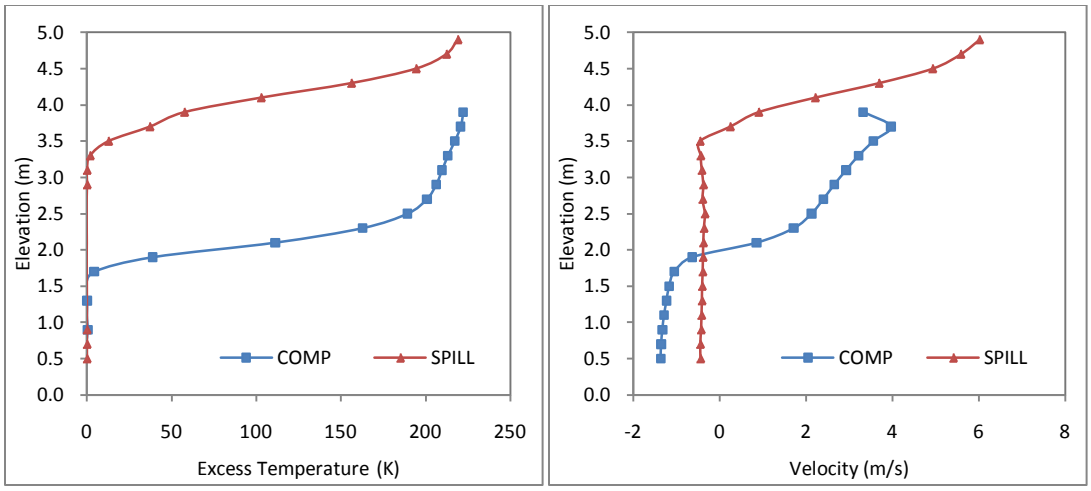

Figure G33: Vertical temperature and velocity profiles for simulation F6R

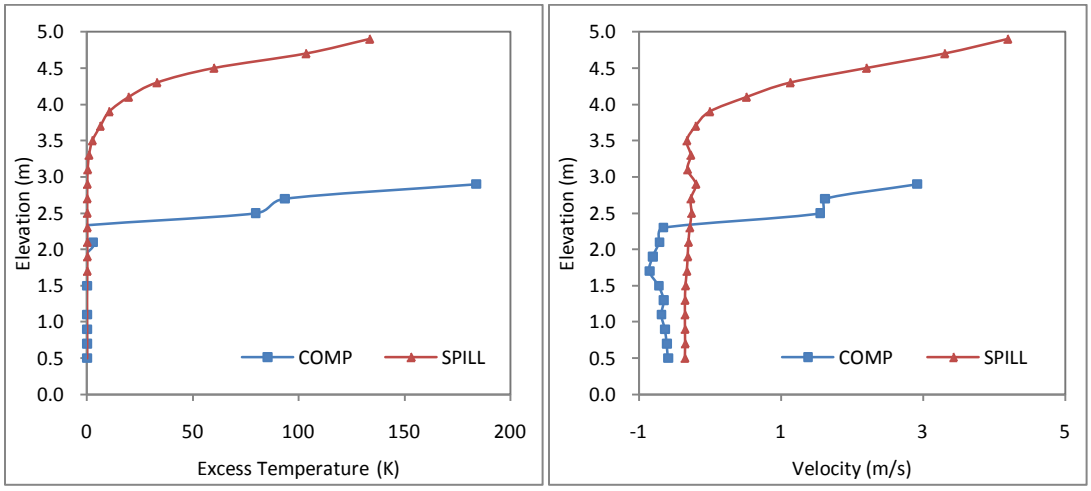

Figure G34: Vertical temperature and velocity profiles for simulation F7R

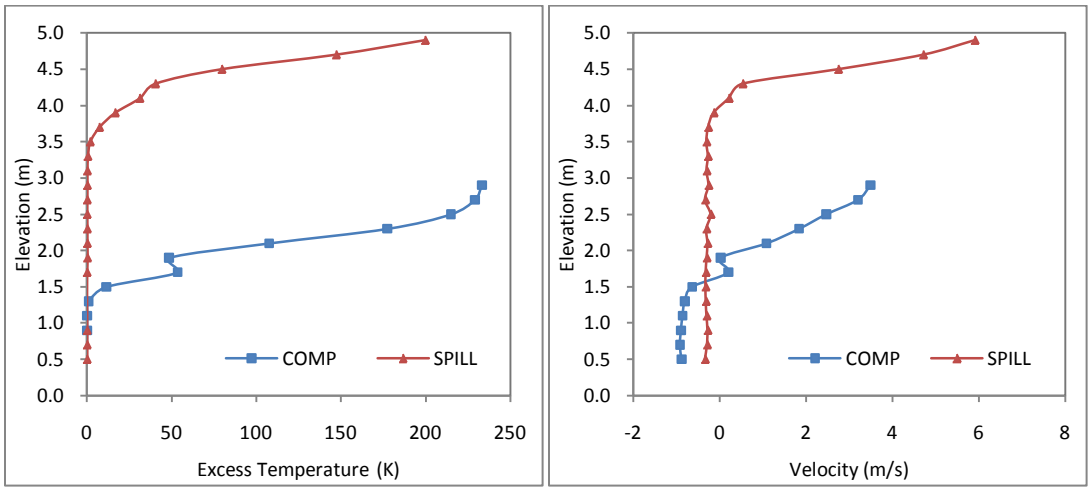

Figure G35: Vertical temperature and velocity profiles for simulation F8R

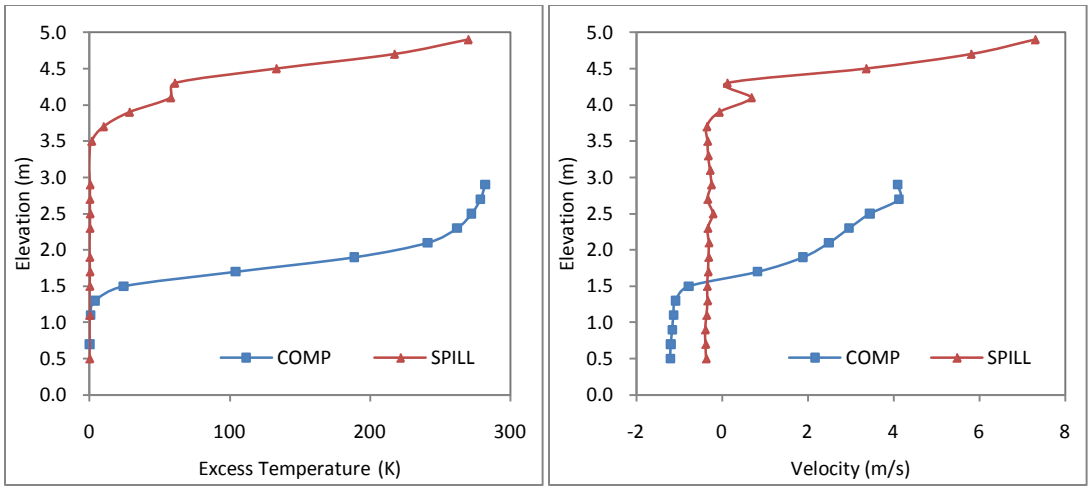

Figure G36: Vertical temperature and velocity profiles for simulation F9R

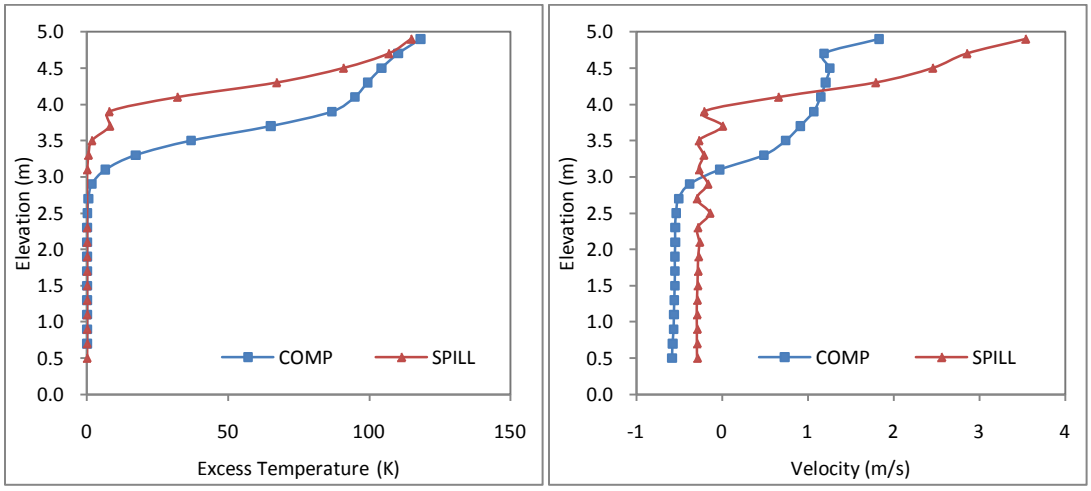

Figure G37: Vertical temperature and velocity profiles for simulation F10R

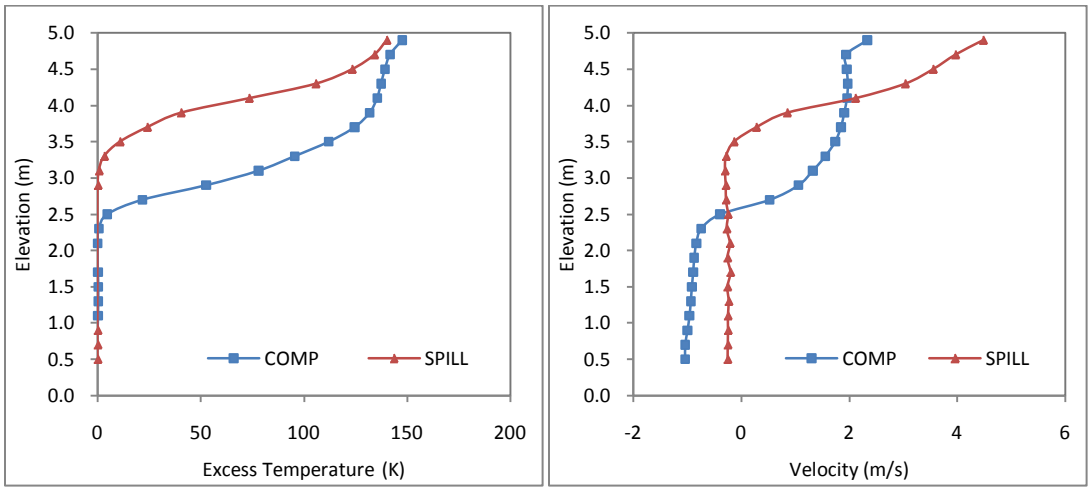

Figure G38: Vertical temperature and velocity profiles for simulation F11R

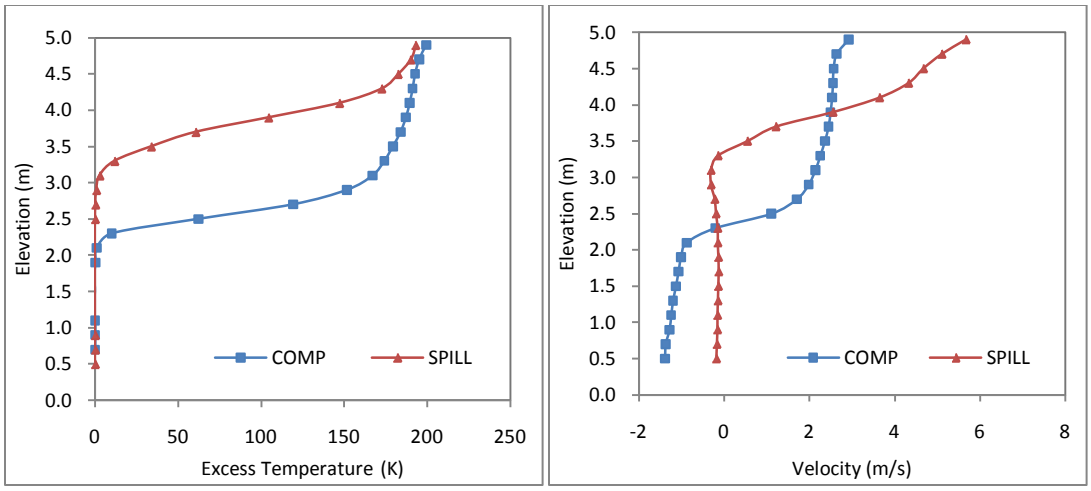

Figure G39: Vertical temperature and velocity profiles for simulation F12R

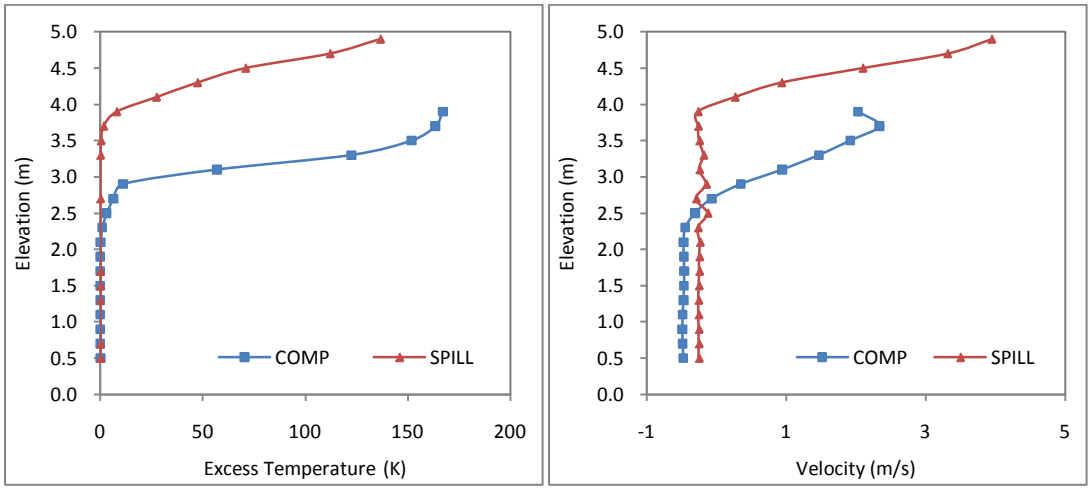

Figure G40: Vertical temperature and velocity profiles for simulation F13R

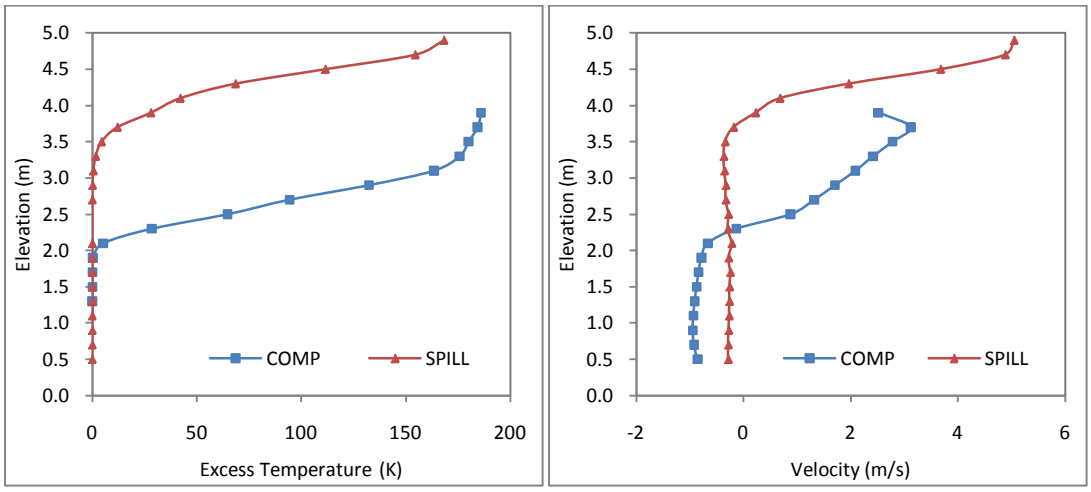

Figure G41: Vertical temperature and velocity profiles for simulation F14R

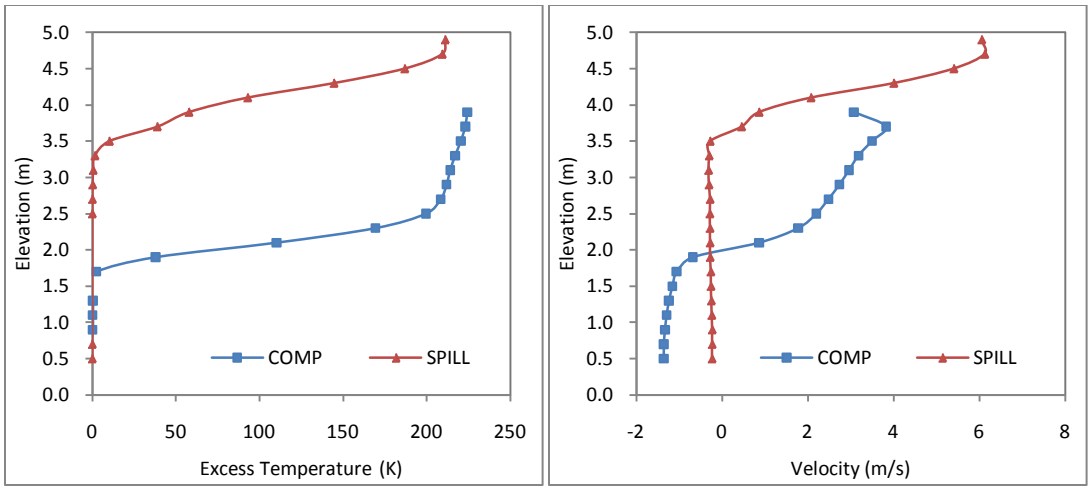

Figure G42: Vertical temperature and velocity profiles for simulation F15R

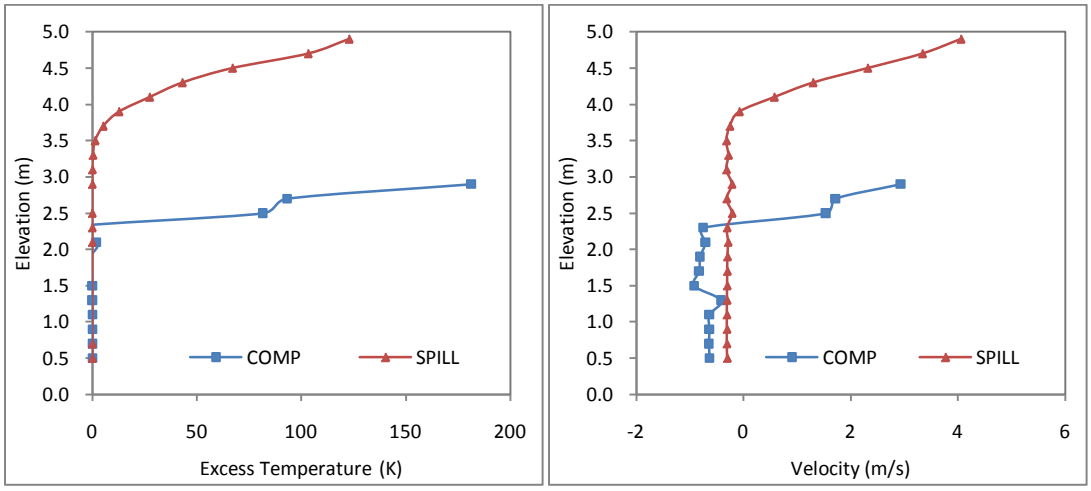

Figure G43: Vertical temperature and velocity profiles for simulation F16R

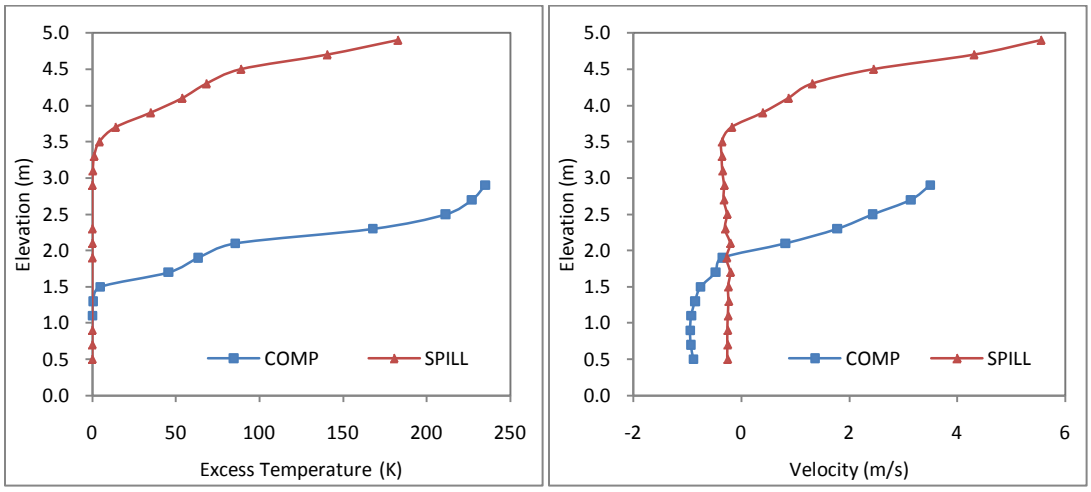

Figure G44: Vertical temperature and velocity profiles for simulation F17R

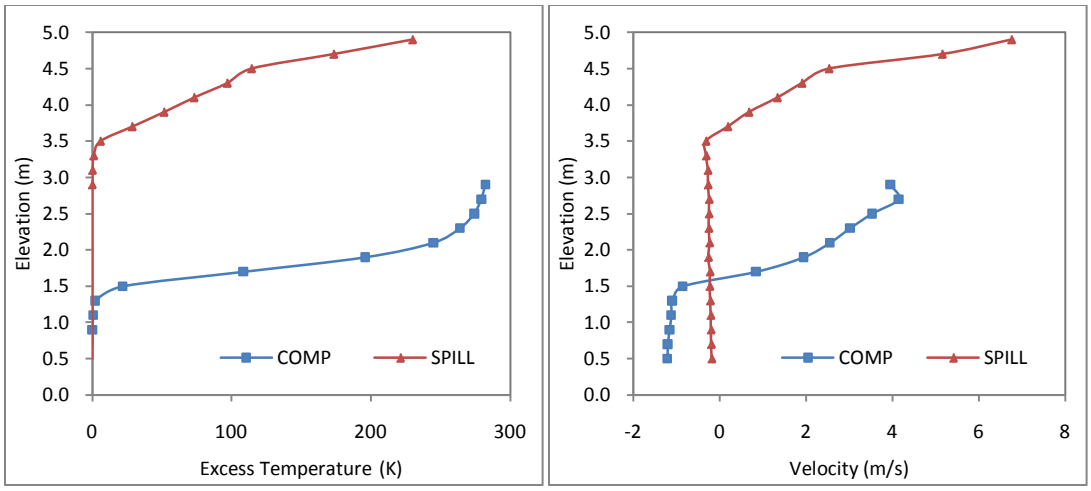

Figure G45: Vertical temperature and velocity profiles for simulation F18R

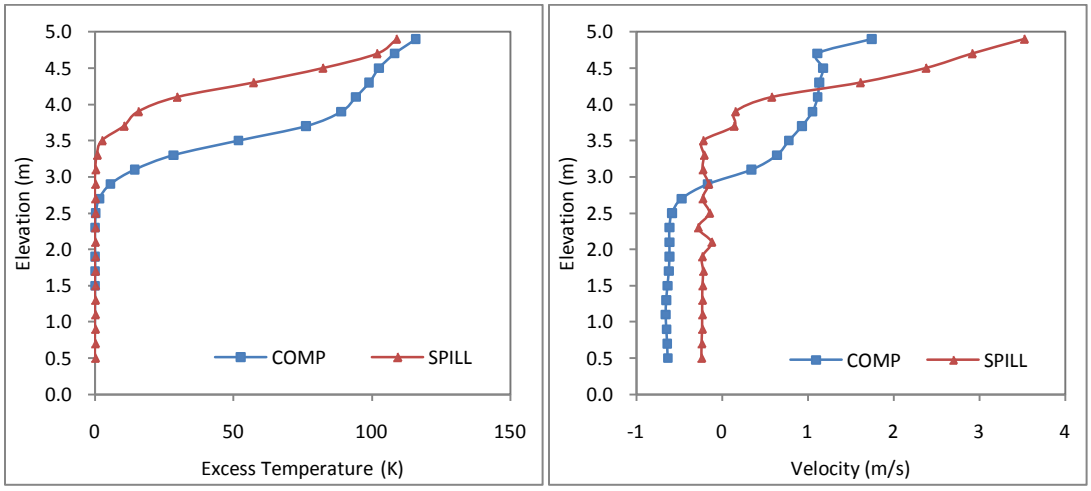

Figure G46: Vertical temperature and velocity profiles for simulation F19R

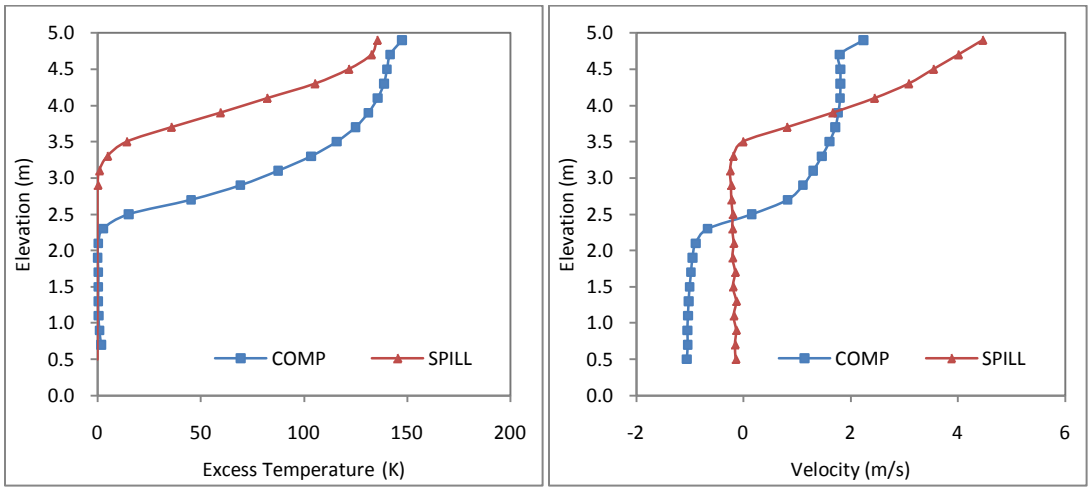

Figure G47: Vertical temperature and velocity profiles for simulation F20R

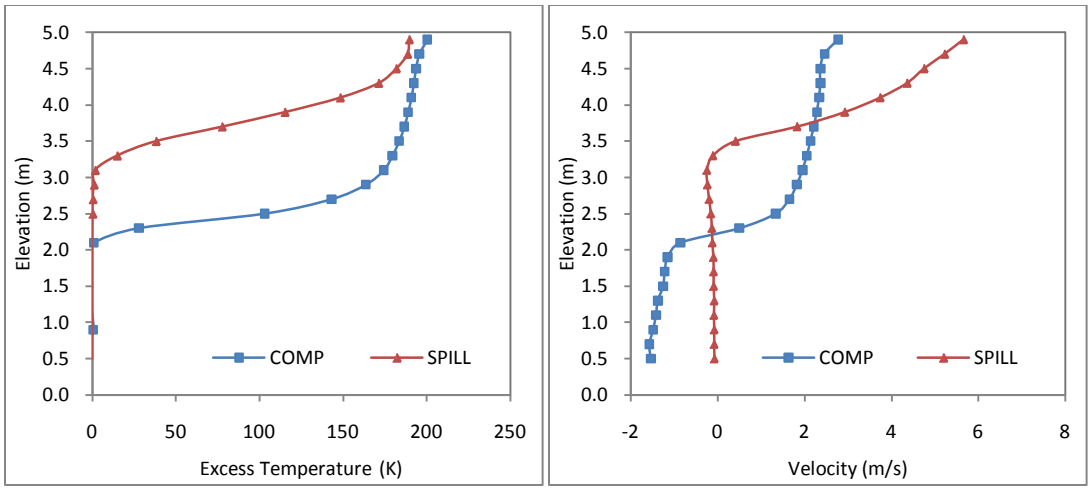

Figure G48: Vertical temperature and velocity profiles for simulation F21R

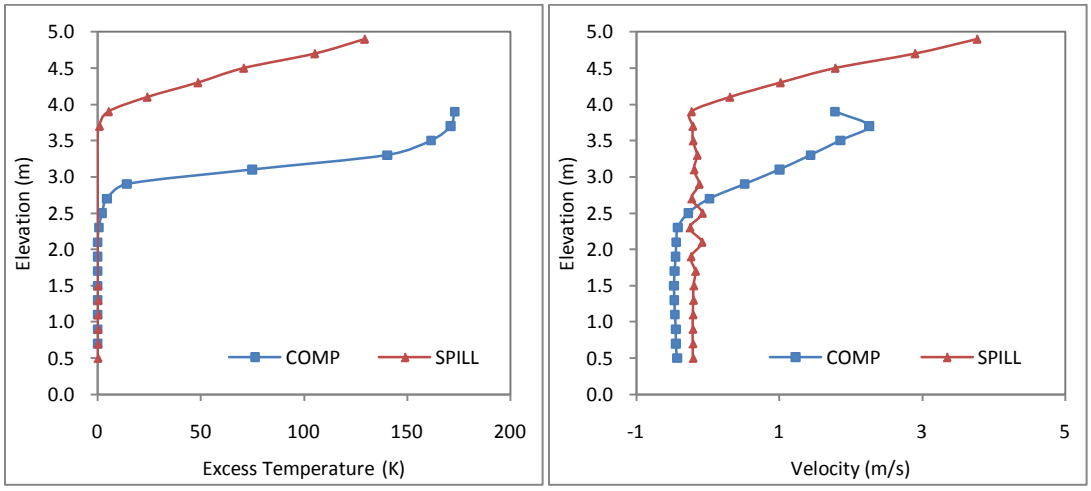

Figure G49: Vertical temperature and velocity profiles for simulation F22R

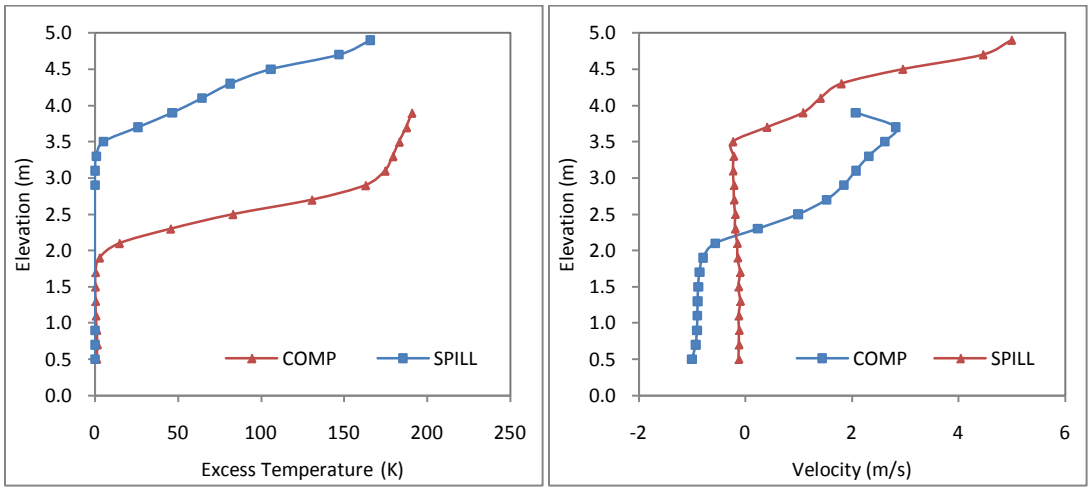

Figure G50: Vertical temperature and velocity profiles for simulation F23R

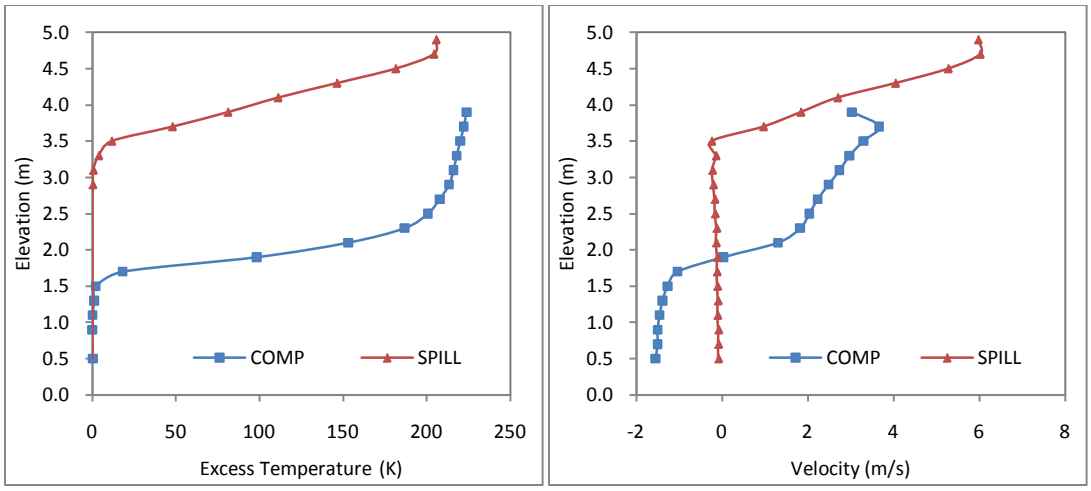

Figure G51: Vertical temperature and velocity profiles for simulation F24R

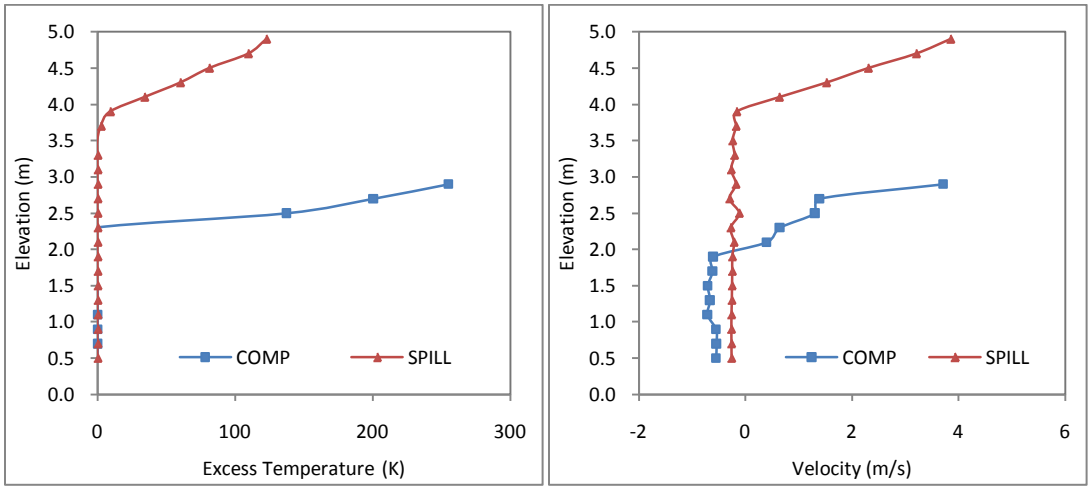

Figure G52: Vertical temperature and velocity profiles for simulation F25R

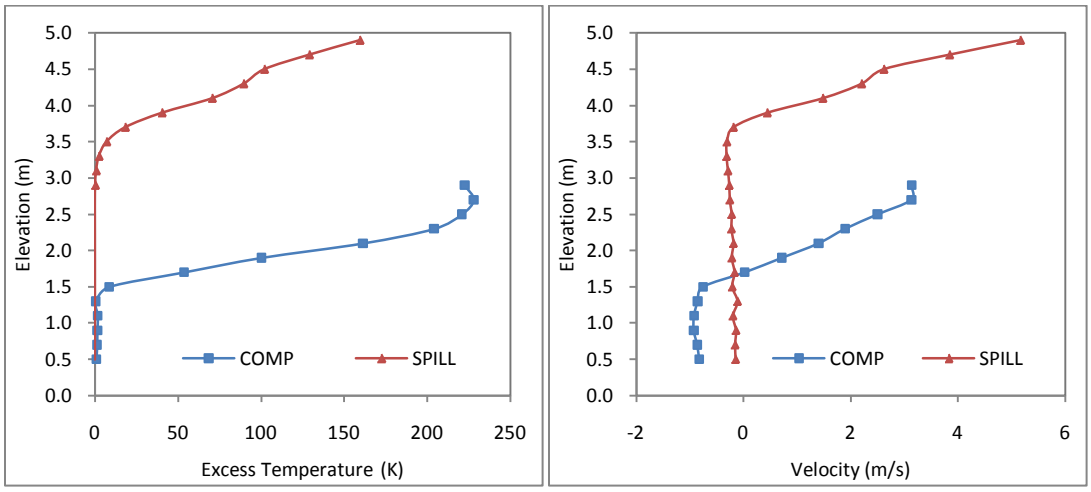

Figure G53: Vertical temperature and velocity profiles for simulation F26R

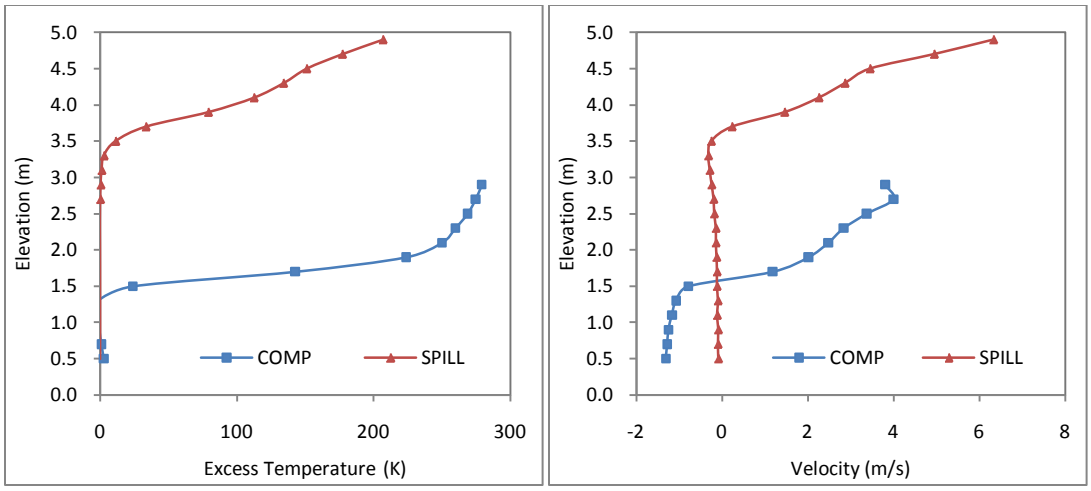

Figure G54: Vertical temperature and velocity profiles for simulation F27R

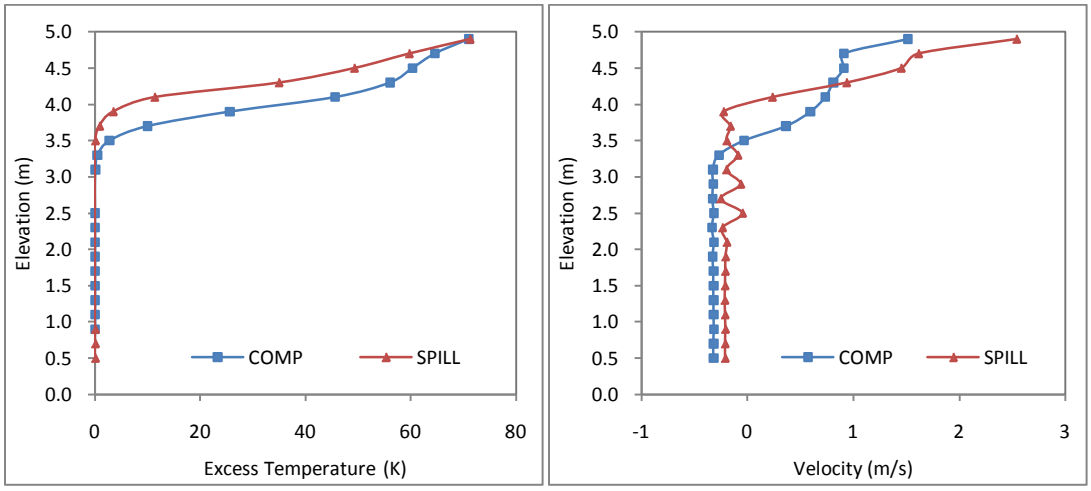

Figure G55: Vertical temperature and velocity profiles for simulation F1RR

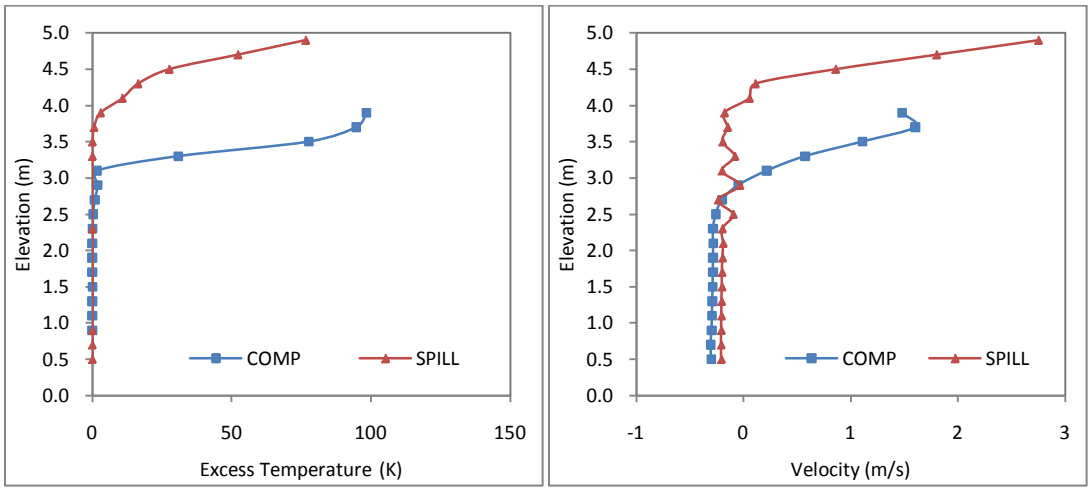

Figure G56: Vertical temperature and velocity profiles for simulation F4RR

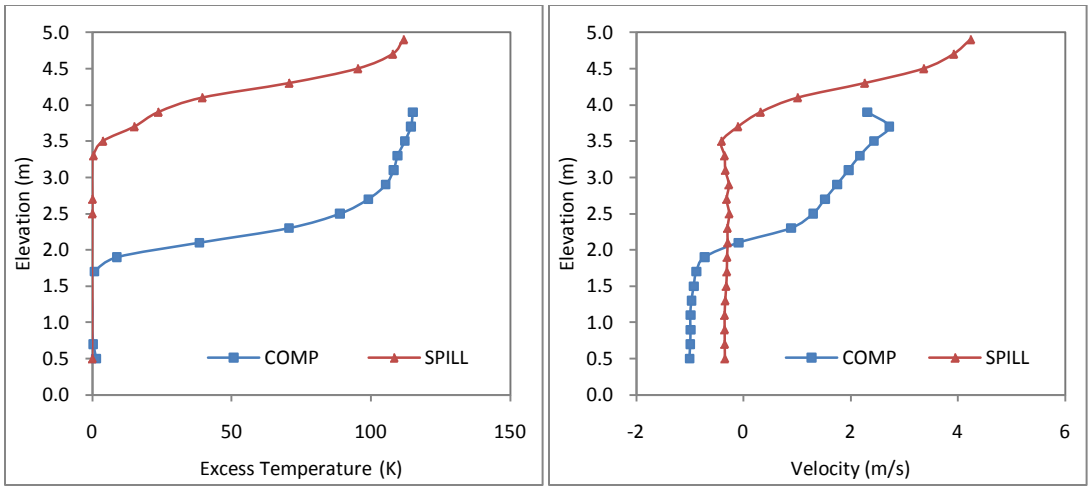

Figure G57: Vertical temperature and velocity profiles for simulation F6RR

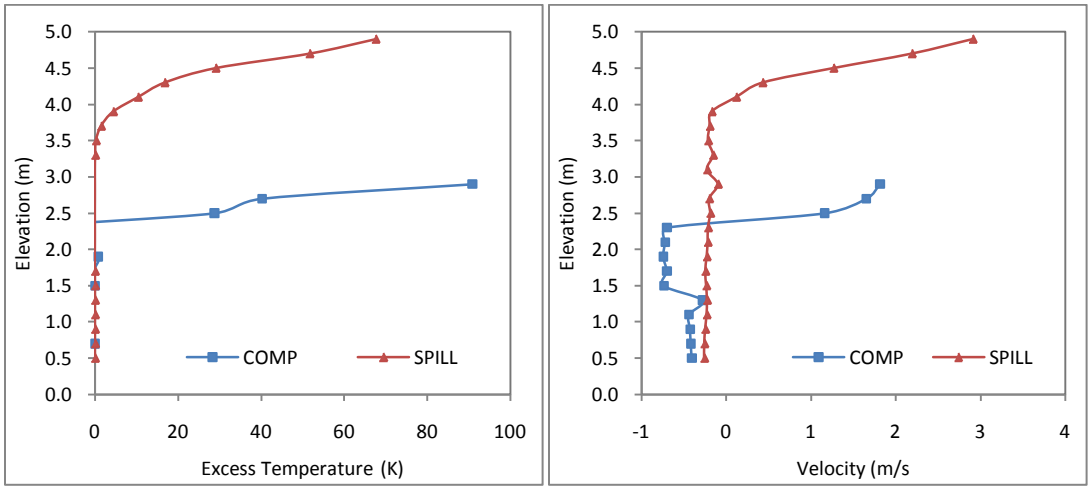

Figure G58: Vertical temperature and velocity profiles for simulation F7RR

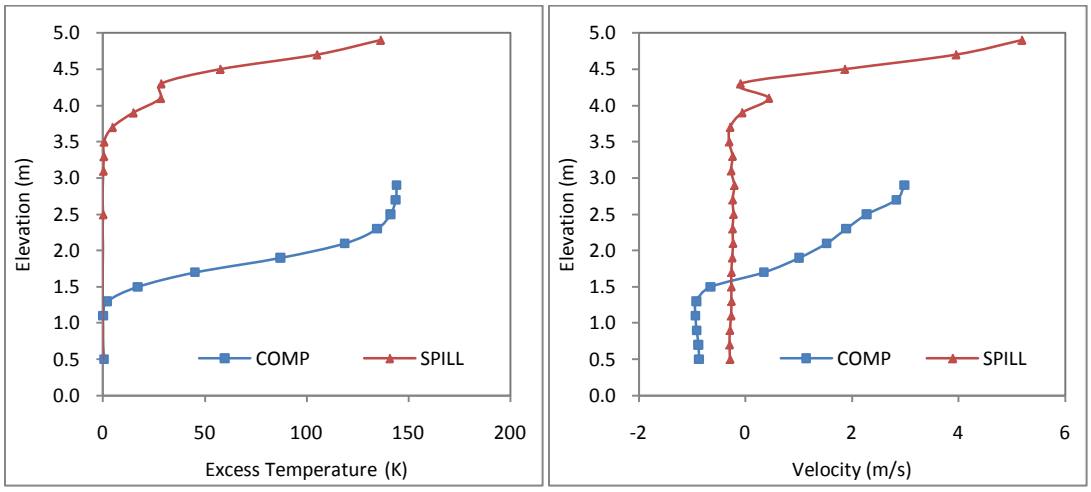

Figure G59: Vertical temperature and velocity profiles for simulation F9RR

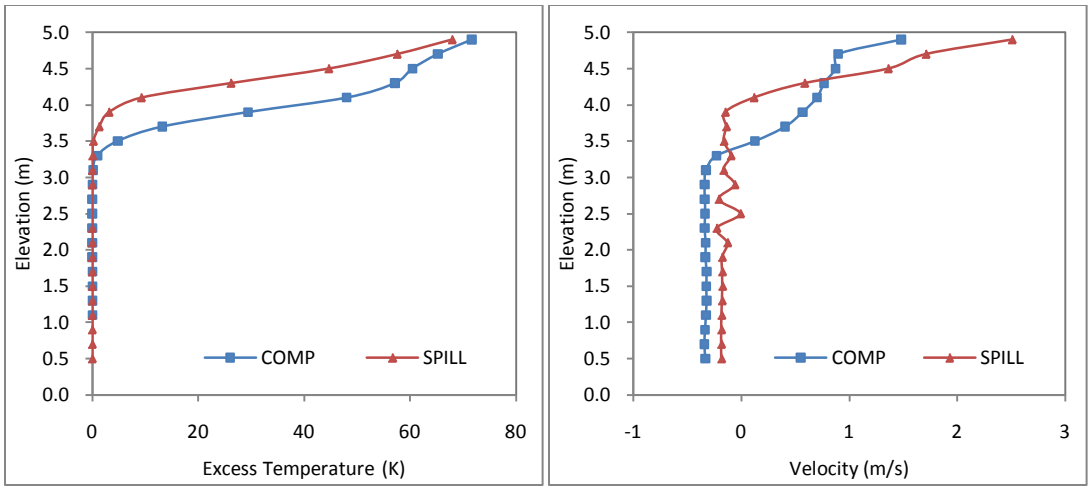

Figure G60: Vertical temperature and velocity profiles for simulation F10RR

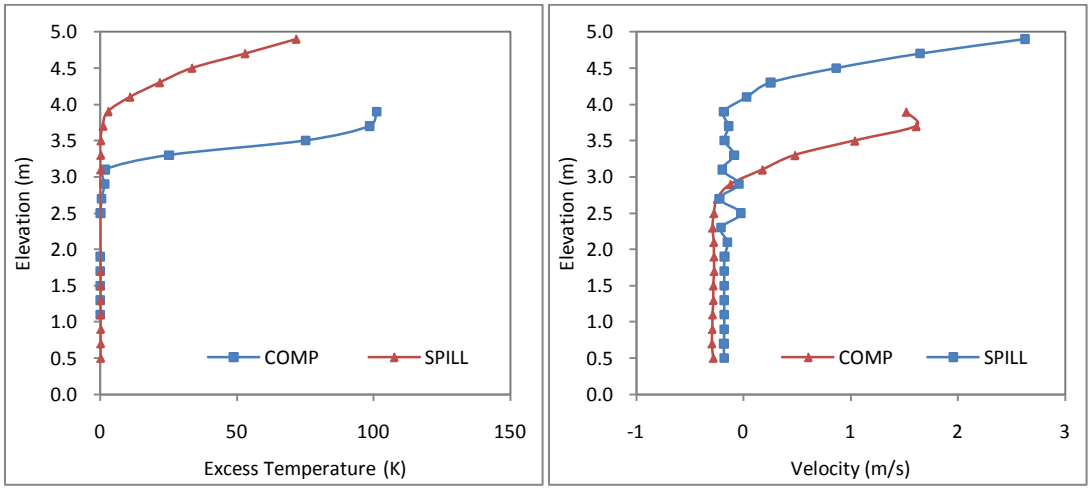

Figure G61: Vertical temperature and velocity profiles for simulation F13RR

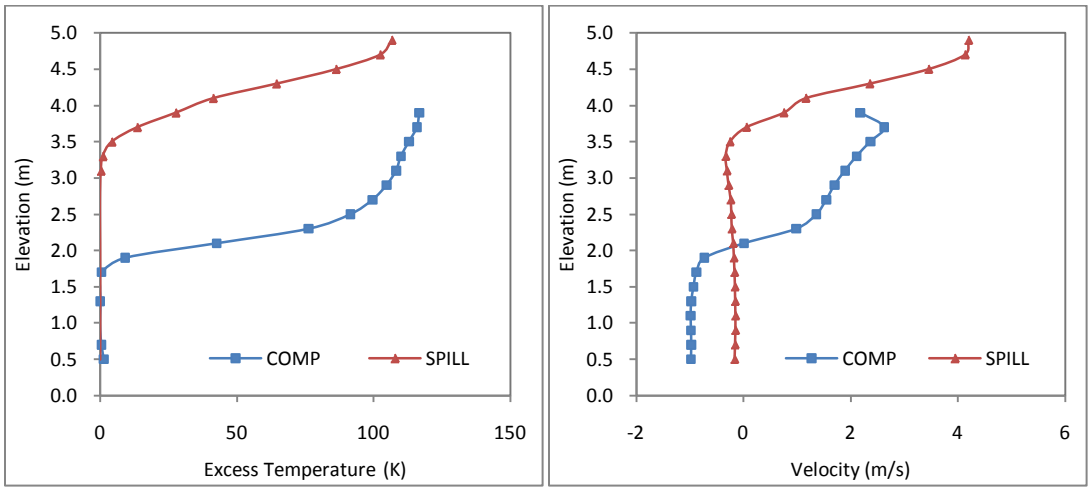

Figure G62: Vertical temperature and velocity profiles for simulation F15RR

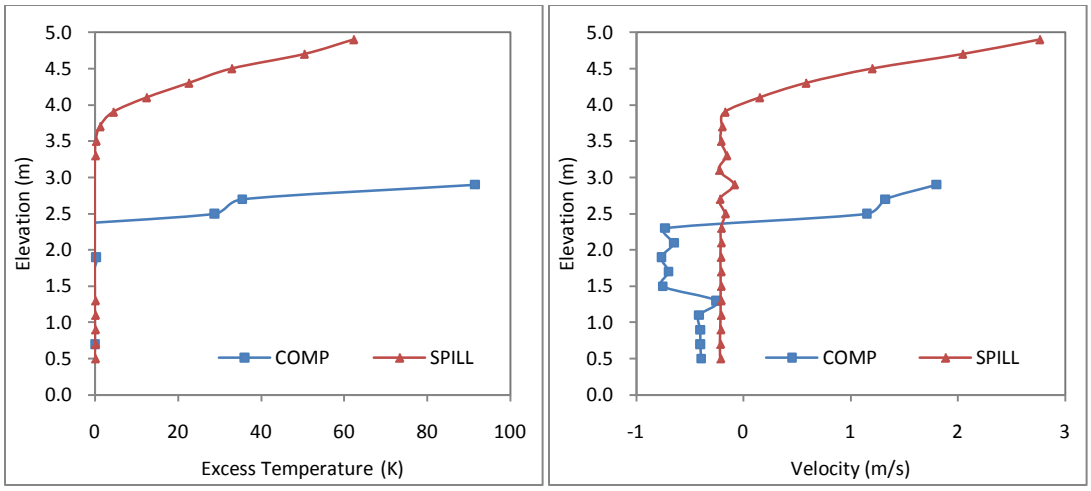

Figure G63: Vertical temperature and velocity profiles for simulation F16RR

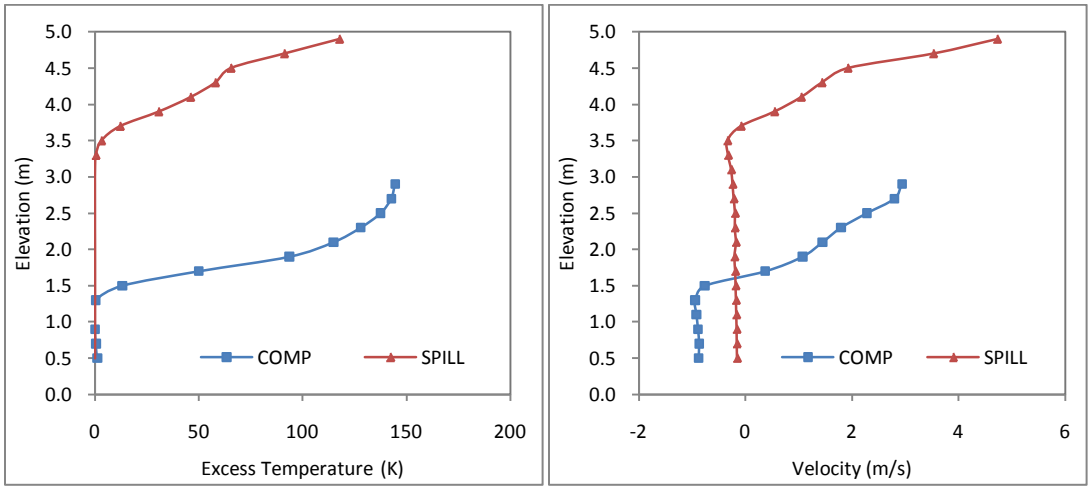

Figure G64: Vertical temperature and velocity profiles for simulation F18RR

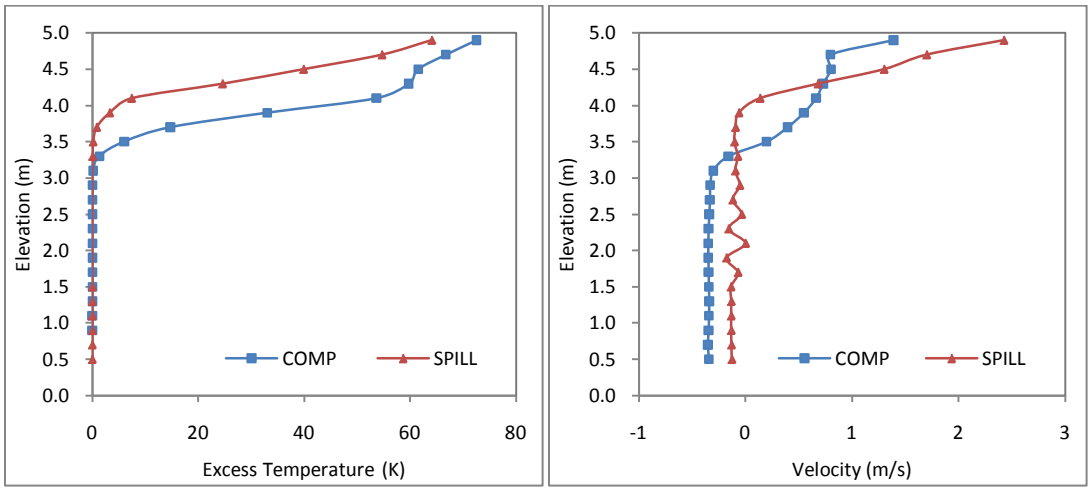

Figure G65: Vertical temperature and velocity profiles for simulation F19RR

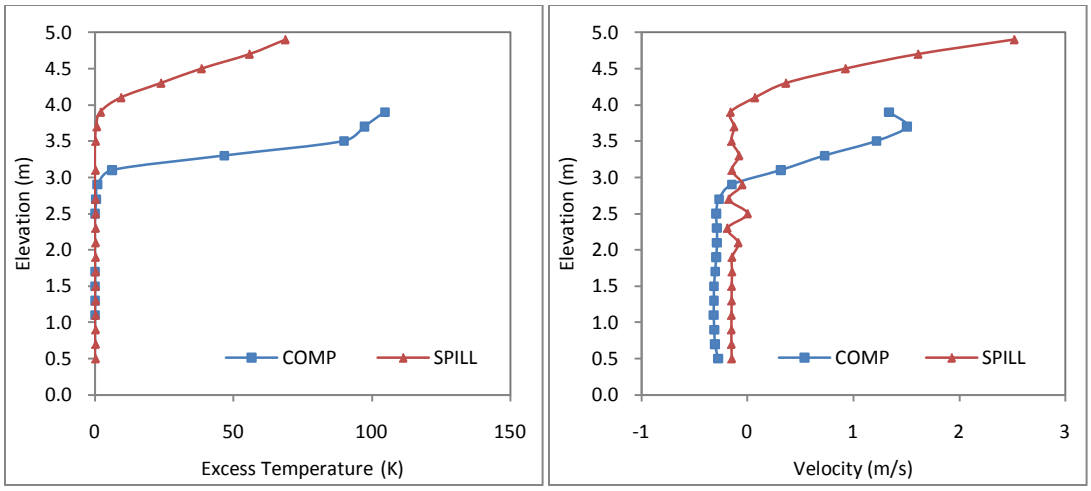

Figure G66: Vertical temperature and velocity profiles for simulation F22RR

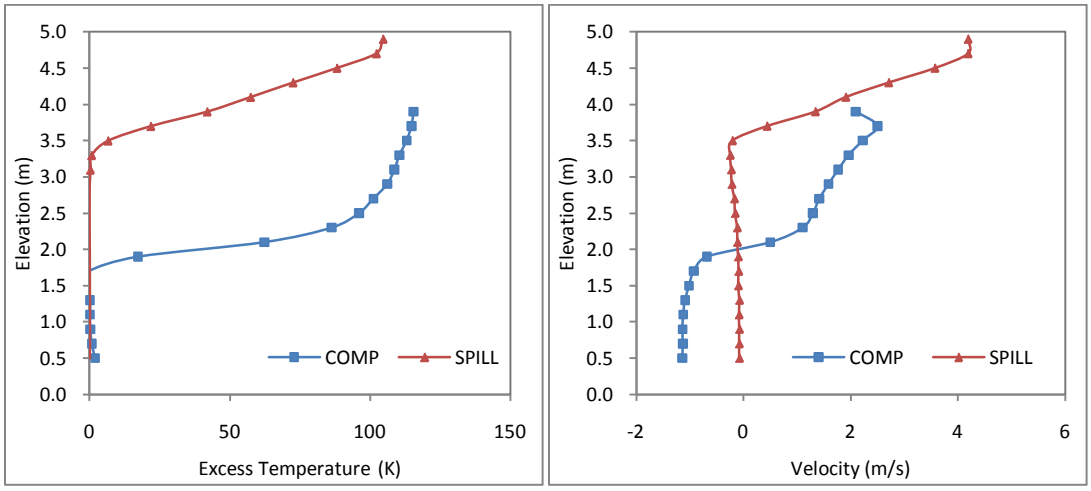

Figure G67: Vertical temperature and velocity profiles for simulation F24RR

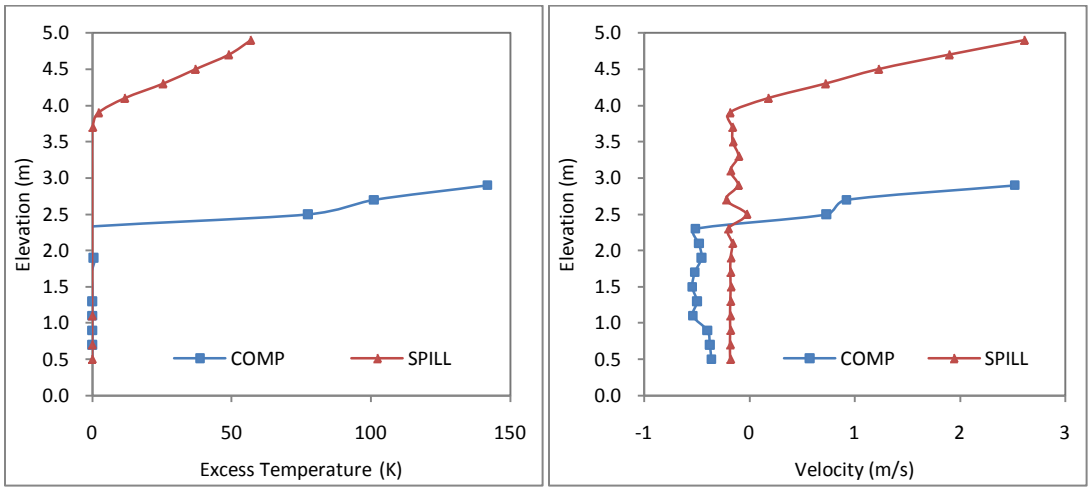

Figure G68: Vertical temperature and velocity profiles for simulation F25RR

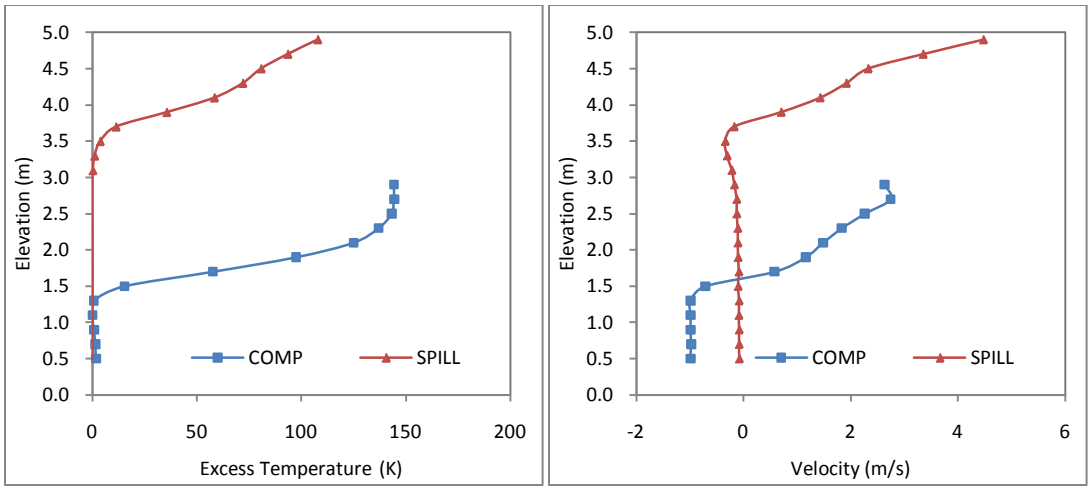

Figure G69: Vertical temperature and velocity profiles for simulation F27RR

11. Bibliography

1. Saxon, R. *Atrium buildings, development and design.* London : The Architectural Press, 1983.
2. National Fire Protection Association. *NFPA 92B Smoke management systems in malls, atria and large areas.* Quincy, MA 2009.
3. Klote, J H and Milke, J A. *Principles of smoke management.* Atlanta, GA : American Society of Heating, Refrigerating and Air-conditioning Engineers, 2002.
4. Cote, A E, et al. *Fire Protection Handbook, 20th Ed, Vol. 1, Chpt 2, Sect 6, pp 11-34.* 20th. Quincy, MA : National Fire Proctection Association, 2008.
5. Purser, D A. Toxicity assessment of combustion products. *SFPE Handbook of Fire Protection Engineering, 3rd Edition, NFPA, Chapter 6, Section 2.* Quincy MA : s.n., 2002.
6. Milke, James A. Smoke management in covered malls and atria. *Chapter 13, Section 4, SFPE Handbook of Fire Protection Engineering, 3rd Edition.* Quincy, MA : NFPA, 2002.
7. Spearpoint, M J. *Fire Engineering Design Guide.* New Zealand : Centre for Advanced Engineering, 2008.
8. T, Jin. *Visibility through fire smoke. Part 5. Allowable smoke density for escape from fire.* s.l. : Report of Fire Research Insititute of Japan. No.42, 1976.
9. Milke, J A. Smoke management for covered malls and atria. *Fire Technology.* 1990, Vol. 26, 3, pp. 223-243.
10. Morgan, H P, et al. *Design methodologies for smoke and heat exhaust ventilation.* s.l. : BRE Report 368, 1999.
11. National Fire Protection Association. *NFPA 101: Life Safety Code.* Quincy, MA 2005.
12. National Fire Protection Association. *NFPA 72: National Fire Alarm and Signaling Code.* Quincy, MA 2009.
13. Morton, B R, Taylor, G I and Turner, J S. Turbulent gravitational convection from maintained and instantaneous sources. *Proc. Royal Society, A234, pp 1-23,.* pp. 1-23.
14. Cetegen, B M, Zukoski, E E and Kubota, T. Entrainment in the near and far field of fire plumes. *Combustion Science and Technology.* 1984, Vol. 39, pp. 305-331.
15. Zukoski, E E. Properties of fire plumes. [ed.] Cox G. *Combustion Fundamentals of Fire.* 1995.

16. Poreh, M and Garrad, G. A study of wall and corner fire plumes. *Fire Safety Journal.* 2000, Vol. 34, 1, pp. 81-98.

17. Aplert, R L. Ceiling Jet Flows. *SFPE Handbook of Fire Protection Engineering, 4th Edition, Chap 2, Sect 2.* NFPA, Quincy, MA, 2008.

18. Hansell, G O, Morgan, H P and Marshall, N R. Smoke flow experiments in a model atrium. *Building Research Establishment Occasional Paper, OP 55.* 1993.

19. Poreh, M, et al. Entrainment by two dimensional spill plumes in malls and atria. *Fire Safety Journal, vol. 30, no.1, pp 1-19.* 1998.

20. Quintiere, J G and DenBraven, K. Some Theoretical Aspects of Fire Induced Flows hrough Doorways in a Room-Corridor Scale Model, NBSIR 78-1512. *National Bureau of Standards (U.S.).* October 1978.

21. Steckler, K D, Quintiere, J G and Rinkinen, W J. Flow induced by fire in a compartment. *Proceedings of the 19th international symposium on combustion.* 1982, pp. 913-920.

22. Quintiere, J G, Rinkinen, W J and Jones, W W. The effects of room openings on fire plume entrainment. *Combustion Science and Technology, vol. 26, no. 5, pp 193-201.* 1981.

23. Prahl, J and Emmons, H W. Fire indused gas flow in an enclosure. *Combustion and Flame, vol. 25, no. 3, pp 369-385.* 1975.

24. Thomas, P H, et al. *Investigations into the flow of hot gases in roof venting. Fire Research Technical Paper No 7.* London : The Stationary Office, 1963.

25. Morgan, H P. The horizontal flow of buoyant gases toward an opening. *Fire Safety Journal, vol. 11, no. 3, pp 193-200.* 1986.

26. Zukoski, E E, Kubota, T and Cetegen, B. Entrainment in fire plumes. *Fire Safety Journal, vol. 3, no. 3, pp 107-121.* 1980.

27. Hinkley, P L. Rates of production of hot gases in roof venting experiments. *Fire Safety Journal, No. 10, pp 57-65.* 1986.

28. Hansell, G O. *Heat and mass transfer process affecting smoke control in atrium buildings.* PhD thesis, South Bank University : s.n., 1993.

29. Chartered Institution of Building Services Engineers. CIBSE Guide Volume E: Fire Engineering. London, CIBSE, 2003.

30. British Standards Instiution. PD 7974: Application of fire safety engineering principles to the design of buildings. Part 2: Spread of smoke and toxic gases within and beyond the enclosure of origin. London, BSI, 2002.

31. Hansell, G O and Morgan, H P. Design approaches for smoke conrol in atrium buildings. BR 258, 1994.

32. Harrison, R. Smoke Control in Atrium Buildings: A study of the thermal spill plume. *Fire Engineering Research Thesis 04/1.* Department of Civil Engineering, University of Canterbury, New Zealand, April 2004.

33. McGrattan, K B, et al. Fire Dynamics Simulator (Version 3) - User Guide. *NISTIR 6784, National Institute of Technology and Standards, 2002.*

34. Ko, Y J. *CFD Study of Balcony Spill Plumes:Focused on the Balcony Area, Master of Applied Science in Civil Engineering Thesis.* Carleton University, Ottawa, ON, Canada : s.n., 2006.

35. Morgan, H P and Gardner, J P. Design principles for smoke ventilation in enclosed shopping centres. *BR 186, BRE.* 1990.

36. Heselden, A J M. Fire problems of pedestrian precincts: Part 1. The smoke production of various materials. *Fire Research Note 856.* Fire Research Station, Borehamwood, 1971.

37. Lee, Shao-Lin and Emmons, H W. A study of natural convection above a line fire. *Journal of Fluid Mechanics, vol. 11, no. 3, pp 353-368.* 1961.

38. Yuan, L U and Cox, G. An experimental study of some line fires. *Fire Safety Journal, vol. 27, no. 2, pp 123-139.* 1996.

39. Rouse, H, Yih, C S and Humphreys, H W. Gravitational convection from a boundary source. *Tellus, 4, pp 201-210.* 1952.

40. Yokoi, S. Study on the prevention of fire spread by hot upward current. *Building Research Institute Report.* Japan, 1960.

41. Kotsovinos, N E. A study of the entrainment and turbulence in a plane buoyant jet. *W M Keck Laboratory of Hyydraulics and Water Resrouces Report KH-R-32.* California Institute of Technology, Pasedena, CA, 1975.

42. Ramaprian, B R and Chandrasekhara, M S. Measurements in vertical plane turbulent plumes. *Journal of Fluids Engineering, vol. 111, no. 1, pp 69-77.* 1989.

43. Morgan, H P and Marshall, N R. Smoke hazards in covered multi-level shopping malls: an experimentally-based theory for smoke production. *BRE Current Paper 48/75.* 1975.

44. Morgan, H P and Hansell, G O. Atrium buildings: Calculating smoke flows in atria for smoke control design. *Fire Safety Journal, vol. 12, no. 1, pp 9-25.* 1987.

45. Miles, S, Kumar, S and Cox, G. The balcony spill plume - Some CFD simulations. *Fire Safety Science - Proceedings of the 5th Symposium of the International Association of Fire Safety Science.* pp. 237-247.

46. Yii, E H. Exploratory salt water experiments of balcony spill plume using laser induced flourescence technique. *Fire Engineering Reseach Report.* University of Canterbury, 1998.

47. Morgan, H P and Marshall, N R. Smoke control measures in a covered two-storey shopping mall having balconies and pedestrian walk ways. *BRE Current paper 11/79.* BRE, 1979.

48. Marshall, N R and Harrison, R. *Experimental studies of thermal spill plumes.* s.l. : Building Research Establishment Occasional Paper, OP1, 1996.

49. Thomas, P H, Morgan, H P and Marshall, N R. The spill plume in smoke control design. *Fire Safety Journal, vol. 30, no.1, pp 21-46.* 1998.

50. Harrison, R. *Entrainment of Air into Thermal Spill Plumes. PhD Thesis.* University of Canterbury, New Zealand : s.n., April 2009.

51. Harrison, R and Spearpoint, M J. Entrainment of air into a balcony spill plume. *Journal of Fire Protection Engineering, vol.16, no.3, pp 211-245.* 2006.

52. Olenick, S M and Carpenter, D J. An Updated International Survey of Computer Models for Fire and Smoke. *Journal of Fire Protection Engineering, Vol. 13.* May 2003.

53. *BRE Global, Watford, UK.*

54. Chow, W K and Li, J. Simulation on natural smoke filling in atrium with a balcony spill plume. *Journal of Fire Sciences, vol. 19, no. 4, pp 258-277.* 2001.

55. National Fire Protection Association. Smoke management systems in malls, atria and large areas. *Publication No. 92B.* 1995, Quincy, MA, 1995.

56. Jones, W W, et al. A technical reference for CFAST: an engineering tool for estimating fire and smoke transport. *National Institute of standards and Technology, NIST TN 1431, Building and Fire Research Laboratory.* Maryland, USA, 2000.

57. Li, J and Chow, W K. Numerical simulations on aerodynamics of thermally induced plumes. *Journal of Fire Sciences, vol. 25, no. 2, pp 119-160.* 2007.

58. *Concentration Heat and Momentum Limited, Wimbledon, London.*

59. Thomas, P H. On the upward movement of smoke and related shopping mall problems. *Fire Safety Journal, vol. 12, no. 3, pp 191-203.* 1987.

60. McCartney, C J. *A CFD Investigation of Balcony Spill Plumes. Master of Applied Science in Mechanical Engineering Thesis.* University of Waterloo, Waterloo, ON, Canada 2006.

61. McGrattan, K B, et al. Fire Dynamics Simulator (Version 5) - Technical Reference Guide, Volume 3: Validation. NIST Special publication 1018-5, 2009.

62. Nowlen, S P. *Enclosure Environment Charaterization Testing for the bAseline Validation of Computer Fire Simulation Codes. NUREG/CR-4681 (SAND86-1296).* Sandia National Laboratory, Albuqueque, New Mexico, March 1987.

63. Hamins, A, et al. Report of Experimental Results for the International Fire Model Benchmarking and Validation Exercise 3. *NIST Special Publication 1013-1, National Institute of Standards and Technology.* Gaithersburg, Maryland, May, 2006.

64. Hurley, M J and Munguia, A. Analysis of FDS Thermal Detector Response Prediction Capability. *NIST GCR 09-921. National Institute of Standards and Technology.* Gaithersburg, MD, January, 2009.

65. Fire Envvironment Tests Under Fire Ceilings. *Test Report R18476-96NK37932.* Underwriters Laboratories, Northbrook, IL, October 1998.

66. Ierardi, J A and Barnett, J R. Quantitative Method for Calibrating CFD Model Calculations. *CIB-CTBUH Conference on Tall Buildings. CIB Publication No. 2900.* Kuala Lumpur, Malaysia, 2003.

67. McGrattan, K B, et al. *Fire Dynamics Simulator (Version 5) - User Guide.* s.l. : NIST Special publication 1019-5, 2008.

68. McDermott, R. FDS Wall Flows Part 1: Straight Channels. *NIST Technical Note 1640, Building and Fire Research Laboratory, National Institute of Standards and Technology.* Gaithersburg, MD, July 2009.

69. Alpert, R L. Ceiling Jet Flows. *SFPE Handbook of Fire Protection Engineering, 3rd Edition, Chap 2, Sect 2.* NFPA, Quincy, MA, 2002.

70. Heskestad, G. Physical Modeling of Fire. *Journal of Fire & Flammability, 6, p. 253.* 1975.

71. Heskestad, G. Fire Plumes, Flame Height and Air Entrainment. *SFPE Handbook of Fire Protection Engineering, 3rd Edition, Chap 1, Sect 2.* NFPA, Quincy, MA, 2002.

72. Motevalli, V and Marks, C. H. Characterizing the Unconfined Ceiling Jet under Steady-State Conditions: A Reassessment. *Fire Safety Science, Preceedings of the Third International Symposium (G. Cox and B. Langford, eds), p. 301.* Elsevier Applied Science, New York, 1991.

73. Heskestad, G and Smith, H. FMRC Serial Number 22485. Factory Mutual Research Corp., Norwood, MA (1976).

74. Schifiliti, Robert P., Meacham, Brian J and Custer, Richard L. P. Design of Detection Systems. *SFPE Handbook of Fire Protection, 3rd Ed.* NFPA, Quincy, MA, 2002.

75. Drysdale, D. *An Introduction to Fire Dynamics.* 2nd Edition. WIley Press.

76. Tewarson, Archibald. Generation of Heat and Chemical Compounds in Fires. *SFPE Handbook of Fire Protection, 3rd Ed.* NFPA, Quincy, MA, 2002.

77. Quintiere, J G. *Fundamentals of fire phenomena.* Wiley Press : s.n., 2006.